Dimensionality-Property Relationships in Functional Hexahydroxytriphenylene- and Cyanide-Containing Materials



Jasper Adamson
St Anne's College
University of Oxford

A thesis submitted for the degree of Doctor of Philosophy

Michaelmas Term 2014

Abstract

This thesis focuses on materials whose properties are directly linked with the dimensionality of their structures. We utilise diffraction techniques to characterise three systems. The first of these is an organic crystal, 2,3,6,7,10,11-hexahydroxytriphenylene tetrahydrate that contains one-dimensional water channels. These channels are polar and net polarity is achieved at low temperatures. The structure undergoes a phase transition to a non-polar state at higher temperatures. Mapping this finding onto an Ising model is undertaken in this thesis. We also investigate the possibility of transforming the same crystals to an organic metal with oxidation. Furthermore, this work characterises two-dimensional layered structures silver(I) tricyanomethanide and nickel(II) cyanide. We show that the former possesses the unprecedented property of negative area compressibility and the latter shows ordinary compressibility behaviour. Both these structures exhibit area negative thermal expansion. Finally, we investigate copper(II) and cobalt(II) doping into the structure of nickel(II) cyanide and demonstrate that the latter leads to a 10-fold increase in area negative thermal expansion.

Extended Abstract

In this thesis, we study materials whose properties are directly linked with the dimensionality of their structures.

The first material examined is 2,3,6,7,10,11-hexahydroxytriphenylene (HHTP) tetrahydrate. We find that due to hydrogen-bonding of the HHTP molecules with the characteristic one-dimensional water channels in the structure, the water dipole orientations in the channels are constrained. This is in contrast to, for example, the most common polymorph of hexagonal ice, ice I_h, where no net dipole is observed due to disorder in the structure. Here we find that, at low temperatures, the channels each obtain a net dipole moment, which due to interactions between the channels 'communicate' with one another and net polarisation is observed. The low temperature structure crystallises in the space group $Pna2_1$, which reflects this polarity. At high temperatures the average structure is centrosymmetric and nonpolar, which result from an order-to-disorder phase transition, where the structure adopts water channel orientations that results in an equal proportion of the low temperature structure and its inverse. Such a phase transition can be characterised by an Ising model on a square lattice and an analysis of the structure in the context of the Ising model is undertaken in this thesis. We further show that there is extensive π-stacking amongst the parent HHTP molecules and thus, we set out to explore the hypothesis that by oxidation of some of the HHTP molecules in the crystals into one of their radical forms, one-dimensional bands could be formed in the structure, giving the material as a whole metallic properties. We do indeed show that oxidation of a portion of the HHTP molecules in the crystals is successful at high temperatures in air. The latter is confirmed by SQUID and EPR measurements. However, these results are coupled by PPMS heat capacity measurements that show the heat-treated crystals to be insulating. Furthermore, 4-point-gold-contact measurements with PPMS at different temperatures show that the heated material does not conduct. We postulate reasons why conductivity might not be observed, despite unpaired electrons being introduced into the system.

Secondly, we investigate two-dimensional layered materials. We look at silver(I) tricyanomethanide and nickel(II) cyanide. Our main interest in these systems is their thermal expansion and compressibility behaviour. It has been concluded based on multiple studies that despite the absence of any strict thermodynamic link between negative thermal expansion and negative compressibility, there is substantial empirical evidence that negative thermal expansion materials often also show negative linear compressibility. Our aim in this project is to prepare and characterise materials that could possess negative area compressibility. In the absence of a structural phase transition, it is a thermodynamic requirement of materials to reduce their volume with increasing pressure, and so negative area compressibility is highest-dimensional negative compressibility response allowed thermodynamically.

We chose to explore materials that exhibit area negative thermal expansion as good candidates for materials to show negative area compressibility. Area negative thermal expansion has been shown previously to arise in the two-dimensional layered structure nickel(II) cyanide and is a direct consequence of the low dimensionality of the material. Another candidate for area negative thermal expansion is silver(I) tricyanomethanide due to its similar layered structure and framework topology. We discover that silver(I) tricyanomethanide does indeed possess area negative thermal expansion and find that whereas nickel(II) cyanide shows ordinary compressibility behaviour, silver(I) tricyanomethanide does indeed possess the unprecedented negative area compressibility. A justification for these apparently conflicting observations is presented in this thesis. Finally, we explore the effect of connecting the layers of nickel(II) cyanide, by incorporating copper(II) and cobalt(II) ions into the structure. Our main focus here is on how this affects the materials' thermal expansion behaviour. Nickel(II) cyanide shows modest area negative thermal expansion within the square-grid layers of the structure and large positive thermal expansion parallel to the layers. We anticipate that the structures containing copper(II) remain square planar, however, our hope was to connect the layers by introducing cobalt(II) centres that can facilitate tetrahedral configuration and hence build a three-dimensional framework. We hypothised that such

an approach would result in coupling between the large positive thermal expansion and small negative area thermal expansion. We do indeed find that cobalt(II) nickel(II) cyanide shows very large negative area thermal expansion of an order of magnitude larger than that of pure nickel(II) cyanide, but the materials formed are substantially more disordered, which makes detailed structural investigations challenging.

The work presented in this dissertation is my own, unless otherwise stated.

Jasper Adamson

Acknowledgements

I am very grateful to my supervisor, Prof. Andrew Goodwin, for his guidance and support throughout this project. Completing a D.Phil. degree can be challenging intellectually and emotionally and hence thank you for all your patient help and support.
A big thank you to all members of the Goodwin group. In particular thanks to Dr. Paul Saines for his help with proof-reading and to Dr. Nicholas Funnell for his help with solving the crystal structures of 2,3,6,7,10,11-hexahydroxytriphenylene tetrahydrate and silver(I) tricyanomethanide and measuring the room-temperature powder patterns for cobalt(II) nickel(II) cyanide. I'd like to thank Part II students Sarah Hodgson and Sarah Hunt for their help with experiments for silver(I) tricyanomethanide and for assisting with data collections. Furthermore, Andrew Cairns helped with synchrotron measurements on nickel(II) cyanide and Matthew Cliffe with Rietveld refinements of the variable-temperature data for cobalt(II) nickel(II) cyanide.
Many thanks to all my collaborators during this project. Dr. Amber Thompson was of unparalleled help with collecting the data and solving the structures of 2,3,6,7,10,11-hexahydroxytriphenylene tetrahydrate. Dr. Matthew Tucker helped collect neutron data for nickel(II) cyanide and Dr. Joseph Hriljac and Dr. Timothy Lucas aided with synchrotron data collections for the same compound. SQUID magnetometry, PPMS heat capacity and conductivity measurements on 2,3,6,7,10,11-hexahydroxytriphenylene samples were performed in collaboration with Dr. Paul Goddard and his D.Phil. student Saman Ghannadzadeh and Dr. Jeffrey Harmer allowed us to perform EPR measurements on the same samples. Prof. David Keen was of great help when preparing the samples of cobalt(II) nickel(II) cyanide.
I am very lucky to have my great friends and especially Margit, Sven and Styna, Marit, Katrin, Kätlin, Graeme and Lucy, Jonathan, Swathi, Christine, Roweida, Eva-Maria and Jan. Thanks for being the wind beneath my wings at this stage of my life in Oxford.
Special thanks to Dr. Richard Gipps for all his help, support and guidance throughout

my doctorate degree.

Finally, I am very grateful to my family for their support and unconditional love. My parents, Arend and Kai, have been of great encouragement during this project. I am very grateful to my brother Sander, his wife Jaana and their little daughter Helerin for their support and to my brother Kaur for being there for me at all times.

17 October 2014

List of publications

Structural Investigation of a Hydrogen Bond Order-Disorder Transition in a Polar One-Dimensional Confined Ice, J. Adamson, N. P. Funnell, A. L. Thompson and A. L. Goodwin, *Phys. Chem. Chem. Phys.*, **16**, 2654-2659, 2014.

Negative area compressibility in silver(I) tricyanomethanide, S. A. Hodgson, J. Adamson, S. J. Hunt, M. J. Cliffe, A. B. Cairns, A. L. Thompson, M. G. Tucker, N. P. Funnell and A. L. Goodwin, *Chem. Comm.*, **50**, 5264-5266, 2014.

Contents

1 Introduction **1**

1.1 Overview . . . 1

1.2 Established dimensionality-property relationships in functional materials 2

1.2.1 Metal-organic frameworks . . . 2

1.2.2 Organic nonlinear optics materials . . . 3

1.2.3 Organic semiconductors . . . 5

1.3 Disorder in functional materials . . . 6

1.4 Negative thermal expansion . . . 14

1.5 Cyanide containing negative thermal expansion networks . . . 25

1.6 Negative compressibility . . . 29

1.7 Aim of the project . . . 32

2 Theory **34**

2.1 Crystallography . . . 34

2.2 X-ray diffraction . . . 36

2.2.1 Diffraction . . . 36

2.3 X-ray powder diffraction . . . 41

2.3.1 Synchrotron powder diffraction . . . 42

2.4 Neutron Diffraction . . . 43

2.4.1 Neutron source . . . 46

2.5 Structure determination from powder diffraction data . . . 46

2.6 The Ising model and order parameter . . . 49

2.7 Birch-Murnaghan equation of state 50

3 Experimental methods **52**

3.1 Synthesis 52

3.1.1 2,3,6,7,10,11-hexahydroxytriphenylene tetrahydrate 52

3.1.2 Silver(I) tricyanomethanide 52

3.1.3 Nickel(II) cyanide 54

3.1.4 Copper(II) nickel(II) cyanide 54

3.1.5 Cobalt(II) nickel(II) cyanide 55

3.2 Single-crystal X-ray diffraction 55

3.2.1 Variable-temperature collections for HHTP·4H_2O 55

3.2.2 Variable-temperature collections for Ag(*tcm*) 56

3.2.3 Variable-pressure collections for Ag(*tcm*) 57

3.3 Powder X-ray diffraction 58

3.3.1 Powder X-ray diffraction characterisation of $Co_xNi_{1-x}(CN)_2$ . . 58

3.3.2 Variable temperature powder X-ray diffraction measurements . . 59

3.3.3 High-pressure powder synchrotron diffraction for $Ni(CN)_2$ . . . 59

3.3.4 Precise room temperature characterisation of $CoNi(CN)_4$ using Mo X-ray radiation 60

3.4 Powder neutron diffraction 60

3.4.1 High-pressure collections for Ag(*tcm*) and $Ni(CN)_2$ 60

3.5 Measurements on original HHTP·4H_2O and heat-treated crystals 61

3.5.1 SQUID measurements 61

3.5.2 PPMS measurements 62

3.5.3 Conductivity measurements 64

3.5.4 EPR measurements 64

3.5.5 Thermogravimetric analysis 65

4 1D ice channels **66**

4.1 Overview 66

4.2 Background . . . 67
4.3 Characterisation of HHTP·4H_2O and discrepancy of the current model 70
4.3.1 Structure of the molecular tetrahydrate . . . 70
4.3.2 Variable temperature study and a new model . . . 71
4.3.3 The low temperature structure . . . 79
4.3.4 The high temperature structure . . . 82
4.3.5 Interconversion mechanism . . . 82
4.4 Order parameter evolution with temperature . . . 83
4.4.1 Relationship to diffraction intensities . . . 83
4.4.2 The Ising model . . . 84
4.5 Summary . . . 89

5 High temperature phase of HHTP·4H_2O 90
5.1 Overview . . . 90
5.2 Background . . . 91
5.2.1 Organic magnetic materials . . . 91
5.2.2 Organic conductors and superconductors . . . 93
5.3 Structural characterisation . . . 96
5.4 Electronic and magnetic characterisation . . . 100
5.5 Summary . . . 104

6 2D layered structures 106
6.1 Overview . . . 106
6.2 Structure of Ag(*tcm*) and $Ni(CN)_2$ . . . 106
6.3 Thermal expansion and compressibility measurements . . . 108
6.3.1 Thermal expansion measurements for Ag(*tcm*) . . . 108
6.3.2 Compressibility measurements for Ag(*tcm*) . . . 108
6.3.3 Compressibility measurements for $Ni(CN)_2$ . . . 111
6.4 Origin of compressibility and thermal expansion behaviour in Ag(*tcm*) . 116
6.5 Origin of compressibility and thermal expansion behaviour in $Ni(CN)_2$. 119

6.5.1 Negative Grüneisen parameter within the layers 122
6.6 Summary 125

7 Expanding into 3D — doped $Ni(CN)_2$ 127

7.1 Overview 127
7.2 Background 128
7.3 Structural effect of doping copper(II) and cobalt(II) into nickel(II) cyanide 132
7.4 Characterisation of cobalt(II) nickel(II) cyanide 134
7.5 Justification for very large area-NTE for cobalt(II) nickel(II) cyanide . 140
7.6 Summary 145

8 Conclusions 146

A Experimental data for HHTP·$4H_2O$ 164

A.1 SCXRD data 164
A.2 The order parameter 170

B Experimental data for Ag(*tcm*) 174

B.1 SCXRD data 174
B.2 Powder neutron diffraction data 186
B.3 High pressure phase 193

C Experimental data for $Ni(CN)_2$ 194

C.1 Powder neutron diffraction data 194
C.2 Powder synchrotron X-ray diffraction data 195

List of Figures

1.1 Dimensionality-property relationships in known materials 4
1.2 Structure of $BaTiO_3$ 7
1.3 Disorder from Pb displacements in PZT 9
1.4 Disorder in $SrMO_2N$ 14
1.5 Chemical bond vibrations under increasing temperature 15
1.6 RUMs in negative thermal expansion materials 17
1.7 Structures of zirconium tungstate and zirconium vanadate 20
1.8 Structure of graphite and hexagonal cadmium 24
1.9 Vibration motion of cyanide bridges 27
1.10 Effect of temperature and pressure on $Ag_3[Co(CN)_6]$ 28
1.11 'Rippling' vibrations in 2D layered $Ni(CN)_2$ 29
1.12 Helical structures of selenium and β-phase of m-dihydroxybenzene . . . 30
1.13 Wine-rack model for NLC framework materials 31

2.1 Representation of the Bragg's Law 37
2.2 Schematic representation of Ewald's Sphere 39
2.3 Debye-Scherrer cones. 42
2.4 Schematic of a synchrotron. 43
2.5 Schematic of the ISIS. 47

3.1 Crystals of $HHTP{\cdot}4H_2O$ 53
3.2 Crystals of $Ag(tcm)$ 53
3.3 Yellow powder of nickel(II) cyanide 54

3.4 Purple powder of cobalt(II) nickel(II) cyanide 55
3.5 Schematic of Merrill-Bassett diamond anvil cell 58
3.6 Schematic of SQUID 63
3.7 Schematic of PPMS heat capacity measurements 63

4.1 Structure of ice XI and ice XI 68
4.2 Structure of $[Cu^{I}_{2}Cu^{II}(CDTA)(4,4'\text{-bpy})$ 69
4.3 Known structure of HHTP·$4H_2O$ 71
4.4 Water channels in the known structure of HHTP·$4H_2O$ 72
4.5 Variable temperature synthesised precession images for HHTP·$4H_2O$ . . 73
4.6 Water channels in the new structure of HHTP·$4H_2O$ 74
4.7 New structural model for HHTP·$4H_2O$ 77
4.8 Lattice parameter evolution with temperature for HHTP·$4H_2O$ 78
4.9 Difference Fourier maps for water molecules in HHTP·$4H_2O$ 80
4.10 Water chains in HHTP·$4H_2O$ 81
4.11 Order parameter variation with temperature for HHTP·$4H_2O$ 85
4.12 Scheme of the ferroelectric ↔ paraelectric transition in HHTP·$4H_2O$ . . 88

5.1 Oxidation states for the HHTP molecule 91
5.2 Stable organic radical crystals 92
5.3 Organic molecular donors for charge transfer complexes 94
5.4 Schematic of a charge-transfer system and HHTP radical system 96
5.5 Heat-treated crystals of HHTP·$4H_2O$ 97
5.6 Rotation images by X-ray diffraction for heated crystals of HHTP·$4H_2O$ 98
5.7 High temperature powder X-ray diffraction data for HHTP·$4H_2O$ . . . 99
5.8 TGA data for HHTP·$4H_2O$ 99
5.9 Powder X-ray diffraction for selected heated HHTP crystals 100
5.10 SQUID susceptibility measurements for HHTP crystals 101
5.11 EPR measurements for HHTP crystals 102
5.12 PPMS heat capacity data for HHTP crystals 103

5.13 Pulse EPR measurements for HHTP crystals 104

6.1 Structure of Ag(*tcm*) and $Ni(CN)_2$ 107
6.2 Thermal expansion and compressibility data for Ag(*tcm*) 109
6.3 Pawley refinement fits for powder neutron diffraction for Ag(*tcm*) . . . 111
6.4 Rietveld refinement fits for powder neutron diffraction for Ag(*tcm*) . . . 112
6.5 Rietveld refinement fits for $Ni(CN)_2$ for powder neutron diffraction . . . 113
6.6 Rietveld refinement fits for $Ni(CN)_2$ for powder synchrotron diffraction 114
6.7 Compressibility results for $Ni(CN)_2$ 115
6.8 Geometric relationship to determine torsion angle for Ag(*tcm*) 117
6.9 Two states for Ag(*tcm*) 118
6.10 Structure of Ag(*tcm*) with area-NTE and NAC mechanism 120
6.11 Lowest energy phonon modes in $Ni(CN)_2$ 122
6.12 'Rippling' of $Ni(CN)_2$ layers and RUMs in $Ni(CN)_2$ 123

7.1 d-orbital splitting in octahedral, tetrahedral and square planar compexes 129
7.2 Structure zinc(II) nickel(II) cyande and suggested structure for cobalt(II) nickel(II) cyanide 131
7.3 PXRD results for copper(II) doping into nickel(II) cyanide 133
7.4 PXRD results for different cobalt(II) doping levels into nickel(II) cyanide 134
7.5 Phase fractions for different cobalt(II) doping into nickel(II) cyanide) . 135
7.6 Fit for cobalt(II) nickel(II) cyanide with Mo radiation 136
7.7 variable temperature fits for cobalt(II) nickel(II) cyande for the whole data range 138
7.8 variable temperature fits for cobalt(II) nickel(II) cyande for a restricted data range 139
7.9 Lattice parameter data for cobalt(II) nickel(II) cyanide 141
7.10 Reflection intensity variation for constant peak shape fitting 142
7.11 Gaussian fits to the variable temperature data 143

7.12 UV/VIS measurements for various cobalt(II) doping levels into nickel(II) cyanide 144
7.13 Volume dependence on θ of cobalt(II) nickel(II) cyanide. 144

A.1 Evolution of the order parameter for HHTP·4H_2O 173

List of Tables

2.1 Table describing the fourteen Bravais lattices. 36

4.1 SCXRD refinement details for HHTP·4H_2O for *Pbcn* structures 72

4.2 SCXRD refinement details for HHTP·4H_2O for $P2_1cn$ structures 75

4.3 SCXRD refinement details for HHTP·4H_2O at $T = 100\,K$ 75

4.4 SCXRD refinement details for HHTP·4H_2O at $T = 240\,K$ 76

5.1 Debye and Einstein temperatures for heat-treated HHTP samples . . . 102

6.1 Thermal expansion and compressibility data for layered materials . . . 124

6.2 Elastic compliance and Grüneisen parameter values 125

A.1 SCXRD refinement details for HHTP·4H_2O at $T = 100\,K$ 164

A.2 SCXRD refinement details for HHTP·4H_2O at $T = 240\,K$ 167

A.3 Variation of unit cell parameters on heating for HHTP·4H_2O 169

A.4 Variation of unit cell parameters on cooling for HHTP·4H_2O 169

A.5 Selected reflection intensities for HHTP·4H_2O 171

A.6 Order parameter values for HHTP·4H_2O 171

B.1 General crystallographic data for Ag(*tcm*) 174

B.2 SCXRD refinement details for Ag(*tcm*) at $T = 100\,K$ on heating 175

B.3 SCXRD refinement details for Ag(*tcm*) at $T = 150\,K$ on heating 176

B.4 SCXRD refinement details for Ag(*tcm*) at $T = 200\,K$ on heating 177

B.5 SCXRD refinement details for Ag(*tcm*) at $T = 250\,K$ on heating 178

B.6 SCXRD refinement details for Ag(*tcm*) at $T = 200\,K$ on cooling 179

B.7 SCXRD refinement details for Ag(*tcm*) at $T = 150\,\mathrm{K}$ on cooling 180
B.8 SCXRD refinement details for Ag(*tcm*) at $T = 100\,\mathrm{K}$ on cooling 181
B.9 SCXRD refinement details for Ag(*tcm*) at $p = 0.08\,\mathrm{GPa}$ 182
B.10 SCXRD refinement details for Ag(*tcm*) at $p = 0.83\,\mathrm{GPa}$ 183
B.11 Structural parameter data on heating using SCXRD 184
B.12 Structural parameter data on cooling using SCXRD 185
B.13 Neutron diffraction refinement details for Ag(*tcm*) at $p = 0.615(6)\,\mathrm{GPa}$ 186
B.14 Neutron diffraction refinement details for Ag(*tcm*) at $p = 0.190(6)\,\mathrm{GPa}$ 187
B.15 Neutron diffraction refinement details for Ag(*tcm*) at $p = 0.265(6)\,\mathrm{GPa}$ 188
B.16 Neutron diffraction refinement details for Ag(*tcm*) at $p = 0.336(6)\,\mathrm{GPa}$ 189
B.17 Neutron diffraction refinement details for Ag(*tcm*) at $p = 0.409(6)\,\mathrm{GPa}$ 190
B.18 Neutron diffraction refinement details for Ag(*tcm*) at $p = 0.500(6)\,\mathrm{GPa}$ 191
B.19 Neutron diffraction refinement details for Ag(*tcm*) at $p = 0.615(6)\,\mathrm{GPa}$ 192
B.20 Structural parameter data for Ag(*tcm*) from powder neutron diffraction 192
B.21 Data for high temperature phase of Ag(*tcm*) 193

C.1 General crystallographic data for $Ni(CN)_2$ 194
C.2 Powder neutron diffraction results for $Ni(CN)_2$ 194
C.3 Powder synchrotron diffraction results for $Ni(CN)_2$ 195

List of Abbreviations and Symbols

0D	zero dimensional
1D	one dimensional
2D	two dimensional
3D	three dimensional
A	area
Å	Ångström unit
a, **b**, **c**	unit cell vectors
AFE	antiferroelectric
α	linear coefficient of thermal expansion
α_a, α_b, α_c	coefficients of thermal expansion along unit cell axes a, b, c
a, b, c	crystallographic axis
4,4'-bpy	4,4'-bipyridine
B_0	bulk modulus
B'	first pressure derivative of bulk modulus
calc	calculated
CDTA	1,2-diaminocyclohexanetetraacetate
χ	phase fraction
DAC	diamond anvil cell
°C	degrees Celsius
d	distance
dπ	indicating π overlap between metal and ligand d orbitals
e	index for states in the Ising model

S	elastic compliance
Eq	equation
ER	ergodic relaxor
f	form factor
FE	ferroelectric
$F(hkl)$	structure factor for a certain reflection
Fig.	figure
F	Fourier
GPa	gigapascal
γ	Grüneisen parameter
$\gg$	much bigger than
$\mathcal{H}$	Hamiltonian function
h	hours
H-bond	hydrogen bond
hBN	hexagonal boron nitride
HHTP	2,3,6,7,10,11-hexahydroxytriphenylene
h, k, l	Miller indices
I	intensity
i	index
ice I_h	hexagonal phase of water ice
I	body centred crystal system
$\in$	is an element of
J	coupling energy
j	index
K	kelvin
Kα	X-ray emission from an electron transitions from a 2p orbital of of the L shell to the innermost K shell
k_B	Boltzmann constant
KDP	potassium dihydrogen phosphate

kJ	kilojoule
K	compressibility factor
l	length
λ	wavelength
LED	light emitting diode
$\leftrightarrow$	phase transition that occurs in both direction
M	metal
MAP	matrix assisted poling
meso	intermediate
µm	micrometre
MK	megakelving
mm	millimetre
MOFs	metal-organic frameworks
mol	mole
M′	metal
N	maximum index
NAC	negative area compressibility
NLC	negative linear compressibility
NLO	non-linear optics
NMR	nuclear magnetic resonance
nn	nearest-neighbour
nnn	next-nearest-neighbour
NTE	negative thermal expansion
P	primitive crystal system
p_{c}	phase transition pressure
PDF	pair distribution function
PLZT	relaxor ferroelectric material $(\mathrm{Pb}_{\frac{1-3x}{2}}\mathrm{La}_x)(\mathrm{Zr}_y\mathrm{Ti}_{1-y})\mathrm{O}_3$
PMN	relaxor ferroelectric material $\mathrm{PbMg}_{\frac{1}{3}}\mathrm{Nb}_{\frac{2}{3}}\mathrm{O}_3$
PNR	polar nanoregion

p	pressure
PTE	positive thermal expansion
PZN	relaxor ferroelectric material $PbZn_{\frac{1}{3}}Nb_{\frac{2}{3}}O_3$
PZT	relaxor ferroelectric material $PbZr_{1-x}Ti_xO_3$
QRUM	quasi rigid unit mode
r	length
Ref.	reference
RUM	rigid unit mode
SCXRD	single-crystal X-ray diffraction
σ_1, σ_2	degenerate bending vibrational modes
C_T	isothermal specific heat
T	temperature
T_g	glass transition temperature
T_c	phase transition temperature
tcm	tricyanomethanide
THz	terahertz
TPa	terapascal
2θ	scattering angle (diffraction)
U	thermal parameter
U_{max}	maximum thermal parameter
V	volume
ω	vibrational frequency
x	distance parameter (crystallography)
ξ	order parameter
ZTA	zirconium toughened alumina
ZTE	zero thermal expansion

Chapter 1

Introduction

1.1 Overview

The structural dimensionality of certain materials, *i.e.*, how the atoms and molecules are connected in three dimensions, directly governs or influences their properties. Such materials include metal-organic frameworks (MOFs) with their respective properties ranging from gas storage to catalysis[1–3], organic non-linear optics (NLO) materials in pursuit for higher data rates in future optical communication technologies[4,5], and organic semiconductors for use in organic light-emitting diodes, organic field-effect transistors or solar cells[6,7]. It is therefore beneficial to discover and describe trends of how a material's properties are impacted by the structural dimensionality of the material. This thesis focuses on materials, whose characteristic one-, two- or three-dimensional (1D, 2D or 3D) structural motifs lead to unusual properties. Such materials encompass properties ranging from potential ferroelectricity of low-dimensional water ice to negative area compressibility (NAC) and negative thermal expansion (NTE) in cyanide-containing 2D and 3D framework materials. This introductory chapter is divided into two main sections. First, we provide a brief overview of dimensionality-property relationships in functional materials. Second, for the unusual properties examined in this thesis, we aim to build a general background of materials possessing these properties

and to bring examples of materials, where these properties arise from the structural dimensionality of the material.

1.2 Established dimensionality-property relationships in functional materials

1.2.1 Metal-organic frameworks

The first examples we consider, the class of materials called MOFs, consist of repeated units of metal cations, termed nodes, linked together by organic ligands, termed linkers, *via* coordination bonds or other weaker interactions.[8] MOFs are typically porous and exhibit topological 1D, 2D and 3D structural motifs.[9] The properties of MOFs, *e.g.* gas storage, catalytic ability and host-guest chemistry, are frequently directly related to the dimensionality of their pores.[1–3] Illustrating examples include MOFs with 2D connectivity that exhibit square-grid layer structures and adsorb gas with a gate opening mechanism. These 2D-MOFs are named elastic layer-structured metal-organic frameworks (ELMs) and could provide a solution for strong adsorption and easy desorption.[10] The first of such materials was $Cu(bpy)_2(BF_4)_2$ or ELM-11.[11] At ambient pressure, the layers in ELM-11 are staggered and the bpy molecules cover the open space of the metal-organic square grids of neighbouring layers and hence hinder adsorption of guest molecules. At elevated pressures, the layers slip with respect to each other, opening the pores, which manifests in rapid uptake of guest molecules.[12] Hence gas adsorption in such layered 2D framework structures depends directly on the dimensionality of the pores with the zero-dimensional (0D) pores in the low pressure structure forbidding gas uptake and the 1D pores in the high pressure structure allowing for fast gas adsorption. Fig. 1.1(a) illustrates the gate opening gas adsorption and desorption mechanism for ELMs.

Furthermore, MOFs with 3D connectivity have been suggested to be potential candi-

dates for hydrogen storage.[13] A pioneering example of such materials is that of MOF-5, where an octahedral three-dimensional network is built with the aid of metal clusters as connecting nodes.[14,15] In MOF-5, these clusters comprise of $(OZn_4)O_{i2}$ units, where in each cluster 12 oxygen atoms belong to carboxylate groups from the organic linkers and hence a 3D network of pores is achieved.[16,17] Such high porosity could potentially allow storage of hydrogen molecules in the structure.[18]

1.2.2 Organic nonlinear optics materials

NLO is the branch of optics that focuses on the behaviour of light in nonlinear media.[21] It is concerned with the interaction of electromagnetic fields with various media in a way that new electromagnetic fields, which are altered in phase, frequency or amplitude from the incident fields, are produced. In general, development of organic NLO materials is driven by the potential of these materials to minimise the size, weight, and power requirements of next-generation computing, telecommunications, and sensing applications.[4,5] This would be achieved through improved performance and simplified processing compared to existing technologies.[4,5] One challenging aspect of organic NLO materials is the organisation of individual molecules into an ordered structure. Fig. 1.1(b) illustrates how reducing lattice dimensionality of the NLO active chromophores, *i.e.*, organising the chromophores into 1D or 2D assemblies, aids the production of these materials. The figure shows how chromophores whose lattice dimensionality is reduced to essentially 1D require much smaller field strengths to achieve an overall ordered structure compared to chromophores with 2D or 3D lattice dimensionality. Recently, this has been utilised in the phenomenon of matrix assisted poling (MAP) of organic NLO materials, which has been introduced for manufacturing these materials.[19,22] This technology involves heating the material near its glass transition temperature and applying an electric field to align the NLO active molecules. The advancement of MAP materials is the use of specific spatially anisotropic interactions of incorporated pendant groups to reduce lattice dimensionality of the NLO

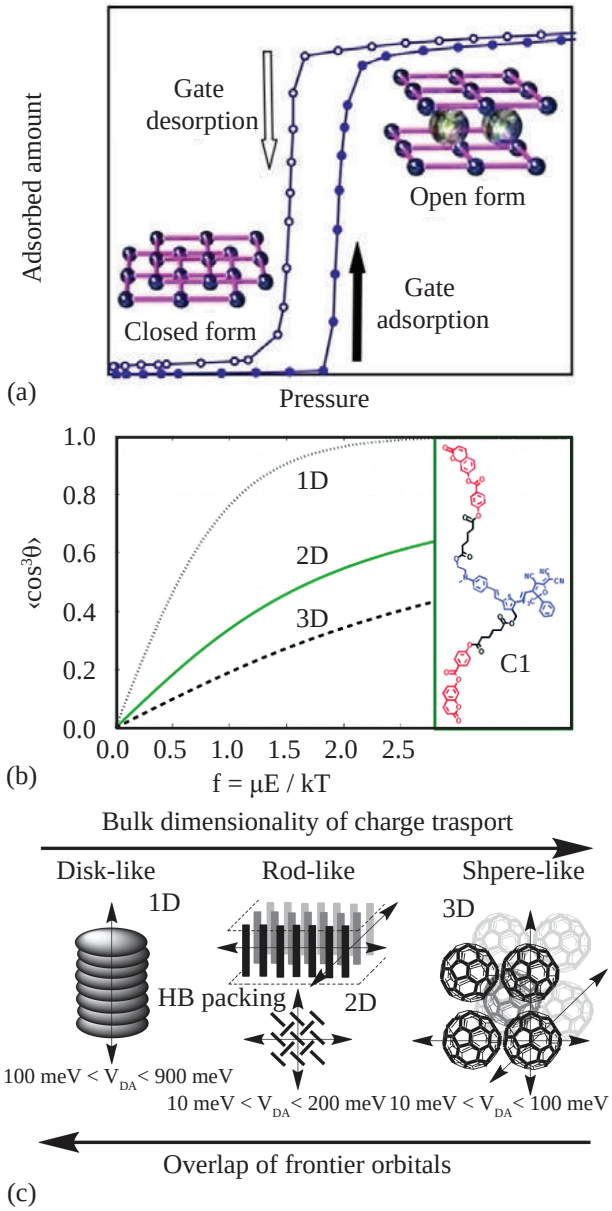

Figure 1.1: Dimensionality-property relationships in known materials with (a) illustrating the gate opening gas adsorption and desorption mechanism for 2D ELMs (Adapted from Ref. 10), (b) showing the variation of structural organisation with varying poling field strength for high and low dimensional NLO materials (Adapted from Ref. 19) and (c) showing the compromise between electronic properties and bulk dimensionality of organic semiconductors (Adapted from Ref. 6 and 20).

active molecule to less than three-dimensional. This restricts the motion and rotational dimensionality of the NLO molecule in the presence of the poling field. For example, courmarin groups have been shown to reduce lattice dimensionality around the NLO active molecule from 3D to effectively 2D.[23] A specific example is that of the dendrimer molecule, denoted as C1, in which the courmarin groups align in the x/y-plane due to intermolecular π-interactions, resulting in an enhanced order of the NLO active chromophore molecules along the z-axis [Fig. 1.1(b)].[19] The reduced rotational dimensionality leads to easier alignment of the chromophores in the presence of the poling field and hence easier manufacturing of organic NLO materials.

1.2.3 Organic semiconductors

Organic molecules based on π-conjugated systems can serve as a part of organic semiconductors.[6,7] In principle, there are two types of dimensionality that need to be considered here. Firstly, dimensionality that refers to the intramolecular conjugation pathway in the molecules, and secondly, dimensionality of how the molecules interact with each other in the bulk structure, *i.e.*, the extent and direction of the supramolecular and electronic interactions between molecules in the bulk material.[6,7] Terms molecular dimensionality and bulk dimensionality are suggested to be used to describe these types of connectivity, respectively. It is advantageous to have isotropic 3D bulk materials for utilisation of organic semiconductors industrially, however, 1D and 2D molecular materials provide the best frontier orbital overlaps and hence largest transfer integrals for the coupling of individual molecules.[6,20] Thus, there are costs and benefits associated with increasing the molecular dimensionality to achieve materials with isotropic properties. These trends are illustrated in Fig. 1.1(c). Linear organic molecules are an example of molecular 1D units. However, the drawbacks of systems based on linear organic molecules are precisely their anisotropic charge-transfer and optical properties and the challenges of aligning the molecules in the bulk material.[24–26] Researchers have therefore looked into molecular and bulk 2D and 3D organic semiconductors to

produce isotropic materials to overcome the problem of anisotropicity and to aid alignment of the molecules *via* intermolecular interactions.[27,28] Examples of investigated 2D molecular materials include discotic molecules, such as systems based on triphenylene cores. These molecules tend to stack in 1D columns, allowing for intracolumnar charge transport.[29] Such 2D molecules aid organisation of the structure, but do not provide a solution for the anisotropic properties of the bulk material. Thus, research into the synthesis of bulk 3D materials based on 3D molecular materials has been undertaken recently, including oligophenylenes[30,31] and spirobifluorene[32]. In addition, examples of extended 3D conjugated systems with tetrahedral geometry have been developed in recent years.[33] In summary, control over molecular and bulk dimensionality in organic semiconductors is crucial for their use in practical applications and is an ongoing and active field of research.

1.3 Disorder in functional materials

The previous section dealt with materials, where dimensionality forms an important part in determining materials' properties and gave examples of materials, where such dimensionality-property relationships are well established. The following sections outline the background for the unusual properties studied in this thesis. We start with disorder in functional materials, move on to negative thermal expansion and finally, negative compressibility. An emphasis is given to the effect of dimensionality on these properties.

A part of this thesis concerns low-dimensional water channels confined to an organic crystal that undergo an order-to-disorder phase transition with the ordered low-temperature phase a potential ferroelectric (FE). Therefore the following sections describe how disorder manifests in ferroelectric properties of certain materials. Known examples of such materials include relaxor ferroelectrics and dipolar glasses. Additionally, oxynitrides illustrate how disorder and dimensionality can affect a material's properties.

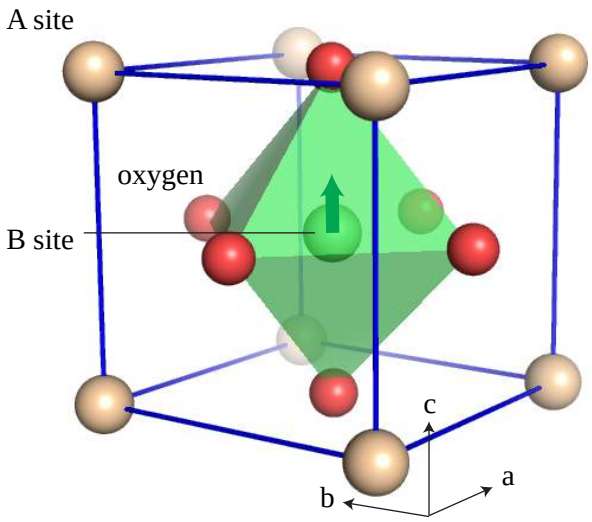

Figure 1.2: The parent pervoskite structure, showing the 12-fold coordinated A-site and the 6-fold coordinated B-site and oxygen atoms. The large arrow indicates the displacement of the B cation to produce a local polarisation. Coupling of these polar displacements is implicated in the ferroelectric response of materials such as $BaTiO_3$ (Adapted from Ref. 34).

Relaxor ferroelectrics Ferroelectricity in oxides is generally related to the displacement of ions and for a material to exhibit ferroelectric properties, this must result in a local separation between the centre of distribution between the positive and negative charge. An example of such materials is $BaTiO_3$, where Ba^{2+} is in a 12-fold coordinated perovskite A-site and Ti^{4+} in a octahedral coordination environment on the B-site. Net polarisation is achieved when the strongly positively charged Ti^{4+} is moved away from the centre of the octahedron and such displacements are correlated throughout the lattice [Fig. 1.2].

In relaxor FE materials, the FE phase transition is broad and depends on frequency, which is thought to result from a combination of factors, including disorder in the crystal structure.[34]

An example of disorder is that of chemical disorder, such as in PZN ($PbZn_{\frac{1}{3}}Nb_{\frac{2}{3}}O_3$) and PMN ($PbMg_{\frac{1}{3}}Nb_{\frac{2}{3}}O_3$), where using a mixture of cations on the B-site can result

in a wide range of different environments for the A-site.[35] Another, and perhaps more subtle, type of disorder, involves displacement of Pb from the centre of the A site as illustrated in Fig. 1.3 for PZT ($PbZr_{1-x}Ti_xO_3$). Two possible displacement schemes for Pb-based FE oxides are shown: 12 $\langle 011 \rangle_c$ directions and 8 $\langle 111 \rangle_c$ directitons, where c denotes indexing based on the parent cubic structure.[36,37] If on the whole, there is an equal number of each displacement, the average structure is preserved, however, due to this disordering, the local environments of Pb cations can be substantially different. The justification for Pb^{2+} displacements is shown by simple geometric considerations, which indicate that the Pb^{2+} is in an environment larger than desirable in these relaxor ferroelectrics, stemming from the Pb—O bond being 'softer' than the B—O bonds. This argument implies that the B—O preferred distance has a greater influence on the final lattice parameter.[38,39] The second-order Jahn-Teller is of great significance in these structures and the change in hybridisation of the Pb^{2+} 5d-states with the oxygen 2p-states that arises from the Pb^{2+} displacements stabilises its off-centering from its octahedral coordination environment.[34] As an example, using high temperature powder synchrotron diffraction, it has been shown that for $x = 0$ ($PbZrO_3$), the Pb^{2+} ions are on average split across the 12 $\langle 011 \rangle_c$ directions.[40] At other compositions, the disorder is across the 8 $\langle 111 \rangle_c$ directions, in accord with neutron diffraction.[41,42] From a dimensionality point of view, it is noteworthy that the Pb^{2+} ions assemble into 1D domains of correlated displacements in the case of $PbZrO_3$. In the case of PZN and PMN, among many others, 2D domains of Pb^{2+} displacements are generated, with each domain a single layer of atoms thick and oriented perpendicular to one of the $\langle 011 \rangle_c$ directions.[41,43]

Upon cooling, relaxor FE materials transform into an ergodic relaxor (ER) state and polar regions of nanometer scale with randomly distributed directions of dipole moments appear.[34] This phase transition preserves the crystal symmetry on the whole, however, the local order of the structure can vary in accord with the disorder described above. Hence in the early 1980s it was put forward that the structure of PLZT $\left[(Pb_{\frac{1-3x}{2}}La_x)(Zr_yTi_{1-y})O_3\right]$ contains a population of small polarised regions of several

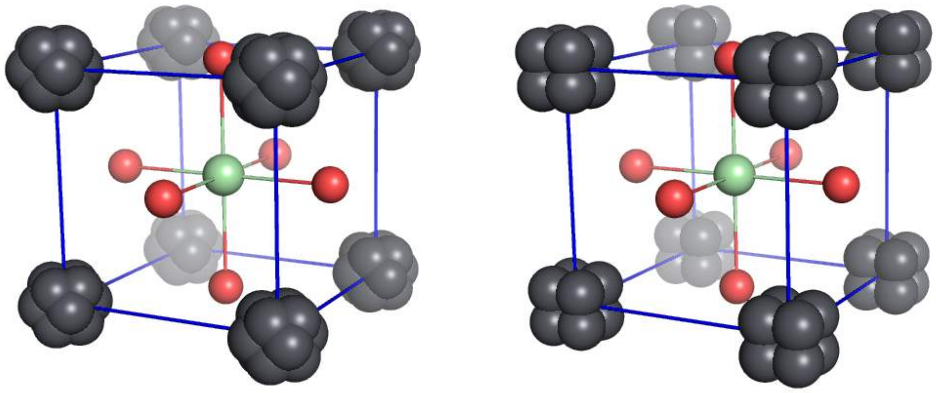

Figure 1.3: Figure showing disorder that results from Pb cation displacements in perovskites with (a) indicating the displacements along the 12 $\langle 011 \rangle_c$ directions and (b) indicating displacements along the 8 $\langle 111 \rangle_c$ directions, where c indicates indexing based on the parent cubic structure (Adapted from Ref. 36).

unit cells.[44]

This idea of small domains, which are referred to as polar nanoregions (PNRs), has become widely accepted for describing the short-range order in lead-based materials.[45–50] At temperatures close to the phase transition temperature the PNRs are mobile, however, at lower temperatures, their dynamics slow down enormously and at low enough temperatures, the PNRs become frozen in to form a nonergodic state.[51] The assumption of the net dipoles from PNRs interacting with each other like individual dipoles has been made in several studies.[52,53] It has further been shown for many relaxor ferroelectrics that PNRs persist even in the nonergodic phase, making this phase in relaxor ferroelectrics substantially different from 'normal' ferroelectric materials. Based on multiple studies, it is concluded that the transition into the nonergodic phase consists in a stepwise increase in the size of PNRs.[35,54] It is noted here that in some relaxors, a spontaneous transition to a FE phase is observed at low temperatures and therefore the nonergodic relaxor state does not exist for these materials.[51] The nonergodic relaxor state can irreversibly be transformed into a FE phase, provided that a large enough external electric field is applied.[51] This observation is a contrast to dipolar

glasses.

Dipolar glasses In dipolar proton/deuteron glasses, the cusp in the dielectric susceptibility is rounded and freezing takes place over a large temperature interval, whereby the material transforms from a high-temperature crystalline phase into a low-temperature glassy state.[51] From a microscopic point of view, a dipolar glass state can be viewed as a randomly frustrated collective state, in which the basic dipolar entities are individual electric dipoles that typically arise from molecular ions or off-centre ions.[51] This is a contrast to the PNR domains as discussed above for relaxor ferroelectric materials. These polar entities have orientational degrees of freedom associated with them and they interact with each other. Dipolar glasses bear similarities with spin glasses, where interactions between the magnetic moments are 'in conflict' and therefore no long-range order can be established.[55] These systems, however, possess a 'freezing in' transition with a new kind of order, where magnetic moments of the spins are aligned at random. Establishing the nature of this new kind of order is still a subject of controversy. The same is in general true for dipolar glasses.

Typical representatives of dipolar glasses are compounds of the type $M_{1-x}B_xXO_4$ (M = K, Rb, Cs, B = NH_4 or ND_4 and X = P, As), for example, $Rb_{1-x}(NH_4)_xPO_4$ and its deuterated isomorph.[56] Another example of dipolar glasses are the the quasi-one-dimensional mixed crystals of betaine phosphate-phosphite of the composition $(BP)_{1-x}(BPI)_x$.[57,58] Moreover, dielectric crystals containing dipolar impurities, *e.g.* $KCl_{1-x}(OH)_x$,[59] $K_{1-x}Li_xTaO_3$,[60] $K_{1-x}Li_xCl$[56] are examples of dipolar glass systems.

In the context of this thesis, it is important that the the disorder in dipolar glasses of the $M_{1-x}B_xXO_4$ family manifests in shuttling of H-bonds between the two possible positions of energy minima.[56] At high temperatures, there is an equal probability of H-bonds being found between two oxygens from adjacent PO_4 units and in the low temperature phase, the H-bonds freeze into just one of the possible positions and therefore, the phase transition results from ordering of the H-bonds. From a dimensionality point of view, it is important to note that the H-bonding network in these systems is

three-dimensional.

It was postulated by Slater in 1941 that in dipolar glasses, the hydrogens are disordered within the H-bonds and follow rules similar to those of Pauling's ice rules with:

1) One and only one proton per hydrogen bond, and

2) Two protons close to a given phosphate, while the other two bonds linking the phosphate to its neighbours have their protons close to the neighbouring phosphates.[61,62]

A shortfall of the Slater model is its lack of a possible mechanism for dynamic behaviour. If one proton moves, Slater's second rule above is broken for two phosphates simultaneously. To correct for that, Takagi introduced HPO_4 and H_3PO_4 groups as intermediate groups in the phase transition to break the second rule.[63] The existence of these groups was later confirmed by deuteron NMR experiments mostly on potassium dihydrogen phosphate (KDP), which showed that incorporating Takagi groups to the model requires less energy than removing deuterons from bonds. Schmidt showed that Takagi groups govern dynamical phenomena such as domain wall motion and dielectric and NMR relaxation in KDP.[64] The aforementioned Takagi groups are created in DPO_4−D_3PO_4 pairs, which migrate through the crystal by switching a deuteron to the other end of its bond with each migration step.

The family of materials of the composition $(BP)_{1-x}(BPI)_x$ encompass quasi-1D H-bonding networks, which is a contrast to the aforementioned $M_{1-x}B_xXO_4$ family. Both components of these systems, BP and BPI, undergo a phase transition from a paraelectric to an antiferrodistortive phase at 355 K and 365 K, respectively.[51] Antiferrodistortive implies that there is a distortion in the structure due to antiferroelectric ordering, which in turn means that neighbouring dipoles oppose each other. In the high-temperature phase, the PO_4 and the HPO_3 groups and the betaine molecules are disordered. They all order in the antiferrodistorive phases, however, the hydrogen atoms connecting the PO_4 and the HPO_3 groups remain disordered. Ordering of these hydrogen atoms results in a ferroelectric or an antiferroelectric phase. The temperature dependence of the dielectric permittivity reflects the materials' quasi-1D H-bonding networks, where coupling between the electric dipolar units within chains

is much stronger than between dipolar units of neighbouring chains. In BP, the coupling of these dipoles within the chains is ferroelectric and between the chains antiferroelectric,[65] whereas in BPI neighbouring chains are coupled ferroelectrically.[66] The $(BP)_{1-x}(BPI)_x$ phase diagram is divided into three regions.[67] At low temperatures, the low composition of BPI range is ferroelectric and the high composition of BPI range antiferroelectric. The middle part of the phase diagram ($0.65 > x > 0.1$) is characterised as a glassy state.[68,69] The latter shows flat dielectric peaks that are characteristic of dipolar glasses.[51]

The mechanism of cooperative rearrangement of dipoles (CRD) has been suggested as a possible relaxation mechanism in dipolar systems.[70] The underlying idea is that the dipolar entities in a disordered polar system undergo collective rotation in the embedding medium and a low-temperature glass state is established by a cooperative freezing-in of the orientational degrees of freedom.

Oxynitrides Solid oxynitrides are an important class of materials that can combine the properties of transition metal oxides and nitrides.[71] Such advantages include greater air and moisture stability than traditional nitrides, but smaller band gaps than pure oxides, which can lead to applicable electronic and optical properties. The properties of oxynitrides range from good water-splitting catalysts[72], photocatalytic applications[73], high dielectric constants[74], nontoxic red-yellow pigments[75], useful host materials for phosphors in white light light emitting diode (LED) devices[76] and notable electronic transport properties[77,78]. The possible order or disorder of anions is an important aspect of the engineering of oxynitride crystal structures and correlated local order of anions often influences the material's properties. The ordering principles in these systems usually dominated by the lattice enthalpy and therefore by bonding energies associated with the anion configuration. M—O and M—N bonds of high valent metals are typically of similar length. As an example, the ranges of Ta—O and Ta—N distances in TaON are 1.99−2.15 Å and 2.07−2.15 Å, respectively, and are therefore very similar.[79] Even though in this particular case oxide and nitride are ordered, crystal-

lographic disorder between the anion sites is observed in many oxynitrides. A recent study has revealed that $AMO_{3-z}N_z$ perovskite oxynitrides contain chains of M—N—M bonds that undergo a 90° turn at each M cation, for which Pauling ice rules predict zero configurational entropy despite the apparent structural disorder.[80] An example of such oxynitrides is $SrMO_2N$: contrary to its expected simple cubic perovskite structure it shows tetragonal symmetry with inequivalent anion sites.[81] This disorder is illustrated in Fig. 1.4(a). The average structure has been interpreted as consisting of *cis*-MO_4N_2 octahedra with four of the anion sites being disordered. This stems from $M(_{d\pi})$—$X(_{d\pi})$ covalency, which favours the *cis*-configuration of the two more strongly bonded ligands in these high valent d^0 transition metal compounds. The result of this is the formation of zigzag M—N chains within two-dimensional layers of the $SrMO_2N$ perovskites. The chains are disordered within the layers, illustrated in Fig. 1.4(b). Therefore the local anion order in AMO_2N and $AMON_2$ perovskites leads to loss of inversion symmetry at each M cation site, although the average crystal structures are centrosymmetric. This is suggested to have a strong influence on the materials properties and account for observations that $ATaO_2N$ (A = Ca, Sr, Ba) oxynitrides do not show FE ordering transitions, unlike pure oxide analogues such as $BaTiO_3$.[82,83]

Another study undertook a full configurational entropy characterisation of such oxynitrides and found that such zigzag M—N chains, ordered within two-dimensional layers, have indeed zero configurational entropy associated with them.[84] On the other hand, $BaTaON_2$ does not show deviations from the cubic symmetry that would reflect confinement of the N atoms to two-dimensional planes and thus, the zigzag TaN chains are assumed to propagate in all three dimensions. Such an arrangement would lead to an extensive configurational entropy of 0.58R. In these calculations, it was assumed that the M—O—M and M—N—M bridges are strictly altering. In more detailed calculations, the oxynitrides have subextensive entropies associated with them, *i.e.*, the entropy is significant for a small number of atoms, but becomes vanishingly small for a large number of atoms, and is strongly dependant on particle size.

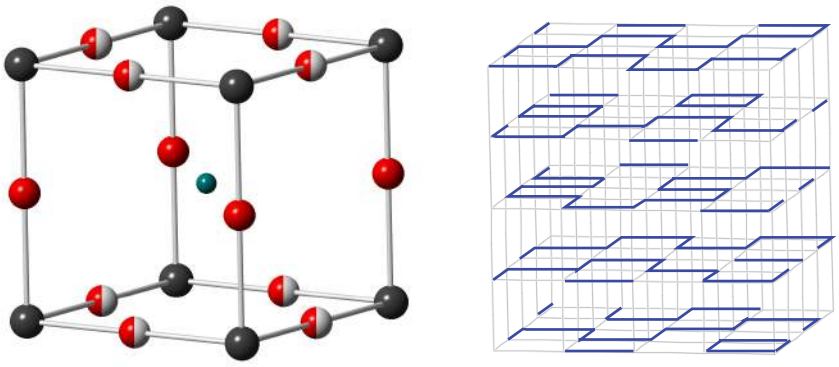

(a) (b)

Figure 1.4: The average structure was interpreted as consisting of *cis*-MO_4N_2 octahedra with four of the anion sites being disordered with (a) showing the average unit cell and (b) the zigzag M—N chains that result from such arrangement. Thus, the structure shows disorder within the 2D layers (Adapted from Ref. 84).

1.4 Negative thermal expansion

Most materials expand when heated. This phenomenon has its origins in the anharmonicity of vibrations between chemically bonded atoms associated with an asymmetric potential well around the zero point [Fig. 1.5].[85] The nature of this asymmetric potential well is such that when heated, the energy of the system rises more when atoms are brought closer together as opposed to the bonds lengthening. Therefore materials tend to increase their dimensions with increasing temperature. Negative thermal expansion materials are materials where $\frac{\mathrm{d}V}{V\,\mathrm{d}T}$ (volume-NTE), $\frac{\mathrm{d}A}{A\mathrm{d}T}$ (area-NTE) or $\frac{\mathrm{d}l}{l\mathrm{d}T}$ (linear-NTE) is/are negative, and hence the material contracts in one or more linear directions with increasing temperature.[86] NTE materials could be useful in areas where materials resistant to thermal shock are required. These materials are of great practical interest and could be used as part of composite materials to tune the thermal expansion of the whole material and to tailor materials with desired thermal expansion coefficients. Thus, materials with industrially useful thermal expansion coefficients, *e.g.* zero thermal expansion (ZTE) or thermal expansion coefficients similar

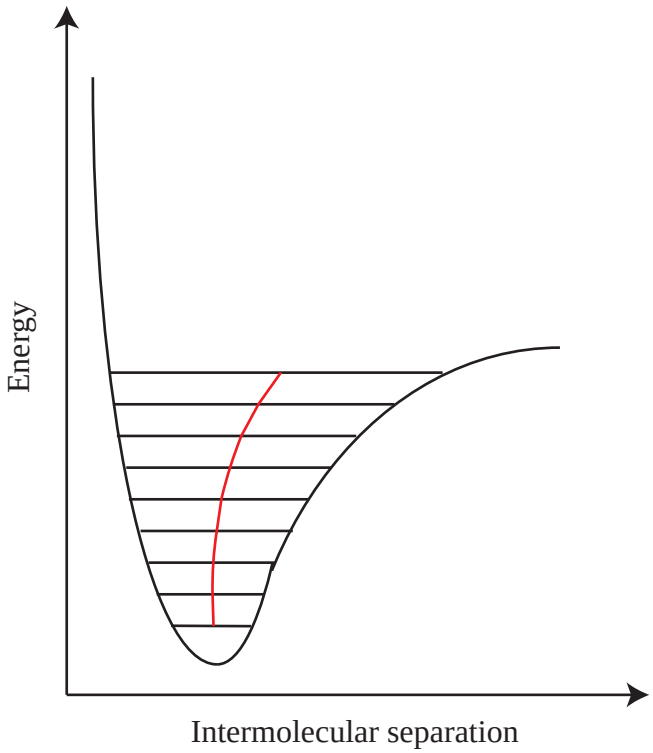

Figure 1.5: Illustration of a typical asymmetric energy potential well associated with a chemical bond. The asymmetry is important as it dictates that the average internuclear separation increases with increasing vibrational energy. This can be seen in the way the mid-points of the vibrational energy levels, illustrated here as horizontal lines, tend to greater distance with increasing energy. In practice, this results in the increase of average bond lengths with increasing temperature.

to those of silica and glass, could be made.[87] These composites could find potential use as substrates for lasers, Bragg diffraction gratings, optical fibres, materials in circuitry, mirrors and other optical devices.[88–90] In this thesis, we examine the influence of materials' structural dimensionality on their thermal expansion behaviour. We study 2D and 3D systems based on cyanide-containing ligands and show that dimensionality of connectivity in these structures can be an important aspect that can influence thermal expansion. Thus, in this chapter we firstly outline examples of known NTE materials, emphasising dimensionality as far as possible. We then present a summary of known

cyanide-based networks, as such frameworks are a focus of this thesis. To build a theoretical background for NTE, we give a summary on phonon modes, rigid unit modes and the Grüneisen theory in the next few paragraphs.

A static lattice model deals with average positions of atoms in a crystal. On the contrary, lattice dynamics extends this concept of a crystal lattice to an array of atoms with finite masses that are capable of motion. This motion is a superposition of vibrations of atoms around their equilibrium sites due to the interaction with neighbouring atoms. Therefore, vibrational modes of polymeric materials are different to those of isolated molecules: vibrational motion in such materials is coupled throughout the material as opposed to a collection of vibrating isolated species. Phonon modes are lattice vibrational modes that can represent such vibrational motion in polymeric materials and generally involve complex vibrational motion of groups of atoms repeated throughout the extended crystalline lattice of a material with some periodicity, which can be related to the periodicity of the lattice itself.[91]

In 1920s, Grüneisen put forward a theory between phonon modes and thermal expansion of the material.[92] The Grüneisen relationship expresses a material's volume coefficient of thermal expansion α_V in terms of its specific heat at constant volume, C_V, its volume, V, and its isothermal compressibility, K, and is given by the equation

$$\alpha_V = \frac{\gamma C_V K}{V}. \tag{1.1}$$

The coefficient γ in this equation is termed the Grüneisen parameter. By definition, α and γ must have the same sign as all other terms in Eq. (1.1) are necessarily positive. In general, phonon modes are classified into two types based on the sign of their associated Grüneisen parameter. Normal longitudinal-type stretching modes are of the type characterised by positive Grüneisen parameters and contribute to overall positive thermal expansion of the material. On the other hand, phonon modes involving transverse vibrational motion typically belong to the category of modes characterised by negative Grüneisen parameters and give rise to an NTE component. The overall thermal expansion behaviour of any given material depends on the relative weightings

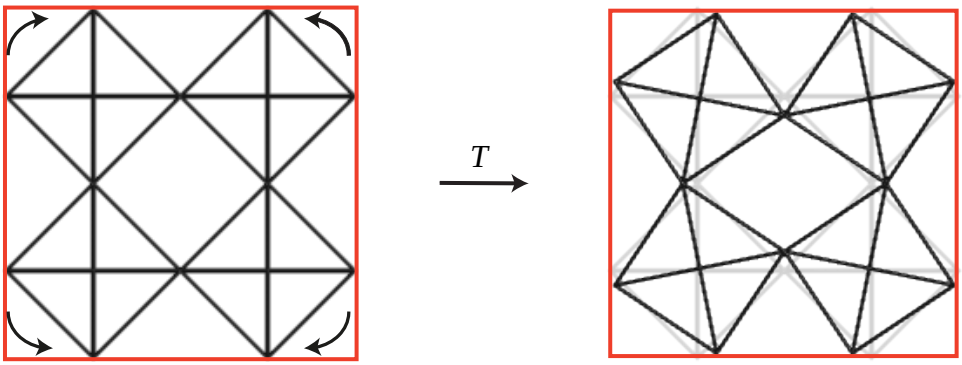

Figure 1.6: Figure showing how 2D RUMs influence materials dimensions. The same principles apply in 3D in materials that possess RUMs or QRUMs.

of the different types of phonon modes, which in turn depends on their energies.

Many polymeric materials can be considered as consisting of rigid polyhedra. These polyhedra are often metal coordination spheres that are joined by corners, edges or faces. The general perovskite structure, for example, can be thought of as corner-sharing MO_6 coordination octahedra. Phonon modes in these materials are termed rigid unit modes (RUMs) if they do not involve deformation of such rigid polyhedra. An example of a RUM in two dimensions is illustrated in Fig. 1.6. RUMs are particularly relevant to the overall thermal expansion behaviour of a material because they do not involve deformation of metal—ligand bond lengths or metal coordination geometries and so generally occur at lower energy than non-RUM type phonon modes.[93] Thus, the Grüneisen parameters of RUMs contribute more significantly to the overall Grüneisen parameter than those of non-RUM type phonon modes.[94] This implies that if RUMs are present in a structure, the consideration of the sign of the Grüneisen parameter associated with these RUMs often provides an indication of the overall thermal expansion behaviour of that material.

Known NTE materials can broadly be categorised into two subgroups: isotropic and anisotropic materials.[95] These materials are dealt with separately in this chapter.

Cubic and isotropic NTE materials Cubic and isotropic NTE materials include alkali halides at low temperatures; cupric structures of the composition M_2O; the fa-

mous large negative thermal expansion material zirconium tungstate (ZrW_2O_8) and related crystals; the cubic zirconium vanadate family of the composition AM_2O_7 (A = Th, Zr, Hf, Sn; M = P, V); silica, zeolites and some glasses and glass ceramics.[95–98]

The most common origin of NTE over a wide temperature range in these materials is related to lattice vibrations (phonons). In many examples, NTE arises from negative-Grüneisen-parameter phonon modes that include transverse vibrations of oxygen atoms in M—O—M bridges. To allow for large-amplitude transverse vibrations in the structures, the tetrahedra and octahedra that the structure composes of undergo coupled librations. These RUMs together with low-energy vibrations involving slight distortions of the polyhedra (quasi-RUMs or QRUMs) contribute to isotropic NTE.[94,95,99–101]. Fig. 1.6 illustrates in 2D how such RUMs decrease the material's dimensions with increasing temperature.

The most famous cubic and isotropic NTE material zirconium tungstate shows NTE behaviour over a wide temperature range between 0 K and 1050 K.[102] The structure was first solved in 1995 by Auray and is illustrated in Fig. 1.7(a).[103] It is composed of corner-sharing ZrO_6 octahedra and WO_4 tetrahedra, with each ZrO_6 connected to six WO_4 units and each tetrahedron connected to only three octahedra, leaving one terminal oxygen [Fig. 1.7(c)]. The magnitude of thermal expansion of zirconium tungstate ($-9.1\,MK^{-1}$ over the temperature range 0 K to 350 K) is of great interest due its similarity to positive coefficients of thermal expansion of many ordinary materials. As NTE was observed over a useful temperature range, including room temperature, zirconium tungstate was seen as the first potential material for use in composite systems. It has been suggested that a number of RUMs and QRUMs contribute to thermal expansion behaviour of zirconium tungstate.[104,105] This mechanistic approach is a subject of controversy and more detailed density functional (DFT) theory calculations need to be undertaken to understand it fully.[106] The magnitude of expansion changes due to an order-disorder phase transition at 448 K (α-ZrW_2O_8 to β-ZrW_2O_8).[107] The transition involves a reorientation of the WO_4 tetrahedra, and causes a discontinuity in the expansion behaviour that is otherwise linear. The cubic symmetry is maintained

throughout this phase transition, and so the NTE behaviour remains isotropic; however, the coefficient of thermal expansion become less negative above 450 K ($-4.9\,\mathrm{MK}^{-1}$ at temperatures between 430 and 950 K).[108]

Analogous structures based on the zirconium tungstate structural topology can be made when substituting either of the metal sites in the structure. Specific examples include Hf on the Zr site and Mo on the W site and materials with NTE properties have been synthesised.[107,109,110] The HfW_2O_8 compound exhibits essentially identical expansion behaviour to ZrW_2O_8 itself, and only a small increase in the temperature of the order-disorder phase transition ($T_p = 463\,\mathrm{K}$) is observed. In contrast, $ZrMo_2O_8$ and $HfMo_2O_8$ do not undergo a transition to the ordered structure, but adopt a disordered structure at all temperatures.

Another example of an NTE mechanism is the case of the zirconium vanadate family. Negative thermal expansion of the zirconium vanadate family was demonstrated in the 1990s.[111] ZrV_2O_7 is thermodynamically stable up to about 1075 K, where decomposition into binary oxides is observed. The ideal ZrV_2O_7 structure is closely related to the rocksalt structure where Zr^{4+} is on the cation site, and $(V_2O_7)^{4-}$ on the anion site [Fig. 1.7(b)]. The V_2O_7 groups order along the threefold rotation axis, constraining the V—O—V bond angles to be linear on average, though local distortions from this average have been observed [Fig. 1.7(d)].[96,112] The Zr^{2+} cations are octahedrally coordinated by oxygen, and the octahedra and tetrahedra form a corner-sharing 3D network. This arrangement of the structure can give rise to transverse vibrations of corner-sharing oxygen atoms, which can result in NTE. In these structures, the mechanism for NTE involves coupled 3D rotation of slightly distorted polyhedral units and non-linear M—O—M bridges and does not include RUMs, but QRUMs only.[99] The coefficient of thermal expansion for ZrV_2O_7 is between -7 and $-10\,\mathrm{MK}^{-1}$ above 375 K, but the materials undergoes a phase transitions to an incommensurate phase at 375 K, and to an ordered cubic phase at 350 K upon cooling.[112–114] In the room temperature cubic phase, 2/3 of the V—O—V linkages are no longer restricted to be linear on average by symmetry, and the expansion coefficient becomes positive.

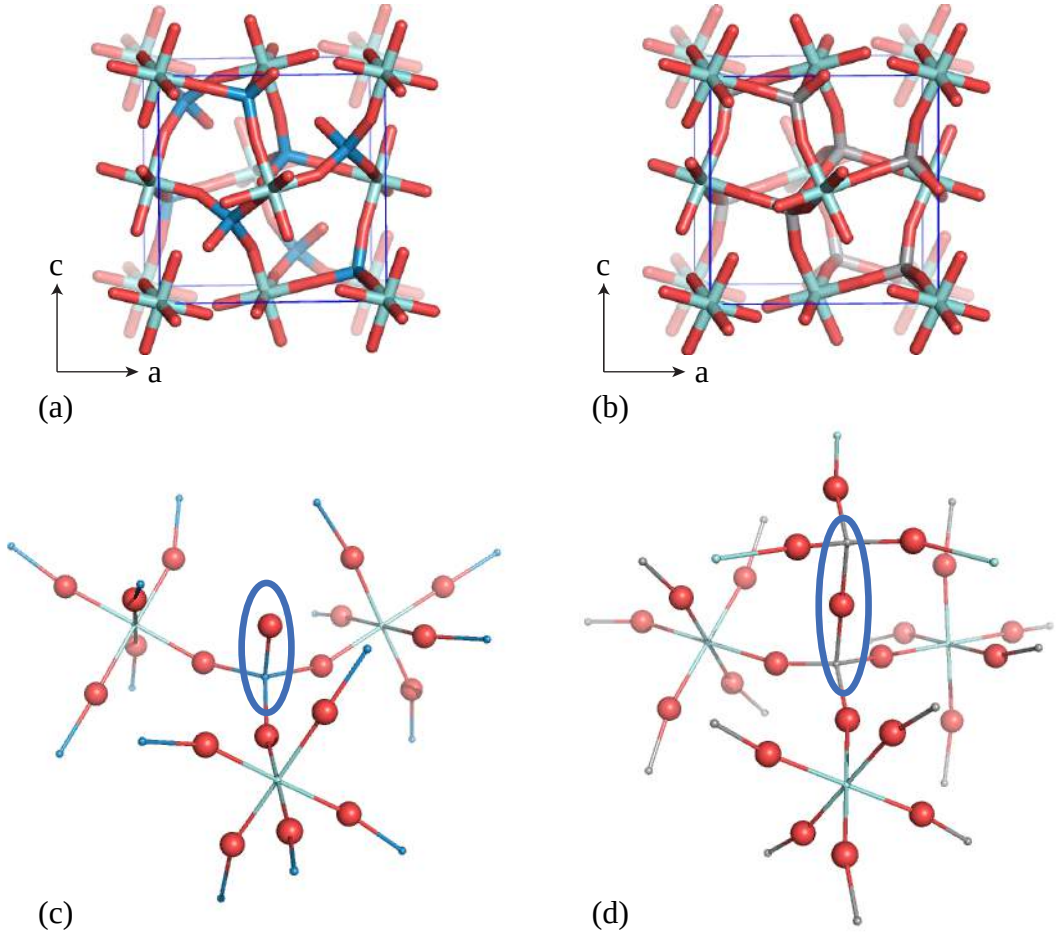

Figure 1.7: Structures of (a) zirconium tungstate structure; (b) zirconium vanadate structures with red representing oxygen, grey vanadium, dark blue tungsten and light blue zirconium; (c) shows the terminal oxygen in zirconium tungstate and (d) V—O—V linkages in the zirconium vanadate structure.

The ZrV_2O_7 structure can accommodate a wide range of tetra- and pentavalent ions.[96] For M = P, the A site cation can be Zr, Hf, Ti, U, Th, Pu, Np, Mo, W, Ce, Pb, Sn, Ge or Si, whereas for the vanadates only the Zr and Hf compounds are known.[112] Moreover, for the arsenates only the Zr and Th compounds have been synthesised.[115,116] These structures can accommodate distortions from the parent structure and for example, SnP_2O_7 and GeP_2O_7 were found to be monoclinic[117], CeP_2O_7 and AnP_2O_7 (An = U, Th, Pu, Np) have been reported as triclinic[118], and ZrP_2O_7 and HfP_2O_7 undergo an orthorhombic distortion[119]. The magnitude of thermal expansion of AM_2O_7 compounds depends on the nature of the A and M cations and the size of the respective polyhedra. Larger polyhedra can accommodate the distortions required for transverse oxygen vibrations more easily. As a result, most phosphates show positive expansion at all temperatures, whereas the vanadates show strong NTE in the high temperature phase. Phosphates with large A cations (*e.g.* CeP_2O_7, AnP_2O_7) show a change from positive to negative expansion with increasing temperature.[120]

Other specific examples include CuCl, which shows NTE below 100 K.[121] NTE in this material reaches its minimum at about 30 K and has the value of $-8\,MK^{-1}$. Initial X-ray diffraction experiments showed that Ag_2O exhibits NTE over its entire range of stability up to 500 K, however, later diffraction experiments up to 280 K suggested that the material shows NTE up to 150 K, slightly positive expansion between 150 K and 220 K and again NTE from 220 K to 280 K.[122,123] Later the phonon spectrum was measured for Ag_2O at 310 K and 150 K and the phonon modes responsible for NTE behaviour were identified.[124] As an example, the siliceous zeolite material chabazite shows NTE values of $-0.5\,MK^{-1}$ to $-16.7\,MK^{-1}$ over the temperature range 293 K to 873 K.[125]

Anisotropic NTE materials In recent years, the number of NTE materials has risen substantially. There are a number of materials that exhibit anisotropic NTE. The most famous of these is the scandium tungstate family of the composition $A_2M_3O_{12}$.[126] $Sc_2W_3O_{12}$ is thermodynamically stable over a wide temperature range and the crystal

structure is composed of a corner-sharing network of ScO_6 octahedra and WO_4 tetrahedra. Geometric analysis has shown that no true RUMs are present in this structure; however, NTE still arises from transverse vibrations of M—O—M′ linkages.[127] Furthermore, many zeolites and zeolitic frameworks (AlPOs, GaPOs) exhibit NTE as their structures are composed of corner-sharing tetrahedral networks and allow for transverse vibrations.[128,129] Over the last years, studies have identified that some MOFs exhibit very large negative and highly anisotropic thermal expansion with a magnitude significantly greater than that for metal oxides and zeolites.[130–133]

Due to the large number of anisotropic NTE materials, the following sections present more detailed examples of materials, where dimensionality of the materials can be linked to their NTE response. Such materials include low-dimensional layered and chain structures. Graphite[134], hexagonal boron nitride (hBN)[135], α-arsenic[136] and hexagonal close-packed zinc and cadmium structures[137] are examples of the former and trigonal selenium[138] and tellurium[139] and the conjugated polymer polydiacetylene[140] examples of the latter.

In anisotropic materials, changing the temperature at fixed strain causes anisotropic thermal stress and the resulting thermal expansion is influenced by the elasticity of the material. Thus, both changes in volume and changes in shape need to be considered and consequently a stress applied in one direction affects the dimensions of the material in other directions.[95] There are two independent dimensions a and c in crystals with 'axial' symmetry, which include tetragonal, hexagonal, trigonal systems and non-crystallographically cylindrical topology.[141] It can be shown that thermal expansion of these materials can be quantified by considering the Grüneisen functions, γ_j, which describe the strain dependent entropy that produces a 'thermal pressure' and the elastic compliances, S_{ij}, which quantify the elastic response of the solid to this 'thermal pressure'. The respective thermal expansion coefficients are represented by equations

$$\alpha_a = \frac{C_T}{V}(K_a\gamma_a + S_{i3}(\gamma_c - \gamma_a)), \tag{1.2}$$

$$\alpha_c = \frac{C_T}{V}(K_c\gamma_c - 2\gamma_{i3}(\gamma_c - \gamma_a)), \tag{1.3}$$

where K_j are the linear compressibilities, C_T is the isothermal specific heat and V the unit cell volume. These equations describe quantitatively how NTE in anisotropic materials is caused by the strain induced 'thermal pressure' or the elastic response of the solids to this strain or a combination of both. The first term on the right-hand-side of Eq. (1.2) and (1.3) corresponds to the direct thermal expansion along the respective axes and the second term can be thought of as a cross-coupling term that describes how thermal expansion in one directions affects thermal expansion in other directions of the material.[136]

A qualitative interpretation of the above equations can be given based on the example of the hexagonal structure of graphite, where elastic cross-coupling is small [Fig. 1.8(a)].[142] The covalently bound layers in this material are held together *via* weak dispersion forces and the structure is therefore very stiff parallel to the layers and compressible perpendicular to them. The phonon modes with atomic motion normal to the layers and parallel to the weak dispersion forces are high in amplitude and have low frequencies, whereas the phonon modes within the layers have low amplitudes and high frequencies.[143] At low temperatures, where graphite exhibits NTE, the low frequency phonon modes become preferentially excited with a resulting compressive thermal stress normal to the planes and tensile stress within the sheets, which manifest in NTE within the sheets. The magnitude of the resulting negative thermal expansion along a is much smaller than that of the positive thermal expansion along c, stemming from the much greater stiffness within the planes than between them. In the context of Eq. (1.2) and (1.3), the implication is that the Grüneisen parameter for the phonon modes within the sheets is negative, whereas the phonon modes with their amplitude normal to the layers have positive Grüneisen parameters. The greater stiffness within the sheets can be attributed to a much smaller compressibility value as opposed to normal to the sheets. Thus, the first term in Eq. (1.2) gives a small and negative coefficient of thermal expansion and in Eq. (1.3) a large and positive coefficient of thermal expansion. Elastic cross-coupling between the two directions is small due to very weak forces between the layers and therefore, the second term on the

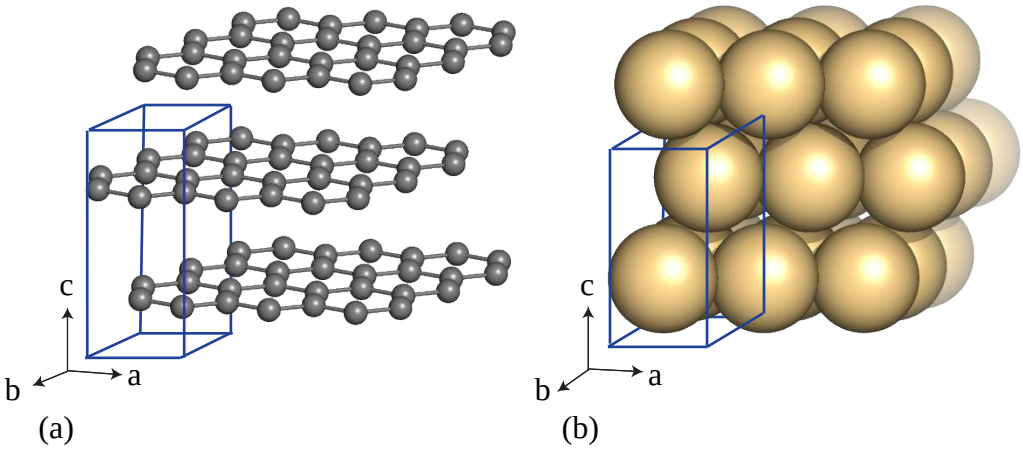

Figure 1.8: Layered structures with (a) representing the hexagonal honeycomb layers of graphite, illustrating the 2D nature of the layers and (b) illustrating the structure of hexagonal close-paced Cd with metallic bonding within and between the layers.

right-hand-side of these equations contributes to thermal expansion much less. NTE in hBN is driven by the same principles.[144] These examples show how the 2D nature of the layers is directly responsible for NTE in these layered structures. Elastic response of the structure plays an important role in NTE in the case of α-arsenic and is even more pronounced in hexagonal close-packed structures of cadmium and zinc.[145,146] In these structures, there is metallic bonding both between and within the layers and hence strong elastic coupling between the directions perpendicular and parallel to the layers [Fig. 1.8(b)]. The Grüneisen parameters are positive at all temperatures and would result in positive thermal expansion, however, due to to large and negative values for S_{13}, the materials exhibit NTE in the direction of the layers.[136]

Similar considerations justify the NTE response for chain structures.[147–149] In these materials, the direction parallel to the chains is stiff and the directions perpendicular to the chains very compressible. A general qualitative mechanism for NTE is comparable to that of graphite: at low temperatures, vibrations perpendicular to the chains are excited preferentially, giving rise to compressive thermal stress perpendicular and tensile thermal stress parallel to the chains, leading to NTE parallel to the chains.

Another example of anisotropic NTE materials that is of interest from a dimensionality point of view, is the mechanism leading to NTE in some aluminosilicate minerals zeolites. The shape and size of the channels formed in these structures depend greatly on the connectivity of the structure. Thermal expansion arises from the rotation of tetrahedra in these structures and deforms the channels. It has been shown by simulations that structures with only 1D channels tend not to show NTE, whereas structures with 2D and 3D channels do.[150,151]

1.5 Cyanide containing negative thermal expansion networks

In recent years, a number of cyanide containing frameworks have shown an NTE response. Since the current work presents examples of dimensionality-NTE relationships in 2D and 3D cyanide frameworks, the examples and mechanism leading to NTE in cyanide-containing networks is considered in more detail.

The first example of cyanide-containing NTE materials was cubic and isotropic $Zn(CN)_2$, which adopts a purely tetrahedral framework, with the tetrahedra connected by a diatomic cyanide linker. NTE in this structure was demonstrated by Williams et al. in 1997.[152] $Fe[Co(CN)_6]$ was the first orthorhombic crystal structure of cyanide-based materials to exhibit NTE, demonstrated in 2004.[153] In recent years, a number of cyanide-containing frameworks have been reported to have large NTE responses. These materials include structures based on the $Cd(CN)_2$ structure, Prussian blue analogues of the composition $M_3[M'(CN)_6]_2$ (M= Mn, Fe, Co, Ni, Cu and Zn and (M′) = Co, Fe), $Ni(CN)_2$, compounds of the composition $LnCo(CN)_6$ (Ln = La, Pr, Sm, Ho, Lu, Y), MCN compounds (M = Cu, Ag, and Au), $In[M(CN)_2]_3$ (M = Ag, Au) and the colossal negative thermal expansion material $Ag_3[Co(CN)_6]$ and its analogues.[154–160] The principle vibrational mechanism of transverse vibrations holds true in these mate-

rials, however, the diatomic nature of cyanide linker provides greater flexibility to the framework.[161]

The M—CN—M′ bridges in these materials possess two doubly-degenerate transverse vibrational modes, denoted by δ_1 and δ_2 [Fig. 1.9]. Assuming constant M—C, N—M′ and C—N bond lengths, these vibrational modes result in a decrease of the M...M′ distance as they involve only bond bending and deviations of the C and N atomic positions from the central bond M...M′ axis. It is assumed here that the masses of the M and M′ atoms are considerably greater than that of either the C or N atoms, and therefore the vibrational motion of the cyanide bridge can be considered in terms of the motion of the C and N atoms alone. RUM theory has been helpful in justifying NTE in a number of cyanide containing frameworks and the transverse vibrations of the CN linkers could directly be observed by pair distribution function (PDF) analysis in $Zn(CN)_2$.[162,163] Moreoever, recent experimental results and DFT calculations have investigated the change of the coefficients of thermal expansion for $Zn(CN)_2$ with varying pressure and temperature.[164] According to a study by Fang et al. the pressure-enhanced α values (averaged over 50–300 K) at 0.0 GPa, 0.2 GPa, and 0.4 GPa are $-12.62\,MK^{-1}$, $-14.09\,MK^{-1}$, and $-15.97\,MK^{-1}$, respectively, compared to the experimental values of $-17.40(18)\,MK^{-1}$, $-18.39(27)\,MK^{-1}$, and $-19.42(23)\,MK^{-1}$ at the corresponding pressures. DFT calculations also confirmed the experimental finding that there is clearly a phase transition in the material and indicated the negative Grüneisen parameter phonon modes that contribute to NTE of the material and indicated that all these modes are RUMs.[165] Moreover, for the $LnCo(CN)_6$ (Ln = La, Pr, Sm, Ho, Lu, Y) series it has been argued that there are non-RUM vibrational modes, which stem from the local instability of the trigonal-prismatic lanthanoid coordination geometry — a unique coordination geometry for lanthanides.[166]

The transverse vibrational modes in many cyanide containing frameworks are of lower energy than the longitudinal bond stretching vibrations also associated with M—CN—M′ bridges.[167] The latter give rise to positive thermal expansion (PTE) and thus, overall thermal expansion behaviour in many cyanide frameworks is a result of the combination

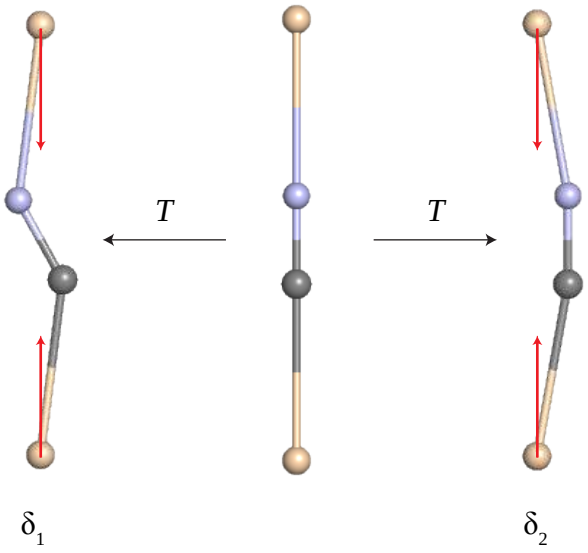

Figure 1.9: Illustration of the two types of transverse vibrational mode present in M—CN—M′ bridges. The central diagram represents the zero point. Each mode is doubly degenerate so that the C and N atoms have rotational freedom about the M...M′ axis. The effect of excitation to higher vibrational energy level on the net M...M′ distance is indicated by the red arrows: note that, in both cases, this distance decreases with increasing vibrational state.

of these vibrations. NTE is observed if the transverse vibrational modes are preferentially populated over the longitudinal stretching vibrations, which depends on the respective energies of these vibrational modes. It is noted that at higher temperature, the stretching vibrational modes become activated and hence this mechanism predicts PTE for cyanide-containing frameworks over an infinite temperature range.

In some cyanide-containing frameworks, including the colossal NTE material $Ag_3[Co(CN)_6]$, metallophilic interactions are important for the material to show an NTE response, which is too large to be justified by the transverse vibrational model only.[160]

$Ag_3[Co(CN)_6]$ is composed of sheets of $[Co(CN)_6]$ octahedra that are separated by layers of Ag^+ ions. The Ag^+ centres are linearly coordinated by two cyanide groups and the Ag...Ag contacts are close to the van der Waals radii along the a direction of the crystal. The latter suggests argentophilic interactions along this direction in the mate-

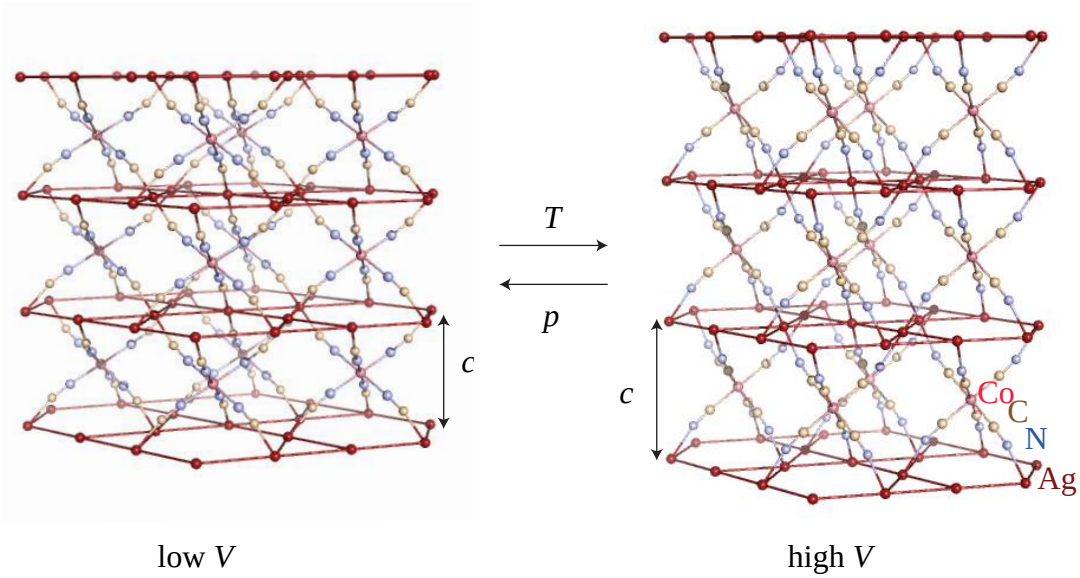

Figure 1.10: Compression mechanism in $Ag_3[Co(CN)_6]$, exaggerated for illustrative purposes. In order for the framework to reduce its volume (either in response to a decrease in temperature or an increase in pressure), it must expand along the trigonal axis (c) (Adapted from Ref. 160).

rial.[168] These Ag...Ag and the corresponding $[Co(CN)_6]$...$[Co(CN)_6]$ contacts increase rapidly with temperature. To preserve the connectivity of the Co—CN—Ag—NC—Co bridges, the strong expansion along the *a* axis must be coupled to equally strong NTE response along the *c* axis [Fig. 1.10].[169]

From a dimensionality perspective, MCN compounds (M = Cu, Ag, and Au) and $Ni(CN)_2$ are of great interest.[170] The former are 1D columnar structures and the latter is a 2D layered structure; consequently strong interactions are constrained to either one or two dimensions, respectively.[156,157,159] Such low-dimensional binding is related to the nature of the cyanide ligand, which forms linear bonds with metal cations and gives rise to low dimensionality. This is a contrast to oxygen ligands, which can coordinate to metal cations in all directions.[167] The framework topology in these materials is determined by the coordination chemistry of the corresponding metal cations and results in square planar d^8 Ni^{2+} and linear d^{10} M^+ coordination with cyanide anions. Such low-dimensional frameworks exhibit weak dispersion forces and electrostatic interactions

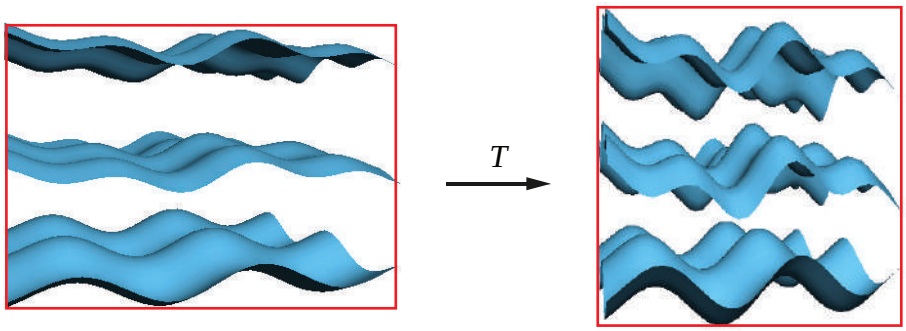

Figure 1.11: 'Rippling' of the 2D layers of $Ni(CN)_2$ that results in large positive thermal expansion perpendicular and small negative thermal expansion within the layers.

between the layers or columns that aid the periodic ordering of the solid as a whole. The dynamical properties of these low-dimensional materials are dominated by the effects of their reduced dimensionality. Vibrational motion in layered materials consists primarily of 'rippling' of the layers and skipping-rope-type transverse displacements in columnar structures [Fig. 1.11]. Such vibrations are due to the transverse vibration of the cyanide bridges, but are now constrained to one or two dimensions.[171] Therefore these distortions result in area-NTE within the planes of $Ni(CN)_2$ and NTE along the chain axis for the MCN family.

1.6 Negative compressibility

In this thesis, we will explore the compressibility behaviour of 2D framework materials based on cyanide-containing ligands. Here we summarise the key aspects of negative compressibility and the materials in which it has been observed.

It is a thermodynamic requirement of a material to decrease its volume under hydrostatic pressure. Therefore, without a pressure-induced phase transition, $-\frac{dV}{Vdp}$ must always be positive. The search for materials that increase in one or two linear dimensions, *i.e.*, $-\frac{dL}{Ldp}$ is negative (negative linear compressibility or NLC) or $-\frac{dA}{Adp}$ is negative (negative area compressibility or NAC) is still at an early stage.[172] Such materials can,

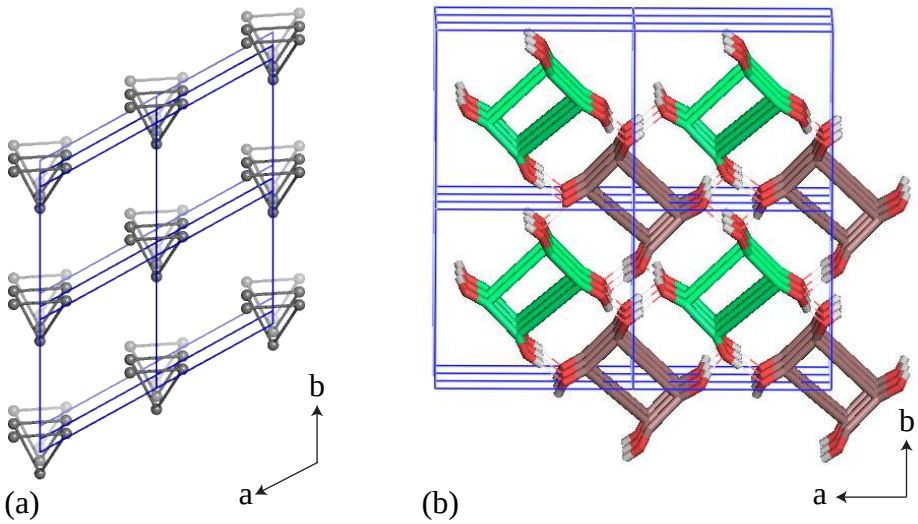

Figure 1.12: Helical structures that show NLC with (a) 1D helices of Se and (b) helical structure of β-phase of m-dihydroxybenzene with dihydroxybenzene units shown as rods.

however, find applications in artificial muscles or pressure detectors for seismic, sonar and aircraft purposes, justifying the search for new materials exhibiting these phenomena.[172] Many earlier NLC materials comprise of helical chains: single helices (*e.g.* Se, Te)[141], or the network of interconnected left- and right-handed helices (β-phase of m-dihydroxybenzene) [Fig. 1.12].[173] In the case of β-phase of m-dihydroxybenzene the arrangement of helical chains with respect to each other allows for the NLC response observed. This mechanism is similar to the 'wine-rack-like' mechanism discussed below. Furthermore, the anisotropicity of the 1D chain structure of CsH_2PO_4 is suggested to determine the material's response to pressure and lead to NLC.[174]

In recent years, materials with 'wine-rack' topologies have demonstrated NLC [Fig. 1.13]. Such materials include methanol monohydrate, ammonium zinc formate and some cyanide based molecular frameworks, including $Ag_3[Co(CN)_6]$ and $Zn[Au(CN)_2]_2$.[175–178] The observed NLC in these systems directly stems from the systems' topological 3D connectivity and links ordinary linear compressibility in two perpendicular directions to NLC in the third. Moreover, a helical arrangement of Au^+ cations in a giant neg-

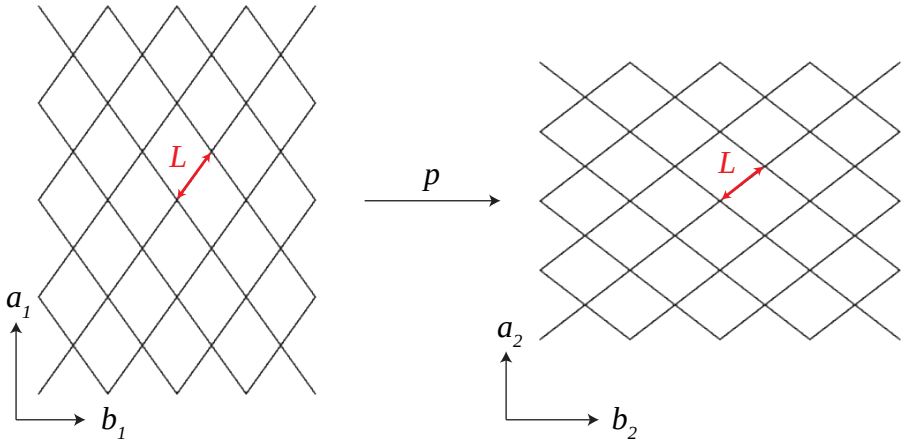

Figure 1.13: 2D wine-rack model for NLC in some framework materials. As hydrostatic pressure is applied, the material expands in one dimensions coupled by a contraction in a perpendicular dimension.

ative compressibility material $Zn[Au(CN)_2]_2$ evoke the NLC response observed in this material. It is noteworthy that the Au^+ cations form very compressible 1D helical chains due to 'aurophilic' interactions, causing the giant NLC in another direction of the material.[179] From a dimensionality point of view, the aforementioned examples illustrate how the structural connectivity in three dimensions must be anisotropic in materials that possess NLC and how NLC in one direction can be achieved or driven by positive compressibility in other directions.

In principle, the most extreme negative compressibility response allowed thermodynamically is that of NAC, whereby a material expands along two orthogonal directions on increasing pressure. The possibility that tetragonal $PbTiO_3$ might show an extremely weak NAC effect has been raised and disputed; similarly weak effects are thought to occur at high pressure in NaV_2O_5 and are predicted for $TlGaSe_2$.[180–183] Instead the remarkably few negative compressibility materials that have been characterised unambiguously expand along only one principal axis when compressed hydrostatically, *i.e.*, negative linear compressibility.[177,179,184–186] The distinction between NLC and NAC is more fundamental than magnitude alone: NAC materials increase their surface area under hydrostatic pressure, and so they can be used as substrates

to provide order-of-magnitude amplification of piezoelectric response in *e.g.* FE sensors.[187]

1.7 Aim of the project

The aim of this project is to examine how structural dimensionality of materials can influence the properties of a variety of functional materials: we study this based on topological examples of 2,3,6,7,10,11-hexahydroxytriphenylene tetrahydrate (HHTP·$4H_2O$), silver(I) tricyanomethanide [Ag(*tcm*)], nickel(II) cyanide [$Ni(CN)_2$] and nickel(II) cobalt(II) cyanide [$NiCo(CN)_4$]. We focus on thermal- and pressure-driven responses and use diffractions techniques as our primary method of understanding structure-property relationships.

HHTP·$4H_2O$ was chosen as the crystal structure was reported to exhibit 1D pores that are filled with water molecules.[188] These pores are similar to the low-dimensional water channels of carbon nanotubes or those reported for low-dimensional confined ices.[189–195] Our hope was to establish crystallographically whether the water channels in HHTP·$4H_2O$ could potentially exhibit FE properties. This would be feasible due to the low-dimensionality of the channels that restricts water molecule orientations, similarly to the aforementioned carbon nanotubes and confined ices. A more detailed description of our hypothesis is given in chapter 4.

One strategy for identifying negative compressibility candidates is to target framework materials that exhibit anisotropic negative thermal expansion (NTE): a material that shrinks in one direction on heating is likely to expand in that same direction on compression.[196] While there is no requirement that deformation mechanisms under temperature and pressure are identical, there is empirical evidence of such a correspondence amongst molecular framework materials.[175,176,178,197] The natural strategy then for identifying NAC candidates is to investigate framework materials that exhibit area-NTE. It is for this reason that we chose to investigate the compressibility and thermal expansion behaviour of $Ni(CN)_2$ and Ag(*tcm*). Area-NTE for the former has

been identified before and results from its 2D structure. The latter is also a 2D framework material and has the layer-like network topology of a form often associated with area-NTE.[156,157,171,198] These observations initiated our high pressure studies on these materials to demonstrate whether they possess NAC.

Furthermore, we set to investigate thermal expansion in $NiCo(CN)_4$ to understand the effect of increasing dimensionality from a 2D to a 3D structure. Our hope here was to connect the layers by introducing Co^{2+} centres, which have d^7 electron configurations, and could facilitate octahedral or tetrahedral connectivity.

The next chapter in this thesis outlines the theory behind various diffraction techniques and the chapter after that outlines experimental methods used during our investigations. This is followed by four experimental chapters. The first of these focuses on the one-dimensional ice channels in $HHTP{\cdot}4H_2O$ and the material's structural response to temperature. The second results chapter reports our investigations into the magnetic and electronic properties of the same system. The third results chapter outlines the thermal expansion and compressibility results and analysis for 2D layered structures, $Ag(tcm)$ and $Ni(CN)_2$, while the fourth chapter illustrates a shift from a 2D material to a 3D material based on the example of $NiCo(CN)_4$.

Chapter 2

Theory

2.1 Crystallography

Crystalline materials are defined by comprising of atoms, molecules, or ions which are arranged in an orderly repeating pattern. These materials have long-range order as the orderly repeating pattern extends in all three spatial dimensions. The structure of crystalline materials is described by two components — the lattice and the motif. A lattice can be described as a regular, infinite array of points, in which every point is in the same environment as any other point. The lattice points are related to each other by translations and they do not carry any information about the composition of the material. Any of the lattice points can be chosen as the origin and other lattice points are given by the equation

$$\mathbf{r} = U\mathbf{a} + V\mathbf{b} + W\mathbf{c}, \tag{2.1}$$

where U, V and W are integers and represent the coordinates of lattice points and $\mathbf{r}$, a vector to any other lattice point. The motif is placed on each lattice point and is the smallest repeating unit of atoms, ions or molecules. The symmetry of the motif can be described by one of the 32 crystallographic point groups.

The smallest volume of the lattice can be described by a unit cell. The unit cell is defined by three axis or lattice parameters (a, b, c) and three angles (α, β and γ). Lattice

geometry in three-dimensions can be represented by three non-coplanar basic repeat vectors a, b and c, which restricts the number of possible shapes to six. These six shapes represent seven symmetry types. In accordance with convention, these vectors a, b and c are chosen such that they form a parallelepipedon of the smallest volume in the lattice, and are parallel to, or coincide with, important symmetry directions in the lattice. This results in non-primitive unit cells. For three dimensional structures, there are unit cells, were lattice points are on pairs of opposite faces, in the middle of the unit cell (body-centered unit cells) and on all faces (face-centered unit cell). Consequently, there are a 14 different three-dimensional lattices, called the Bravais lattices.[199] Each of these Bravais lattices is described by a unit cell and by the vectors a, b and c and is therefore a combination of one of the seven different symmetry types with one of the five lattice centerings:

1. Primitive (P) — one equivalent lattice point at each corner of the unit cell.
2. Body centred (I) — one additional lattice point at the centre of the cell.
3. Face centred (F) — one additional lattice point at the centre of each of the faces of the cell.
4. Rhombohedral (R) — two additional lattice points in the unit cell.
5. Centred on a single face (A, B or C) — one additional lattice point at the centre of one of the cell faces.

The different Bravais lattices are represented in Table 2.1. When translational symmetry operations, *i.e*, screw axes and glide planes, are added to the symmetry of the 14 Bravais lattices and the 32 point groups of the constituents of the crystal, a total of 230 different crystallographic space groups are obtained. The latter describe all the symmetry relationships in a structure.

Planes of atoms within the crystal can be labeled with respect to the origin and the points where they intersect the a, b and c axes. There are three integers h, k, and l, called Miller indices, that define a plane intercepting a at $\frac{a}{h}$, b at $\frac{b}{k}$ and c at $\frac{c}{l}$.

Table 2.1: Table describing the fourteen Bravais lattices.

Unit Cell	Lattice Parameters	Angles	Bravais Lattice
Triclinic	$a \neq b \neq c$	$\alpha \neq \beta \neq \gamma \neq 90°$	P
Monoclinic	$a \neq b \neq c$	$\alpha = \gamma = 90° \neq \beta \neq 90°$	P C
Orthorhombic	$a \neq b \neq c$	$\alpha = \beta = \gamma = 90°$	P A,B,C, F I
Tetragonal	$a = b \neq c$	$\alpha = \beta = \gamma = 90°$	P I
Trigonal	$a = b = c$	$\alpha = \gamma = \beta \neg 90°$	P R
Hexagonal	$a = b \neq c$	$\alpha = \beta = 90°$ $\gamma = 120°$	P
Cubic	$a = b = c$	$\alpha = \gamma = \beta = 90°$	P F I

2.2 X-ray diffraction

2.2.1 Diffraction

When X-rays, electromagnetic waves with the wavelength of the order of magnitude of 1 Å, encounter atoms, they are diffracted by the electron clouds of the atoms. If the atoms are arranged periodically on a crystalline lattice, and the incident X-ray wave is a monochromatic parallel beam, the diffracted waves interfere in a way that only in a few directions constructive interference will take place, resulting in a non-zero intensity diffracted beam. This is demonstrated in Fig. 2.1 and the reflection condition is given by

$$n\lambda = 2d \sin\theta, \tag{2.2}$$

This relationship allows us to establish the periodic crystal structure from its diffraction pattern and is known as Bragg's law.[200] This can be undertaken most easily when the diffracting planes and the wavelength of the incident beam are of a similar order of magnitude. Crystallographic planes are typically separated by 0.1 Å to 1000 Å and this makes X-rays, neutrons and electrons all suitable for determining a crystal structure.

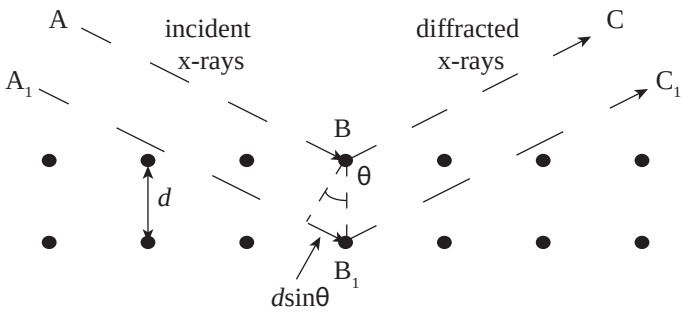

Figure 2.1: The diffracted X-rays exhibit constructive interference when the distance between paths ABC and $A_i B_i C_i$ differs by an integer number of wavelengths (λ).

Laue Equations

In 1912, Max Von Laue developed the equations which correlate scattering angles and the size and orientation of the unit cell spacings in the crystal.[201] He postulated that for constructive interference to occur, there must be a path difference of an integer number of wavelengths between two scattering planes. Consequently, if $\mathbf{k}_i$ is the wave-vector of the incident beam and $\mathbf{k}_s$ is the wave-vector of the scattered beam then

$$\mathbf{k}_i - \mathbf{k}_s = \Delta\mathbf{k}. \tag{2.3}$$

A geometric analysis leads to the three Laue equations:

$$a\cos\alpha_n + a\cos\alpha_0 = a_i\lambda, \tag{2.4}$$

$$bcos\beta_n + b\cos\beta_0 = b_i\lambda, \tag{2.5}$$

$$c\cos\gamma_n + c\cos\gamma_0 = c_i\lambda, \tag{2.6}$$

where a, b and c correspond to the lattice spacing in the unit cell, α_n, β_n, γ_n and α_0, β_0, γ_0 are the incident and outgoing angles of the beam to the x-, y- and z-axis, respectively and a_i, b_i, c_i are integer values. In 1913, Bragg combined these equations into a single formula, known as the Bragg's law and given in section 2.2.1.

Reciprocal space

The concept of reciprocal space helps us understand diffraction for 3D crystals. Each real space lattice plane d_{hkl} can be converted into reciprocal lattice point at a distance of d^*_{hkl} from the origin as described by the equation

$$d^*_{hkl} = \frac{1}{d_{hkl}}. \tag{2.7}$$

Thus, the units in reciprocal space are Å^{-1} and the respective unit cell parameters are represented by a^*, b^* and c^* with the angles α^*, β^* and γ^* being defined as 180° minus the real space angle.[202] Therefore a plane with Miller indices in real space can be represented by a vector in reciprocal space and is given by its constituents by

$$\mathbf{d^*_{hkl}} = h\mathbf{a^*} + k\mathbf{b^*} + l\mathbf{c^*}. \tag{2.8}$$

Ewald's Sphere

The Ewald Sphere is used to determine which sets of lattice planes will diffract radiation of a given wavelength, λ. Bragg's law can be rearranged to give equation

$$\sin\theta = \frac{\lambda}{2d} \tag{2.9}$$

and substituting d^*_{hkl} into this equation gives

$$\sin\theta = \frac{d^*_{hkl}\lambda}{2}. \tag{2.10}$$

For constructive interference to occur, this condition must be met and is represented schematically by the Ewald's Sphere [Fig. 2.2].[202] The sphere is located so that its circumference passes through the origin (point O in Fig. 2.2) of the reciprocal lattice. The incident radiation beam is placed along a radius of the sphere passing through the origin of the reciprocal lattice. When 2θ equals 180°, then d^*_{hkl} lies parallel to

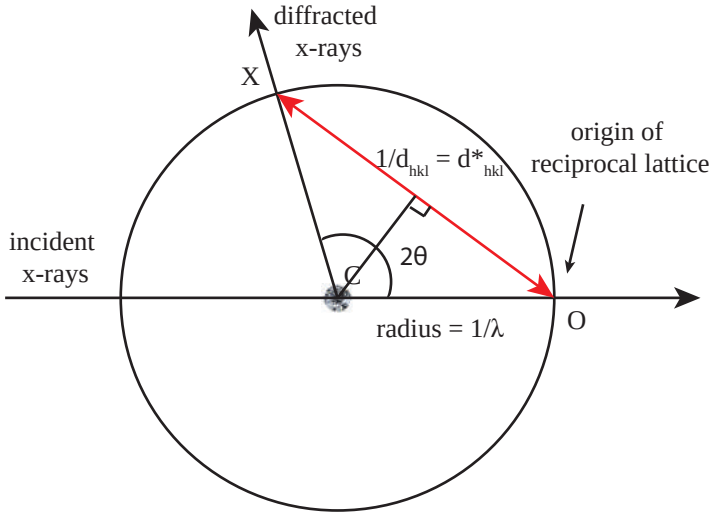

Figure 2.2: Schematic representation of Ewald's Sphere.

the incident beam and it can be derived from Eq. (2.10) that the radius of the sphere is equal to $1/\lambda$. Therefore only reciprocal lattice points that lie on the surface of a sphere with radius $1/\lambda$ will be seen using radiation of the wavelength λ. Rotating the crystalline sample relative to the incident radiation has the effect of rotating the sphere around the origin so different reciprocal lattice points are on the surface (point X in Fig. 2.2).

Diffraction process

We firstly define the atomic scattering factor f as

$$\text{atomic scattering factor } f = \frac{\text{amplitude scattered by atom}}{\text{amplitude scattered by a single electron}}. \tag{2.11}$$

At zero scattering angle, all the scattered waves are in phase and the scattering amplitude is the simple sum of the contributions from all Z electrons, *i.e.*, $f = Z$. With increasing scattering angle, f falls below Z as the destructive interference effects between Z scattered waves increase. Atomic scattering factors are plotted as a function of angle (usually expressed as $\sin\theta/\lambda$).

The scattering amplitude of a unit cell is determined by the sum of the scattering amplitudes of the atomic scattering factors from all the atoms in the unit cell. This quantity is described by the structure factor and given by the equation:

$$\text{structure factor } F_{hkl} = \frac{\text{amplitude scattered by the atoms in the unit cell}}{\text{amplitude scattered by a single electron}}. \quad (2.12)$$

F_{hkl} expresses both the amplitude of the scattered waves from a reflecting plane with Miller indices h, k and l and the phase angle of the scattered wave and is therefore a complex number. Crystal structure determination can broadly be divided into two processes: (a) the determination of the size and shape of the unit cell from the geometry of the diffraction pattern, and (b) the determination of the lattice type and distribution of the atoms in the structure from the relative intensities of the diffraction spots. The intensity of the diffraction peaks is proportional to the square of F_{hkl} and therefore the information regarding the phase of F_{hkl} is lost in diffraction experiments. Determining the phase of the scattered beams to reconstruct a crystal structure from its diffraction pattern is a complex problem.

F_{hkl} can be represented mathematically by the equation

$$F_{hkl} = \sum_{n=0}^{n=N} f_n \exp 2\pi i(hx_n + ky_n + lz_n). \quad (2.13)$$

Electron density in a crystal structure is a continuous function and can be represented by the equation

$$\rho_{xyz} = \sum\sum\sum |F_{hkl}| \cos 2\pi(hx + ky + zn - \Phi_{hkl}), \quad (2.14)$$

where ρ_{xyz} is the electron density at a given point at x, y, z and Φ_{hkl} is the phase of the h, k, l reflection.[203] As discussed above, the amplitude of F_{hkl} is proportional to the intensity of diffraction peaks, whereas the phase information is much harder to recover. There are methods derived to overcome this problem known as the Phase Problem. Typical choices for determining the structures of small molecules, such as systems

studied in this thesis, are the Patterson method[204] and Direct methods[205].

Patterson method The structure of small molecules can be solved even without the phase information. The Patterson function is obtained by calculating a map using the squared structure factor magnitudes, $|F_{hkl}|^2$, and all the phases set to zero. The Patterson map shows peaks at every position that corresponds to an interatomic vector in the structure. This method has been successful for solving small molecules and is most useful for structures containing a few heavy atoms and many light ones due to the vectors between heavy atoms being very prominent.

Direct methods Direct methods is a statistical approach, which is most helpful in determining structures that contain many light atoms. In the case of direct methods, the missing phase information can be reconstructed directly from mathematical relationships between the structure factors. The method involves putting constraints on electron density, *e.g.* that it is positive everywhere or that it is located into distinct atomic peaks. Obtaining information about the phase and amplitude of one structure factor, places constraints on other structure factors. The strongest relationship of this form is the three phase invariant: in this case, the constraints of positivity and atomicity imply that when three reflections whose Miller indices sum to zero are strong, the phases of those reflections must sum to a value near zero. Phases are then chosen for a few strong reflections and phases for other reflections are generated using phase relationships among strong reflections. Once enough phases have been calculated, the electron density may be calculated and can be interpreted in terms of atomic positions. The applicability of direct methods decreases as the number of atoms increases.

2.3 X-ray powder diffraction

The equations and methods above describe single crystal x-ray diffraction for crystals with no flaws. It is, however, not always possible to grow single crystal samples of de-

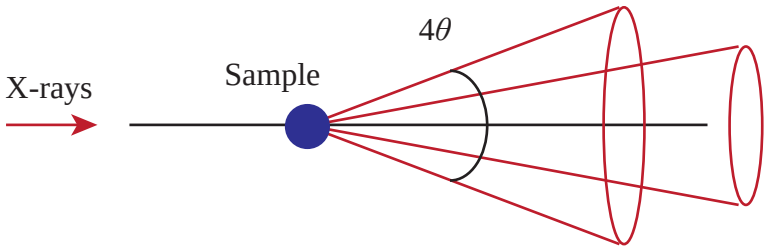

Figure 2.3: Schematic showing the generation of Debye-Scherrer cones from a powder sample.

sired materials. An alternative is a polycrystalline or 'powder' sample, which consists of many crystallites. Powder samples have by definition a very large number of crystallites in them and therefore there will always be some that are aligned at the Bragg angle for every plane with h, k and l with respect to the incident beam. Therefore the scattering vectors lie on sphere surfaces with radii of d^*_{hkl} and not individual lattice points as in single crystal X-ray diffraction. Therefore the condition for constructive interference is only satisfied when the scattering vectors lie on the intersection of the Ewald sphere and a series of concentric spheres, with radii of d^*_{hkl}, located at the origin of the reciprocal lattice. This results in a series of concentric cones, which are known as the Debye-Scherrer cones.[199] When the latter are intersected by a detector, they are seen as rings of varying intensity [Fig. 2.3]. The drawback of powder x-ray diffraction is that it is difficult to assign each ring with an h, k and l value, because the rings from planes of different h, k and l values, but the same d-spacing, lie on top of each other. Another drawback is that planes with similar values for d-spacing may have overlapping features, making structure solution more difficult.

2.3.1 Synchrotron powder diffraction

For creation of X-rays in a synchrotron, electrons from an electron gun (1 in Fig. 2.4) are accelerated by a linear accelerator (1 in Fig. 2.4) and then in a booster synchrotron ring (2 in Fig. 2.4) until they approach the speed of light, followed by their release

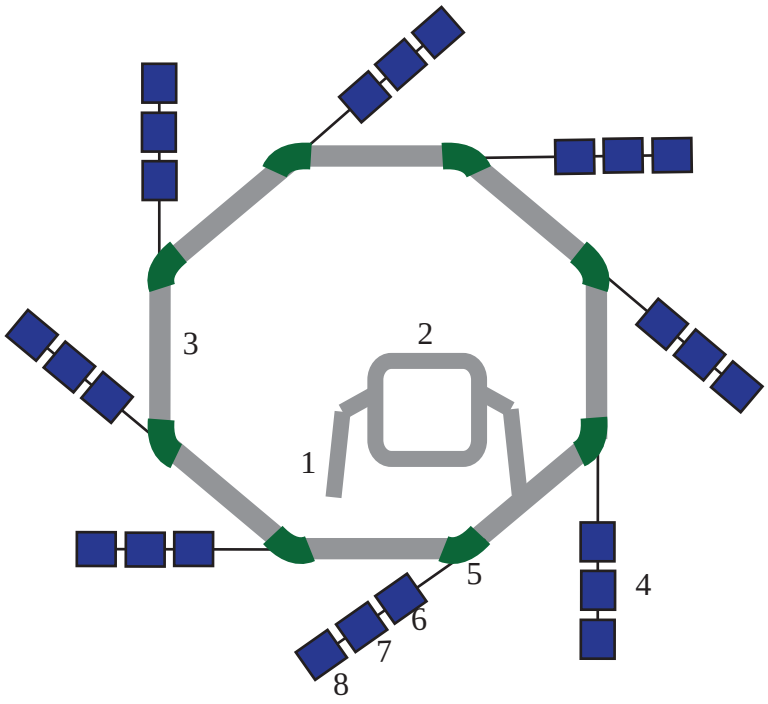

Figure 2.4: Schematic showing a synchrotron.

into the storage ring (3 in Fig. 2.4). The storage ring is a series of straight sections interspersed with bending magnets. When the electron path is bent by a bending magnet, Brehmstrahlung radiation is emitted. Because of the electron energy and the strength of magnetic field of the bending magnet, the Brehmstrahlung radiation is mainly in the form of X-rays. The X-rays are directed into beamlines (4 in Fig. 2.4), where measurements are taken. A typical beamline consists of a front end, optics hutch, experimental hutch and control cabin (5, 6, 7, 8 in Fig. 2.4, respectively).[206]

2.4 Neutron Diffraction

Neutron diffraction is a complementary technique to X-ray diffraction. X-rays are scattered by the electron clouds of atoms, whereas neutrons are scattered by the atomic nuclei. This has an implication that neutron diffraction gives more accurate atomic positions, since it is not influenced by electrons being concentrated into interatomic

bonds or being delocalised. This is particularly true for hydrogen atoms, where bonds to hydrogens often appear too short when determined by X-ray diffraction. These bond lengths can accurately be determined *via* neutron diffraction. On the other hand neutrons have less energy than X-rays, resulting in weaker scattering and therefore larger samples are needed. The weaker interactions with materials equally present an advantage, namely allowing measurements in special environments (*e.g.* furnaces or cryostats) to be performed. The neutron scattering cross section for isotopes varies randomly with their position in the periodic table. This has a consequence that light atoms and atoms with close positions in the periodic table can be distinguished. Furthermore, neutron scattering factors do not vary significantly with θ/λ, meaning that more information can be extracted from a powder pattern at high theta angles. This is a contrast to X-rays, where the scattering intensity decays with increasing *d*-spacing. Finally, the neutron has an intrinsic spin ($I = \frac{1}{2}$) and so a magnetic dipole moment. Thus, neutrons interact with magnetic fields generated by unpaired electrons distributed throughout the solid. If these are distributed in a periodic manner, diffraction from these will result in magnetic diffraction peaks.

There are three types of interactions of neutrons with the atomic nuclei:

1. Elastic scattering with no energy transfer and the scattering can be coherent or incoherent.

2. Inelastic scattering with the energy of the scattered radiation being different from the incident radiation.

3. Absorption with the incident neutron being incorporated into sample nuclei.

Coherent elastic scattering is the interaction utilised in diffraction. Furthermore, the very high incoherent but low coherent scattering lengths for hydrogen cause diffraction patterns to have high backgrounds and lower resolution. In practice, this means that for accurate structure refinement, substitution of ^{1}H for ^{2}D is required as ^{2}D possesses low incoherent and high coherent scattering lengths. Moreover, some isotopes such as ^{10}B strongly absorb neutrons, which makes data collection very difficult.

Neutrons can be viewed as waves, whose wavelength can be given by their momentum

according to the de Broglie relationship

$$\lambda = \frac{h}{m \cdot \nu}, \tag{2.15}$$

where $m \cdot v$ is the momentum of the neutrons.[207] During neutron diffraction, the momentum transfer of neutrons, Q is measured. This can be given in terms of the incident and scattered wavevector by the equation

$$\mathbf{Q} = \mathbf{k_i} - \mathbf{k_s}. \tag{2.16}$$

The magnitude of $\mathbf{k}$ is given by $|k| = \frac{2\pi}{\lambda}$. For elastic neutron scattering there is no energy transfer between the neutron and the sample, so that $|k_i| = |k_s|$. There is, however, a change in direction of the wavevector, so that the neutron diffraction peaks can be collected as a function of $\mathbf{Q}$ by only using neutrons of a specific energy or collecting data at a specific angle.

Using a pulsed neutron source, it is possible to use the entire neutron beam and collect data as a function of the time taken for a neutron to reach the sample from the target, which is known as the time-of-flight (tof). From the time-of-flight and path length from the target to the sample, it is possible to calculate the speed and hence energy of the neutron. From the de Broglie relationship it can be deduced that

$$\lambda = \frac{hT}{Lm}, \tag{2.17}$$

where L is the path length of the neutrons and T the time-of-flight. Combining this with the Bragg equations, allows the measurement of all the d-spacings from the same scattering angle *via* the equation

$$d = \frac{hT}{Lm \sin\theta_0}. \tag{2.18}$$

2.4.1 Neutron source

Neutrons can be generated either by nuclear fission reactions in a nuclear reactor or using a spallation source. Neutron diffraction measurements in this thesis were performed at ISIS in the UK, which uses a spallation neutron source that produces a pulsed beam of neutrons. This technique is described here in more detail. At first H^- ions are generated by an electric discharge. Then the H^- are gathered into bunches and accelerated by a radio frequency quadrupole accelerator and then by a LINAC to 70 MeV [Fig. 2.5]. Upon leaving the LINAC, they lose their electrons by passing through a thin alumina foil, and the resulting H^+ collected in a synchrotron storage ring. The protons in the synchrotron storage ring are accelerated further to 800 MeV and separated into two bunches. Kicker magnets are used for extracting the bunches and direct them to a tungsten target. The huge energy of H^+ forces the tungsten atoms to release some of their neutrons, which creates an intense sharp pulse. In order to lower the speed of the neutrons such that it is suitable for neutron scattering measurements, the neutrons are passed through a moderator. The moderator is composed of small hydrogen-containing molecules, *e.g.* methane or water. Repeated collisions with hydrogen, which has a large scattering cross-section, transfer the excess energy from neutrons.[208]

2.5 Structure determination from powder diffraction data

In this section we describe two types of refinement, which were used for refinement of the data in this thesis — Pawley refinement[209] and Rietveld refinement[210].

The first of these, Pawley refinement, breaks down the pattern into its constituent integrated intensities, I_{hkl}, utilising a least squares analysis. Pawley suggested that angle-dispersive powder diffraction profiles could be fitted with only the following pa-

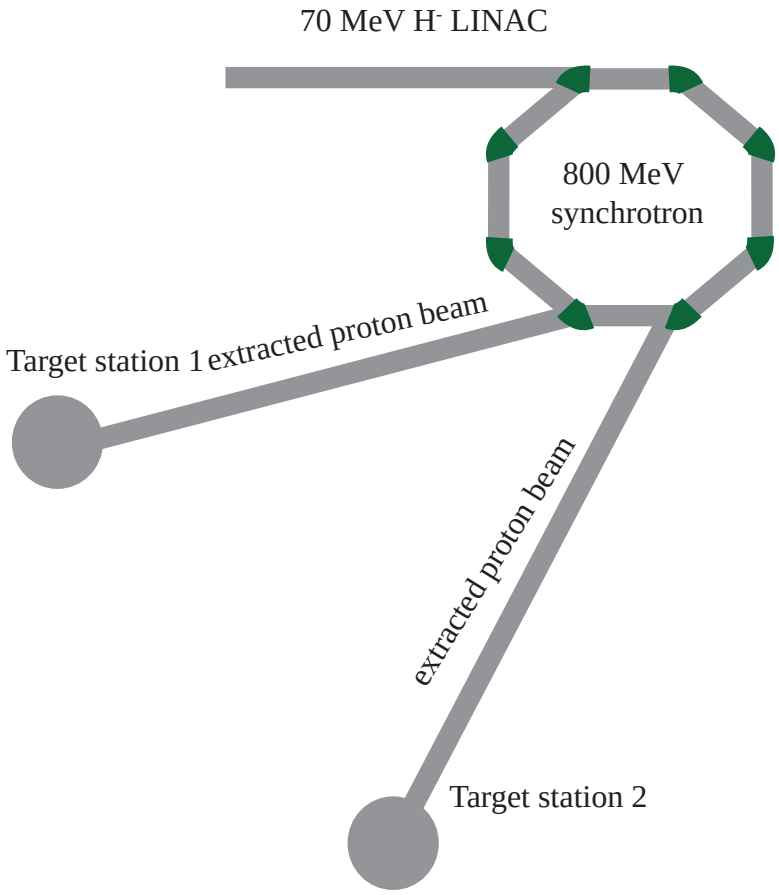

Figure 2.5: Schematic of ISIS – a neutron spallation source.

rameters:

I_{hkl} — Intensity of each reflection with indices hkl;

A,B,C,D,E,F — Unit-cell metric tensor parameters;

$2\theta_{zero}$ — Instrumental zero error;

U,V,W — Peak-width parameters;

η, etc. — Other peak-shape parameters.

Pawley refinement assumes Gaussian peak shapes and that an adequate unit cell for the structure is found by a peak fitting program, however does not require information about the structure of the crystals to obtain a fit. It is therefore a good technique to acquire lattice parameters, when the exact structural motif of the powder is not known.

Rietveld refinement is based on a curve fitting procedure by means of a least squares

refinement that minimises the difference between the observed and calculated patterns instead of individual reflections. The parameter that is minimised is termed residual S_y and is given by the equation

$$S_y = \sum_i w_i(y_i - y_{ci})^2, \tag{2.19}$$

where $w_i = 1/y_i$, y_i is the observed intensity at point i and y_{ci} the calculated intensity at the same point. The Rietveld method models the shape of the Bragg reflections with a peak function such as Gaussian, Lorenzian or pseudo-Voigt. It is assumed in this method that the calculated intensity at any point in the pattern is a sum of intensities of all overlapping peaks at that point. The calculated intensity at each point is given by the equation

$$y_{ci} = y_{bi} + s\sum_K L_K|F_K|^2\phi(2\theta_i - 2\theta_K)P_K A, \tag{2.20}$$

where y_{bi} is background intensity, s is scale factor, K are miller indicies of the Bragg reflection, L_K Lorentz polarisation, $|F_K|^2$ structure factor and multiplicity factor for the Kth Bragg reflection, ϕ is peak shape, ($2\theta_i$ - $2\theta_K$) resolves sample displacement and instrument misalignment, P_K preferred orientation and A absorption. The fit is quantified by several statistical R-values:

1. the profile R value, given as

$$R_p = \frac{\sum|y_i - y_{ci}|}{|y_i|}. \tag{2.21}$$

2. The weighted profile R value, given as

$$R_{wp} = \left[\frac{\sum(w_i y_i - w_i y_{ci})^2}{\sum(w_i y_i)^2}\right]^{\frac{1}{2}}. \tag{2.22}$$

3. The expected profile R value, given as

$$R_{exp} = \left[\frac{N-P}{\sum(w_i y_i)^2}\right]^{\frac{1}{2}}, \tag{2.23}$$

where N is the number of observables and P the number of refined parameters. 'Goodness of fit' is given by the ratio of R_{wp} to R_{exp} and is represented by the symbol χ^2. This value is approaching 1 with an increasingly good fit and values up to 2.5 are considered acceptable.

2.6 The Ising model and order parameter

The Ising model describes ferromagnetism in statistical mechanics.[211] In our study, we have adapted this model to ferroelectricity. In the case of ferromagnetism, the model describes discrete variables that represent magnetic dipole moments of atomic spins that can be in one of two states (+1 or −1). In our investigations we use the dipole moment associated with each individual water channel as the discrete variable and similarly to ferromagnetism the states of these are constrained to +1 or −1. The magnetic spins (or electric dipoles) are arranged on a lattice and they are allowed to interact with each other. The one-dimensional Ising model has no phase transition, however, the two-dimensional Ising model on a square lattice used in this study is one of the most simple models that allows for a phase transition. In our work we use this model to map the phase transition from a ferroelectric to paraelectric regime. Depending on the interaction energies between the dipole moments on the lattice, a phase transition temperature can be calculated. Similarly, knowing the phase transition temperature (as is the case in our study), an estimate for the interaction energy can be achieved. The Ising model takes into an account the lattice sites ▲ that each have a set of adjacent lattice sites forming a d-dimensional lattice. Each site is associated with a discrete variable e_k that can have a value of +1 or −1. For two adjacent sites the interaction energy is $J_{i,j}$.[212] The Ising model undergoes a phase transition between an ordered and a disordered phase in 2 dimensions or more.[211] Without an external field the Hamiltonian for the Ising model can be written as

$$\mathcal{H} = -J_{\mathrm{nn}} \sum_{i,j \in \mathrm{nn}} e_i e_j. \tag{2.24}$$

The configuration probability is given by the Boltzmann distribution with inverse temperature β as

$$P_\beta(e) = \frac{e^{-\beta H(e)}}{Z_\beta}, \tag{2.25}$$

where $\beta = (k_\mathrm{B}T)^{-1}$ and Z_β is a normalisation constant. It has been shown that the system is disordered for small β, whereas for large β the system exhibits ferromagnetic order. Similarly to this, our system is expected to be ferroelectrically ordered at low temperatures and paraelectric at higher temperatures. It is defined here that ferroelectric ordering implies a property of certain materials to have a spontaneous electric polarization that can be reversed by the application of an external electric field.[213] Therefore all the dipole moments in the system point in the same direction in the ferroelectric phase. Paraelectric implies non-linear polarisation when an external electric field is applied. However, as the field is reversed, the polarisation of a paraelectric material reverses to zero.[214]

The order parameter is a measure of order in a structure and ranges from 0 to 1. It is conventional to have the disordered phase associated with the order parameter value of 0 and the ordered phase with the order parameter value of 1. An example of an order parameter is the net magnetisation in a ferromagnetic system undergoing a phase transition. For liquid/gas transitions, the order parameter is the difference of the densities.

2.7 Birch-Murnaghan equation of state

The Birch-Murnaghan isothermal equation of state was first published in 1947 by F. Birch.[215] This relationship describes the dependence of the volume of a body and the pressure to which it is subjected.

Finite strain in a material is given by:

$$f = \frac{1}{2}\left[\left(\frac{V_0}{V}\right)^{\frac{2}{3}} - 1\right] \tag{2.26}$$

and the internal energy of the system is defined as a Taylor expansion of the strain, given by:

$$U = a + bf + cf^2 + df^3 + ... \tag{2.27}$$

The pressure is a derivative of this equation and is given by:

$$p = -\left(\frac{\partial U}{\partial f}\right)\left(\frac{\partial f}{\partial V}\right). \tag{2.28}$$

The second- and third-order Birch-Murnaghan isothermal equation of state is given by:

$$p(V) = 3\frac{B_0}{2}\left[\left(\frac{V_0}{V}\right)^{\frac{7}{3}} - \left(\frac{V_0}{V}\right)^{\frac{5}{3}}\right] \tag{2.29}$$

$$p(V) = 3\frac{B_0}{2}\left[\left(\frac{V_0}{V}\right)^{\frac{7}{3}} - \left(\frac{V_0}{V}\right)^{\frac{5}{3}}\right]\left\{1 - \frac{3}{4}\left(B_0' - 4\right)\left[\left(\frac{V_0}{V}\right)^{\frac{2}{3}} - 1\right]\right\}, \tag{2.30}$$

where p is the pressure, V_0 is the reference volume, V is the deformed volume, B_0 is the bulk modulus, and B_0' is the derivative of the bulk modulus with respect to pressure. The bulk modulus is defined as

$$B_0 = -V\left(\frac{\partial P}{\partial V}\right)_{p=0}. \tag{2.31}$$

Chapter 3

Experimental methods

3.1 Synthesis

3.1.1 2,3,6,7,10,11-hexahydroxytriphenylene tetrahydrate

Powdered HHTP·H_2O was obtained from Tokyo Chemical Industry UK. Successive recrystallisations from acetone and a 1:1 volume mixture of water and acetone yielded dark red needle-like crystals from slow evaporation. The crystal habit is illustrated in Fig. 3.1.

3.1.2 Silver(I) tricyanomethanide

All reagents were obtained from commercial suppliers (Sigma Aldrich and Alfa Aesar) and used as delivered. Suitable precautions were taken when handling potassium tricyanomethanide, K(*tcm*); in particular, contact with strong acids was avoided in order to minimise the risk of evolving HCN.

Single-crystal samples were prepared as follows: saturated aqueous solutions of $AgNO_3$ (50 mg) and K(*tcm*) (50 mg) were added to opposite sides of a single glass H-cell. The cell was filled carefully with ice-cold H_2O. Over a period of 7 days, colourless

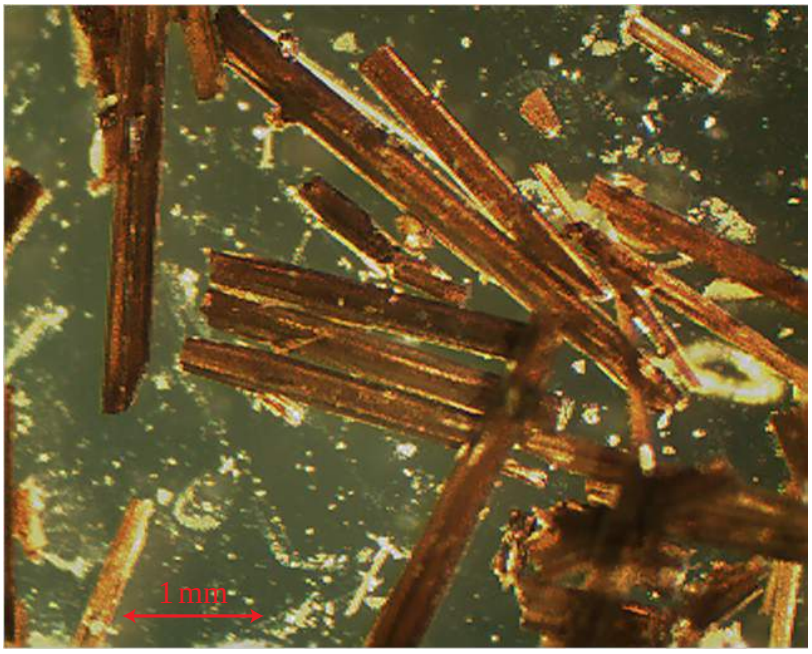

Figure 3.1: Optical microscopy image of representative crystals of HHTP·4H_2O, prepared as described in the main text. The crystal habit is rectangular prismatic, with the long axis parallel to the c crystal axis, *i.e.*, the confinement axis.

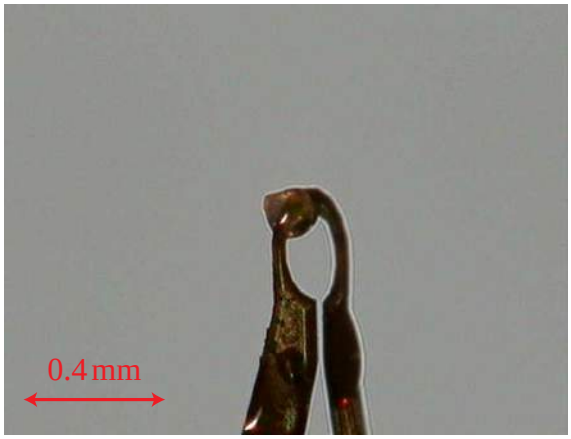

Figure 3.2: Optical microscopy image of representative crystals of Ag(*tcm*), prepared as described in the main text.

transparent crystals of Ag(*tcm*) grew on the arms of the H-cell. A crystal of Ag(*tcm*) is shown in Fig. 3.2. Powder samples were readily prepared by precipitation from equimolar saturated aqueous solutions of $AgNO_3$ and K(*tcm*), followed by filtering, washing (H_2O) and drying under vacuum (50 °C).



Figure 3.3: Yellow powdered sample of $Ni(CN)_2$, prepared as described in the main text.

3.1.3 Nickel(II) cyanide

The sample used in diffraction studies was prepared by heating $Ni(CN)_2{\cdot}4H_2O$ (Alfa Aesar) under vacuum at 200 °C for 24 h. The resulting yellow powder was stored in a vacuum desiccator to prevent rehydration. The yellow sample is shown in Fig. 3.3.

3.1.4 Copper(II) nickel(II) cyanide

All reagents were obtained from commercial suppliers (Sigma Aldrich and Alfa Aesar) and used as delivered. An aqueous solution of nickel(II) nitrate hexahydrate $[Ni(NO_3)_2 \cdot 6\,H_2O]$ and copper(II) sulfate pentahydrate $[CuSO_4 \cdot 5\,H_2O]$ in appropriate concentrations were added to a solution of potassium cyanonickelate(II) $[K_2Ni(CN)_4]$. Samples were prepared between $Ni(CN)_2$ and $Cu_{0.5}Ni_{0.5}(CN)_2$ using Cu^{2+}/Ni^{2+} ratios that differed incrementally by 5%. The samples were filtered and the resulting filtrates were colourless, indicating that all Cu^{2+}/Ni^{2+} had been incorporated in the precipitates.



Figure 3.4: Purple powdered sample of $CoNi(CN)_4$, prepared as described in the main text.

3.1.5 Cobalt(II) nickel(II) cyanide

All reagents were obtained from commercial suppliers (Sigma Aldrich and Alfa Aesar) and used as delivered. An aqueous solution of nickel(II) nitrate hexahydrate [$Ni(NO_3)_2 \cdot 6\,H_2O$] and cobalt(II) sulfate heptahydrate [$CoSO_4 \cdot 7\,H_2O$] in appropriate concentrations were added to a solution of potassium cyanonickelate(II) [$K_2Ni(CN)_4$]. Samples were prepared between $Ni(CN)_2$ and $Co_{0.5}Ni_{0.5}(CN)_2$ using Co^{2+}/Ni^{2+} ratios that differed incrementally by 5%. The samples were filtered and the resulting filtrates were colourless, indicating that all Co^{2+}/Ni^{2+} had been incorporated in the precipitates. The samples were heated and a colour change to purple of the highest cobalt(II) concentration samples was observed [Fig. 3.4].

3.2 Single-crystal X-ray diffraction

3.2.1 Variable-temperature collections for HHTP·4H_2O

Single-crystal X-ray diffraction (SCXRD) data were collected on a single-crystal of HHTP·4H_2O (0.025 mm × 0.026 mm × 0.030 mm) using an Oxford Diffraction (Agilent Technologies) SuperNova (Mo Kα radiation) equipped with an Oxford Cryosystems cryostream.[216] The sample was coated in perfluoropolyether oil and placed in the cold N_2 open flow of an Oxford CryoSystems Cryostream[216] at 100 K, data were then collected on heating the sample to 240 K in 10 K intervals. The crystal was then heated to 260 K to ensure the sample had undergone complete transformation, before it was cooled to 240 K. Subsequent data collections between 240 and 130 K were also carried out. Data were integrated and corrected for absorption using CrysAlisPro.[217] The structure was solved using the data collected at 100 K, using SIR92[218] and refined against F^2 using full-matrix least squares, as implemented in CRYSTALS.[219] All non-hydrogen atoms in the 100 K structure were refined with anisotropic displacement parameters. Hydrogen atoms were visible in the difference map and positioned as described in Section 4.3.2. At 240 K, only the non-hydrogen atoms bound to the HHTP moiety were refined with anisotropic displacement parameters; water oxygens were split over two sites and refined with isotropic displacement parameters, with partial occupancies of 50%. Hydrogen atoms in both structures were located using a difference Fourier map — detailed information on the treatment of hydrogen atoms is given further below.

It is noted here that the single crystal X-ray diffraction measurements were performed with the help of Dr. Amber Thompson and the structures solved with the help of Dr. Nicholas Funnell.

3.2.2 Variable-temperature collections for Ag(*tcm*)

SCXRD measurements were performed using an Agilent Technologies SuperNova (Mo Kα radiation, λ = 0.71073 Å) fitted with an Oxford Cryosystems cryostream.[216] A small crystal, with dimensions 0.044 mm × 0.052 mm × 0.094 mm, was mounted on a glass fibre using nail varnish. Full data collections were performed at temperature

intervals of 10 K, on heating and subsequent cooling, between 100 and 250 K. Unit cell parameters were determined and refined using CrysAlisPro.[217] The structure was solved with SIR92[218] and refined by full-matrix least squares using CRYSTALS.[219] All atoms were refined anisotropically against F^2. A thermal-similarity constraint was applied to the C1 and N1 atoms for all heating data and for cooling data collected between 210 and 250 K. The refinement details are given in Tables B.1—B.8.

It is noted here that experimental work on silver(I) tricyanomethanide was carried out by two part II students in the group, Sarah Hodgson and Sarah Hunt. Single crystal X-ray diffraction measurements were performed with the help of Dr. Amber Thompson. The structures were solved in collaboration with Andrew Cairns, Matthew Cliffe and Dr. Nicholas Funnell.

3.2.3 Variable-pressure collections for Ag(*tcm*)

Variable-pressure SCXRD measurements were performed using an Agilent Technologies Gemini diffractometer (Mo Kα radiation, λ = 0.71073 Å). A single-crystal of Ag(*tcm*) was loaded in a Merrill-Bassett diamond anvil cell with an opening angle of 85°, equipped with a steel gasket and beryllium backing discs [Fig. 3.5]. A small ruby chip was also loaded in the cell allowing pressure determination *via* ruby fluorescence.[220] Fluorinert was used as pressure-transmitting medium. Data were collected at four pressure points between ambient pressure and 2.39 GPa. The data were indexed and integrated with CrysAlisPro.[217] Reflections arising from the Be backing discs and the diamond anvils were omitted. The crystal structure was solved using SIR92[218] and refined against F^2 using CRYSTALS.[219] All non-silver atoms were refined isotropically with geometric restraints owing to a poor data-to-parameter ratio, resulting shading of reciprocal space by the diamond anvil cell body. The refinement details are given in Tables B.9 and B.10.

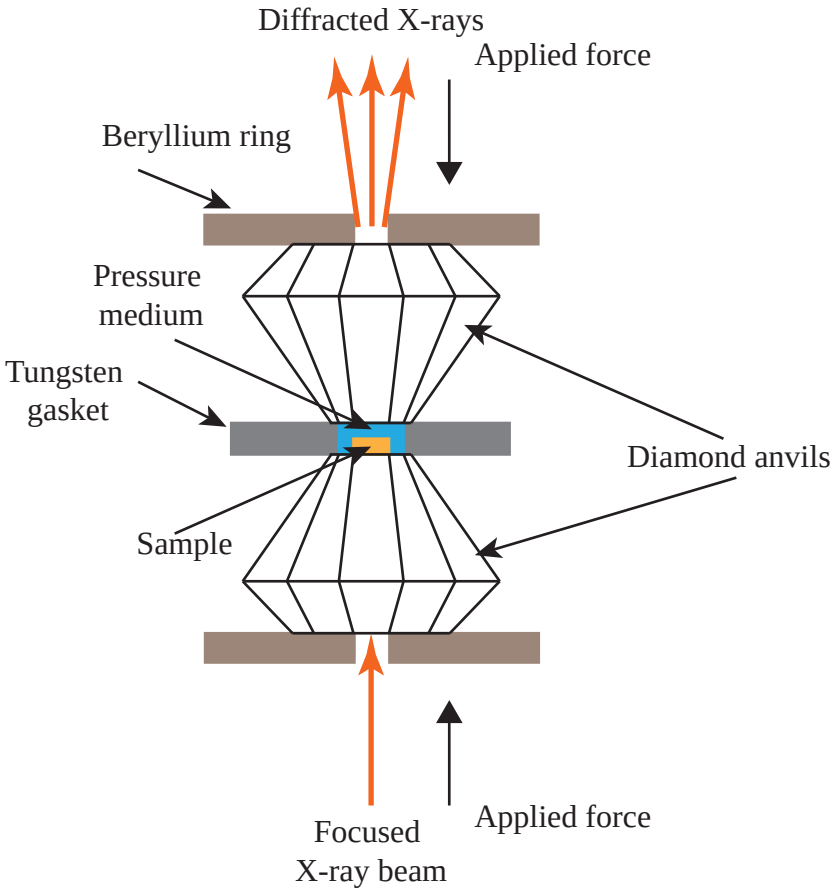

Figure 3.5: Schematic of a Merrill-Bassett diamond anvil cell.

3.3 Powder X-ray diffraction

3.3.1 Powder X-ray diffraction characterisation of $Co_xNi_{1-x}(CN)_2$

PXRD patterns for the samples were measured at room temperature with the Siemens D5000 diffractometer using a Cu X-ray target. The Siemens diffractometer operates in Bragg-Brentano geometry and the Ge monochromator selects Cu Kα_1 radiation only. The single wavelength radiation ($\lambda = 1.5406\,\text{Å}$). A high-temperature set-up was used for the data collections and the data collections taken under vacuum. At first, the samples were heated to 200 °C and held there for 1.5 h to dehydrate the samples and then cooled back to room temperature, where a room temperature pattern for analysis was measured. The data was collected with a step size of 0.06° in the data range 6.75°

$< 2\theta < 80°$.

3.3.2 Variable temperature powder X-ray diffraction measurements

Variable temperature diffraction studies on powdered the original HHTP·$4H_2O$ crystals and heat-treated HHTP·$4H_2O$ samples were performed on the Siemens D5000 diffractometer using either the high temperature setup under vacuum, or the low temperature attachment under helium atmosphere.

The same attachment was used to characterise $CoNi(CN)_4$ at elevated temperatures. At first, the samples were heated to 200 °C and held there for 1.5 h to dehydrate the samples and then cooled back to room temperature, where a room temperature pattern for analysis was measured. Then consecutive measurements were taken every 15 °C up to 300 °C. The data was collected with a step size of 0.06° in the data range $6.75° < 2\theta < 80°$. In order to produce a suitable dataset for Pawley analysis, the intensity and the step size of the first five, the second five and so on data points were averaged. Unit cell dimensions for $CoNi(CN)_4$ were extracted using the Pawley method (TOPAS Academic[221]) with the help of Matthew Cliffe.

3.3.3 High-pressure powder synchrotron diffraction for $Ni(CN)_2$

The experiment was performed at the I15 beamline of the Diamond Light Source with an incident monochromatic wavelength of 0.162 Å.[222] Measurements were performed in a modified Merrill-Bassett diamond-anvil cell (DAC) with diamond culets of 450 µm. The diamond cell used for these experiments allows access to the angular range $4\theta = 50°$. Silicon oil was used as the pressure-transmitting medium and the loading of the DAC had to be done in a glovebox to avoid absorption of water. Ruby chips, evenly distributed in the pressure chamber, were used to measure the pressure in both experiments by the ruby fluorescence method.[223] Pressures measured in different ruby

chips are within 0.1 GPa below 11 GPa and within 0.2 GPa at the maximum pressure of the experiments. The observed intensities were integrated as a function of 2θ in order to give conventional, one-dimensional diffraction profiles. CeO_2 was used to calibrate the beam centre and sample to detector distance. Variable pressure runs were performed up to 2.6 GPa.

It is noted here that the synchrotron measurements were performed with the help of Andrew Cairns, Dr. Matthew Tucker, Dr. Joseph Hriljac and Dr. Timothy Lucas.

3.3.4 Precise room temperature characterisation of $CoNi(CN)_4$ using Mo X-ray radiation

The $CoNi(CN)_4$ sample was loaded into a 1 mm diameter silica capillary; the capillary sealed and Mo X-ray data was collected on the Panalytical X'Pert Pro diffractometer, which uses a Scintillation detector. The Mo X-ray data for nickel(II) cobalt(II) cyanide were measured with the help of Dr. Nicholas Funnell. Data were collected in the range of $3.005° < 2\theta < 139.995°$ with a step size of 0.005° with data collection time of 5 seconds at each data point. Unit cell dimensions for $CoNi(CN)_4$ were extracted using the Pawley method (TOPAS Academic[221]) with the help of Matthew Cliffe.

3.4 Powder neutron diffraction

3.4.1 High-pressure collections for Ag(*tcm*) and $Ni(CN)_2$

Neutron diffraction was undertaken at the ISIS spallation source, utilising the PEARL high pressure time-of-flight diffractometer.[224] PEARL is a neutron time-of-flight powder diffractometer that specialises in studying material under high pressure. For both samples, a systematic change in pressure was introduced *via* a V4 Paris-Edinburgh cell. A TiZr gasket, containing a powdered sample of silver(I) tricyanomethanide or nickel(II) cyanide, fluorinert (a pressure transmitting medium) and a pellet of Pb (a

pressure calibrant), was positioned in a ZTA (zirconia toughened alumina) anvil with a Los Alamos single toriodol profile. The pressure was systematically adjusted between ambient pressure and 2 GPa, with data sets collected in the range $0 < d < 4.1$ Å. The calculated pressures were determined using the third-order Birch-Murnaghan equation of state known for Pb ($V_0 = 30.354$ Å^3, $B_0 = 42.0$ GPa and $B' = 5.71$), which relates pressure (p) and volume (V), the latter determined from the refined lead cell lattice parameter.

Unit cell dimensions for Ag(*tcm*) were extracted using the Pawley method (TOPAS Academic[221]). The atomic coordinates and isotropic displacement parameters of silver(I) tricyanomethanide were refined *via* the Rietveld method. Distance restraints and angle restraints were implemented for the tcm^- ligands, with each −CN linkage assumed to be linear and bond lengths restrained to 1.156 Å. The peak shape function used was pseudo-Voigt, of both Lorentzian and Gaussian character. Refinement details are shown in Tables B.13—B.19.

Unit cell dimension for $Ni(CN)_2$ were determined by using the GSAS Rietveld refinement package, utilising the microstrain broadening and stacking faults model, using a multiphase refinement including the sample and the Pb pressure marker.[225]

It is noted here that the neutron diffraction experiments were performed with the help of Dr. Matthew Tucker and the samples were prepared by Sarah Hunt and Sarah Hodgson.

3.5 Measurements on original HHTP·4H$_2$O and heat-treated crystals

3.5.1 SQUID measurements

Magnetometry characterises materials' properties that depend on the magnetic moments associated with the spin and orbital motions of electrons. Superconducting

Quantum Interference Device (SQUID) is a very sensitive magnetometer. It consists of a closed superconducting loop with two Josephson junctions that lie in parallel in a superconducting loop, as illustrated in Fig. 3.6.[226] To measure the sample's magnetic properties, the sample is moved through superconducting detection coils. If the sample is not magnetic, the input current passes through both of the Josephson junctions equally. If the sample is magnetic, the induced current is in the same direction of the applied current in one of the branches and in the opposite direction in the other branch. From the variation of this current, the material's magnetic properties can be determined. The measurements in this thesis were performed on accurately weighted samples contained in a gelatine capsule, packed tight with cotton wool, and mounted in a plastic drinking straw. Measurements on empty capsules were performed separately to eliminate any background contributions. The straw was attached to the example rod using Kapton tape. The sample environment is a Helium flow cryostat, which can be cooled to a base temperature of 1.6 K. In collaboration with Dr. Paul Goddard, these SQUID measurements were performed on heat-treated HHTP·4H_2O in the Department of Physics using the Quantum Design Magnetic Property Measurement Systems XL. Firstly, susceptibility measurements were carried out from 30 K to 2 K and then a 2 K magnetisation experiment was performed on the original HHTP·4H_2O crystals and the oven-treated samples.

3.5.2 PPMS measurements

The heat capacity measurements presented in this thesis were performed using a Quantum Design Physical Properties Measurement System (PPMS).[227] For heat capacity measurements, the platform, which holds the sample, is connected to a thermal bath. Heat is transferred to the latter by thin wires, which also serve as electrical contacts for the heater and resistance thermometer. A good thermal contact between the bottom surface of the sample and the platform is ensured during measurements [Fig. 3.7]. The heater supplies a fixed amount of power $P(t)$ for a length of time t, and is then turned

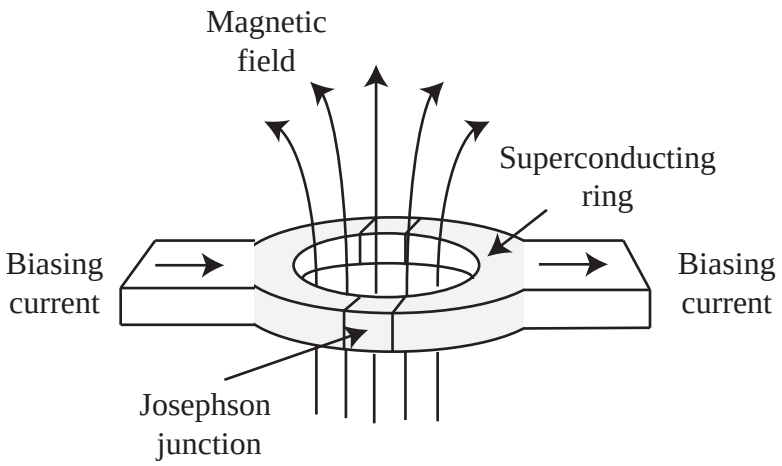

Figure 3.6: Schematic of SQUID with Josephson junctions and the superconducting ring shown.

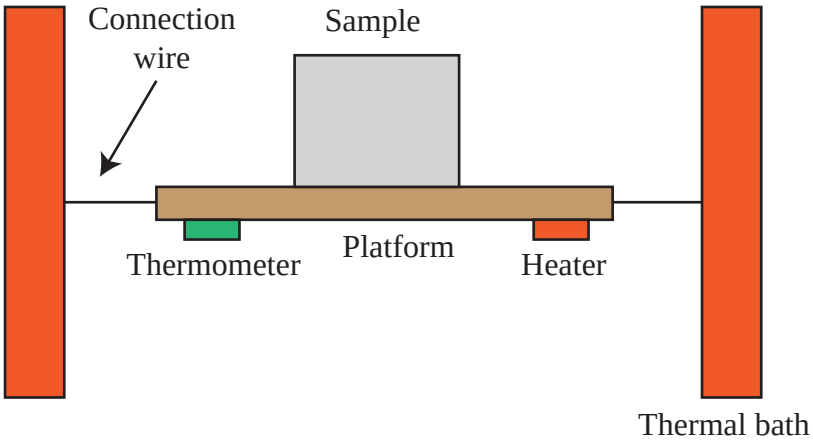

Figure 3.7: Schematic of PPMS heat capacity measurements.

off. The temperature of the sample and platform assembly rises due to the applied heat, but the thermal bath remains at constant temperature. The sample and platform assembly then cools through radiation and conduction through the wires when the heater is turned off. The software connected to the PPMS assembly quantifies the heat transferred. In collaboration with Dr. Paul Goddard, PPMS heat capacity measurements were performed in the Department of Physics. The heat capacity measurements were carried out from 300 K to 50 K in 50 K steps and then steps of 5 K down to 2 K on the original HHTP·4H_2O crystals and the oven-treated samples.

3.5.3 Conductivity measurements

In collaboration with Dr. Paul Goddard, the four point d.c. conductivity measurements were performed in the Department of Physics using the Quantum Design Physical Property Measurement System on compressed pellets of the oven-treated samples of HHTP crystals.[227] Additionally four-point conductivity measurements were performed on different oven-treated samples at ambient conditions.

3.5.4 EPR measurements

In the absence of a magnetic field, an electron spin, $S = 1/2$, has two degenerate energy levels as magnetic moment associated with the electron is randomly orientated. When an external magnetic field is applied, the electron spin S will align parallel or anti-parallel to the field. This results in the splitting of the spin state into two non-degenerate energy levels, $m_s = \pm 1/2$. The splitting between the two spin states has energy of

$$\Delta E = g\mu_B B_0, \tag{3.1}$$

where g is the g-factor (a proportionality constant), μ_B is the Bohr magneton, and B_0 is the static magnetic field. If the system is exposed to electromagnetic radiation equal to the energy difference between the energy levels, the photon is absorbed by the system. To measure this absorption, the electron spins are irradiated with a fixed frequency microwave radiation and the magnetic field is altered. When the field reaches resonance conditions, microwaves are absorbed by the electron spins and this absorption is observed experimentally. EPR spectra were recored on the X-band (10 GHz) CW EPR spectrometer and a CW/pulse X/W band (10 GHz/94 GHz) Elex680 EPR spectrometer in collaboration with Dr. Jeff Harmer. The samples were loaded in EPR tubes and the measurements taken.[228]

3.5.5 Thermogravimetric analysis

Thermogravimetric analysis (TGA) was carried out on the HHTP·$4H_2O$ crystals using a Perkin Elmer TGA7. Thermogravimetric analysis measures the loss of sample mass with time as temperature is changed. The analysis was performed under inert gas atmosphere. 4.29 mg of sample was placed in a pre-weighed platinum sample pan and the measurements were taken from 30 °C to 150 °C at a rate of 10 °C per minute.

Chapter 4

1D ice channels

4.1 Overview

In this chapter, we study the temperature-dependent evolution of 1D ice polarisation in the crystalline molecular hydrate HHTP·$4H_2O$.[188] HHTP-containing systems are of great current interest in the field of molecular framework materials, where they are favoured for their thermal robustness and attractive porosity/sorption properties.[229,230] We will show that 1D water-filled channels within HHTP·$4H_2O$ exhibit a polar ↔ para-electric transition, which makes the material an excellent candidate for investigation of ice-based ferroelectric responses. It is noteworthy that disorder of alignment of these channels plays an important part in determining the structural phase transition. At high temperatures, the channels are disordered to give a centrosymmetric structure, whereas at low temperatures the channels all have net polarisation that points in the same direction. The phase transition results directly from the 1D ice channels with the HHTP molecules maintaining their positions between different phases.

4.2 Background

Whether the dipolar nature of the water molecule might be translated into a polar form of ice is a question that has its origin in the very earliest studies of hydrogen bonding in solid phases of water. The most common polymorph of water ice, hexagonal ice or ice I_h, has a simple tetrahedral arrangement of hydrogen bonds between the oxygen of one water molecule and a hydrogen from each of two adjacent water molecules. Whilst maintaining this tetrahedral arrangement of water molecules, there is nearly an infinite number of thermally available arrangements of water molecule dipoles above 160 K. Disorder plays an important role in the ice I_h structure at these temperatures and it is noteworthy that the protons are positioned according to the Bernal-Fowler rules: two hydrogen atoms (protons) lie near each oxygen atom, with only one proton residing on each H-bond. The hydrogen atoms are constantly moving in the ice structure, whilst satisfying these rules [Fig. 4.1(a)].[231]

At lower temperatures, a proton-ordered phase may be the most stable form, but such a state has never been observed, as the kinetics of proton reorientation become very slow at these temperatures [Fig. 4.1(b)].[231–233] In fact, it has been predicted to take 10^{4} years for a full phase transition from ice I_h to a proton-ordered polymorph ice XI.[234] Thus, configurational entropy and kinetics of bulk ices is such that, to date, the only successful approaches to developing polar phases have involved symmetry lowering *via* *e.g.*, surface layer deposition and dimensionality reduction in confined phases.[235–238] Even the nature of the supposedly-polar ice XI obtained on ion doping at low temperatures remains controversial. Much of the evidence of the earlier studies of obtaining ice XI with the aid of dopants and impurities was based on the electrical and heat capacity measurements of the materials and recent neutron diffraction studies concluded that proton-ordered ice phases were *not* observed. Instead the earlier measurements can be explained simply by the known sluggish polarisation kinetics behaviour of the ice.[233,235,239]

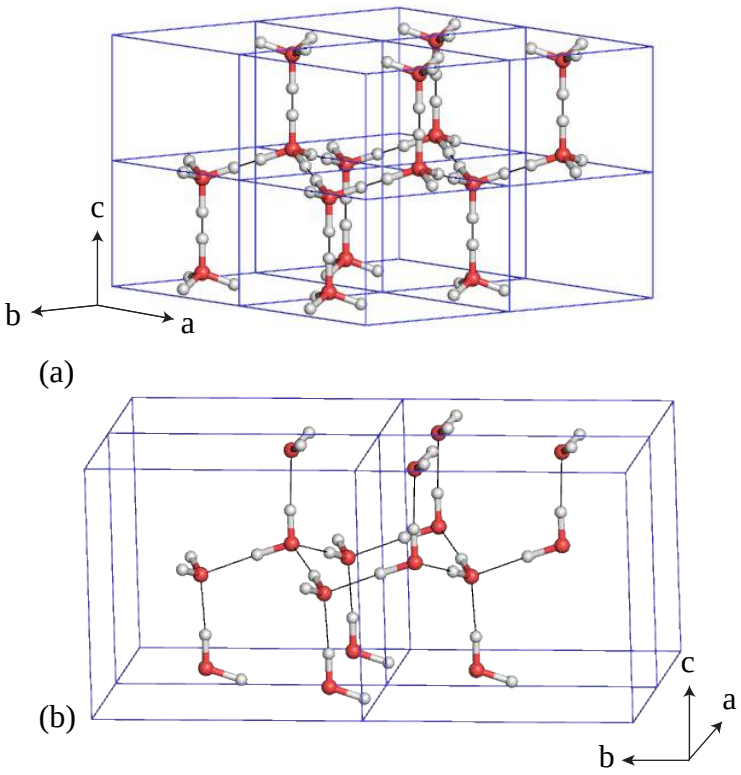

Figure 4.1: Ice structures with (a) hexagonal ice I_h structure with disordered hydrogens shown and (b) the supposedly ferroelectric ice XI structure with ordered hydrogens shown. The hydrogens are shown with 50% occupancy in (a) and 100% occupancy in (b).

In the context of this thesis, examples of dimensionality lowering to obtain FE ice are of interest. For some time, the focus of such confinement studies has been on water-filled carbon and inorganic nanotubes.[189–194] In such systems, the dipole orientations of water molecules are restricted due to the reduced dimensionality and hence allow for faster reorientation of dipoles due to reduced dipole configurations. However, the primary application of polar ices is in FE devices and relies on switchable bulk dipolar alignment, which is difficult for nanotube conglomerates: it is hard to achieve interactions between water channels inside individual carbon nanotubes. Consequently the design strategy has recently shifted to exploiting aligned voids within nanoporous crystalline hosts.[240,241] For example, water confined to nanochannels in the

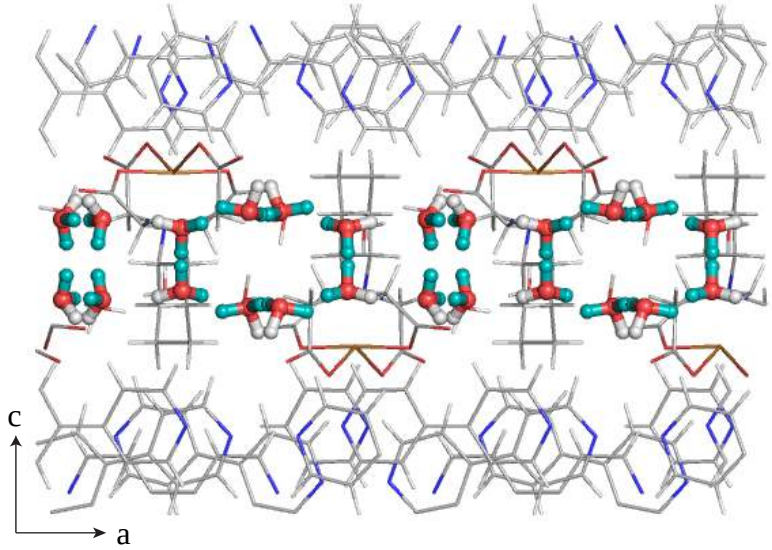

Figure 4.2: Structure of $[Cu^{I}_{2}Cu^{II}(CDTA)(4,4'\text{-bpy})]\cdot 12H_2O$ showing the 1D water channels that show ferroelectric hysteresis at temperatures below 277 K. The ordered hydrogens are shown in light grey and the disordered hydrogens in dark green (Adapted from Ref. 241).

framework material $La_2Cu_3[NH(CH_2COO)_2]_6$ exhibits antiferroelectric ordering below the confined liquid to solid transition at 350 K.[242] In addition, 1D 'water wires' within a copper-based coordination polymer $[Cu^{I}_{2}Cu^{II}(CDTA)(4,4'\text{-bpy})]$ have been shown to undergo a spontaneous transition between liquid and FE states at 277 K.[195] In such materials, 1D channels are directly responsible for obtaining ferroelectrically ordered ice [Fig. 4.2]. However, despite the observation of dielectric hysteresis in the FE phase of $[Cu^{I}_{2}Cu^{II}(CDTA)(4,4'\text{-bpy})]$, perhaps the most obvious distinction between the formation of polar states in these confined ices and that in traditional FE phases such as $PbTiO_3$ is that polarisation always seems to emerge on cooling from a *liquid* parent state rather than from a paraelectric phase.[243] This suggests there exists only minimal distinction between the energy scales associated with long-range dipole alignment within and between nanopores and is likely the origin of the relatively weak and temperature-specific FE hysteresis observed for these systems.[195]

4.3 Characterisation of HHTP·4H_2O and discrepancy of the current model

4.3.1 Structure of the molecular tetrahydrate

As in all known 2,3,6,7,10,11-hexahydroxytriphenylene (HHTP) cocrystals, the structure of the studied HHTP·4H_2O is dominated by the stacking of triphenylene cores into 1D columns [Fig. 4.3(a)(b)].[188,244,245] This structural stacking motif is well-known for triphenylene cores in the case of a large and separate family of discotic liquid crystals.[246] In HHTP·4H_2O, the surface of these columns is decorated by hydrophilic —OH groups, and consequently the voids between columns are ideally suited for water coordination. In a previous structural study of HHTP·4H_2O, it was shown that H_2O molecules contained within these voids form an elaborate hydrogen-bonding network.[188] Moreover, the water connectivity is one dimensional, such that the system can reasonably be considered a molecularly-confined 1D ice.

There were two features of the ice-like hydrogen-bonding network proposed in the study by Thébault et al. that seemed to be counterintuitive and so prompted this structural study. First, the crystal symmetry reported in Ref. 188 was a centrosymmetric orthorhombic space group *Pbcn* that places inversion centres within the hydrogen-bonding network. This crystallographic observation has the effect of forcing direct O—H$\cdots$H—O contacts that would be considered improbable within the established framework of ice physics [Fig. 4.4]. Secondly, the anisotropic displacement parameters associated with the water O atoms were anomalously large, considering the temperature at which data were collected (100 K; root-mean-squared displacement $\sqrt{U_{\max}} \simeq 0.4$ Å).

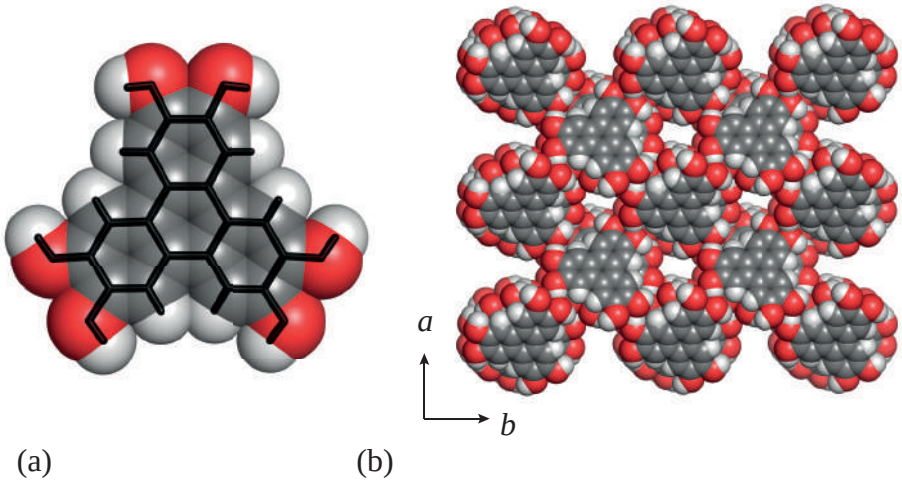

Figure 4.3: (a) The HHTP molecule is planar with a hydrophobic core and hydrophilic exterior with red denoting oxygen, black carbon and grey hydrogen. (b) As in many solid triphenylenes, the crystal structure of HHTP·4H_2O consists of a triangular array of triphenylene columns.[188,244] The voids between neighbouring HHTP columns are strongly hydrophilic. It is within these channels that the water molecules are located.

4.3.2 Variable temperature study and a new model

In order to rationalise these crystallographic observations, a single-crystal sample of HHTP·4H_2O was prepared and its X-ray diffraction pattern as a function of temperature was measured.[218,219,247] Diffraction data at 10 K intervals over the range 100—240 K was collected, throughout heating regime, and over the range 130—240 K throughout cooling regime.

For data sets between 190 K and 240 K, it was possible to refine a satisfactory structural model based on the *Pbcn* solution of Ref. 188. The refinement values across these temperatures upon heating are given in Table 4.1. However, close examination of the diffraction patterns themselves shows that a set of weak reflections forbidden in the *Pbcn* space group were unaccounted for by such a model at lower temperatures. The intensity of these reflections was temperature dependent. They were strongest

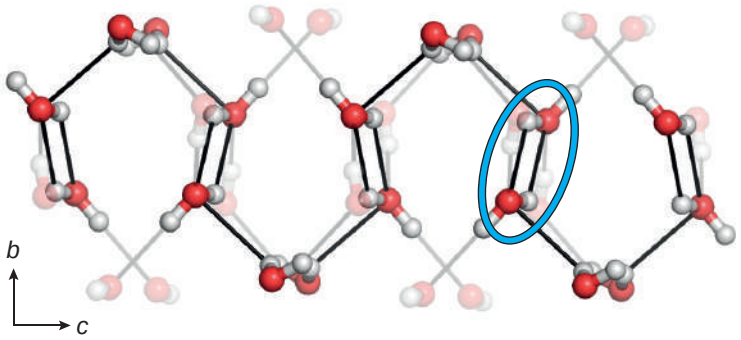

Figure 4.4: Neighbouring water molecules within a single pore are connected *via* hydrogen-bonding interactions to form a 1D ice with its chain axis parallel to the crystal c axis. In the reported structure of Ref. 188, the presence of inversion centres results in O—H$\cdots$H—O contacts between some neighbouring H_2O molecules (circled). The transparent atoms in the figure are hydroxyl groups from the organic HHTP molecule that are also part of the hydrogen-bonding network (Adapted from Ref. 188).

Table 4.1: SCXRD refinement details for HHTP·4H_2O at high temperatures.

Temperature	No. of Reflections ($I/\sigma > 2.0$)	Goodness of Fit	$R(I/\sigma > 2.0)$
240	1609	0.9963	0.0487
230	1703	0.9465	0.0405
220	1698	1.0195	0.0471
210	1718	0.9783	0.0497
200	1719	1.0387	0.0508
190	1725	1.1526	0.0498

at the lowest temperatures but undetectable at 240 K [Fig. 4.5]. The reflections appeared on the $(0kl)$ plane with $k = 2n + 1$, where n is an integer. Therefore in the low temperature structure the b-glide is violated as these reflections are systematically absent for the b-glide. Making use of the associated reflection conditions, it was possible to assign the low-temperature structure with the space group $P2_1cn$, which is a

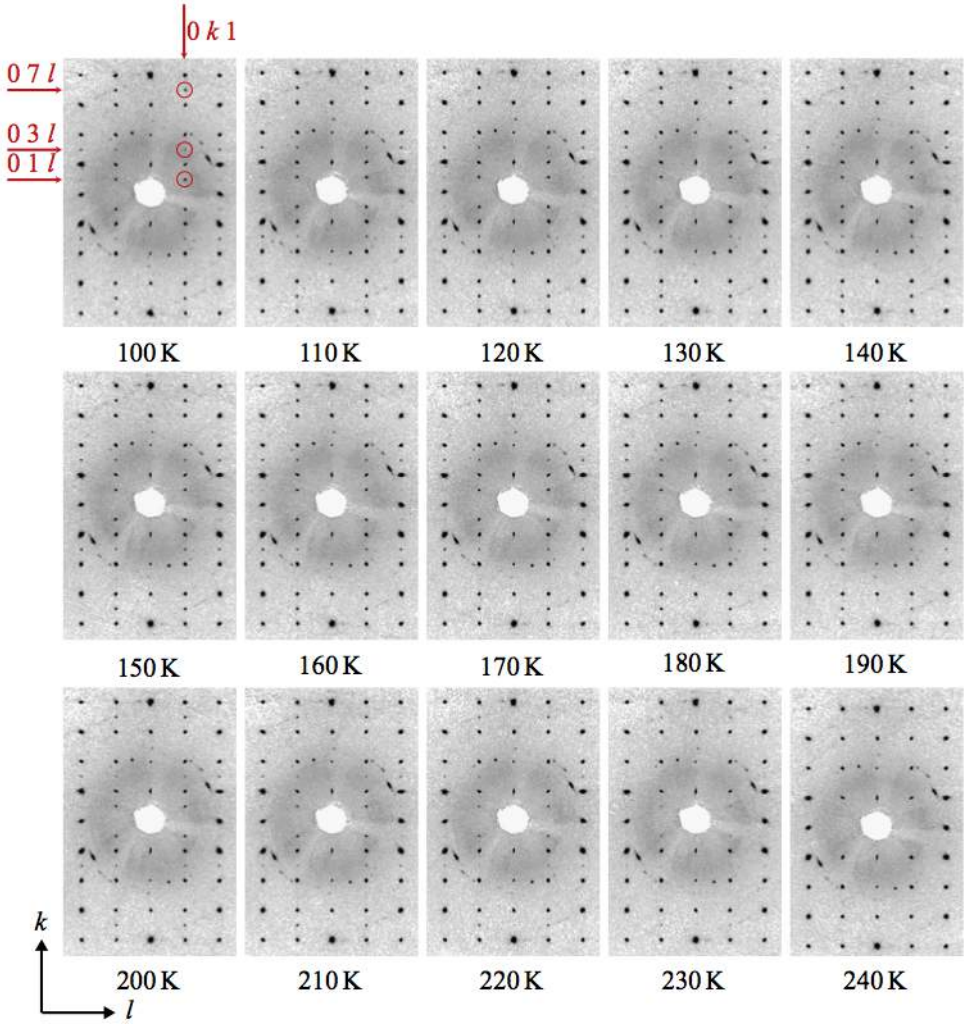

Figure 4.5: Synthesised precession images of the $(0kl)$ plane, showing the decay of systematic absence violations for *Pbcn*. The systematic absences visible for the (071), (031) and (011) reflections are denoted with red circles on the 100 K image. Their intensities decrease with temperature and are completely absent by 240 K.

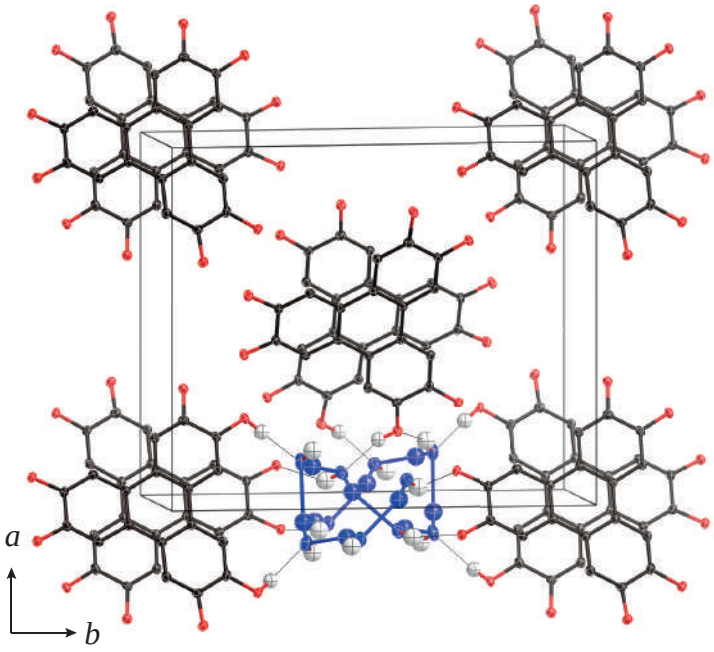

Figure 4.6: Representation of the $P2_1cn$ structural model of low-temperature HHTP·4H_2O, refined against data collected at 100 K. Most H and solvent atoms have been omitted for clarity. Shown in thermal ellipsoid representation is a single hydrogen-bonding network involving included water molecules. Thermal ellipsoids are drawn at the 50% probability level.

maximal subgroup of *Pbcn* obtained by removing the inversion symmetry operation. Subsequent refinement of the 100 K data set in this lower-symmetry setting gave an improved structural model in which both the hydrogen-bonding connectivity and water O atom displacement parameters made physical sense. This model is illustrated in Fig. 4.6 with the hydrogen bond arrangements shown in Fig. 4.7. The hydrogen bonds between hydroxyl groups of the HHTP molecule and oxygen of the water molecule are in the distances range of 1.863 Å to 2.061 Å and the hydrogen bonds between water molecules are in the range of 1.761 Å to 2.190 Å . As a comparison, the typical length of hydrogen bond in ice I_h is 1.793 Å.[248] Therefore the hydrogen bonds in this structure make physical sense. The hydrogen bonds between hydroxyl groups of the

HHTP molecule and oxygen of the water molecule in Ref. 188 are similar length to the ones presented in this study, however, hydrogen bonds between water molecules are between 2.761 Å and 2.930 Å and are therefore much longer in comparison to this study and the hydrogen bonds in ice I_h.

The refinement details for the low-temperature structure below 190 K are given in Table 4.2. Selected crystal structure refinement details are reported here in Tables 4.3 and 4.4 for the high- and the low-temperature structures to provide the reader with an idea of the crystal structure and full refinement details for the high-and low-temperature structures are brought in Tables A.1 and A.2. Variable-temperature lattice parameters

Table 4.2: SCXRD refinement details for HHTP·4H_2O across the whole temperature range.

Temperature	No. of Reflections ($I/\sigma > 2.0$)	Goodness of Fit	$R(I/\sigma > 2.0)$
180	1789	0.9745	0.0344
170	1798	0.9859	0.0339
160	1800	0.9718	0.0336
150	1801	0.9892	0.0331
140	1805	0.9853	0.0329
130	1811	0.9935	0.0325
120	1822	0.9793	0.0320
110	1819	0.9882	0.0306
100	1836	1.0051	0.0308

are given in Tables A.3 and A.4; the corresponding trends are illustrated in Fig. 4.8. The lattice parameter evolution shows a continuous phase transition.

Table 4.3: SCXRD data collection and refinement details for HHTP·4H_2O at T= 100 K on heating.

Radiation	Mo Kα, $\lambda = 0.71073$ Å

Formula	$C_{18}H_{20}O_{10}$
M, g mol^{-1}	396.35
Z	4
Crystal Size (mm)	0.03 × 0.10 × 0.19
Crystal System	Orthorhombic
Space Group	$P2_1cn$
a (Å)	14.20002(19)
c (Å)	16.7353(2)
c (Å)	7.17809(9)
V (Å^3)	1705.82(4)
No. of Reflections ($I/\sigma > 2.0$)	1836
Goodness of Fit	1.0051
$R(I/\sigma > 2.0)$	0.0308

Estimated standard deviations are given in parentheses.

Table 4.4: SCXRD data collection and refinement details for HHTP·4H_2O at T= 240 K on heating.

Space Group	$Pbcn$
a (Å)	14.2568(2)
b (Å)	16.7791(2)
c (Å)	7.2308(1)
V (Å^3)	1729.73(4)
No. of Reflections($I/\sigma > 2.0$)	1609
Goodness of Fit	0.9963
$R(I/\sigma > 2.0)$	0.0487

Estimated standard deviations are given in parentheses.

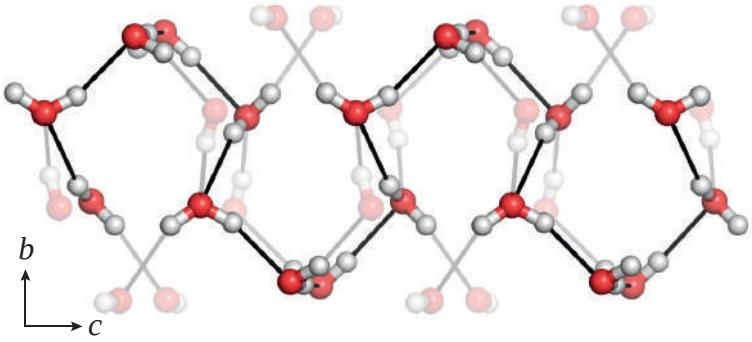

Figure 4.7: In the absence of inversion symmetry, the hydrogen bonding arrangement within ice-like chains involves only O—H$\cdots$O contacts. The transparent atoms indicate hydroxyl groups from the HHTP molecules.

The conventions for placing the unit cell origin differ between the space groups *Pbcn* and $P2_1cn$. In order to facilitate direct comparison of the atomic coordinates, we have implemented an origin shift for the $P2_1cn$ structure solution (100 K). This choice of nonstandard origin generates a number of alerts in checkCIF; these are arising purely from the origin shift and are eliminated if the standard origin is chosen.

Treatment of water molecules

Particular care was given to hydrogen atom placement owing to the disordered nature of the water channel sub-structure. For the 100 K dataset, following initial anisotropic refinement of non-hydrogen atoms, all hydrogen atoms were located using a difference Fourier map. Hydrogen atom positions and isotropic thermal parameters were refined with soft restraints prior to their inclusion in the final refinement using a riding model (as described in Ref. 249).

Scattering by hydrogen atoms makes a larger relative contribution to low angle reflection intensities, owing to a greater fall-off in scattered intensity than that of non-hydrogen atoms (see Fig. 5 in Ref. 249). Thus, truncating the data to lower resolutions has the effect of enhancing the electron density attributed to hydrogen atoms (1.1 Å has

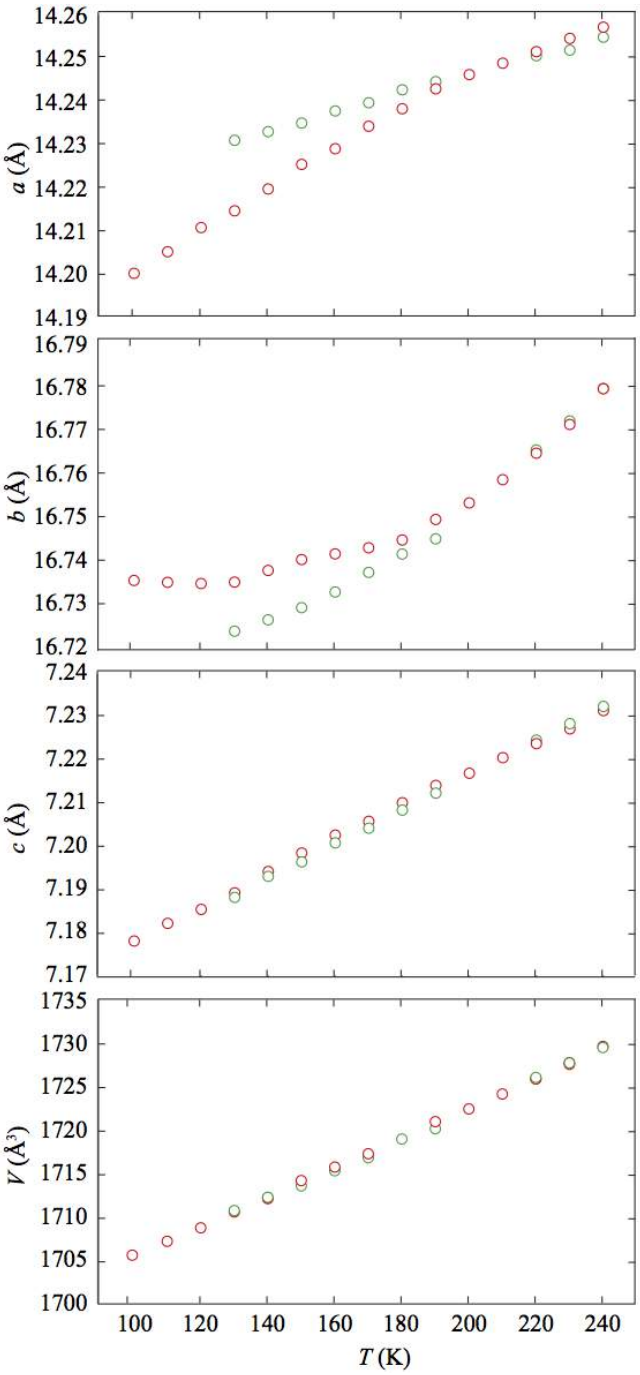

Figure 4.8: Thermal dependence of the lattice parameters, indicating the lack of hysteresis on cooling. Red circles represent the heating and green circles the cooling data. The deviation at low temperatures observed for the a and b axes is likely attributable to partial dehydration of the framework after sustained exposure to dry N_2 gas.

been identified as a suitable cut-off). Fig. 4.9(a) shows a generalised difference Fourier section calculated in the vicinity of the water molecules using the data below 1.1 Å, when the occupancies of the water hydrogens are set to zero. For all four molecules, there are clearly defined regions of density for each of the hydrogens.

A similar procedure was followed for the 240 K data, however the initial coordinates of the water molecules were derived from the ordered, low temperature structure. The *b*-glide symmetry operator, not present at 100 K, collapses the four water molecules onto two positions, resulting in a superposition of the two water channel meso-helices (O400 maps onto O100, and O300 onto O200), Thus, each water molecule is half occupied. Refinement of the oxygen with anisotropic thermal parameters is unstable due to correlation caused by the close proximity of the two sites. Hydrogen atom positions and isotropic thermal parameters were then refined with soft restraints prior to their inclusion in the final refinement using a riding model as for the structure determined at 100 K. Fig. 4.9(b) shows a generalised difference Fourier section when the hydrogen atom occupancies are set to zero.

4.3.3 The low temperature structure

The distinction between $P2_1cn$ and $Pbcn$ space groups for the structural models of low-temperature HHTP·4H_2O is crucial because the former is a polar space group, whereas the latter is not. The structural feature responsible for polarity within the $P2_1cn$ model is the ice-like hydrogen-bonding network within the water-filled channels: *i.e.*, the aforementioned ice rules break inversion symmetry [Fig. 4.7]. While there are two polar 1D ice chains within the crystallographic unit cell, these are related to one another by the crystal symmetry in a way that reinforces the polarisation component parallel to the *a* crystal axis [Fig. 4.10(a,b)]. The chain geometry is of interest in its own right within the context of helical polymer motifs: it takes the rarely-observed form of a so-called "directed *meso*-helix", an object with polarisation components both along and normal to the helix axis.[250,251] So whereas the polarisation

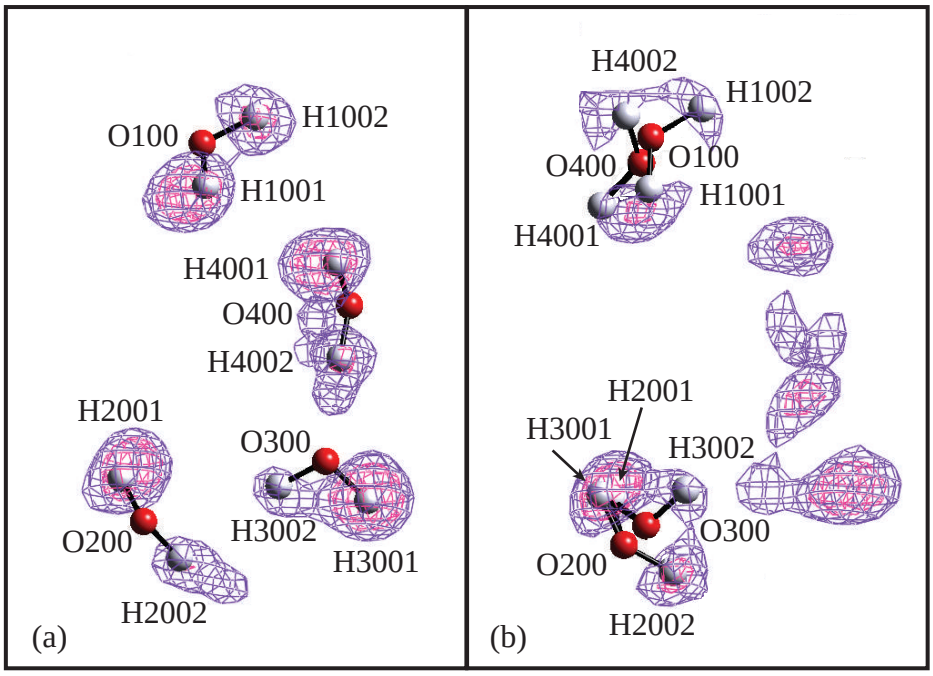

Figure 4.9: Generalised section of the difference Fourier maps for the water molecules with hydrogen occupancies set to 0 and the data truncated at 1.1 Å for (a) 100 K ($Pna2_1$) and (b) 240 K ($Pbcn$). The unoccupied density in (b) becomes symmetry-related to the other regions of density by the b-glide that is generated by the phase transition. When hydrogen occupancies are set to 1 (in (a)) and 0.5 (in (b)), no density is visible.

associated with 1D ices is usually parallel to the confinement axis, in this system the net polarisation is perpendicular to that axis (the parallel component cancelling between adjacent chains).[241] From a practical viewpoint, the advantage is that the crystal habit is to grow as square prisms with their long axis parallel to c; consequently the surface area is maximised in perpendicular directions — the optimal geometry for exploiting any ferroelectric response.

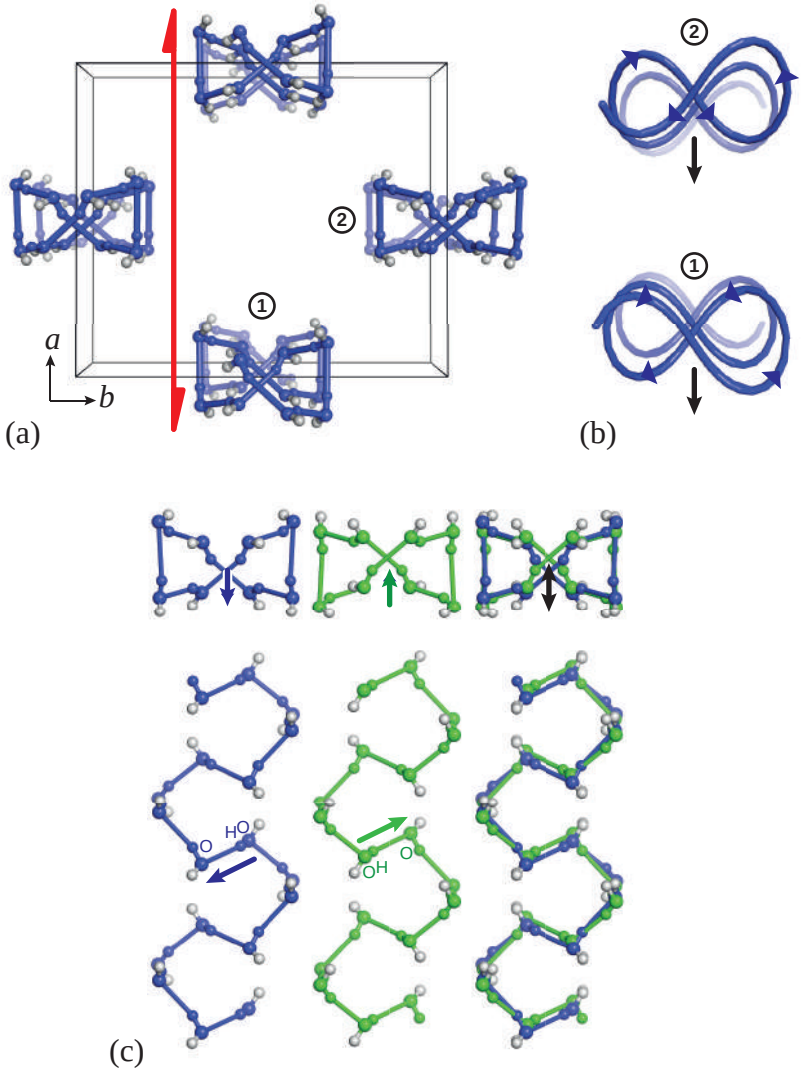

Figure 4.10: (a) The low-temperature $P2_1cn$ structure of HHTP·$4H_2O$ contains two non-superimposable ice-like chains, here numbered '1' and '2'. These are related by crystallographic symmetry; *e.g.* by the 2_1 screw-axis shown. (b) These ice-like chains adopt directed *meso*-helical geometries, giving rise to a non-cancelling polarisation parallel to the *a* crystallographic axis. Arrows have been drawn on each *meso*-helix to emphasise the direction of O—H···O hydrogen bond donation. (c) The left and centre panels illustrate the ice-like network for the two polarisation states. At temperatures above 240 K, HHTP·$4H_2O$ exists in a paraelectric phase in which these states and their inverse occur throughout the crystal structure.

4.3.4 The high temperature structure

Turning next to the X-ray diffraction data collected at 240 K, we find that at this temperature the additional reflections forbidden in *Pbcn*, but allowed in $P2_1cn$, have negligible intensity. Consequently there is no crystallographic justification for lowering the symmetry beyond *Pbcn* in this case. We obtain a numerically-satisfactory structure refinement using the model of Ref. 188; however this does not address our earlier concerns regarding the physicality of this model. Instead we find that we obtain a better (and more meaningful) fit to the data using a disordered *Pbcn* model containing equal proportions of the low-temperature $P2_1cn$ structure and its inverse. At temperatures above 240 K, HHTP·$4H_2O$ exists in a paraelectric phase in which both states occur throughout the crystal structure [Fig. 4.10(c)]. The resulting average structure has *Pbcn* symmetry and is most meaningfully understood in terms of an equal-population superposition of the two polarisation states. These respective orientations have opposite polarisation along *a* and hence the overall polarisation of the structure disappears at these temperatures.

4.3.5 Interconversion mechanism

From a crystal chemical viewpoint, one might anticipate a relatively small enthalpy cost associated with interconversion of the two possible polarisation states. By comparing the HHTP molecule geometry in our $P2_1cn$ structure with that observed in the *Pbcn* refinements (either ours for data collected at 240 K, or that reported in Ref. 188), we find a root-mean-squared deviation in atomic positions of less than 0.04 Å. Consequently the interconversion mechanism involves concerted proton shuttling within the ice-like chains, much as has been observed elsewhere for ferroelectric materials based on bistable hydrogen-bonding interactions.[252,253] In the present case, the intercoupling mechanism is *via* hydrogen bonding between ice-like chains and the hydroxyl groups of the HHTP molecules. Because the H_2O—HHTP hydrogen bonding topology

is independent of chain polarisation, the degree of 'communication' between chains is suggested to be very small. The dipolar interactions between neighbouring chains do not require changes in the molecular geometry of the HHTP molecules.

4.4 Order parameter evolution with temperature

The transition from polar to paraelectric states of HHTP·$4H_2O$ can be quantified using an order parameter derived from the intensities of those reflections unique to the $P2_1cn$ space group. Fig. 4.11 shows the temperature evolution of a small relevant portion of the diffraction pattern across the transition: here the three reflections (011) (031) and (071) are forbidden in $Pbcn$ and can be seen to decrease in intensity with heating.

4.4.1 Relationship to diffraction intensities

The relevant order parameter for this order/disorder transition can be related directly from the structure factor expression. We consider the system to consist of fractions χ and $(1-\chi)$ of the low-temperature $P2_1cn$ structure and its inverse (obtained by action of a b-glide perpendicular to a); the corresponding order parameter is consequently

$$\xi = 2\chi - 1. \tag{4.1}$$

Using this construction, the structure factor associated with $(0kl)$ reflections is

$$F(0kl) = \chi \sum_{j=1}^{N} f_j \exp[2\pi i(ky_j + lz_j)] +$$
$$+(1-\chi)\sum_{j=1}^{N} f_j \exp\{2\pi i[k(y_j + \frac{1}{2}) + lz_j]\} =$$
$$= \sum_{j=1}^{N} f_j \exp[2\pi i(ky_j + lz_j)][\chi + (1-\chi)\exp(\pi i k)].$$

For those $(0kl)$ reflections forbidden in $Pbcn$ (*i.e.*, k odd), we have

$$F(0kl) = (2\chi - 1)F_{P2_1cn}(0kl), \tag{4.2}$$

where $F_{P2_1cn}(0kl)$ is the relevant structure factor for the ordered $P2_1cn$ phase. Consequently $I(0kl) = |F(0kl)|^2$ is proportional to ξ^2 and ξ to $\sqrt{I(0kl)}$. For each of these reflections, the corresponding order parameter ξ was calculated for each temperature according to

$$\xi(0k1) = \alpha_k \left[\frac{I(0k1)}{I(042)}\right]^{1/2}, \tag{4.3}$$

where α_k is a temperature-independent scaling parameter, $I(hkl)$ is the measured intensity of the (hkl) reflection, and the parent (042) reflection was used for normalisation for its combination of strong intensity at all temperatures and well-defined peak profile. The parameter ξ takes the value of zero within the paraelectric regime and is non-zero whenever there is long-range correlation of the 1D ice polarisations. The temperature dependence of ξ for these three reflections is illustrated in Fig. 4.11, where the values at 240 K should be interpreted as the result obtained by integrating background fluctuations in the diffraction images. In the absence of a well-defined discontinuity in the function $\xi(T)$, we can conclude that the phase transition is likely to be second-order in nature. By comparing the results of heating and cooling runs, we find no evidence of hysteresis at the transition; however the limiting magnitude of the order parameter $\xi(T \to 0)$ is only $\sim 75\%$ the value obtained at the start of the experiment [Fig. A.1]. This discrepancy may have one of two origins: either some desorption of H_2O occurred on heating to 260 K or relaxation kinetics play a significant role in determining the degree of polar ordering over the experiment timescale.

4.4.2 The Ising model

To interpret the order parameter variation shown in Fig. 4.11 we construct a mapping of the polarisation state of HHTP·4H_2O onto the square Ising model. Each 1D ice chain

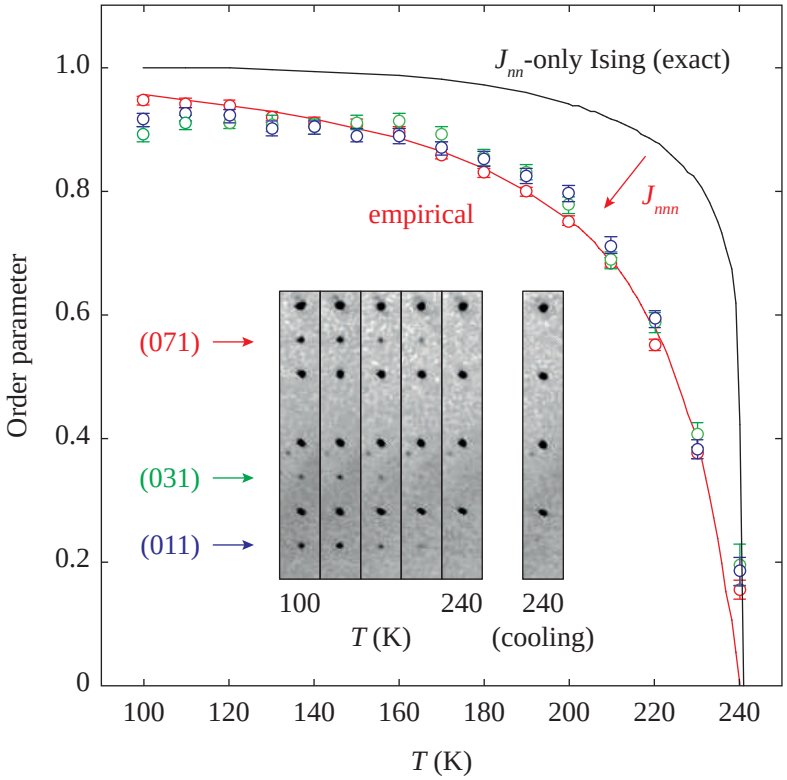

Figure 4.11: Thermal variation in the order parameter ξ, calculated from the intensities of three representative systematic absence violations according to Eq. (4.3) (data points). The absence of a clear discontinuity at the transition temperature $T_c \simeq 240\,^{\circ}\mathrm{C}$ suggests the order/disorder transition is second order in nature. Relevant sections of the single-crystal diffraction patterns are shown in the inset; these illustrate the disappearance of $(0k1); k = 2n+1$ reflections on heating towards T_c. The nearest-neighbour square lattice Ising model discussed in the text predicts a sharper transition (thin line) than is observed experimentally.[212] The inclusion of frustrated next-nearest-neighbour terms in the ordering Hamiltonian is known to give rise to a temperature dependency similar to the empirical curve fit shown here [bold line; Eq. (4.7)].

is capable of adopting either one of two configurations consistent with the ice rules — these are the orientations related to one another by the inversion centre present in *Pbcn* but absent in $P2_1cn$ — and so can be assigned one of the two states $e \in \{1, -1\}$ allowed in an Ising model. It is noted here that in the crystallographic analysis above demonstrates that even in the high-temperature phase the alignment within each 1D chain is ordered, however the correlation between chains loses its long range order at high temperatures. For each 1D chain there are four equidistant nearest-neighbours to which its Ising state (*i.e.*, polarisation) will be coupled *via* subtle reorganisation of the connecting HHTP molecules or dipolar interactions. [Fig. 4.12(a)]. The corresponding energy scale J_{nn} is (by symmetry) identical for all nearest-neighbours of all chains, giving the canonical Hamiltonian

$$\mathcal{H} = -J_{\mathrm{nn}} \sum_{i,j \in \mathrm{nn}} e_i e_j. \tag{4.4}$$

The topology of this coupled system is that of the square net and is two-dimensional because each 1D chain acts as a collective object. As such we can interpret the hydrogen bond order/disorder transition in HHTP·4H_2O as a specific manifestation of the general and well-established problem of the square Ising model [Fig. 4.12(b)].[212,254,255] In the case that nearest-neighbour interactions are the only interactions of relevance to the order/disorder process then the corresponding equilibrium behaviour of the square Ising model is known exactly.[212] One anticipates a second-order phase transition between ordered (or, in the case of HHTP·4H_2O, polar) and disordered (*i.e.*, centrosymmetric) states at the critical temperature

$$T_{\mathrm{c}} = \frac{J_{\mathrm{nn}}}{k_{\mathrm{B}}} \frac{2}{\ln(1+\sqrt{2})}. \tag{4.5}$$

The temperature-dependence of the order parameter (≡ magnetization in Onsager's formulation[212]) follows the closed form

$$\xi = \left[1 - \sinh^{-4}(2J_{\mathrm{nn}}/k_{\mathrm{B}}T)\right]^{1/8}, \tag{4.6}$$

which predicts a more sudden variation in $\xi(T)$ near T_c than we observe experimentally [Fig. 4.11].

In practice it is likely that next-nearest-neighbour interactions cannot altogether be neglected in a physical system such as we study here. The inclusion of appropriate additional terms into the Hamiltonian of Eq. (4.4) leads to a surprisingly-complex (and still controversial) system for which no exact solution is obtainable.[255–257] Of relevance to the present situation is the observation that next-nearest-neighbour coupling constants J_{nnn} of opposite sign to J_{nn} have the effect of reducing the order parameter at lower temperatures to give a thermal variation more similar to that which we find to occur in HHTP·4H_2O.[255] This is the so-called 'frustrated Ising model', for which the phase transition is actually very weakly first-order.[257] So there may be some suggestion that 1D ice polarisations couple in a ferroelectric sense for nearest neighbours in HHTP·4H_2O but in an antiferroelectric sense for next-nearest neighbours. Actually the situation is even more complex in this case because the orthorhombic crystal symmetry gives rise to two distinct types of next-nearest neighbours—a problem for which we are not aware of any prior theoretical groundwork. What is known is that the relationship between J_{nn} and T_c given in Eq. (4.5) holds even for the frustrated Ising case, and so we can estimate the interchain coupling strength in HHTP·4H_2O to be $\sim$0.9 kJ mol^{-1}. For comparison the interaction energy between two water molecules is estimated to lie between 18.8 and 30.1 kJ mol^{-1}; consequently, this system displays an excellent discrimination between inter- and intra-chain energy scales.[258] In the absence of a closed form for the temperature dependence of the order parameter for a frustrated square Ising model, we have used an empirical fit in Fig. 4.11 of the form

$$\xi = \left(\frac{x}{1+x} \right)^{\nu}, \tag{4.7}$$

where $x = \alpha(T - T_c)/T$, and α and ν are constants.

We attribute the accessibility of a paraelectric state in HHTP·4H_2O to the very weak inter-chain coupling, which allows hydrogen bond disorder to occur without melting of the oxygen sublattice. We note specifically that the H_2O oxygen atom positions remain

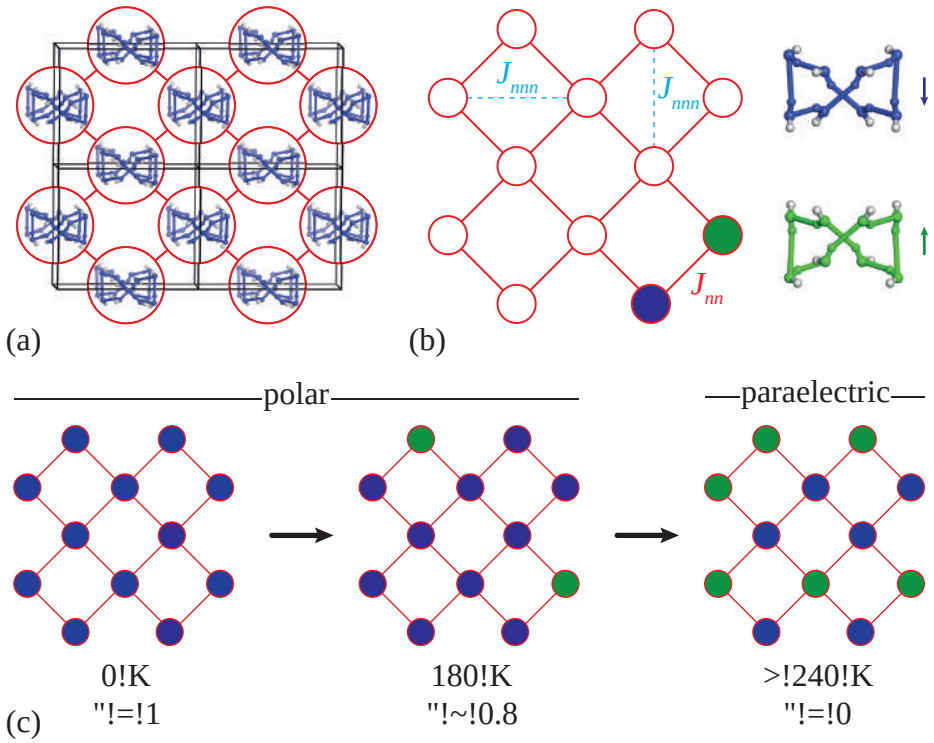

Figure 4.12: (a) Each 1D ice-like chain interacts with four neighbouring chains *via* HHTP hydroxyl groups. (b) The network of coupled chains has the square lattice topology. Because each chain can adopt one of two polarisation states (indicated here by filled and open circles; *cf.* Fig. 4.10), there is a direct mapping between long-range ordering of ice polarisations in HHTP·4H_2O and the general problem of ordering on the Ising square lattice. Here J_{nn} describes the coupling strength between neighbouring 1D chains. By virtue of the orthorhombic crystal symmetry there are in fact two inequivalent next-nearest-neighbour couplings J_{nnn} and J'_{nnn}, the parity and relative magnitude of which will contribute to the discrepancy observed between experimental and theoretical $\xi(T)$ curves as shown in Fig. 4.11; (c) At temperatures below T_{c} the system adopts a polar state in which the majority of sites share the same state ($\xi > 0$), but at temperatures greater than 240 K there is an equal population of both states and the system is said to be paraelectric.

well-defined even at temperatures above $T_c \simeq 240\,\mathrm{K}$; the larger-than-expected oxygen displacement parameter observed reflects only the superposition of two half-occupied oxygen sites associated with each of the two polarisation states. This observation distinguishes the behaviour of paraelectric HHTP·$4H_2O$ from that of the high-temperature phases of the related 1D ices $[Cu(C_6H_4NO_2)_2]$ and $[Cu^{I}_2Cu^{II}(CDTA)(4,4'\text{-bpy})]$, within which long-range diffusive motion of the H_2O occurs. Consistent with the small magnitude of J_{nn} is the negligible difference in HHTP geometries we observe across the order/disorder transition, which in turn explains the remarkable weakness of the additional diffraction intensities associated with symmetry breaking.

4.5 Summary

In summary, we find that the molecular hydrate HHTP·$4H_2O$ exhibits a hydrogen bond order/disorder transition near $T_c \simeq 240\,\mathrm{K}$ that is associated with the development at low temperatures of long-range ferroelectric coupling between polar 1D ice chains [Fig. 4.12(c)]. The phase transition behaviour we observe maps qualitatively onto the problem of ordering on the Ising square lattice, with the accessibility of a paraelectric phase at temperatures above T_c suggesting that ferroelectric switching of the low-temperature polar phase should be possible. Finally, our study also illustrates how molecular systems might host confined ice phases in a manner normally associated with porous covalent networks or carbon/inorganic nanotube arrays.

Chapter 5

High temperature phase of $HHTP{\cdot}4H_2O$

5.1 Overview

In the course of this study, we investigated whether the 1D nature of the $HHTP{\cdot}4H_2O$ structure could be exploited to produce a 1D metal. The results are brought in this chapter. The highly symmetrical molecule HHTP can exhibit seven oxidation states [Fig. 5.1].[259] Three of these are radical molecules in a semiquinone oxidation state.
In this part of the thesis, we investigate the incorporation of these radical molecules into the crystal structure of $HHTP{\cdot}4H_2O$ and explore the crystals' electronic and magnetic properties. Our goal was to use the aforementioned neutral crystals based on HHTP and to then provoke oxidation of the HHTP molecules to radical forms by oxygen in air *via* heat treatment. As discussed previously, HHTP stacks in columns in the $HHTP{\cdot}4H_2O$ crystals and our hypothesis was that by oxidising the individual molecules to one of the radical forms, 1D conducting bands could be obtained within the crystal. The following sections describe the results of these investigations and bring a general literature background of organic materials that exhibit useful electronic and magnetic properties.

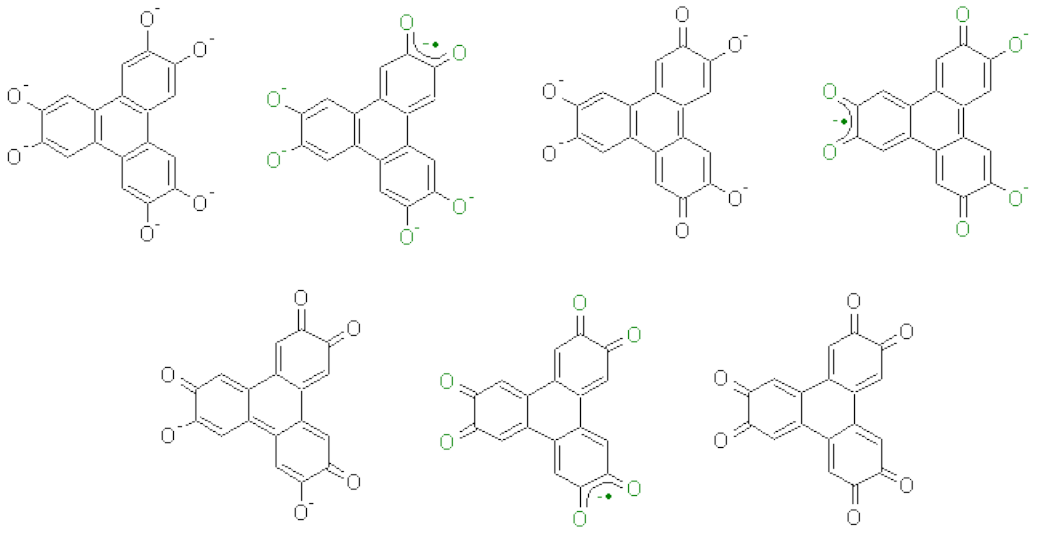

Figure 5.1: Oxidation states of HHTP. Oxygens are marked with green in the radical semiquinone forms.

5.2 Background

The majority of organic compounds known are comprised of an even number of electrons, deployed into covalent bonds with two electrons in a pair. Therefore the magnetic moments of the spins are effaced and net diamagnetism is observed. There are, however, examples of stable organic radical molecules, which have been isolated as single-crystals, and can exhibit magnetic properties. A short overview of these systems is given in the following paragraphs.

5.2.1 Organic magnetic materials

By virtue of their instability and reactivity, organic radicals need to be further stabilised in crystal structures. To achieve this, the molecular structure of the organic radical can be adjusted to a) embody heteroatoms and electron withdrawing groups to stabilise the radical *via* dative or captodative interactions, b) incorporate large σ-donating substituents to stabilise the radical *via* hyperconjucation and c) incorporate aromaticity to stabilise the radical *via* π-electron delocalisation. A number of stable

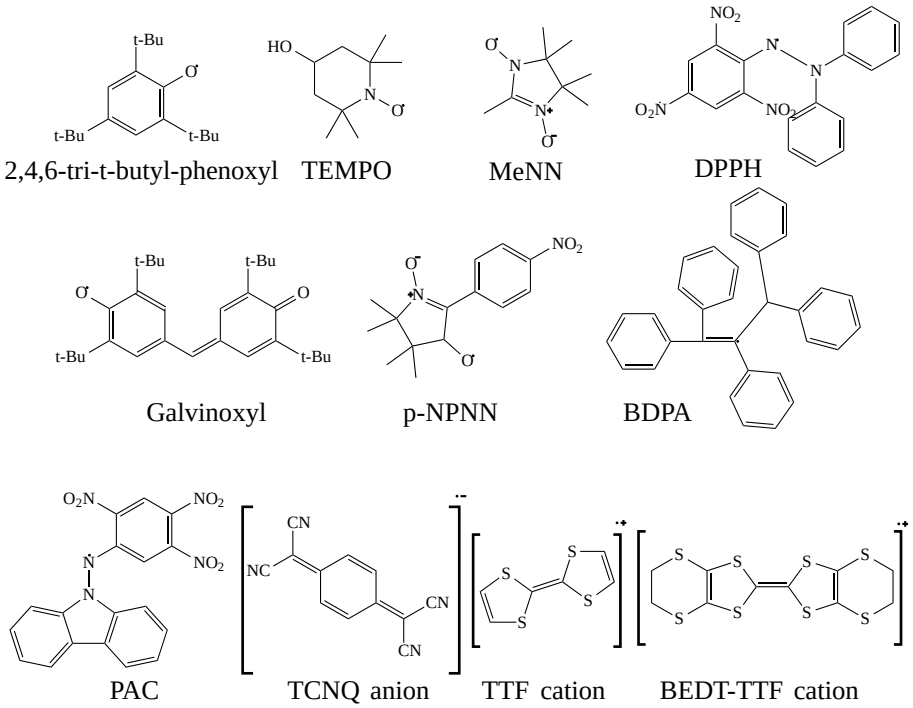

Figure 5.2: Different stable radicals isolated as single-crystals, adapted from.

organic radical crystals have been synthesised to date and examples of these are given in Fig. 5.2.[260]

In many cases, these organic radical crystals exhibit paramagnetism in accordance with the Curie-Weiss law, $\chi_m = \frac{C}{T-\theta}$. The magnetic susceptibility of the crystals indicates weak antiferromagnetic interactions between the radicals at low temperatures, which stem from the tendency of the molecules to form covalent bonds with spins antiparallel. On the other hand, ferromagnetic interactions in such crystals are very rare and are of interest to scientists.

The first organic crystals to exhibit ferromagnetism were found in the 1960s. The study of galvinoxyl in 1969 by K. Mukai et al. made it the first organic molecule to show intermolecular ferromagnetic interactions.[261] Based on this discovery, rules were established for the search of new organic ferromagnets. As the quest in the field of organic superconductors culminated in the 1970s, the search for organic ferromagnets was shelved until the 1980s. It was then when organic superconductors started to appear rapidly and the interest towards organic ferromagnets arose again. Among others,

crystals of p-NPNN, verdazyls, TANOL and TEMPO derivatives were synthesised, all of which, albeit at very low temperatures, show a ferromagnetic transition.[260]

Approaches of raising the magnetic ordering temperature well above room temperature include utilising molecular magnets, where organic groups are combined with transition metals or rare earth metal ions. These can subdivided further into two categories:

1) Closed shell molecular magnets, where the organic compound has an even number of electrons and does not exhibit magnetism itself, but helps to mediate magnetism between transition metal ions. An example of these is the Prussian blue, $Fe_4(Fe(CN)_6)_3 \cdot 14\,H_2O$, where magnetic coupling between the Fe^{3+} and the Fe^{2+} ions is mediated *via* the cyanide linkers.[262] Further examples include linkers incorporating cyanide (CN), dicyanamide ($N(CN)_2$), tricyanomethanide ($C(CN)_3$) groups.[263]

2) Open shell molecular magnets, where the unpaired spins can reside both on the organic molecule and the corresponding metal. Examples of these are charge-transfer (CT) salts based on TCNE, TCNQ and TTF. The organic molecule either donates or accepts an electron to form a complex with the metal, which can then undergo a magnetic transition.[264]

5.2.2 Organic conductors and superconductors

The previous section dealt with stable organic radical crystals and ferromagnets and with molecular magnets based on organic molecules. This section aims to give a brief overview of the history and progress in the field of organic conductors and superconductors.

In 1954, Akamatu et al. synthesised the first conducting organic material without any metal atoms present: a perylene-bromine salt, which is an important benchmark for the development of organic conductors and superconductors.[265] The next breakthrough was in the 1960s and 1970s when the electron acceptor TCNQ and electron donor TTF were synthesised. The two molecules were combined to produce a CT salt, which shows anisotropic quasi-one-dimensional metallic properties.[266] The material exhibits metal-

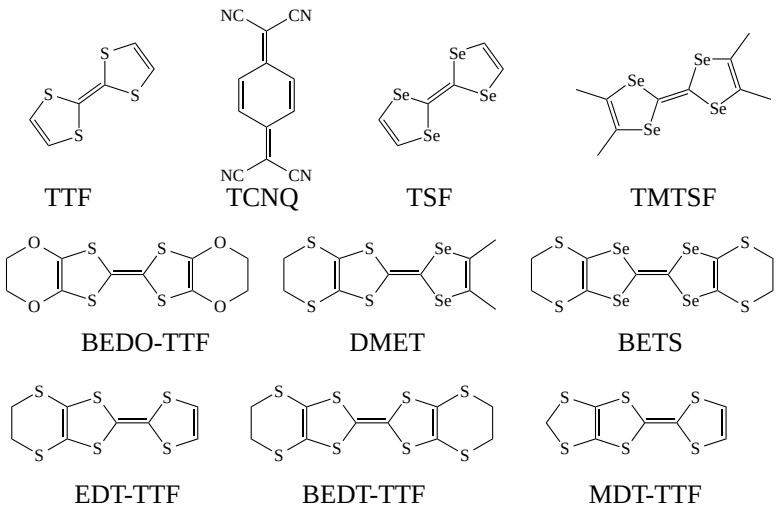

Figure 5.3: Different organic donors for superconducting charge transfer complexes.

lic conductivity of $\sigma \approx 10^4\,\mathrm{S\,cm^{-1}}$ at 60 K. By way of comparison, elemental Cu exhibits conductivity of $\sigma \approx 10^6\,\mathrm{S\,cm^{-1}}$ and elemental Fe of $\sigma \approx 10^5\,\mathrm{S\,cm^{-1}}$ at room temperature.

In 1979, the first quasi-one-dimensional organic superconductor, $(TMTSF)_2PF_6$ was synthesised.[267] The superconducting transition temperature (T_C) of this material is 0.9 K, but a pressure of about 6.5 kbar is required to suppress an insulating phase transition. Further successes included the first ambient pressure organic superconductor based on the perchlorate salt of TMTTF with $T_C = 1.4\,\mathrm{K}$.[268] Other salts based on TMTTF (Fabre-salts) and TMTSF (Bechgaard-salts) have been synthesised, but the majority of these require exertion of high pressures to see superconductivity.[269]

Quasi-two-dimensional charge transfer complexes, employing the organic donor and the acceptor monolayers as alternating sheets in the crystal, were the next research interest in the area of organic superconductors.[264] Fig. 5.3 illustrates some examples of the most important organic donors embodied in these systems. An outstanding example is BEDT-TTF, first synthesised by Mizuno et al., and a short summary of this system is given in the next paragraph.[270]

The first BEDT-TTF based superconductor reported was $(BEDT\text{-}TTF)_2ReO_4$ with $T_C \approx 2\,\mathrm{K}$.[271] Since then a number of BEDT-TTF based superconductors have been

investigated. The crystal structures of these superconductors are varied, and can be distinguished by a prefix, e.g α-, β-, κ-, λ-, θ- etc. The κ-phase of the (BEDT-TTF) charge transfer salts had the highest superconducting transition temperatures for a long time in the area of organic superconductors. Examples of these include κ-(BEDT-TTF)$_2$Cu(NCS)$_2$ ($T_C \approx 10.4\,K$), κ-(BEDT-TTF)$_2$Cu[N(CN)$_2$]Br ($T_C \approx 11.8\,K$), κ-(BEDT-TTF)$_2$Cu[N(CN)$_2$]Cl ($T_C \approx 12.8\,K$) and κ-(BEDT-TTF)$_2$I$_3$ ($T_C \approx 4\,K$).[272] A lot of work and effort has gone into characterising these and other BEDT-TTF based oragnic superconductors and understanding the underlying mechanism for their properties.

The enhancement of T_C of organic superconductors ceased after the discovery of κ-(BEDT-TTF)$_2$Cu[N(CN)$_2$]Cl and chemists felt a need for a new target in the field of organic conductors and superconductors. The first ferromagnetic organic metal was reported in 2000 by Coronado et al. and combined the organic metal layers of BEDT-TTF with ferromagnetic anion layers of $MnCr(C_2O_4)_3$.[273] Furthermore, in 1999, the first antiferromagnetic organic superconductor was reported, κ-$BETS_2FeBr_4$ with T_c of 1.1 K, and in 2001, the first field-induced organic superconductor, λ-$BETS_2FeCl_4$ was introduced.[264] Another class of organic superconductors includes the superconducting fullerenes, and particularly Cs_2RbC_{60}, presented in 2011, with the highest transition temperature of $T_C = 33\,K$ among organic superconductors.[274]

The results summarised in the previous sections have focused on charge transfer complexes with separate donor and acceptor layers. It is, however, interesting to note that the first single-component molecular metal [Ni-(tmdt)$_2$] was synthesised in 2001 by Tanaka et al.[275] This result links in well with the study of the HHTP ligand, where a single molecule based organic system and its electrical and magnetic properties have been investigated as part of this study.

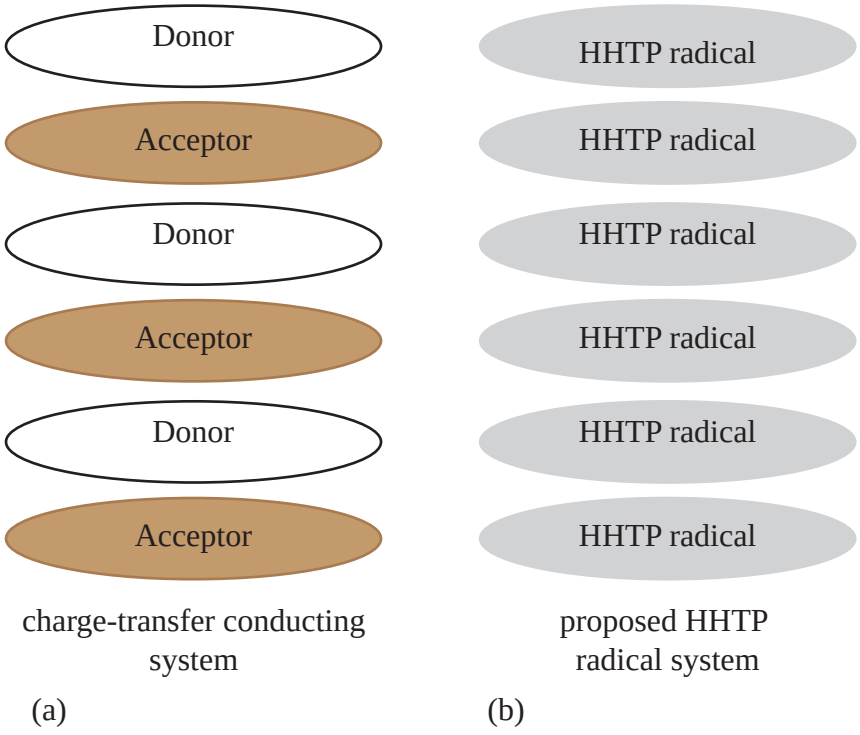

Figure 5.4: Schematic of a charge-transfer system and HHTP radical system with (a) showing the arrangement of donor and acceptor constituents for typical conducting charge transfer salts and (b) showing the suggested HHTP radical system that comprises of a single component.

5.3 Structural characterisation

This stacking arrangement in HHTP·4H_2O facilitates considerable π-overlap between the HHTP molecules, allowing for the possibility of one dimensional bands along the stacking direction. Our hypothesis was that it would be possible to oxidise the HHTP molecules into one of their radical forms and therefore create 1D bands where the unpaired electrons are free to move when a current is applied. This system would be a contrast to typical charge-transfer systems, which consist of donor and acceptor molecules. The suggested HHTP system would comprise of a single component [Fig. 5.4].

To probe this argument and to oxidise the neutral HHTP molecules to the radical

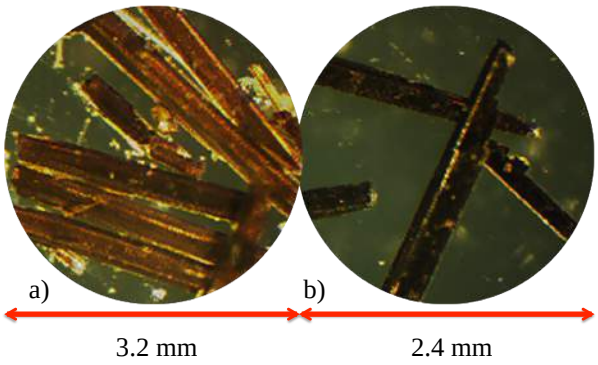

Figure 5.5: Crystals of HHTP: (a) the as synthesised red and transparent HHTP·4H_2O crystals and (b) the oven treated black crystals.

forms for the incorporation of free electrons into the crystals, the samples were heat-treated at a 100 °C for ten days. After this treatment, the crystals were black and opaque, which is a drastic change from their original red and transparent appearance [Fig. 5.5]. The heat treated black and opaque crystals were no longer single-crystalline and contained small cracks in their morphology, making their structural characterisation challenging. To confirm that the stacking arrangement of the D_{3h} symmetry molecules had been retained over the heat treatment, rotation images in the direction of the one-dimensional stacks on a single-crystal X-ray diffractometer were taken. 6-fold symmetry of the patterns was observed, confirming that the stacking arrangement of the HHTP molecules had still been preserved at high temperatures [Fig. 5.6(a)].

To gain some more structural insight and to explore the changes in the intermolecular distance along the stacking axis, single-crystal X-ray diffraction studies on the red HHTP·4H_2O crystals were performed at 60 °C and synthesised precession images were calculated. In the (110) plane in reciprocal space, where the a^* corresponds to the stacking direction, an appearance of a new phase could be observed. This phase has a large a^* value associated with it and hence has a decreased distance between the molecules along the stacking axis, which could be explained by the corrugated HHTP sheets becoming planar and closer in proximity upon dehydration [Fig. 5.6(b)]. This results in increased π-overlap between the molecules at elevated temperatures.

In light of these findings and to explore the high temperature structures in more detail,

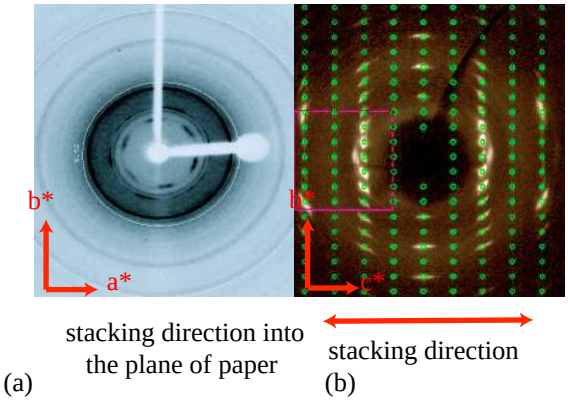

Figure 5.6: Structural studies of the oven-treated crystals: (a) rotation image of the oven treated crystals looking down the stacking direction indicating 6-fold symmetry and (b) synthesised precession image of the 110 plane in reciprocal space, illustrating the appearance of a new phase at 60 °C. The green dots illustrate where the peaks should be positioned in the HHTP·4H_2O structure. The new peaks can be seen either side of the second column of the green dots from the centre along the stacking direction.

we performed high temperature variable temperature powder X-ray diffraction on the HHTP·4H_2O crystals [Fig. 5.7].

It is noteworthy that the crystals undergo two phase transitions: at around 40 °C and 120 °C. The first phase transition can partially be explained by the loss of three of the four water molecules per HHTP molecule in the structure as confirmed by thermogravimetric analysis and the second by the loss of the final water molecule [Fig. 5.8]. Loss of water can be accompanied by oxidation and to probe whether oxidation to the radical species had occured, we chose two samples to study in further detail: one near the second phase transition temperature at a 100 °C and another after the second phase transition temperature at 153 °C. Our reasoning behind that included the argument that the pattern for the structure after the second phase transition looks more simple than after the first phase transition and could be a single phase. Indexing the pattern with EXPO2009[276] gave a monoclinic $P2_1/m$ crystal structure with $a = 11.4$ Å, $b = 13.76$ Å, $c = 9.30$ Å and $\beta = 121.68°$. Therefore two samples of the red crystals

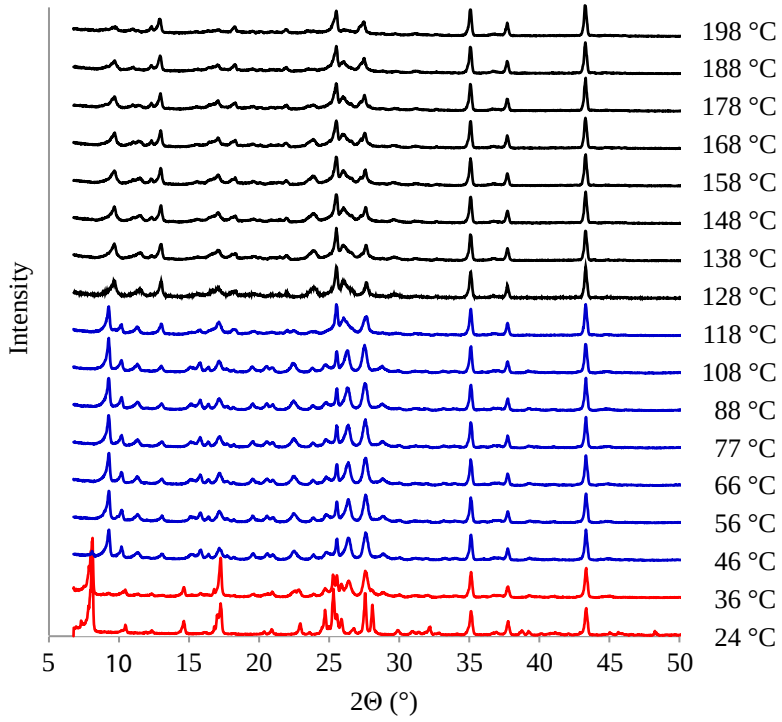

Figure 5.7: High temperature variable temperature powder X-ray studies illustrating two phase transitions for HHTP·4H_2O. Different phases are marked with different colours.

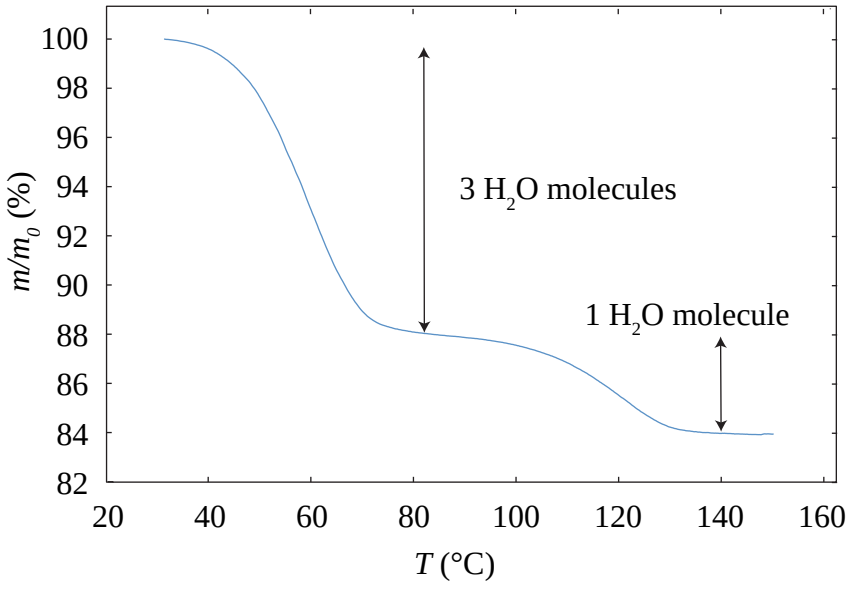

Figure 5.8: Thermogravimetric analysis data indicating the loss of 4 water molecules from the structure of HHTP·4H_2O.

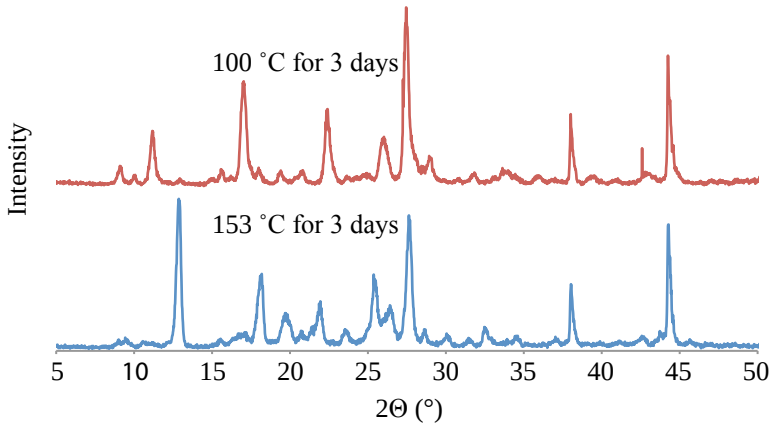

Figure 5.9: Powder X-ray diffraction data for heat treated samples at 100 °C and 153 °C for 3 days.

were heat treated in an oven at 100 °C and 153 °C and their evolution monitored by powder X-ray diffraction. Conversion to the desired phases was achieved within three days [Fig. 5.9]. These samples were used in the following electronic and magnetic characterisation experiments.

5.4 Electronic and magnetic characterisation

SQUID susceptibility measurements were performed on the 153 °C sample and a temperature sweep resulted in observed magnetisation at temperatures below 12 K [Fig. 5.10]. A field sweep at 2 K indicated paramagnetism with a moment of $3{\cdot}10^{-6}\,\mu_B$/molecule. The red and transparent HHTP·$4H_2O$ crystals exhibited diamagnetism under the same conditions.

Electron paramagnetic resonance spectroscopy (EPR) was used to further investigate the crystals' electronic properties. The red HHTP·$4H_2O$ crystals did not absorb microwaves during the experiment and no signal was observed, whereas both the oven treated samples showed the presence of unpaired electrons of the order of 10^{-4} electrons/molecule [Fig. 5.11]. Both SQUID and EPR measurements indicate that the number of introduced unpaired electrons is relatively small and hence only very few

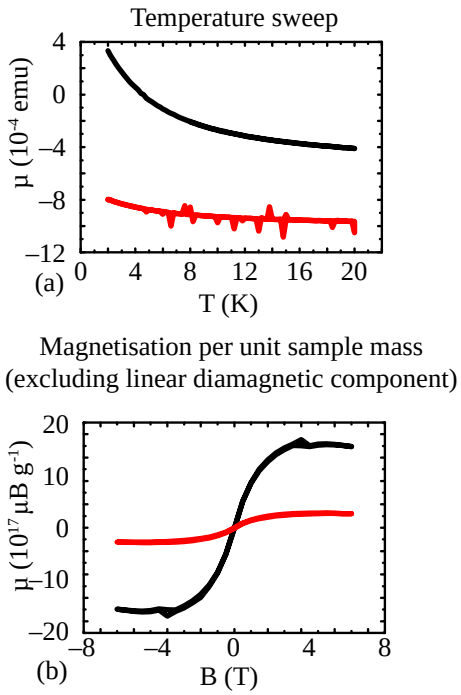

Figure 5.10: SQUID susceptibility measurements for the red and black crystals: (a) temperature sweep and (b) field sweep. Red lines represent the data for red crystals and black lines the data for heat treated black crystals.

of the HHTP molecules have been oxidised to a radical oxidation state. This is in contrast to the anticipated 1 electron/molecule and it is therefore likely that oxidation to the non-radical oxidation states of the molecule has taken place.

The next step was to perform heat capacity measurements on a physical property measurement system (PPMS) on the samples and the measurements showed insulating behaviour across 300 K to 0 K, with relatively high Debye temperatures, comparable to those of graphite or diamond Table 5.1 [Fig. 5.12].

To probe the crystals' conductivity, standard four-contact d.c. conductivity measurements on compressed pellets of the crystals at 300 K, 200 K, 100 K and 2 K using PPMS were performed, however, no conductivity was observed.

There might be different reasons for why these systems do not exhibit conductivity at the conditions studied, even though unpaired electrons are present according to EPR and SQUID measurements. Firstly, the crystals might be coated with an insulating

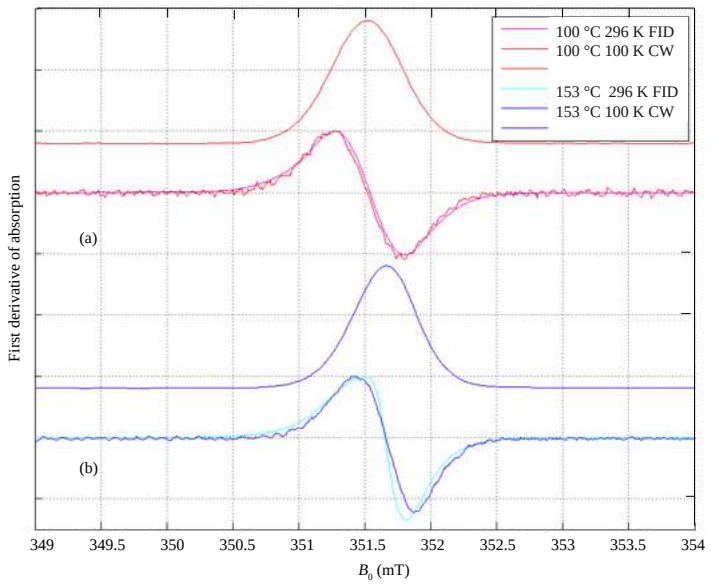

Figure 5.11: Comparison between the CW EPR and the FID-detected EPR spectra. The two methods give the same result with unpaired electrons observed: (a) data for the 100 °C and (b) data for the 153 °C at 100 K and 296 K.

Table 5.1: Debye and Einstein temperatures of the samples heat treated at 100 °C and 153 °C. In comparison, the Debye temperature of diamond, θ_D, is 2240 K whereas two Debye temperatures, θ_D, are used for graphite, 614 K for the vibrations with weak restoring forces and 2100 K for the remaining modes of vibration.

Temperature	100 °C sample	153 °C sample
Debye T (K)	1332	1807
Einstein T_1 (K)	430	472
Einstein T_2 (K)	167	169
Einstein T_3 (K)	61	59.5

surface layer. Secondly, there might be relatively free electrons, which are localised in the region immediately around the molecules and cannot move easily between them, either parallel or perpendicular to the chains. Similar considerations are limiting conductivity in graphite, which while having good conductivity in the planes, is not a

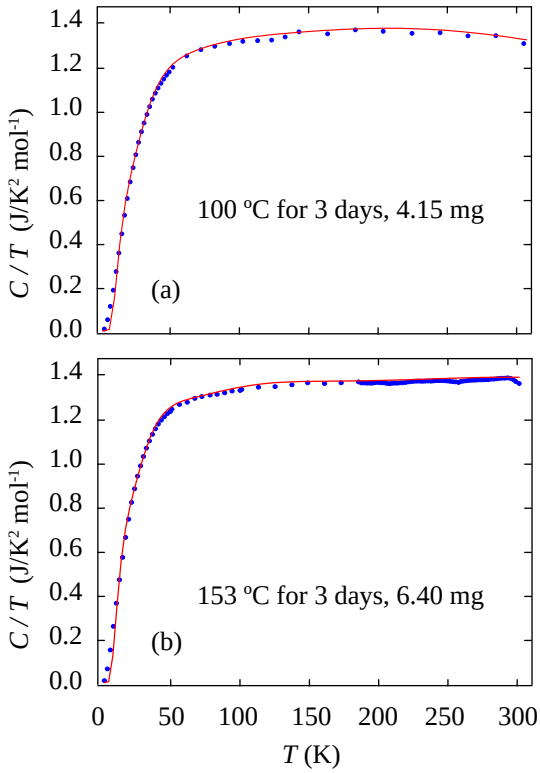

Figure 5.12: PPMS heat capacity data for (a) the 100 °C sample and (b) the 153 °C sample from 300 K to 0 K. The blue dots illustrate heat capacity measurements against temperature and the red lines are fits to the data, taking into account one Debye and three Einstein temperatures.

good conductor in the inter-plane direction. Thirdly, below some temperature, a one-dimensional metal will inevitably become insulating. There are two reasons for this:
1) in the case of extremely one dimensional materials any amount of defects will destroy the metallic state and
2) even clean or quasi-one-dimensional systems will have a metal-insulator transition, a Peierls transition, due to electronic interactions.[277]
More elaborate pulse EPR studies were performed to study the localisation of the free electrons. Davies-ENDOR spectra for the samples show the signals from proton hyperfine couplings to have a maximum $A_{max}(^{1}H)$ at about 15 MHz. This value is large and indicates that the unpaired electrons are highly localised.[278] The same information can be extracted from the HYSCORE spectrum, which shows both the ^{1}H and ^{13}C signals

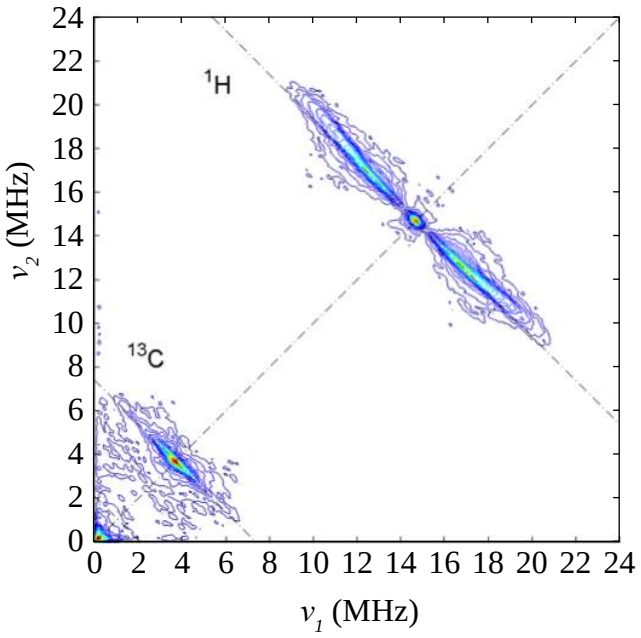

Figure 5.13: Pulse EPR data for the heat-treated samples with HYSCORE spectrum for the 153 °C sample at 100 K with both ^{1}H and ^{13}C signals observed.

[Fig. 5.13]. The data are consistent with the ENDOR data and show large ^{1}H hyperfine couplings with $A_{max}(^1H)$ close to 15 MHz. The shape of the ^{1}H ridge indicates large dipolar contributions to the hyperfine couplings, again evidence for the electron localisation on one molecule, rather than delocalisation across the one-dimensional stacks. This localisation of the electrons explains why conductivity was not observed during the standard four-contact d.c. measurements on the heat treated crystals as the electrons are not free to move between molecules along the one-dimensional stacks and hence conducting bands are not formed.

5.5 Summary

We have demonstrated that 2,3,6,7,10,11-hexahydroxytriphenylene tetrahydrate acquires unpaired electrons upon heat treatment. The synthesised red and transparent HHTP·4H_2O crystals become black and opaque at elevated temperatures and exhibit two phase transitions. The electronic properties of the structure after the second phase

were studied in more detail and it is noteworthy that the heat treated crystals, while retaining their columnar stacking arrangement, show weak paramagnetic interactions at low temperatures. Further studies confirm the electrons to be localised on single molecules, rather than delocalised across the one-dimensional stacks, and therefore the electrons are not free to move along the stacks and no conductivity is observed in these samples.

Chapter 6

2D layered structures

6.1 Overview

In this chapter we present the investigation into compressibility and thermal expansion behaviour in 2D layered structures. We focus on silver(I) tricyanomethanide [Ag(*tcm*)] and nickel(II) cyanide [$Ni(CN)_2$] [Fig. 6.1]. We demonstrate here the structure's response to temperature for Ag(*tcm*), whereas thermal expansion behaviour of $Ni(CN)_2$ has been shown previously.[156] It is noteworthy that both Ag(*tcm*) and $Ni(CN)_2$ exhibit area-NTE within the layers. Moreover, despite both these structures consisting of 2D layers, we demonstrate that Ag(*tcm*) exhibits NAC under pressure, whereas $Ni(CN)_2$ shows ordinary compressibility behaviour.

6.2 Structure of Ag(*tcm*) and $Ni(CN)_2$

In Ag(*tcm*), each Ag^+ cation is coordinated by three tcm^- anions in an approximately trigonal arrangement and likewise each tcm^- anion is coordinated by three Ag^+ centres.[279,280] The resulting hexagonal (6,3) topology is sufficiently open that two honeycomb networks interpenetrate within each layer of the crystal structure. Adjacent

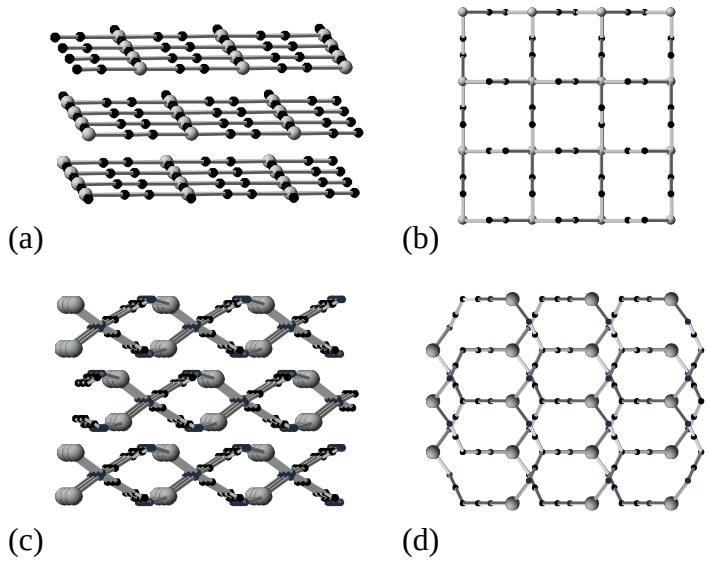

Figure 6.1: (a) The structure of $Ni(CN)_2$, showing the monoatomic layers in this material and (b) one single square-grid layer. (c) Structural representation of Ag(*tcm*), showing its flexible 2D layers and (d) a representation of a single layer of the Ag(*tcm*).

layers interact *via* long Ag$\cdots$N contacts [d(Ag$\cdots$N)>3 Å] that are sufficiently weak that the material behaves essentially as a 2D framework, capable even of intercalation chemistry.[280] The sinusoidal nature of each individual net is prerequisite for the parallel interpenetration. This structure was first reported in 1966 by Konnert and Britton from photographic data and confirmed later by Robson et al. to contemporary levels of precision.[281,282]

$Ni(CN)_2$ has been proposed as an inorganic analogue of graphene and is capable of forming intercalates and even nanotubular structures.[283–285] Despite $Ni(CN)_2$ having been known for almost a century, its structure was determined only recently.[156] As in graphite, $Ni(CN)_2$ consists of a layered topology: the metal atoms are connected *via* the linear coordination motif M—CN—M to form two-dimensional square-grid layers. It has recently been shown that there is no true periodicity in the stacking arrangement of these square-grid layers, which indicates the material to be of low dimensionality.[157]

6.3 Thermal expansion and compressibility measurements

6.3.1 Thermal expansion measurements for Ag(*tcm*)

Using SCXRD, we first established the thermal expansion behaviour of Ag(*tcm*) to verify whether or not the material exhibits area-NTE. Because the material crystallises in the orthorhombic (polar) space group $Ima2$, its thermal expansivity is uniquely determined by the relative rate of change of the unit cell lengths with temperature.[279,286] We observe essentially linear thermal variation in these parameters over the temperature range 100—250 K [Fig. 6.2(a)], yielding coefficients of thermal expansion of $-48(3)$, $+200(2)$ and $-54.0(4)\,\mathrm{MK}^{-1}$ along the a, b, and c axes, respectively.[286] As is increasingly found to be the case for molecular frameworks, the magnitudes of these values are large indeed compared to those obtained for traditional engineering materials, for which one expects linear coefficients of thermal expansion in the vicinity of $+20\,\mathrm{MK}^{-1}$ (*i.e.*, a 0.2% increase in linear dimension for each 100 K temperature rise).[287–289] What is clear is that Ag(*tcm*) does exhibit area-NTE, with an area coefficient of thermal expansion for the (a,c)-plane, $\alpha_{(0\imath0)} = -102(3)\,\mathrm{MK}^{-1}$, that is the most extreme negative value reported for a layered material. The material undergoes a 1% reduction in area for each 100 K rise in temperature — more than an order of magnitude larger than the corresponding values for area-NTE systems such as graphite and $Ni(CN)_2$ ($\alpha_A = -2.4$ and $-13\,\mathrm{MK}^{-1}$, respectively).[286,290,291]

6.3.2 Compressibility measurements for Ag(*tcm*)

In order to determine whether or not Ag(*tcm*) exhibits NAC, we performed a series of neutron diffraction measurements across the pressure range $0 < p < 2$ GPa using the PEARL instrument at ISIS. The use of neutron radiation helps maximise the scat-

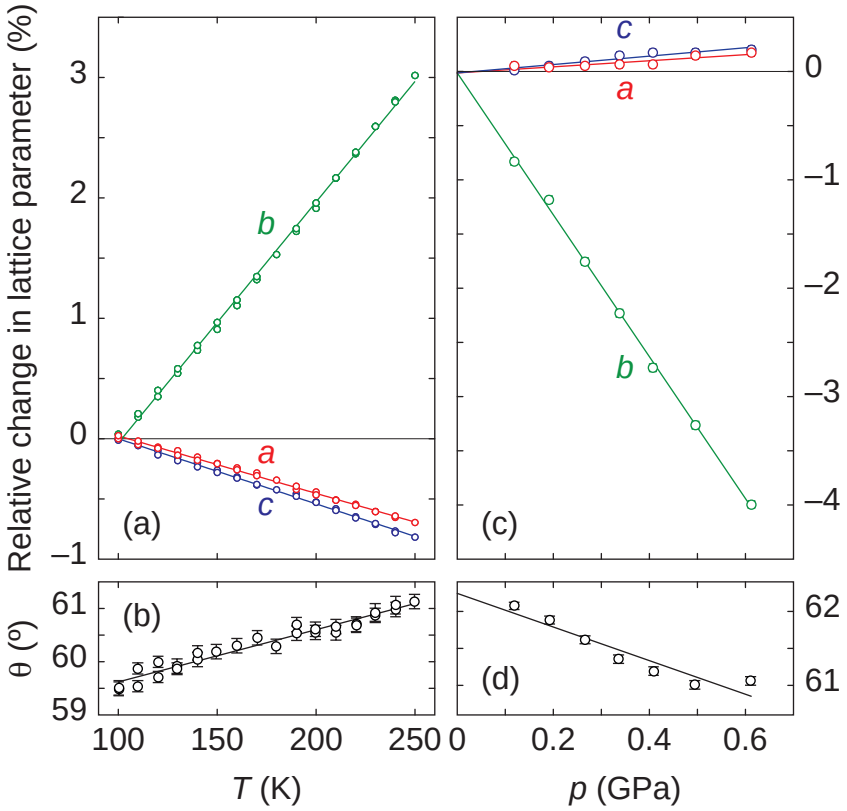

Figure 6.2: (a) The thermal variation of lattice parameters for Ag(*tcm*), determined using SCXRD measurements, is illustrated here for ease of comparison as a % change relative to the extrapolated value at 100 K. Solid lines are weighted linear fits to the data obtained using the program PASCal.[286] (b) The corresponding variation in inter-network angle θ indicates an increase in layer rippling on heating. (c) The pressure dependence of lattice parameters, measured using variable-pressure neutron diffraction, is represented as a % change relative to the extrapolated value at 0 GPa. (d) The corresponding variation in θ now indicates a decrease in layer rippling under compression.

tering contrast between C and N atoms by reducing the scattering difference between the heavier and the lighter atoms, which is all the more important for measurements performed in the high-background sample environments required for variable-pressure experiments. We found that, for powdered samples, the ambient phase is stable upto 0.615(6) GPa, but by 0.672(7) GPa it has transformed reversibly to a related phase with symmetry not higher than monoclinic [Fig. 6.3 and Table B.21]. The same transformation occurs at higher pressures ($0.83 < p_c < 1.47$ GPa) in single-crystal experiments. Rietveld refinement against the corresponding neutron diffraction patterns revealed an increase in a and c parameters is evident from these data [Fig. 6.2(c)], with the anomalous expansion of the material in these directions being allowed by a much more rapid decrease in the interlayer spacing (given by the lattice parameter b). Fits to the data are shown in Fig. 6.4. Our variable-pressure lattice parameter data can be converted into compressibilities using the relationship $K_\ell = -\left[\partial(\ln \ell)/\partial p\right]_T$, from which we obtain $K_a = -3.5(6)\,\mathrm{TPa}^{-1}$, $K_b = +66(20)\,\mathrm{TPa}^{-1}$, and $K_c = -4.0(6)\,\mathrm{TPa}^{-1}$. Consequently, the compressibility is negative everywhere within the (a, c)-plane, with the magnitude of NAC quantified by the corresponding area compressibility $K_{(0\bar{1}0)} = K_a + K_c = -7.5(8)\,\mathrm{TPa}^{-1}$.

Conventional engineering materials (*e.g.* iron) have linear compressibilities $K \sim 5\,\mathrm{TPa}^{-1}$ that correspond to a decrease of *ca* 0.5% in length for each 1 GPa pressure increase;[292] consequently, the NAC behaviour of Ag(*tcm*) is essentially as strong as the positive area compressibility of these 'normal' phases. Moreover, despite the fact that the orthorhombic symmetry of Ag(*tcm*) allows for different behaviour in the a and c directions, we find that both its compressibility and its thermal expansivity are essentially isotropic within the entire (a, c) plane. Isotropy is important for NAC applications because it avoids composite warping and performance breakdown.[187]

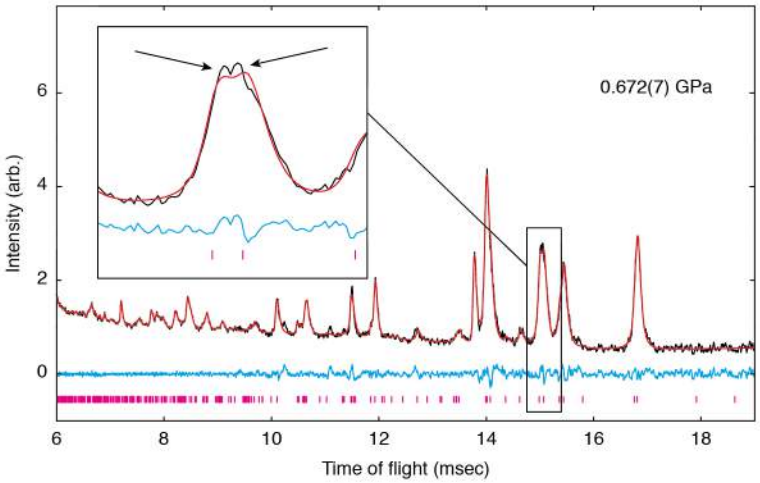

Figure 6.3: Pawley refinement of the powder neutron diffraction data for the high-pressure phase of Ag(*tcm*). Data are shown in black, the Pawley fit in red and the difference in blue. Reflections are represented by the pink tick marks. The inset graphic shows an expanded region of the pattern, indicated by the black box and the arrows show the peak splitting that is a consequence of symmetry lowering.

6.3.3 Compressibility measurements for $Ni(CN)_2$

For $Ni(CN)_2$, we collected powder neutron diffraction patterns at 8 pressure points up to 0.78 GPa at ISIS, utilising the PEARL instrument, and synchrotron X-ray diffraction powder patterns at 5 pressure points up to 2.4 GPa, using the I15 beamline at Diamond. Fits to the data are shown in Fig. 6.5 and Fig. 6.6 and lattice parameter variation in Table C.2 and Table C.3. Fig. 6.7 illustrates the results with the material showing ordinary linear compressibility in all directions, albeit much more strongly along the stacking axis than in any direction parallel to the square-grid sheets. Thermal expansion and compressibility coefficients in this paper were calculated from experimental data using the program PASCal.[198] Lattice parameters at each pressure point were determined with their variation was fitted according to a set of empirical expressions,

$$x(p) = x_0 + \alpha(p - p_c)^{\lambda}. \tag{6.1}$$

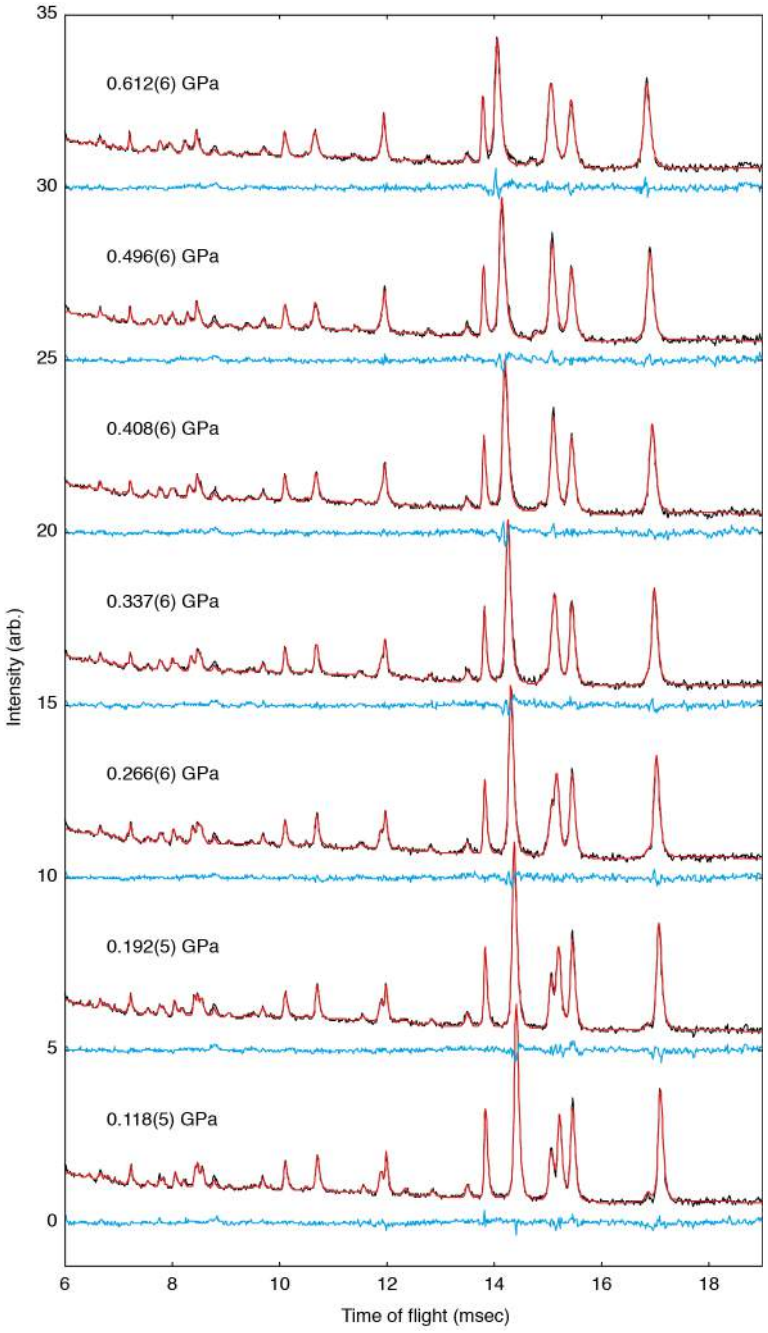

Figure 6.4: Powder neutron diffraction data (black lines), Rietveld fits (red lines) and difference curves (data − fit, blue curves) for Ag(*tcm*). Data for successive pressure points have been translated by five intensity units.

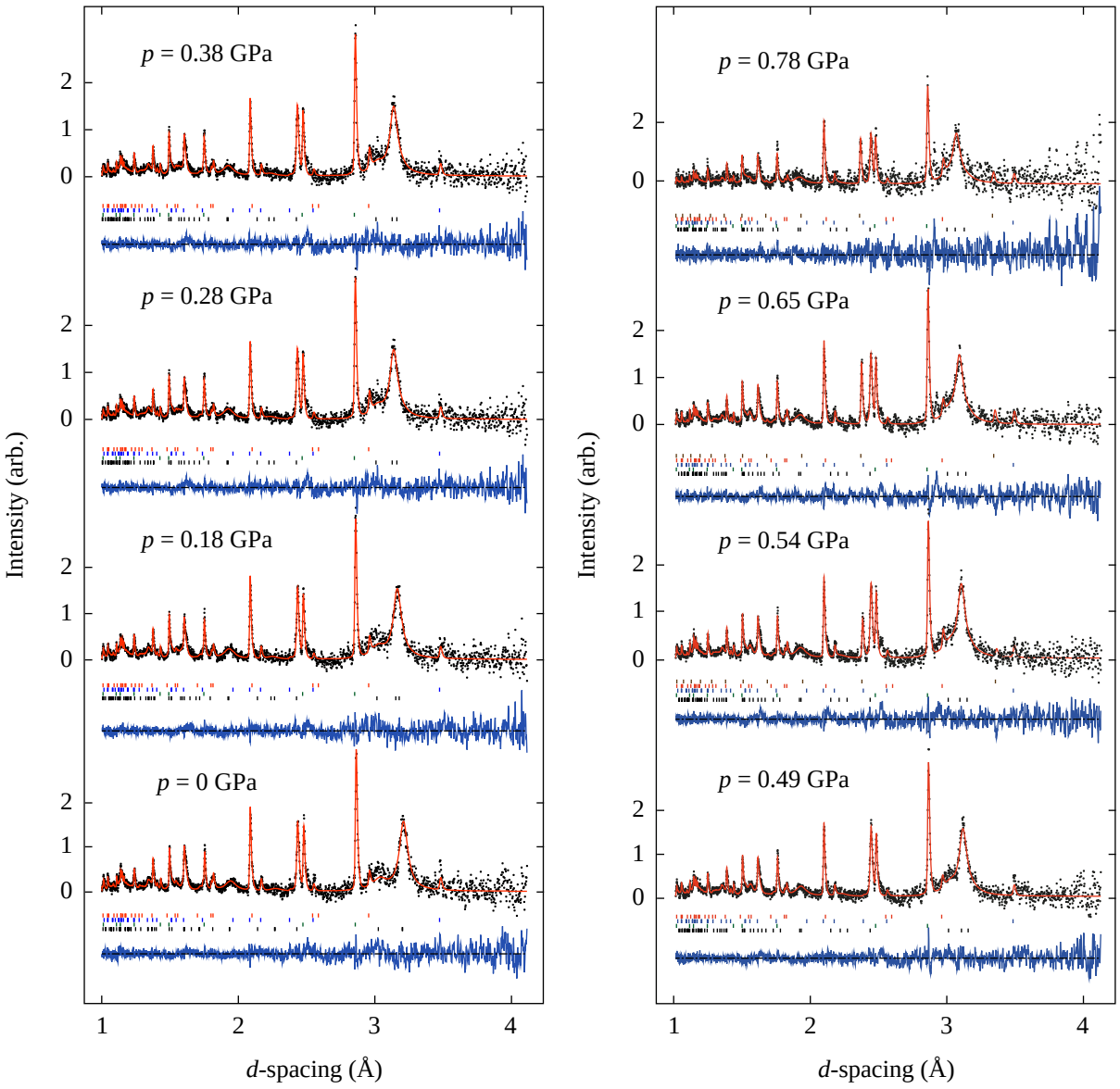

Figure 6.5: GSAS fits (red) to powder neutron diffraction data (black), with difference curves (data−fit) shown in blue for $Ni(CN)_2$.

Error-weighted fits to the lattice parameters enabled calculation of a smooth compressibility curve for each direction in the lattice. The pressure dependence of the unit cell volume was fitted well by a third-order Birch-Murnaghan equation of state.[293] The mean values for linear compressibilities were $K_a = 2.0(20)\,\mathrm{TPa}^{-1}$ and $K_c = 46.3(18)\,\mathrm{TPa}^{-1}$ [Fig. 6.7(b)]. The Birch-Murnaghan fit results in a bulk modulus of

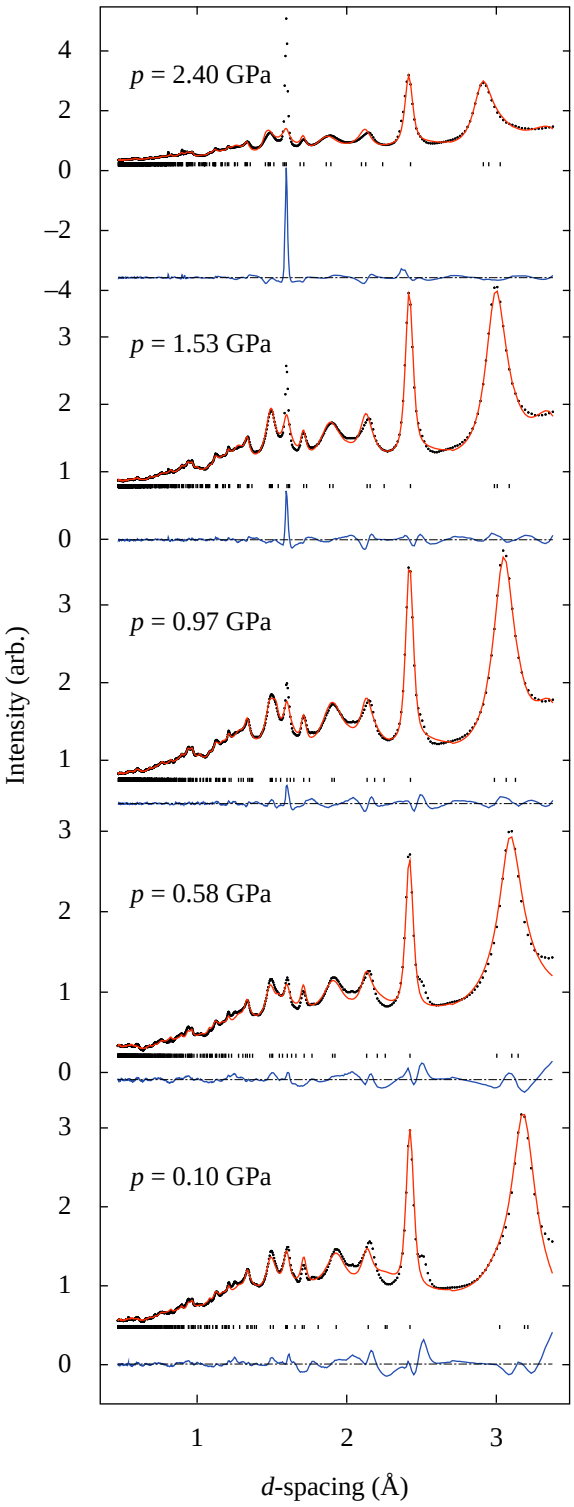

Figure 6.6: GSAS fits (red) to powder synchrotron diffraction data (black), with difference curves (data−fit) shown in blue for $Ni(CN)_2$.

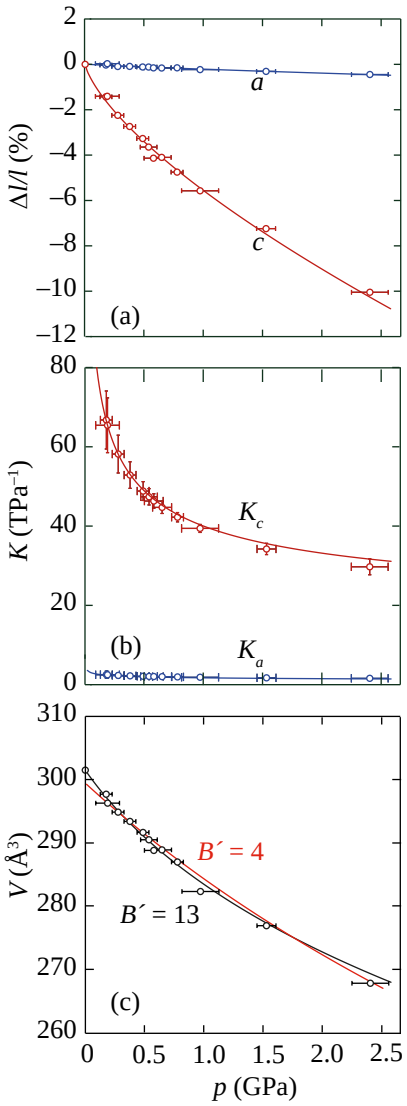

Figure 6.7: (a) Pressure-dependence of the lattice parameters of $Ni(CN)_2$ using powder neutron diffraction and synchrotron radiation, (b) compressibilities extracted *via* an empirical fit (continuous lines in (b)). The data show $Ni(CN)_2$ to exhibit ordinary linear compressibility in all directions, but the material is much more compressible in the stacking direction of the square-grid layers than in any direction perpendicular to the square-grid sheets. (c) Volume per unit cell for $Ni(CN)_2$. The continuous black line indicates the third-order Birch-Murnaghan fit and the continuous red line shows the the second-order Birch-Murnaghan fit, respectively.

B_0 = 11.2(13) GPa and its first pressure derivative of B' = 13(20) [Fig. 6.7(c)]. Examples of bulk modulus values for other known materials are 6.6 GPa for $Ru_3(Co)_{12}$, 25 GPa for NaCl, 37 GPa for quartz and 440 GPa for diamond and comparing these these values to this system suggests that $Ni(CN)_2$ is initially very soft and becomes harder rapidly upon pressure.[294] Additionally, we see phase change in the structure of $Ni(CN)_2$. In this work, we are interested in the compressibility behaviour of $Ni(CN)_2$ itself, however, indexing this phase change with a structure will form part of the future work of the research group.

6.4 Origin of compressibility and thermal expansion behaviour in Ag(*tcm*)

The microscopic mechanism responsible for area-NTE and NAC can be deduced from the variation in framework geometry during heating. The established model of area-NTE in layered materials predicts coupling between NTE and the extent of layer 'rippling', as quantified by the inter-network torsion angle θ [Fig. 6.10].[295] A graphical representation of the relationship between the inter-network torsion angle θ and the Ag(*tcm*) crystal structure is given in Fig. 6.8. Straightforward trigonometric analysis leads to:

$$\tan\left(\frac{\theta}{2}\right) = \frac{2(y_{N2} - \frac{1}{2})b}{c}, \tag{6.2}$$

$$\theta = 2\tan^{-1}\left[\frac{2(y_{N2} - \frac{1}{2})b}{c}\right]. \tag{6.3}$$

This expression is used to calculate the values of θ given in Tables B.11 and B.12, and plotted in Fig. 6.2(b)(d).

To calculate the required coefficients of thermal expansion from the values θ, we make use of the geometric relationship illustrated in Fig. 6.9. The length r is considered

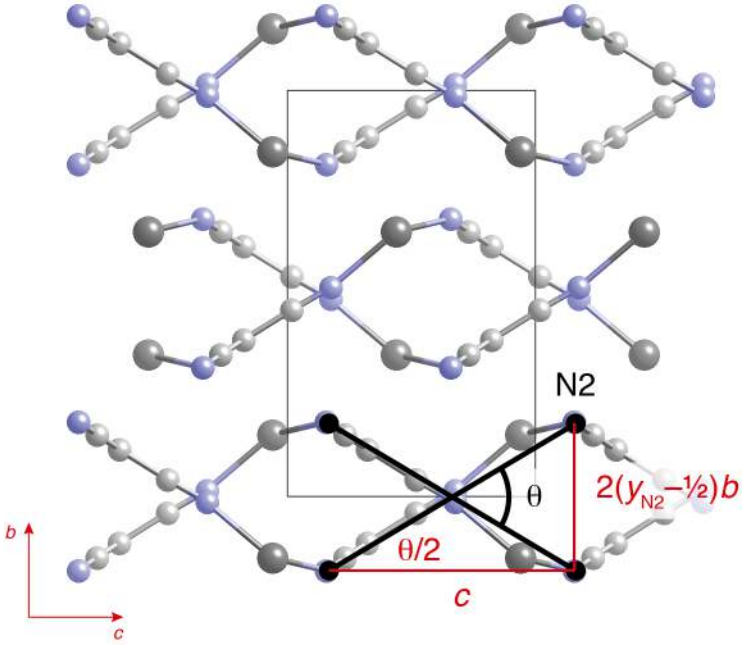

Figure 6.8: Geometric relationship used to determine the inter-network torsion angle θ. This representation of the crystal structure of Ag(*tcm*) is viewed down the a crystal axis. The four atoms covered by large black circles are all nitrogen N2 atoms.

constant with respect to temperature and/or pressure (*i.e.*, the bond lengths within the honeycomb lattice of Ag(*tcm*) are considered temperature-/pressure-independent. We then have

$$\ell = r\cos\left(\frac{\theta}{2}\right), \tag{6.4}$$

$$\frac{\mathrm{d}\ell}{\mathrm{d}T} = -r\sin\left(\frac{\theta}{2}\right)\cdot\frac{1}{2}\frac{\mathrm{d}\theta}{\mathrm{d}T}. \tag{6.5}$$

Hence

$$\alpha_A = \frac{2}{\ell}\frac{\mathrm{d}\ell}{\mathrm{d}T} = -\frac{r\sin\left(\frac{\theta}{2}\right)}{r\cos\left(\frac{\theta}{2}\right)}\cdot\frac{\mathrm{d}\theta}{\mathrm{d}T} \tag{6.6}$$

$$= -\theta\tan\left(\frac{\theta}{2}\right)\alpha_\theta, \tag{6.7}$$

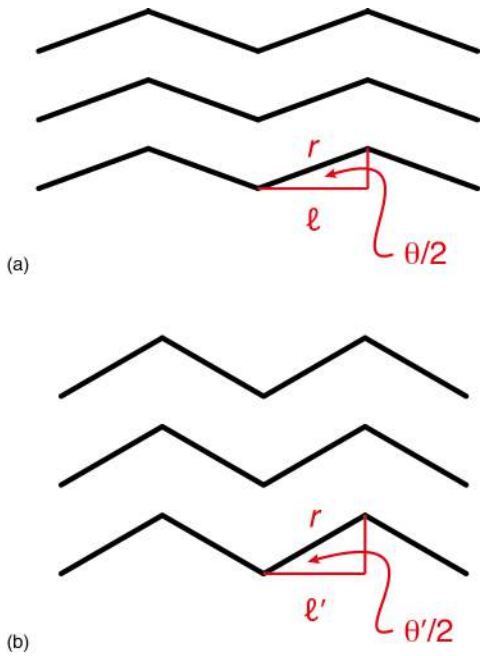

Figure 6.9: Geometric relationship used to derive equations of relating coefficients of thermal expansion and compressibility for Ag(*tcm*)]. This is a schematic representation of a puckered, layered, system in two states (*e.g.*, temperatures or pressures) (a) and (b). The total layer area, which is proportional to r^2, is conserved in both states; the deformation mechanism involves a change in the puckering angle $\theta/2$ (the factor of two included for consistence with the derivation of derivatives of the equations). The corresponding change in cross-sectional length ℓ can be used to relate the rate of change of θ to a corresponding area coefficient of thermal expansion α_A or area compressibility K_A.

as required, where $\alpha_\theta = \mathrm{d}(\ln\theta)/\mathrm{d}T$. The analogous expression for compressibility is

$$K_A = -\theta \tan\left(\frac{\theta}{2}\right) K_\theta \tag{6.8}$$

can be derived using the same approach.

Therefore temperature dependence of θ can be used to estimate the value of α_A attributable to layer rippling: our data give $\alpha_A^{\mathrm{calc}} = -101\,\mathrm{MK}^{-1}$, which is within ex-

perimental error of the observed value of $-102(3)\,\mathrm{MK}^{-1}$. Consequently, we can be confident that the mechanism illustrated in Fig. 6.10(c) is responsible for area-NTE in Ag(*tcm*).

That NAC is driven by the same layer-rippling mechanism as area-NTE and is evident in the variation of the parameter θ with increasing pressure [Fig. 6.2(d)]. The volume reduction accommodated by rapid collapse of the interlayer spacing (note $K_b \gg 5\,\mathrm{TPa}^{-1}$) evidently couples with a reduction in the degree of layer rippling: $\mathrm{d}\theta/\mathrm{d}p < 0$. To substantiate further our interpretation of the NAC mechanism, the recasted Eq. (6.7) in terms of compressibilities gives K_A^{calc} =-26 TPa^{-1}. That the measured area compressibility $K_{(010)}$ =-7.5(8) TPa^{-1} is somewhat smaller in magnitude reflects the expected $\sim$10 TPa^{-1} contribution from (positive) bond compressibilities omitted from the geometric formalism of Eq. (6.7), as discussed elsewhere for NLC materials.[288] Indeed, that the p/T correspondence inferred in Fig. 6.10(c) holds qualitatively for Ag(*tcm*) is immediately evident in the close relationship between the temperature- and pressure-induced lattice parameter and layer rippling parameter variations documented in Fig. 6.2.

6.5 Origin of compressibility and thermal expansion behaviour in $Ni(CN)_2$

Area-NTE of $Ni(CN)_2$ has previously been discussed in terms of its calculated phonon modes.[157] The five lowest frequency dispersionless phonon modes contribute to area-NTE within the sheets of $Ni(CN)_2$, resulting in reduction of the interlayer Ni...Ni distances. The lowest three of these phonon modes involve vibrations perpendicular to the layers and can be interpreted in terms of the 'rippling' mechanism — resulting in an increased interlayer separation and smaller effective layer area — and drive the large linear PTE perpendicular and the area-NTE parallel to the sheets [Fig. 6.11(a)]. The remaining two phonon modes are in the plane of the $Ni(CN)_2$ layers and involve

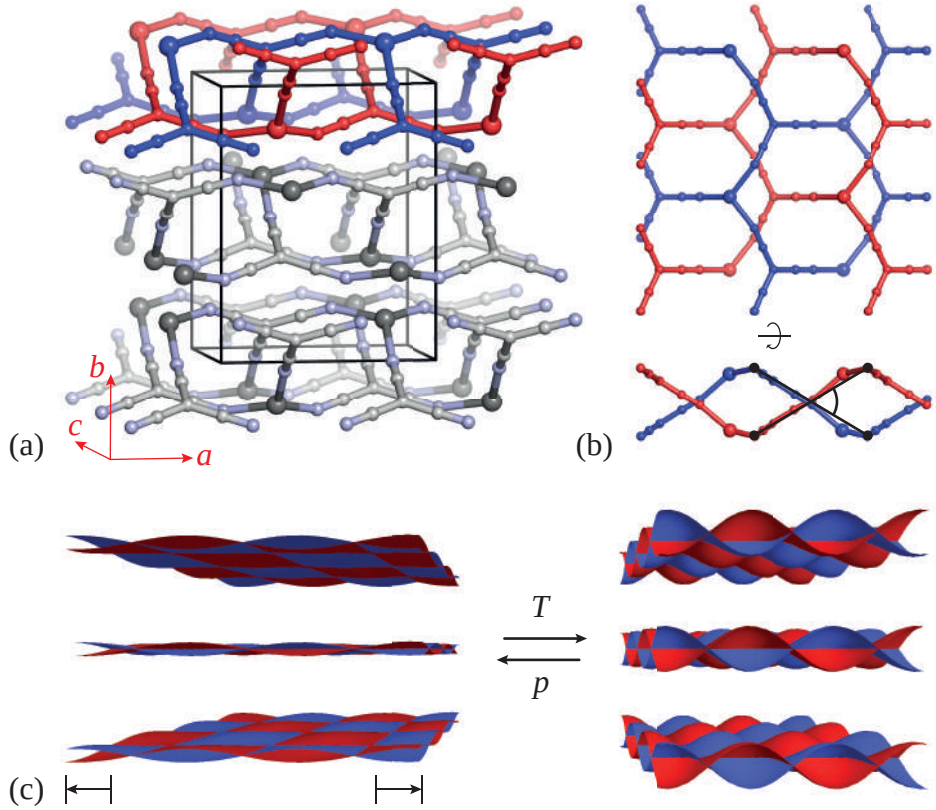

Figure 6.10: (a) The crystal structure of Ag(*tcm*) is composed of stacked, doubly-interpenetrating (6,3)-nets in which both Ag^+ (large spheres) and tcm^- ions (smaller spheres) function as trigonal nodes. (b) The extent of rippling of layers (viewed along $\boldsymbol{b}$ and a in the top and bottom parts of this panel, respectively) can be quantified by the inter-network angle θ. (c) The generic mechanical response of a layered material links volume expansion to increasing interlayer separation and increasing layer rippling. The cross-sectional area of each layer is maximised by reducing θ, and hence increases during volume reduction under hydrostatic compression.

transverse vibrations of the Ni—CN—Ni linkages and contribute to area-NTE with increasing temperature [Fig. 6.11(b)].

In order to justify the observed ordinary compressibility behaviour in all directions, we take a look at the dispersionless phonon modes under pressure. Similarly to Ag(*tcm*), 'rippling' of the layers — resulting from the phonon modes in Fig. 6.11(a) — would result in NAC in $Ni(CN)_2$. On the contrary, the dominance of the phonon modes in Fig. 6.11(b) would lead to ordinary compressibility behaviour and a decrease in the effective layer area. The resulting compressibility behaviour is determined by the combined effect from these two sets of phonon modes. As ordinary compressibility is observed within the sheets, the in-plane phonon modes must obtain a dominant effect under pressure. This can be justified by drawing comparisons to similar layered systems that are made of layers of a thickness of single atoms, *e.g.* hexagonal boron nitride and graphite, and their Grüneisen parameter, which relates the change in phonon frequencies to the change in volume. The Grüneisen parameter is given by the formula

$$\gamma_i = -\frac{V}{\omega_i}\frac{\partial \omega_i}{\partial V}, \tag{6.9}$$

and is known to be negative within the layers for hexagonal boron nitride and graphite. By virtue of structural similarity, assuming a negative Grüneisen parameter for $Ni(CN)_2$ within the sheets would lead to an increase in the vibrational energy of the in-plane phonon modes when the systems's volume is decreased. Thus, these phonon modes gain energy and become more populated under increasing hydrostatic pressure.

We can visualise the effect of the in-plane phonon modes by considering the in-plane rigid unit modes. With increasing pressure, the RUMs tilt, leading to a decrease in the effective layer area. As discussed before, this is opposed by 'rippling' of the layers with tilting of the RUMs a more dominant effect under hydrostatic pressure [Fig. 6.12].

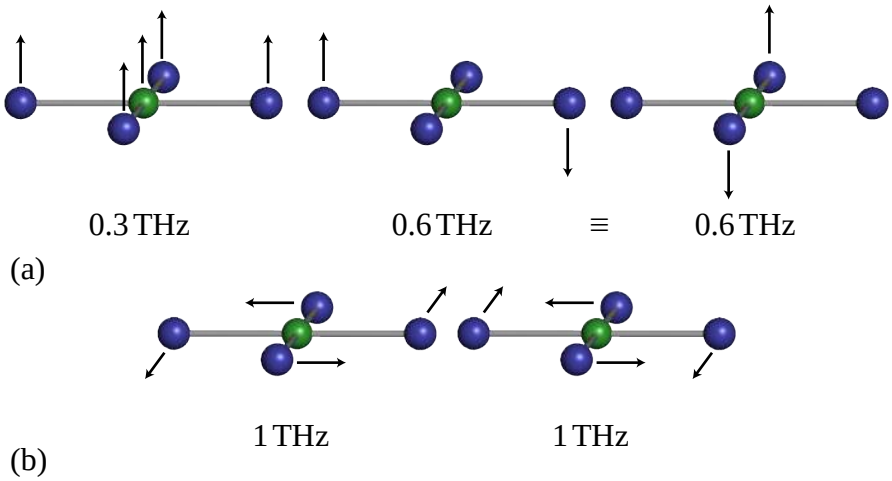

Figure 6.11: (a) Three lowest energy phonon modes in $Ni(CN)_2$ contributing to 'rippling of the layers' and (b) phonon modes involving transverse vibrations of the Ni−CN−Ni linkages that decrease the effective layer area of the system (Adapted from Ref. 157).

6.5.1 Negative Grüneisen parameter within the layers

To further justify the assumption of a negative Grüneisen parameter for $Ni(CN)_2$, a more thorough comparison to boron nitride and graphite is undertaken. Table 6.1 shows variable temperature and pressure data for $Ni(CN)_2$, hexagonal boron nitride, graphite, and for the two phases of the colossal thermal expansion material $Ag_3[Co(CN)_6]$. The latter serves as a useful example of a framework material for comparison. From these data, it is clear that all the layered systems show area-NTE parallel to the sheets and PTE perpendicular to this direction. Contrary to the framework material $Ag_3[Co(CN)_6]$, which exhibits NLC along the same crystallographic direction as it shows NTE behaviour, the layered structures show ordinary compressibility within the sheets.

To justify the latter, we take a look at the thermodynamic formalisms that was discussed in the introduction and that relates thermal expansion to a material's compressibility in anisotropic materials, which omitting shear terms, can be written by the

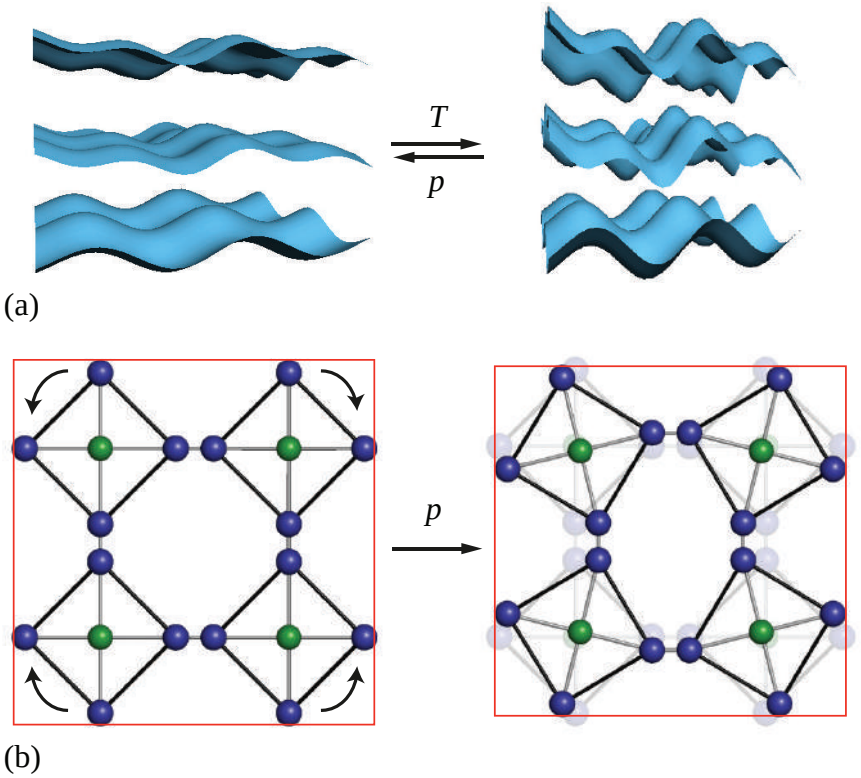

Figure 6.12: (a) 'Rippling' of the $Ni(CN)_2$ layers, which contributes to area-NTE within the sheets and PTE perpendicular to the layers with increasing temperature and NAC within the sheets and ordinary compressibility perpendicular to the layers with rising pressure and (b) 'tilting' of the $Ni(CN)_2$ RUMs within the sheets, contributing to NTE and ordinary compressibility within the layers. The RUMs in (b) dominate the material's compressibility behaviour.

equation:

$$\alpha_i = \frac{C_T}{V} \sum_j S_{ij} \gamma_j, \tag{6.10}$$

where C_T is the isothermal specific heat, V the unit cell volume, $S_{i,j}$ the elastic compliances, and γ_j the components of the anisotropic Grüneisen function (weighted sums over the anisotropic Grüneisen mode parameters).[141] For the layered structures discussed in this paper, two values of the thermal expansion coefficient and compressibility tensor need to be considered, one perpendicular to and one parallel to the layers. For

Table 6.1: Thermal expansion and compressibility data for layered materials (boron nitride, graphite and nickel(II) cyanide) and for the two phases of the colossal NTE and NLC material $Ag_3[Co(CN)_6]$, denoted I and II, with I the phase at ambient conditions and II the high pressure phase.

Structure	α_a (MK^{-1})	α_c (MK^{-1})	K_a (TPa^{-1})	K_c (TPa^{-1})	B (GPa)	B'	Ref.
$Ni(CN)_2$	−6.5(1)	61.8(3)	2.0(2)	46.3(2)	11.2(13)	13(2)	156
Graphite	−1.20(10)	28.0(16)	0.80(3)	28.0(2)	33.8(3)	8.9(10)	141,142,296
hBN	−2.73(8)	38.0(11)	0.457(5)	11.9(3)	17.27(12)	3.33(2)	144,297
I	140.0(1.1)	−124.5(4)	115(8)	−76(9)	6.5(3)	-	160,298
II	13.3(25)	−23(3)	15.2(9)	−5.3(3)	11.8(7)	13.5(12)	298

each of these directions Eq. (6.10) can be rewritten as

$$\alpha_a = \frac{C_T}{V}(K_a\gamma_a + S_{i3}(\gamma_c - \gamma_a)), \tag{6.11}$$

$$\alpha_c = \frac{C_T}{V}(K_c\gamma_c - 2S_{i3}(\gamma_c - \gamma_a)). \tag{6.12}$$

Table 6.2 gives the literature values for S_{i3} and the Grüneisen parameters for graphite and hexagonal boron nitride: S_{i3} is negative for hexagonal boron nitride and graphite, whereas γ_a is negative and γ_c positive. Taking these values into account, both the first and the second term on the right-hand side of Eq. (6.11) are negative and contribute to an overall NTE in the direction parallel to the layers as is experimentally observed. For Eq. (6.12), both terms contribute to positive thermal expansion perpendicular to the layers. Similar considerations are thought to apply in the case of $Ni(CN)_2$.

Table 6.2: Elastic compliance tensor S_{i3} and Grüneisen parameter values for layered graphite and hexagonal boron nitride.

Structure	S_{i3}	γ_a	γ_c	Reference
Graphite	-0.3	-0.97	0.44	[141]
hBN	-0.097	-1	0.4	[299]

6.6 Summary

In summary, we find that silver(I) tricyanomethanide exhibits area negative thermal expansion between 100 K and 250 K and negative area compressibility over the pressure range $0 < p < 0.612$ GPa with an essentially isotropic area thermal expansion and isotropic compressibility of similar magnitude (but opposite sign) to that of established engineering materials. From a structural viewpoint, these phenomena can be understood in terms of pressure- and temperature-driven layer 'rippling' that acts to decrease the layer cross-sectional area with increasing temperature and decrease the effective layer area at larger hydrostatic pressures. Variable-pressure and temperature spectroscopic measurements may provide valuable additional insight into the subtle variations in bonding interactions that occur throughout this process.[300] In favour of immediate application of Ag(*tcm*) in ultra-high-precision sensing devices are (i) the ease with which large single-crystal samples can be prepared under ambient conditions and using readily-available solvents, and (ii) its optical transparency. Moreover, the polarity of its crystal structure offers the possibility of designing multifunctional devices based on Ag(*tcm*) in which the interplay between responses to electric field, temperature, and pressure are exploited to produce piezoelectric and thermoelectric devices. Furthermore, we have demonstrated that the layered structure $Ni(CN)_2$ possesses ordinary compressibility behaviour in the direction of its layers. This can be justified by a negative Grüneisen parameter within the sheets, which means that the in-plane phonon modes dominate the material's compressibility behaviour. This con-

trasts to Ag(tcm), where 'rippling' of the layers leads to negative area compressibility.

Chapter 7

Expanding into 3D — doped $Ni(CN)_2$

7.1 Overview

Nickel(II) cyanide has a square planar layered structure that arises from the d^8 electron configuration of the metal and the respective crystal field stabilisation energy [Fig. 7.1(b)]. In this chapter, we aim to dope nickel(II) cyanide with other transition metals to increase the dimensionality of the structure. Transition metal cations that would allow for tetrahedral or octahedral geometry could potentially connect the 2D layers in nickel(II) cyanide and enforce a 3D topology. The first transition metal we investigate is copper(II) that has a characteristic d^9 electron configuration. We find that the structures containing copper(II) remain square planar and a justification for this is given in this chapter. The second transition metal we explore is cobalt(II) with d^7 electron count and we do indeed show that an evolution to a 3D structure is seen with increasing cobalt(II) doping levels.

7.2 Background

In transition metal compounds, crystal field stabilisation plays an important role in determining the arrangement of the ligands around the metal centre [Fig. 7.1(a)(b)]. The most common coordination environment for transition metals is octahedral, where the five d-orbitals are divided into a set of three degenerate low-lying t_{2g} orbitals and two degenerate higher orbitals, e_g. This stems from the fact that some of the d-orbitals feel the effects of the ligand electrons much more strongly than others. In an octahedral crystal field, the d_{z^2} and $d_{x^2-y^2}$ orbitals experience stronger electron repulsion from the electrons of the ligands than the d_{xy}, d_{xz} and d_{yz} orbitals as the former point directly towards the ligands, which leads to the arrangement of d-orbitals discussed above. However, towards the end of the first row, four-coordinate transition metal centres are known, including d^7 to d^{10} electron configurations for metal cations cobalt(II), nickel(II), copper(II), copper(I) and zinc(II). The possible geometries are tetrahedral and square planar, with their respective d-orbital splitting given in Fig. 7.1(b).

The respective ligands can in general be classified into two groups: weak field ligands and strong field ligands. For strong field ligands, there are strong σ-donating and π-accepting effects between the ligand and the metal centre, which makes the relative splitting between the d-orbitals particularly large, whereas weak field ligands split the d-orbitals to a lesser extent. The nature of these ligands can directly determine the coordination environment around the metal cations. For the metal centres described above, there is competition between octahedral, tetrahedral and square planar geometries. The relative crystal field splitting of d-orbitals is shown in Fig. 7.1(b). It is noted here that d^{10} is a particular case where all the d-orbitals filled with pairs of electrons and therefore there is no additional crystal field stabilisation energy. This implies that if the metal centre is coordinated by four ligands, the four ligands will arrange themselves to be as far as possible and hence a tetrahedral coordination environment is achieved.[301]

For octahedral complexes, there is only one possibility of filling the orbitals for d^8 and

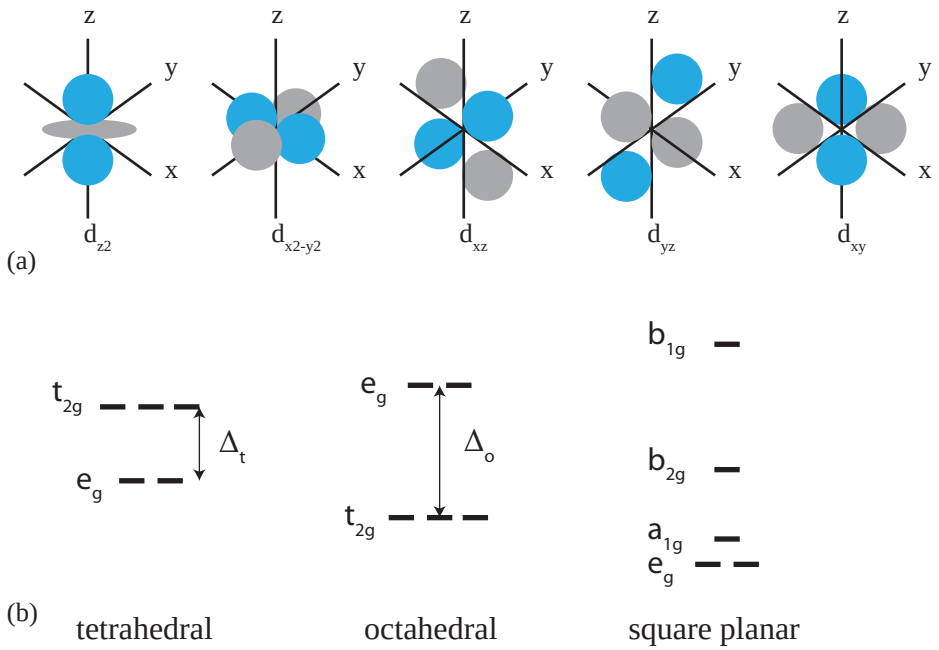

Figure 7.1: (a) The five d-orbitals, (b) tetrahedral, octahedral and square planar crystal field splitting diagrams.

d^9 electrons, whereas d^7 complexes can be either low-spin or high-spin, depending on the relative crystal field splitting and the nature of the ligand. If the splitting between the t_{2g} and the e_g orbitals is small, as is the case for weak field ligands, a high-spin d^7 complex is obtained, where all orbitals are filled with one electron at first and then the remaining two electrons are paired with other electrons in the low-lying t_{2g} orbitals. If the splitting between the t_{2g} and the e_g orbitals is large, as is true for strong field ligands, a low-spin complex is achieved, where the t_{2g} orbitals are filled first with pairs of electrons and only then the e_g orbitals are filled. This results from the fact that the energy penalty for pairing electrons in the low-lying t_{2g} orbitals is smaller than the energy to raise the electrons to the e_g orbitals. The crystal field splitting for tetrahedral complexes is relatively smaller compared to octahedral complexes and therefore almost all tetrahedral complexes obtain a high-spin configuration.[301] Furthermore, square planar complexes have one high energy anti-bonding orbital. Strong field ligands make the relative splitting between the d-orbitals particularly large and would result in a low-spin square planar complex. For weak field ligands, where the anti-bonding orbital

is lower, the square planar complex is destabilised.[301]

Firstly, examining the strong field ligands with a d^7 metal centre, we can determine that square planar geometry is most stabilised as for this coordination environment only bonding orbitals are filled with electrons and the highest occupied orbital is lower in energy than for octahedral or tetrahedral geometry. The same applies to d^8 metal centres with strong field ligands.[301] Therefore cobalt(II) and nickel(II) obtain square planar geometries with strong field ligands, such as carbenes and carbon-bound cyanide.[302]

Secondly, weak field ligands with d^7 and d^8 electron configuration destabilise square planar geometry as the anti-bonding orbital is now lower in energy. Therefore, there is competition between tetrahedral and octahedral complexes and depending on the possible number of ligands and the ligand field strength, both can be achieved. The crystal field stabilisation energy is maximised for d^7 tetrahedral arrangement, where the doubly degenerate e_g set of orbitals is completely filled with pairs of electrons and the triply degenerate t_{2g} set is filled with a single electron per orbital. This is the reason why cobalt(II) has by far the most tetrahedral complexes. Thus, cobalt(II) and nickel(II) obtain tetrahedral arrangements with four weak field ligands, such as halogen anions. Specific examples include tetrachloronickelate(II) and tetrachlorocobaltate(II)[301]

Thirdly, weak field and strong field ligands can be treated together for d^9 as there is only one possibility of filling the orbitals for all geometries. With four ligands, the preferred geometry can be either square planar or tetrahedral, however, it is noted here that the crystal field stabilisation energy for tetrahedral coordination for d^9 electron configuration is only $2/5\Delta_t$ and is therefore very small. Consequently copper(II) can adapt a square planar structure even with weak field ligands.[301]

It is noteworthy that a structure based on nickel(II) and zinc(II) adopts a 3D framework geometry with the nickel(II) cations square planar and the zinc(II) pseudo-tetrahedral with the θ angle shown in Fig. 7.2 equal to 110.43°.[303]

Zinc(II) has d^{10} electron configuration and hence there is no crystal field stabilisation with respect to coordination geometry. Thus, we hypothise that in this structure the structural geometry is governed by the preference for square planar geometry of

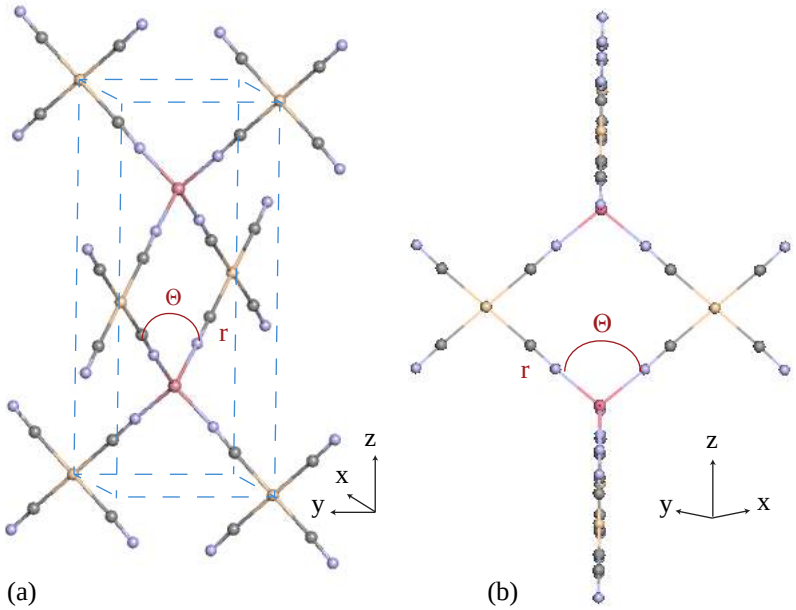

Figure 7.2: (a) Structure of $ZnNi(CN)_4$ and (b) showing the angle θ in the structure. We suggest here that the $CoNi(CN)_4$ is similar to this established structure (Adapted from Ref. 303).

nickel(II) and the optimal distribution of the ligands in space around the zinc(II) cation.

Our hope was to establish whether cobalt(II) and copper(II) would remain square planar in the nickel(II) cyanide structure. The main contribution from the cyanide highest occupied molecular orbital (HOMO) and the lowest unoccupied molecular orbital (LUMO) is from the carbon of the ligand. Therefore a carbon-bound cyanide is a strong field ligand allowing for good σ-donation and π-backbonding. A nitrogen-bound cyanide is poorer for both of these bondings due to smaller contributions to the HOMO and LUMO of the cyanide ion from the nitrogen orbitals and is therefore a weaker field ligand. As discussed above, we would expect copper(II) to remain square planar for both weak field and strong field ligands and it is therefore anticipated that copper(II) remains square planar in the nickel(II) cyanide structure, irrespective of whether it is bound to the carbon or the nitrogen of the cyanide. For cobalt(II) there are three options: firstly, if cobalt(II) is bound to the nitrogen of the cyanide, the doped metal

can be in a tetrahedral coordination environment due to a weak field ligand; secondly, if cobalt(II) is carbon-bound to the cyanide via ligand exchange (the synthesis starts with potassium tetracyanonickelate(II), where nickel is carbon-bound to the cyanide), the structure could remain square planar due to a strong field ligand; and thirdly, it can be the case that some cyanides are carbon- and some nitrogen-bound. We start this chapter by exploring various doping levels of copper(II) and then cobalt(II) into nickel(II) cyanide and the evolution of the structures.

7.3 Structural effect of doping copper(II) and cobalt(II) into nickel(II) cyanide

Samples of doping Cu^{2+} into $Ni(CN)_2$ were prepared in 5% doping increments from 0% of Cu^{2+} to 50% of Cu^{2+}. The samples were characterised at room temperature with PXRD measurements. These results are illustrated in Fig. 7.3. It is noted here that based on previous structural studies, the first peaks in these diagrams refers to the (002) and the second peak to the (110) reflections and therefore the former corresponds to the interlayer and the latter to intralayer separation.[156] It is clear from the data that the peak corresponding to the interlayer separation moves towards smaller interlayer separation gradually with an increasing doping level. Furthermore, the peak corresponding to the M—CN—M distances remains about constant up to 15% of Cu^{2+} and then a phase change occurs, where a new peak at larger distances gradually grows with increasing doping level. This is thought to result directly from the d^9 electron configuration, which remains square planar. The d^9 metal centre is more electron rich, which decreases σ-donating from the ligand anti-bonding σ^*-orbital and increases backbonding to the ligand π^*-orbital — both of which result in increased electron density in ligand anti-bonding orbitals and hence longer ligand bond lengths. The most significant result is that copper(II) remains square planar as is expected for a d^9 metal centre both with four weak field and four strong field ligands.

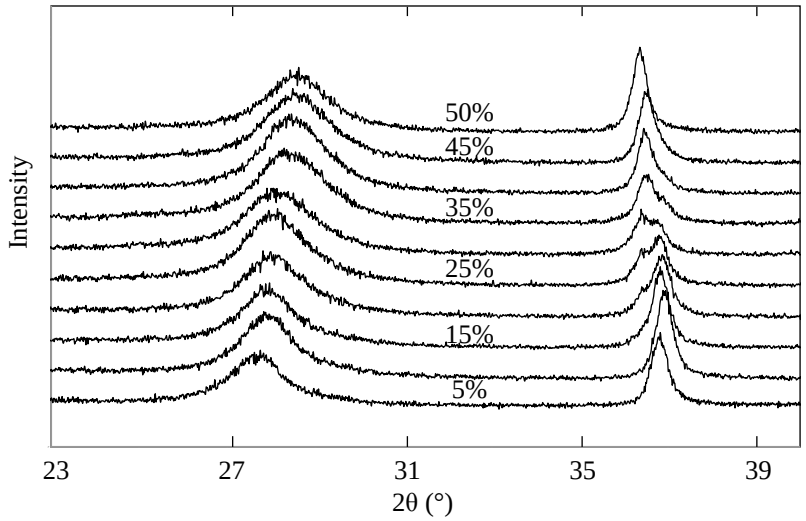

Figure 7.3: The evolution of PXRD patters for copper(II) doping into nickel(II) cyanide with increasing doping level.

Samples of doping Co^{2+} into $Ni(CN)_2$ were prepared in 5% doping increments from 0% of Co^{2+} to 50% of Co^{2+}. These results are illustrated in Fig. 7.4(a). It is clear from these data that the $Ni(CN)_2$ layered topology is stable up to 15% doping level, whereafter a phase change occurs. Samples containing cobalt(II) show fluorescence with traditional copper X-rays and hence the powder patterns are not easily indexed. Based on these data, we suggest here that the samples with doping level of 25% of Co^{2+} and 50% of Co^{2+} are structures in their own right and the intermediate concentrations are a mixture of these two phases. The alternative possibility is a complete mixing of cobalt and nickel cations in the structure with only one structure per composition. The data in Fig. 7.4(b) is the same PXRD data for a smaller data range and the pattern for 25% of Co^{2+} contains four broad peaks and the pattern for 50% of Co^{2+} contains two broad peaks. Close examination of the diffraction patterns suggest that the intermediate patterns are an evolution of one end phase to another, rather than independent structures. To certify this, we obtained fits to the data with each intermediate composition having a contribution from both end phases [red lines in Fig. 7.4(b)]. We obtained reasonably good fits and the evolution of the proportion of the 25% phase is shown in Fig. 7.5. We can indeed see that the variation of the proportion of this

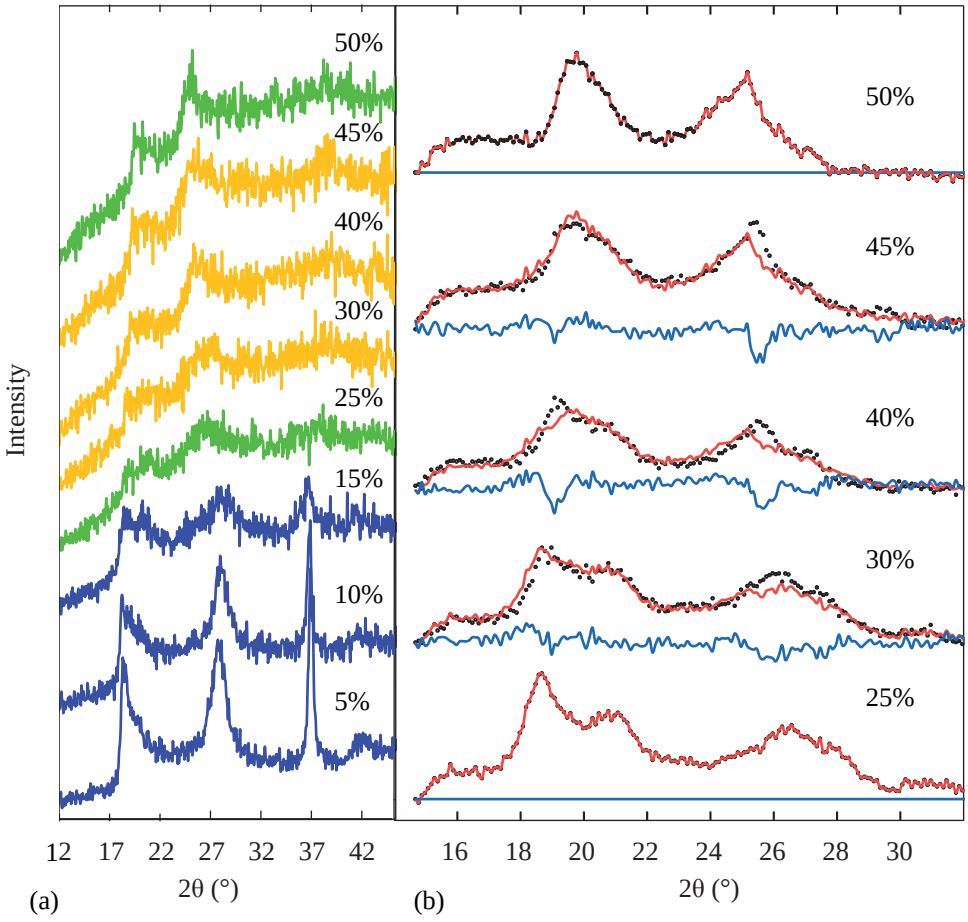

Figure 7.4: (a) Room-temperature PXRD patterns for various doping levels of Co^{2+} into $Ni(CN)_2$ across the whole doping range and (b) fits to the two component mixtures for 25% to 50% doping level. Each of the fits in (b) contain a fraction of the 25% and 50% structure. We suggest here that the samples with doping levels 50% and 25% are different structures and the intermediate concentrations are a linear mixture of these.

phase with Co^{2+} concentration is linear and hence gives credibility to our hypothesis.

7.4 Characterisation of cobalt(II) nickel(II) cyanide

We chose to characterise the $CoNi(CN)_4$ structure at room temperature in more detail due to its compositional similarity to the zinc(II) nickel(II) cyanide structure. Samples

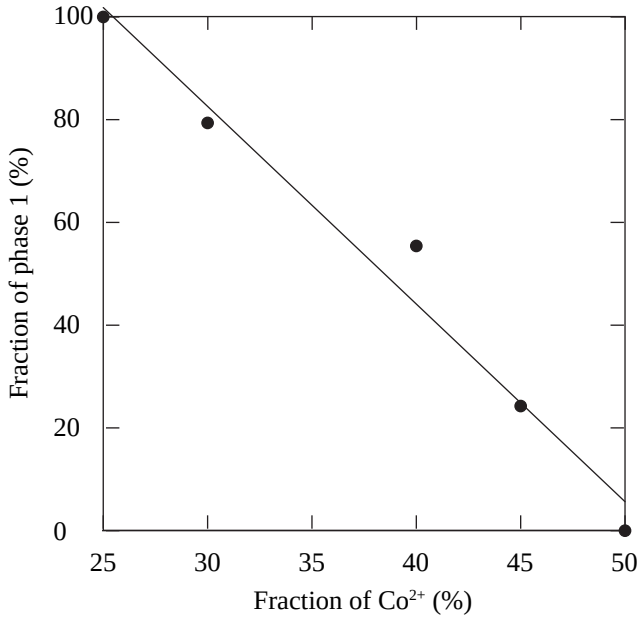

Figure 7.5: Phase fraction variation with Co^{2+} doping level for the phase with 25% of Co^{2+} cations.

containing cobalt(II) show fluorescence with traditional copper X-rays and hence we chose to characterise the structure with molybdenum radiation at room temperature, where fluorescence is avoided when cobalt(II) centres are present in the structure. The energy of molybdenum X-rays is sufficiently high not to match with differences of electron levels in cobalt(II) and hence prevent electron transitions that could result in fluorescence. The measured powder pattern has very broad peaks, suggesting the structure to be very noncrystalline. Due to the broad features in the powder pattern, a Rietveld refinement of the structure was not successful, however we proceeded to obtain a Pawley fit with TOPAS Academic.[221] The fit is shown in Fig. 7.6 and was obtained using the space group $P\bar{4}2/mcm$, which is the space group for the zinc(II) nickel(II) cyanide structure. We used 6 peak shape parameters, 2 lattice parameters for tetragonal symmetry, 2 background terms and 105 reflection intensities to obtain the fit. It is of interest that cobalt(II) is tetrahedrally coordinated in this structure. This could suggest that no ligand exchange occurs during the synthesis and cobalt(II) is bound to a weaker field ligand and hence to the nitrogen of the cyanide anion. An

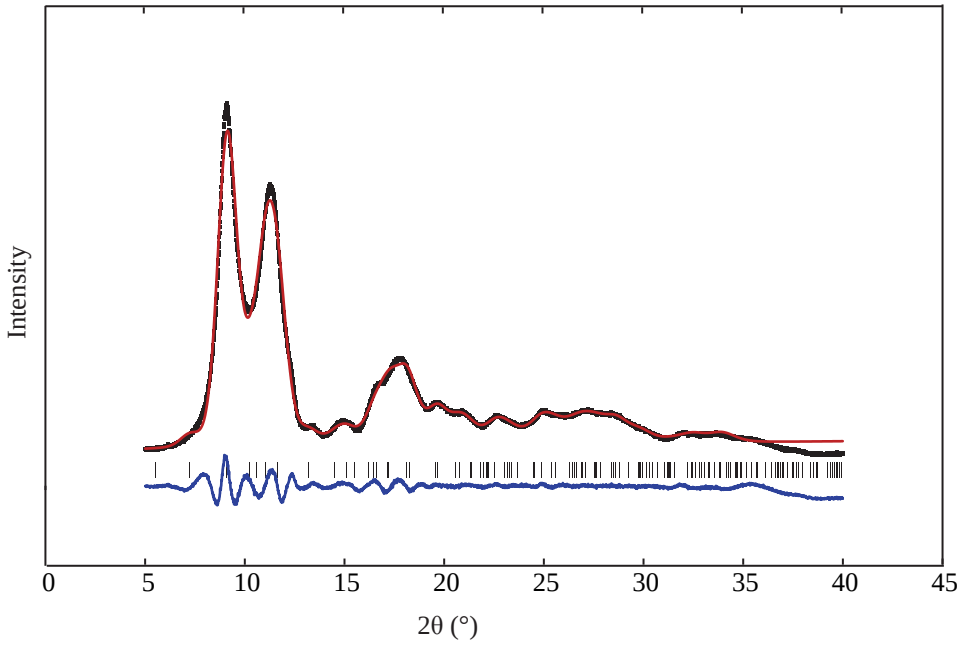

Figure 7.6: Pawley fit for cobalt(II) nickel(II) cyanide with Mo X-ray radiation.

intermediate case, where some of the cyanides are nitrogen- and some cyanide-bound to both nickel(II) and cobalt(II) is feasible.

We next measured variable temperature data for $CoNi(CN)_4$ using copper K-alpha X-rays. We used copper X-rays here as the structure was successfully determined above. We could therefore obtain lattice parameters with fitting only a few peaks that could be observed even with fluorescence. Fitting a small number of peaks would still enable us to determine the lattice parameters, since we have already obtained the structure. We calculated five different fits to these variable temperature data to find the best set of fits that represents the variable temperature data. Firstly, we obtained fits for the whole range of variable temperature data ($2\theta = 12°$—$80°$) and performed two different Pawley refinements:

Set 1 – We extracted the peak intensities from the previous room temperature sample and kept their ratios constant for the variable temperature refinements. The fits are shown in Fig. 7.7(a) and 4 background terms, 6 peak shape terms, 1 strain parameter, 1 scale parameter and 2 lattice parameters were used,

Set 2 – We kept peak shapes from the room temperature refinement constant and

allowed intensities to vary. The fits are shown in Fig. 7.7(b) and 4 background terms, 1 strain parameter, 1 scale parameter, 2 lattice parameters and 139 varying intensities were used.

Further to this, we restricted the data range (2θ = 14°—30°) and obtained the same two kind of fits described above:

Set 3 – We extracted the peak intensities from the previous room temperature sample and kept their ratios constant for the variable temperature refinements. These fits are illustrated in Fig. 7.8(a) and 4 background terms, 6 peak shape terms, 1 strain parameter, 1 scale parameter and 2 lattice parameters were used,

Set 4 – We kept peak shapes from the room temperature refinement constant and allowed intensities to vary. These fits are illustrated in Fig. 7.8(b) and 4 background terms, 1 strain parameter, 1 scale parameter, 2 lattice parameters and 66 varying intensities were used.

The lattice parameter evolution for all these fits are shown in Fig. 7.9. At first look at the data, the fits for the constant peak shape data seem better than for constant intensity data. For the latter the high-angle data is not well fitted, which we attribute to fluorescence that is particularly strong for high angles. On close examination of the peak intensities, we see that the (112) reflection intensity completely disappears for the high temperature fits for these data, where peak shapes were held constant [Fig. 7.10]. This is a direct result of the data treatment where intensities are allowed to vary and peak shapes are kept constant. Therefore we argue that the constant peak shapes fits do not represent the data well since one strong reflection completely disappear with temperature, suggesting a phase change, rather than be characteristic of thermal expansion of a single phase. We therefore conclude that constant intensity fits represent the data more accurately. Set 1, with a wide 2θ range, does not provide a good fit to the high angle data, attributed to fluorescence, and we therefore conclude that the best representation for the experimental data are the restricted range and constant intensity fits (Set 3).

Further to this, we undertook Gaussian peak shape fitting to the data, where each of

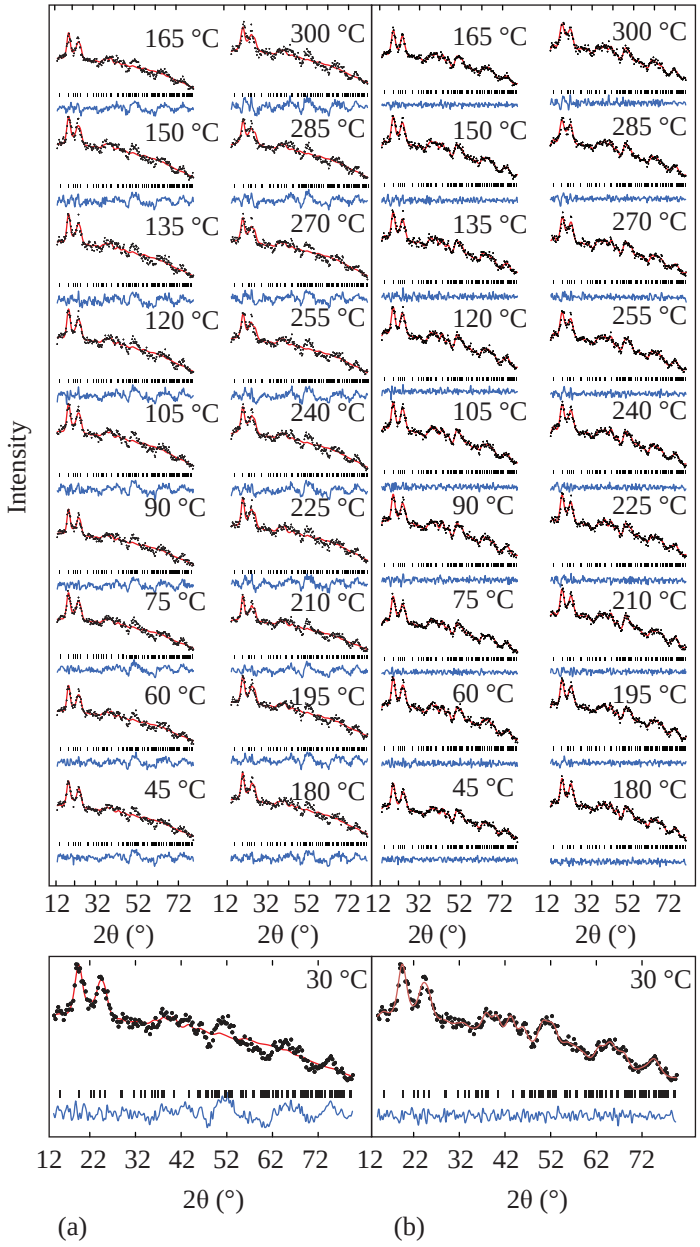

Figure 7.7: (a) Pawley fits to the data using constant intensities extracted from the room temperature Mo X-ray data and (b) using constant peak shape and allowing the intensities to vary for the whole data range.

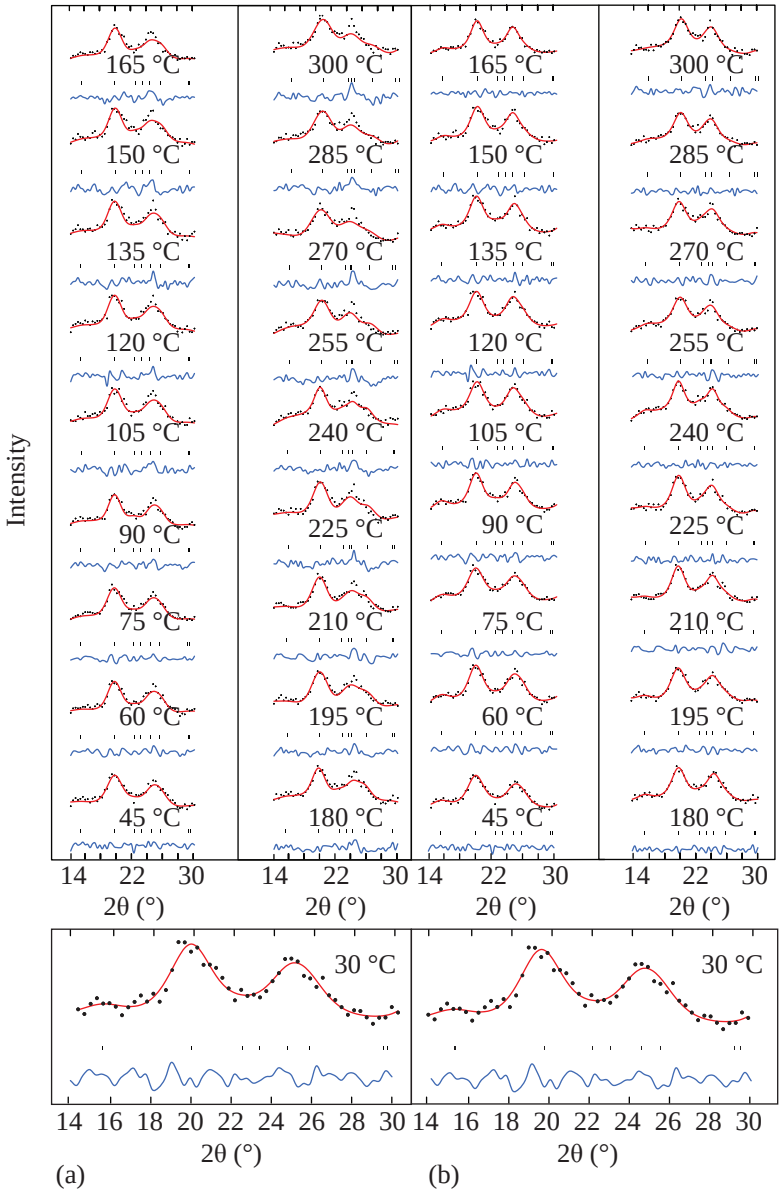

Figure 7.8: (a) Pawley fits to the data using constant intensities extracted from the room temperature Mo X-ray data and (b) using constant peak shape and allowing the intensities to vary for a restricted data range.

the two peaks in the restricted data range was fitted with a Gaussian peak (Set 5). The results are shown in Fig. 7.11 with the peaks fitted very well with this method. This is a consequence of the fact that we do not impose any structural constraints on the fits and fit the data without pre-extracted intensities or peak shapes and without a structural model.

To put the Gaussian peak fitting into context, we converted the obtained d-values into a and c lattice parameters, assuming that the two peaks in the data range $2\theta = 14°$—$30°$ corresponds to the (012) peak and the second peak to the (004) peak in the $P\bar{4}2/mcm$ model [Fig. 7.10]. These reflections have by far the highest intensity in the room temperature Mo X-ray data and are therefore thought to represent the peaks well. The results are shown in Fig. 7.9(b) and as a comparison the same graph shows the constant intensity and restricted data range results (Set 3). From both these data, we obtain similar thermal expansion coefficient using PASCal[198]. The values for the Gaussian fits are $\alpha_a = -210(10)\,\mathrm{MK}^{-1}$, $\alpha_c = 113(8)\,\mathrm{MK}^{-1}$ and $\alpha_V = -339(25)\,\mathrm{MK}^{-1}$ and for Set 3 are $\alpha_a = -220(20)\,\mathrm{MK}^{-1}$, $\alpha_c = 71(10)\,\mathrm{MK}^{-1}$ and $\alpha_V = -441(40)\,\mathrm{MK}^{-1}$. Thus, this materials shows very large area-NTE with an overall negative volume expansion. Comparing this to nickel(II) cyanide, we can see the corresponding negative thermal expansion is about 20 times larger in the structure of $CoNi(CN)_4$.

7.5 Justification for very large area-NTE for cobalt(II) nickel(II) cyanide

We examine the structure to find a justification for the very large area-NTE observed. It has been shown previously that if cobalt(II) is tetrahedrally coordinated by cyanide ligands, there are electron transitions observed in UV/VIS spectroscopy at 595 nm and 560 nm.[304] UV/VIS measurements on our samples indicate that with increasing doping of cobalt(II), we start to see these electron transitions and they are particularly strong for $CoNi(CN)_4$ [Fig. 7.12]. We therefore can conclude that the cobalt(II) cations are in

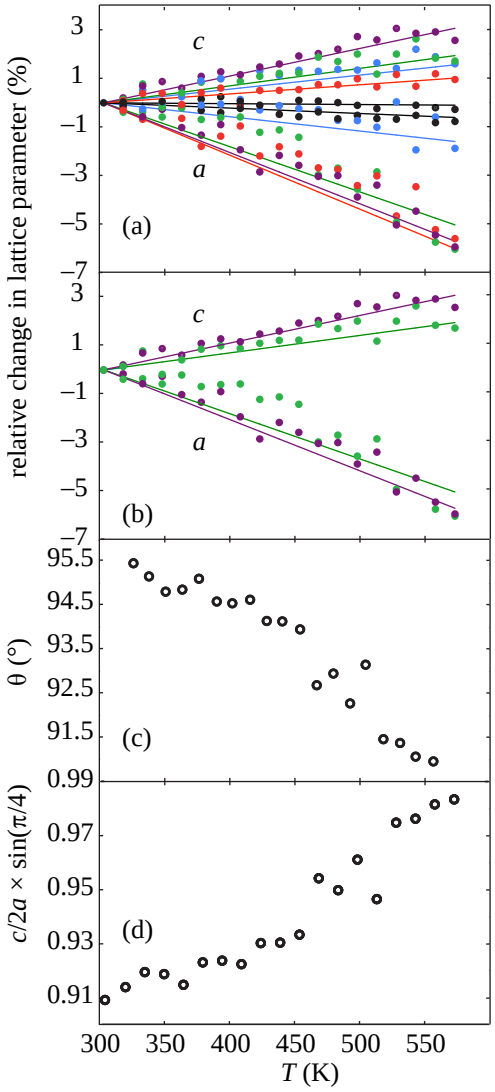

Figure 7.9: (a) Lattice parameters for all fits for $CoNi(CN)_4$ with the sets described in the main text being represented by blue for Set 1, black for Set 2, purple for Set 3, red for Set 4 and green for Set 5. (b) lattice parameter variation for constant intensity and restricted range data together with lattice parameters obtained from the Gaussian peak fitting, (c) variation of angle θ with temperature for the constant intensity and restricted range data and (d) variation of $\frac{c}{2a \sin \frac{\pi}{4}}$, a quantity that approaches 1 as θ approaches 90°,

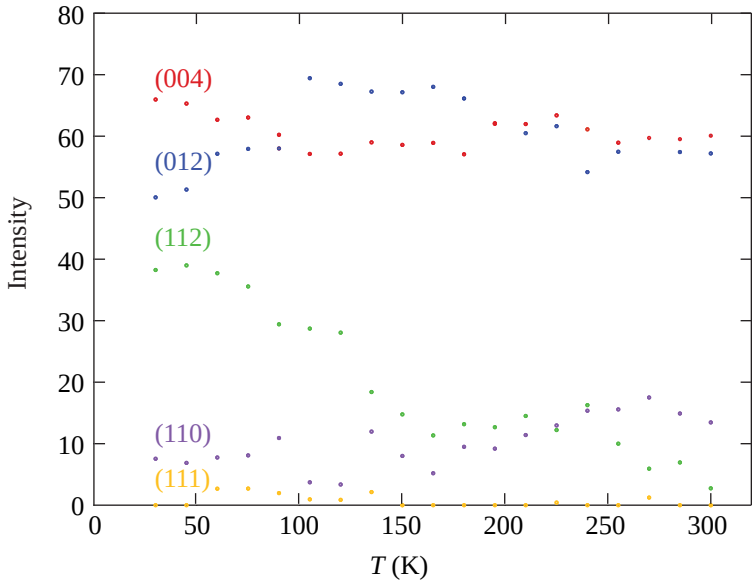

Figure 7.10: Reflection intensity variation for constant peak shape fitting with the (112) reflection intensity varying significantly with temperature.

tetrahedral coordination environments in the structure. This is in agreement with the structural model in Fig. 7.2 that we obtained a good Pawley fit for, shown previously in Fig. 7.6.

The angle θ in the structure is approaching 90° as seen from the restricted data range and constant intensity data (Set 3) [Fig. 7.9(c)(d)]. The ratio $\frac{c}{2a\sin\frac{\pi}{4}}$ relates the θ angle trigonometrically to the a and c lattice parameters and is approaching 1. Based on the structure in Fig. 7.2, we can show that the a and c lattice parameters are given by

$$a = \frac{2r}{\sqrt{2}}\sin\frac{\theta}{2}, \tag{7.1}$$

$$c = 4r\cos\frac{\theta}{2} \tag{7.2}$$

and therefore the volume of one unit cell is given by

$$V = 8r^3\sin^2\frac{\theta}{2}\cos\frac{\theta}{2}. \tag{7.3}$$

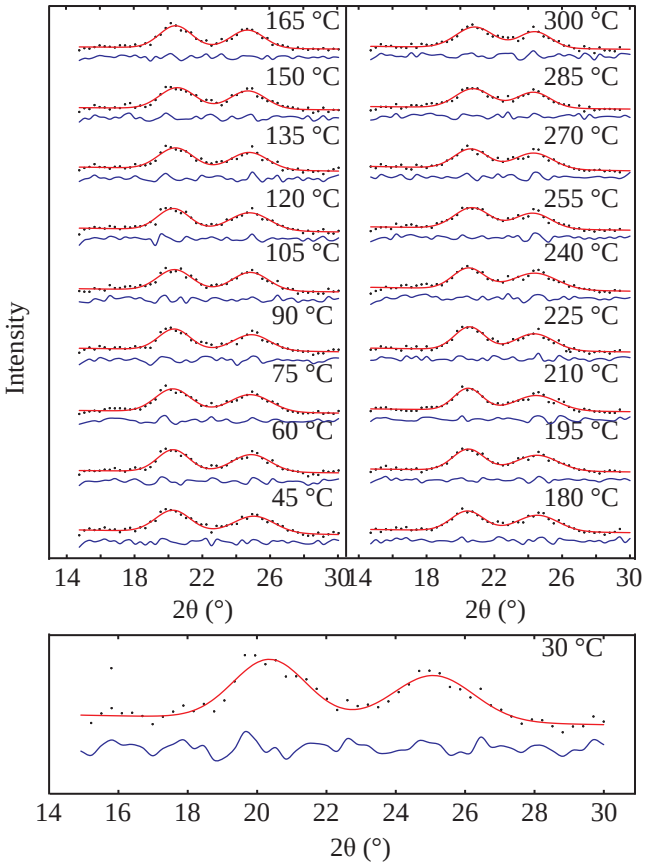

Figure 7.11: Gaussian fits to the restricted data range variable temperature PXRD data for $CoNi(CN)_4$.

It is assumed here that the length r, which corresponds to the M—CN—M linkage remains constant with temperature and the thermal expansion arises from the change in the θ angle and the respective changes in the lattice parameters. We have plotted the volume change with θ in Fig. 7.13 and it can be seen that as the θ angle decreases below the tetrahedral angle, the volume of the structure decreases gradually.
The vibrational entropy at high temperatures is give by the equation

$$S_{vib} = k_B(\ln \frac{k_B T}{\hbar\omega} + 1), \tag{7.4}$$

where k_B is the Boltzmann constant, $\hbar$ the reduced Planck constant and ω the vibrational frequency of a certain vibration. It is argued here that the dominant contribution to vibrational entropy will be from transverse vibrational modes, which have a negative

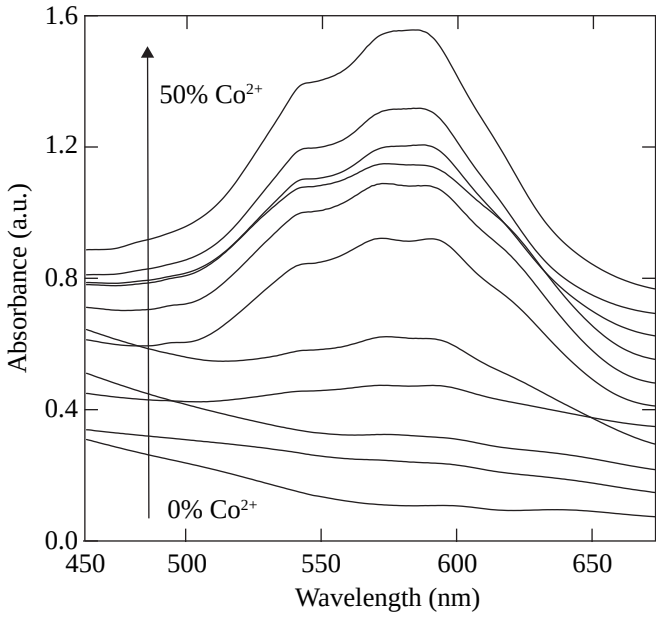

Figure 7.12: UV/VIS measurements for various cobalt(II) doping levels into nickel(II) cyanide.

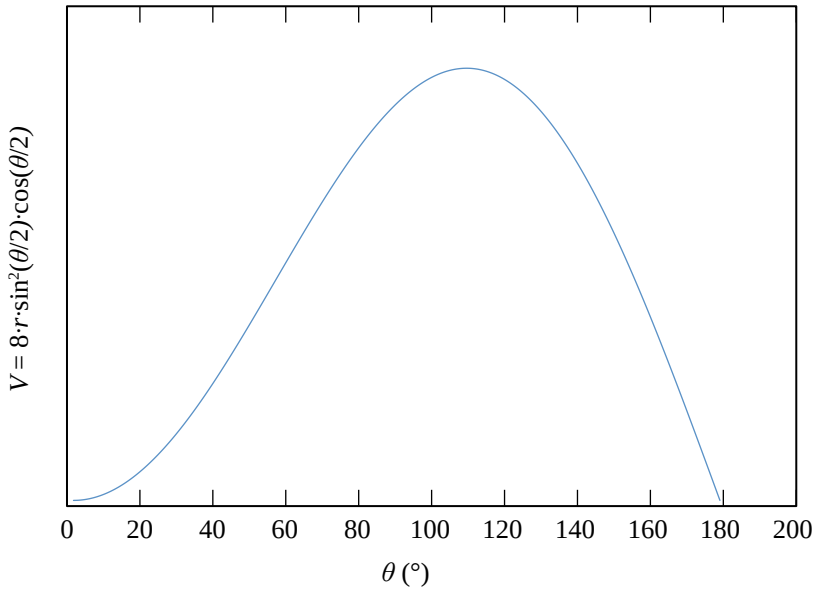

Figure 7.13: Volume dependence on the pseudo-tetrahedral angle θ of cobalt(II) nickel(II) cyanide. It can be seen that as θ decreases, the volume will also decrease.

Grüneisen parameter. The Grüneisen parameter is related to the changes in volume by

$$\gamma_i = -\frac{V}{\omega}\frac{\partial \omega}{\partial V} \tag{7.5}$$

If the vibrational frequency of the transverse vibrations decreases, the vibrational entropy will increase according to Eq. (7.4). This decrease in ω is related with a volume decrease according to Eq. (7.5) as γ_i is negative for transverse vibrational modes. The volume decrease is achieved by decreasing the tetrahedral angle θ as seen above. Therefore decreasing the angle θ reduces the volume of the structure and thereby increases the vibrational entropy of transverse vibrational modes. The exact mechanism of NTE in this structure is not known, but we can say with confidence that the decrease in the tetrahedral angle around cobalt(II) leads to an increase in the vibrational entropy.

7.6 Summary

In summary, we show that samples of nickel(II) cyanide that have been doped with various levels of copper(II) remain square planar. This is thought to result from the fact that metal centres with d^9 electron configurations prefer square planar geometry with both weak field and strong field ligands. On the contrary, doping cobalt(II) into nickel(II) cyanide results in a number of phases, where the structure containing 25% of cobalt(II) and the structure containing 50% of cobalt(II) are thought to be independent structures and the intermediate concentrations of cobalt a mixture of these phases. Furthermore, we show that $CoNi(CN)_4$ has very large area-NTE, which is coupled by overall volume-NTE. This is argued to result from transverse vibrational modes, which link a decrease in volume to an increase in vibrational entropy.

Chapter 8

Conclusions

In conclusion we find that for materials studied in this thesis, dimensionality is an important aspect for understanding their properties. 2,3,6,7,10,11-hexahydroxytriphenylene tetrahydrate undergoes an order to disorder phase transition due to the characteristic one-dimensional water channels in the structure. Lowering dimensionality of water is crucial for obtaining polar phases of water or ice and this holds true for the system studied here, where at low temperatures the one-dimensional water channels each obtain a net dipole moment. It is noted that symmetry breaking plays an important role in the case of these crystals and the order to disorder phase transition. Symmetry lowering in the structure of 2,3,6,7,10,11-hexahydroxytriphenylene tetrahydrate arises from inversion symmetry breaking in the water channels and hence the low-temperature ordered structure is indexed with a space group $P2_1cn$ as opposed to $Pbcn$ for the high temperature structure. The symmetry lowering is induced by ferroelectric ordering of water channels in the pores of the organic crystals, whereby the average structure is no longer centrosymmetric.

In addition, we examine if the material could form one-dimensional metallic bands due to the arrangement of the HHTP molecules in one-dimensional stacks. Despite the lack of conductivity in the materials, we hope that such one-dimensional stacks of aromatic organic molecules could be shown to conduct in other structures.

Furthermore, we demonstrate that the two-dimensional layered structure of nickel(II)

cyanide and silver(I) tricyanomethanide is directly related to the materials' area negative thermal expansion response and show that vibrational motion determines compressibility behaviour for both of these materials, with the latter showing unprecedented negative area compressibility.

Finally, we demonstrate how expanding a two-dimensional structure into three dimensions can impact the materials thermal expansion based on the topological example of cobalt(II) nickel(II) cyanide. This material is a three-dimensional framework material and our hypothesis here is that due to an increased vibrational entropy that is linked with a volume reduction with temperature, the material shows very large area negative thermal expansion.

Based on these examples it can be concluded that a material's structural dimensionality is often very important for its properties. We hope that this thesis has helped to build trends to identify materials with certain functional properties — be it the case of low-dimensional ferroelectric ices or negative compressibility materials.

As part of the future work of it would be of great interest to measure the ferroelectric hysteresis of the low temperature structure of 2,3,6,7,10,11-hexahydroxytriphenylene tetrahydrate. This could be achieved by setting up a Sawyer-Tower circuit to determine the materials' polarisation response to an applied electric field. Furthermore, it would be fascinating to investigate the high-pressure phases of silver(I) tricyanomethanide and nickel(II) cyanide further. Variable-temperature and -pressure characterisation of these phases in detail would form an exciting route to take in the future. It would also be interesting to build a charge-transfer system with an electron-poor aromatic molecule and HHTP and to see if conductivity in the systems could be evoked then. Furthermore, expanding the series of doped metal cations into the structure of nickel(II) cyanide could lead to potentially exciting discoveries and it would also be fascinating to build metal-organic frameworks based on HHTP and transition metal cations.

Bibliography

[1] W. L. Leong and J. J. Vittal, *Chem. Rev.*, 2010, **111**, 688–764.

[2] A. Y. Robin and K. M. Fromm, *Coord. Chem. Rev.*, 2006, **250**, 2127–2157.

[3] A.-X. Tian, J. Ying, J. Peng, J.-Q. Sha, H.-j. Pang, P.-P. Zhang, Y. Chen, M. Zhu and Z.-M. Su, *Cryst. Growth Des.*, 2008, **8**, 3717–3724.

[4] L. R. Dalton, S. J. Benight, L. E. Johnson, D. B. Knorr, I. Kosilkin, B. E. Eichinger, B. H. Robinson, A. K. Y. Jen and R. Overney, *Chem. Mater.*, 2010, **23**, 430–445.

[5] W.-J. Kuo, G.-H. Hsiue and R.-J. Jeng, *Macromol. Chem. Phys.*, 2001, **202**, 1782–1790.

[6] P. J. Skabara, J.-B. Arlin and Y. H. Geerts, *Adv. Mater.*, 2013, **25**, 1948–1954.

[7] J. Roncali, P. Leriche and A. Cravino, *Adv. Mater.*, 2007, **19**, 2045–2060.

[8] M. Alhamami, H. Doan and C.-H. Cheng, *Materials*, 2014, **7**, 3198–3250.

[9] R. Haldar and T. K. Maji, *Cryst. Eng. Comm.*, 2013, **15**, 9276–9295.

[10] H. Kajiro, A. Kondo, K. Kaneko and H. Kanoh, *Int. J. Mol. Sci.*, 2010, **11**, 3803–3845.

[11] R. Kitaura, K. Seki, G. Akiyama and S. Kitagawa, *Angew. Chem. Int. Ed.*, 2003, **42**, 428–431.

[12] A. J. Fletcher, E. J. Cussen, D. Bradshaw, M. J. Rosseinsky and K. M. Thomas, *J. Am. Chem. Soc.*, 2004, **126**, 9750–9759.

[13] Y. Sun, L. Wang, W. Amer, H. Yu, J. Ji, L. Huang, J. Shan and R. Tong, *J. Inorg. Organometal. Polymer. Mater.*, 2013, **23**, 270–285.

[14] H. Li, M. Eddaoudi, M. O'Keeffe and O. M. Yaghi, *Nature*, 1999, **402**, 276–279.

[15] H. Kim, S. Das, M. G. Kim, D. N. Dybtsev, Y. Kim and K. Kim, *Inorg. Chem.*, 2011, **50**, 3691–3696.

[16] N. L. Rosi, J. Eckert, M. Eddaoudi, D. T. Vodak, J. Kim, M. O'Keeffe and O. M. Yaghi, *Science*, 2003, **300**, 1127–1129.

[17] L. J. Murray, M. Dinca and J. R. Long, *Chem. Soc. Rev.*, 2009, **38**, 1294–1314.

[18] D. Saha, S. Deng and Z. Yang, *J. Por. Mater.*, 2009, **16**, 141–149.

[19] S. J. Benight, L. E. Johnson, R. Barnes, B. C. Olbricht, D. H. Bale, P. J. Reid, B. E. Eichinger, L. R. Dalton, P. A. Sullivan and B. H. Robinson, *J. Chem. Phys. B*, 2010, **114**, 11949–11956.

[20] R. A. Marcus, *Rev. Mod. Phys.*, 1993, **65**, 599–610.

[21] H. S. Nalwa, *Appl. Organomet. Chem.*, 1991, **5**, 349–377.

[22] D. L. Elder, S. J. Benight, J. Song, B. H. Robinson and L. R. Dalton, *Chem. Mater.*, 2014, **26**, 872–874.

[23] Y. Mori, K. Nakaya, X. Piao, K. Yamamoto, A. Otomo and S. Yokoyama, *J. Pol. Sci. A: Pol. Chem.*, 2012, **50**, 1254–1260.

[24] M. Leclerc, *Adv. Mater.*, 1999, **11**, 1491–1498.

[25] P. Blanchard, P. Verlhac, L. Michaux, P. Frère and J. Roncali, *Chem. A Eur. J.*, 2006, **12**, 1244–1255.

[26] H. E. Katz, J. G. Laquindanum and A. J. Lovinger, *Chem. Mater.*, 1998, **10**, 633–638.

[27] D. Demus, J. W. Goodby, G. W. Gray, H. W. Spiess and V. Vill, *Handbook of Liquid Crystals, Low Molecular Weight Liquid Crystals I: Calamitic Liquid Crystals*, John Wiley & Sons, 2011.

[28] N. Boden, R. Bushby, J. Clements, B. Movaghar, K. Donovan and T. Kreouzis, *Phys. Rev. B*, 1995, **52**, 13274.

[29] L. Schmidt-Mende, A. Fechtenkötter, K. Müllen, E. Moons, R. H. Friend and J. MacKenzie, *Science*, 2001, **293**, 1119–1122.

[30] A. Cravino, S. Roquet, O. Alévêque, P. Leriche, P. Frère and J. Roncali, *Chem. Mater.*, 2006, **18**, 2584–2590.

[31] J. Cremer and P. Bäuerle, *J. Mater. Chem.*, 2006, **16**, 874–884.

[32] U. Bach, D. Lupo, P. Comte, J. Moser, F. Weissörtel, J. Salbeck, H. Spreitzer and M. Grätzel, *Nature*, 1998, **395**, 583–585.

[33] S. Roquet, R. de Bettignies, P. Leriche, A. Cravino and J. Roncali, *J. Mater. Chem.*, 2006, **16**, 3040–3045.

[34] D. J. Goossens, *Acc. Chem. Res.*, 2013, **46**, 2597–2606.

[35] A. A. Bokov and Z. G. Ye, *J. Mater. Sci.*, 2006, **41**, 31–52.

[36] T. R. Welberry and D. J. Goossens, *J. Appl. Cryst.*, 2008, **41**, 606–614.

[37] A. Amin, R. E. Newnham, L. E. Cross and D. E. Cox, *J. Solid State Chem.*, 1981, **37**, 248–255.

[38] N. E. Brese and M. O'Keeffe, *Acta Cryst. B*, 1991, **47**, 192–197.

[39] I. D. Brown, *Chem. Rev.*, 2009, **109**, 6858–6919.

[40] Y. Kuroiwa, Y. Terado, S. J. Kim, A. Sawada, Y. Yamamura, S. Aoyagi, E. Nishibori, M. Sakata and M. Takata, *Jap. J. Appl. Phys.*, 2005, **44**, 7151.

[41] T. R. Welberry, D. J. Goossens, R. L. Withers and K. Z. Baba-Kishi, *Metall. Mater. Trans. A*, 2010, **41**, 1110–1118.

[42] K. Z. Baba-Kishi, T. R. Welberry and R. L. Withers, *J. Appl. Cryst.*, 2008, **41**, 930–938.

[43] H. You and Q. M. Zhang, *Phys. Rev. Lett.*, 1997, **79**, 3950–3953.

[44] G. Burns and F. H. Dacol, *Phys. Rev. B*, 1983, **28**, 2527–2530.

[45] G. Xu, Z. Zhong, Y. Bing, Z. G. Ye and G. Shirane, *Nat. Mater.*, 2006, **5**, 134–140.

[46] G. Xu, J. Wen, C. Stock and P. M. Gehring, *Nat. Mater.*, 2008, **7**, 562–566.

[47] R. E. Cohen, *Nature*, 2006, **441**, 941–942.

[48] M. Deluca and G. Pezzotti, *J. Phys. Chem. A*, 2008, **112**, 11165–11171.

[49] T. R. Welberry, M. J. Gutmann, H. Woo, D. J. Goossens, G. Xu, C. Stock, W. Chen and Z.-G. Ye, *J. Appl. Crystallogr.*, 2005, **38**, 639–647.

[50] A. A. Bokov and Z. G. Ye, *J. Mater. Sci.*, 2006, **41**, 31–52.

[51] C. René and E. Turcotte, *Handbook of Material Science Research*, Nova Science Publishers, 2010.

[52] N. Takesue, Y. Fujii and H. You, *Phys. Rev. B*, 2001, **64**, 184112.

[53] C. Stock, R. Birgeneau, S. Wakimoto, J. Gardner, W. Chen, Z.-G. Ye and G. Shirane, *Phys. Rev. B*, 2004, **69**, 094104.

[54] G. Xu, G. Shirane, J. Copley and P. Gehring, *Phys. Rev. B*, 2004, **69**, 064112.

[55] K. Binder and A. P. Young, *Rev. Mod. Phys.*, 1986, **58**, 801.

[56] U. Höchli, K. Knorr and A. Loidl, *Adv. Phys.*, 1990, **39**, 405–615.

[57] I. Fehst, M. Paasch, S. Hutton, M. Braune, R. Böhmer, A. Loidl, M. Dörffel, T. Narz, S. Haussühl and G. McIntyre, *Ferroelectr.*, 1993, **138**, 1–10.

[58] W. Schildkamp and J. Spilker, *Zeit. Krist.*, 1984, **168**, 159–172.

[59] A. Loidl, K. Knorr, J. Hessinger, R. Böhmer, I. Fehst and U. Höchli, *J. Non.-Cryst. Sol.*, 1991, **131**, 269–274.

[60] Y. Yacoby and S. Just, *Solid St. Commun.*, 1974, **15**, 715.

[61] J. C. Slater, *J. Chem. Phys.*, 1941, **9**, 16–33.

[62] L. Pauling, *J. Am. Chem. Soc.*, 1935, **57**, 2680–2684.

[63] Y. Takagi, *J. Phys. Soc. Jpn.*, 1948, **3**, 273–274.

[64] V. H. Schmidt, *Phys. Rev.*, 1967, **164**, 749.

[65] J. Albers, A. Klöpperpieper, H. Rother and K. Ehses, *Phys. Solid. A*, 1982, **74**, 553–557.

[66] J. Albers, A. Klöpperpieper, H. Rother and S. Haussühl, *Ferroelectr.*, 1988, **81**, 27–30.

[67] I. F. H. Ries, R. Böhmer and A. Loidl, *Z. Phys. B: Condens. Matter*, 1996, **99**, 401.

[68] H. Bauch, G. Völkel, R. Böttcher, A. Pöppl, H. Schäfer, J. Banys and A. Klöpperpieper, *Phys. Rev. B*, 1996, **54**, 9162.

[69] S. Lanceros-Méndez, G. Schaack, M. Köhler and A. Klöpperpieper, *Ferroelectr.*, 1996, **176**, 73–90.

[70] R. Pirc and R. Blinc, *Ferroelectr.*, 2009, **379**, 30–34.

[71] J. P. Attfield, *Cryst. Growth Des.*, 2013, **13**, 4623–4629.

[72] R. Asahi, T. Morikawa, T. Ohwaki, K. Aoki and Y. Taga, *Science*, 2001, **293**, 269–271.

[73] M. Higashi, R. Abe, T. Takata and K. Domen, *Chem. Mater.*, 2009, **21**, 1543–1549.

[74] Y.-I. Kim, P. M. Woodward, K. Z. Baba-Kishi and C. W. Tai, *Chem. Mater.*, 2004, **16**, 1267–1276.

[75] M. Jansen and H. P. Letschert, *Nature*, 2000, **404**, 980–982.

[76] Y. Q. Li, A. C. A. Delsing, G. de With and H. T. Hintzen, *Chem. Mater.*, 2005, **17**, 3242–3248.

[77] A. B. Jorge, J. Oró-Solé, A. M. Bea, N. Mufti, T. T. M. Palstra, J. A. Rodgers, J. P. Attfield and A. Fuertes, *J. Am. Chem. Soc.*, 2008, **130**, 12572–12573.

[78] A. Kusmartseva, M. Yang, J. Oró-Solé, A. M. Bea, A. Fuertes and J. P. Attfield, *Appl. Phys. Lett.*, 2009, **95**, 2.

[79] D. Armytage and B. E. F. Fender, *Acta Cryst. B*, 1974, **30**, 809–812.

[80] D. Logvinovich, S. G. Ebbinghaus, A. Reller, I. Marozau, D. Ferri and A. Weidenkaff, *Zeit. Anorg. All. Chem.*, 2010, **636**, 905–912.

[81] M. Yang, J. Oró-Solé, J. A. Rodgers, A. B. Jorge, A. Fuertes and J. P. Attfield, *Nat. Chem.*, 2011, **3**, 47–52.

[82] Y.-I. Kim, P. M. Woodward, K. Z. Baba-Kishi and C. W. Tai, *Chem. Mater.*, 2004, **16**, 1267–1276.

[83] M. Jansen and H. P. Letschert, *Nature*, 2000, **404**, 980–982.

[84] P. J. Camp, A. Fuertes and J. P. Attfield, *J. Am. Chem. Soc.*, 2012, **134**, 6762–6766.

[85] S. Chaplot, R. Mittal and N. Choudhury, *Thermodynamic Properties of Solids: Experiments and Modeling*, Wiley, 2010.

[86] C. Ho and R. Taylor, *Thermal Expansion of Solids*, ASM International, 1998.

[87] D. Taylor, *Br. Ceram. Trans. J.*, 1984, **83**, 129.

[88] A. W. Sleight, *Current Opinion in Solid State and Materials Science*, 1998, **3**, 128–131.

[89] A. Sleight, *Inorg. Chem.*, 1998, **37**, 2854–2860.

[90] J. O. Evans, *J. Chem. Soc., Dalton. Trans.*, 1999, **19**, 3317–3326.

[91] J. Patterson and B. Bailey, *Solid-State Physics: Introduction to the Theory*, Springer, 2010.

[92] E. Grueneisen, H. Geiger and K. Scheel, *Handbuch der Physik (Verlag Julius Springer, Berlin)*, 1926, **10**, 1–59.

[93] S. Billinge and F. Thorpe, *Local Structure from Diffraction*, Springer US, 1998.

[94] V. Heine, P. R. L. Welche and M. T. Dove, *J. Am. Cer. Soc.*, 1999, **82**, 1793–1802.

[95] G. D. Barrera, J. A. O. Bruno, T. H. K. Barron and N. L. Allan, *J. Phys.: Condens. Matter*, 2005, **17**, R217–R252.

[96] C. Lind, *Materials*, 2012, **5**, 1125–1154.

[97] W. Miller, C. W. Smith, D. S. Mackenzie and K. E. Evans, *J. Mater. Sci.*, 2009, **44**, 5441–5451.

[98] K. Takenaka, *Sci. Tech. Adv. Mater.*, 2012, **13**, 013001.

[99] A. K. A. Pryde, K. D. Hammonds, M. T. Dove, V. Heine, J. D. Gale and M. C. Warren, *J. Phys.: Cond. Matt.*, 1996, **8**, 10973.

[100] G. Ernst, C. Broholm, G. R. Kowach and A. P. Ramirez, *Nature*, 1998, **396**, 147–149.

[101] M. G. Tucker, A. L. Goodwin, M. T. Dove, D. A. Keen, S. A. Wells and J. S. O. Evans, *Phys. Rev. Lett.*, 2005, **95**, 255501.

[102] T. Mary, J. Evans, T. Vogt and A. Sleight, *Science*, 1996, **272**, 90–92.

[103] M. Auray, M. Quarton and M. Leblanc, *Acta Cryst. C: Cryst Struct. Commun.*, 1995, **51**, 2210–2213.

[104] A. K. Pryde, K. D. Hammonds, M. T. Dove, V. Heine, J. D. Gale and M. C. Warren, *J. Phys.: Condens. Mater.*, 1996, **8**, 10973.

[105] A. K. Pryde, K. D. Hammonds, M. T. Dove, V. Heine, J. D. Gale and M. C. Warren, *Phase Trans.*, 1997, **61**, 141–153.

[106] A. Sanson, *Chem. Mater.*, 2014, **26**, 3716–3720.

[107] J. Evans, T. Mary, T. Vogt, M. Subramanian and A. Sleight, *Chem. Mater.*, 1996, **8**, 2809–2823.

[108] A. W. Sleight, *Annual. Rev. Mat. Sci.*, 1998, **28**, 29–43.

[109] S. Allen, N. R. Warmingham, R. K. Gover and J. S. Evans, *Chem. Mater.*, 2003, **15**, 3406–3410.

[110] C. Closmann, A. Sleight and J. Haygarth, *J. Solid State Chem.*, 1998, **139**, 424–426.

[111] V. Korthuis, N. Khosrovani, A. Sleight, N. Roberts, R. Dupree and W. J. Warren, *Chem. Mater.*, 1995, **7**, 412–417.

[112] J. Evans, J. Hanson and A. Sleight, *Acta Cryst. B*, 1998, **54**, 705–713.

[113] A. V. T. Khosrovani, K.; Sleight, *J. Solid State Chem*, 1997, **132**, 355.

[114] R. Withers, J. Evans, J. Hanson and A. Sleight, *J. Solid State Chem.*, 1998, **137**, 161.

[115] H. Onken, *Naturwissenschaften*, 1965, **52**, 344.

[116] G. Le Flem, J. Lamic and P. Hagenmuller, *Bull. Soc. Chim. Fr.*, 1966, **6**, 1880.

[117] R. Gover, N. Withers, S. Allen, R. Withers and J. Evans, *J. Solid State Chem.*, 2002, **166**, 42.

[118] K. White, P. L. Lee, P. J. Chupas, K. Chapman, E. A. Payzant, A. C. Jupe, W. Bassett, C.-S. Zha and A. P. Wilkinson, *Chem. Mater.*, 2008, **20**, 3728–3734.

[119] G. W. Stinton, M. R. Hampson and J. S. Evans, *Inorg. Chem.*, 2006, **45**, 4352–4358.

[120] G. Wallez, P. E. Raison, N. Dacheux, N. Clavier, D. Bykov, L. Delevoye, K. Popa, D. Bregiroux, A. N. Fitch and R. J. Konings, *Inorg. Chem.*, 2012, **51**, 4314–4322.

[121] M. Vaccari, R. Grisenti, P. Fornasini, F. Rocca and A. Sanson, *Phys. Rev. B*, 2007, **75**, 184307.

[122] B. J. Kennedy, Y. Kubota and K. Kato, *Solid State Commun.*, 2005, **136**, 177 – 180.

[123] M. Gupta, R. Mittal, S. Rols and S. Chaplot, *Phys. B.: Condens. Matter*, 2012, **407**, 2146 – 2149.

[124] T. Lan, C. W. Li, J. L. Niedziela, H. Smith, D. L. Abernathy, G. R. Rossman and B. Fultz, *Phys. Rev. B*, 2014, **89**, 054306.

[125] D. A. Woodcock, P. Lightfoot, L. A. Villaescusa, M.-J. Díaz-Cabañas, M. A. Camblor and D. Engberg, *Chem. Mater.*, 1999, **11**, 2508–2514.

[126] T. Mary and A. Sleight, *J. Mater. Res.*, 1999, **14**, 912–915.

[127] J. Tao and A. Sleight, *J. Solid State Chem.*, 2003, **173**, 442–448.

[128] P. Lightfoot, D. A. Woodcock, M. J. Maple, L. A. Villaescusa and P. A. Wright, *J. Mater. Chem.*, 2001, **11**, 212–216.

[129] W. Miller, C. Smith, D. Mackenzie and K. Evans, *J. Mater. Sci.*, 2009, **44**, 5441–5451.

[130] J. S. O. Evans, Z. Hu, J. D. Jorgensen, D. N. Argyriou, S. Short and A. W. Sleight, *Science*, 1997, **275**, 61–65.

[131] J. D. Jorgensen, Z. Hu, S. Teslic, D. N. Argyriou, S. Short, J. S. O. Evans and A. W. Sleight, *Phys. Rev. B*, 1999, **59**, 215–225.

[132] S. C. Abrahams, *J. Chem. Phys.*, 1966, **45**, 2745.

[133] J. S. O. Evans and T. A. Mary, *Int. J. Inorg. Mater.*, 2000, **2**, 143.

[134] J. Nelson and D. Riley, *Proc. Phys. Soc.*, 1945, **57**, 477.

[135] W. Paszkowicz, J. Pelka, M. Knapp, T. Szyszko and S. Podsiadlo, *Appl. Phys. A*, 2002, **75**, 431–435.

[136] R. W. Munn, *J. Phys. C.: Solid State Phys.*, 1972, **5**, 535–542.

[137] R. McCammon and G. White, *Philos. Mag.*, 1965, **11**, 1125–1134.

[138] R. Grosse, P. Krause, M. Meissner and A. Tausend, *Journal of Physics C: Solid State Physics*, 1978, **11**, 45.

[139] T. Gibbons, *Phys. Rev. B*, 1973, **7**, 1410.

[140] D. Batchelder, *J. Pol. Sci. A: Pol. Chem.*, 1976, **14**, 1235–1240.

[141] R. W. Munn, *J. Phys. C*, 1972, **5**, 535–542.

[142] A. C. Bailey and B. Yates, *J. Appl. Phys.*, 1970, **41**, 5088–5091.

[143] G. D. Barrera, J. A. O. Bruno, T. H. K. Barron and N. L. Allan, *J. Phys.: Cond. Matt.*, 2005, **17**, R217.

[144] B. Yates, M. J. Overy and O. Pirgon, *Philos. Mag.*, 1975, **32**, 847–857.

[145] G. K. White, *J. Phys. C: Solid State Phys.*, 1970, **5**, 2731.

[146] T. H. K. Barron, J. G. Collins and G. K. White, *Adv. Phys.*, 1980, **29**, 609.

[147] R. M. Barron, T. H. K. Barron, P. M. Mummery and M. Sharkey, *Can. J. Chem.*, 1988, **66**, 718.

[148] J. André, J.-L. Bredas, J. Delhalle, J. Ladik, G. Leroy, C. Moser and D. Bloor, 1980, **113**, 14–34.

[149] U. Arnold and P. Grosse, *Phys. Status Solidi*, 1968, **28**, K93.

[150] P. Tschaufeser and S. C. Parker, *J. Phys. Chem.*, 1995, **99**, 10609–10615.

[151] A. Bieniok and K. D. Hammonds, *Micropor. Mesopor. Mater.*, 1998, **25**, 193.

[152] D. J. Williams, D. E. Partin, F. J. Lincoln, J. Kouvetakis and M. O'Keeffe, *J. Solid State Chem.*, 1997, **134**, 164–169.

[153] S. Margadonna, K. Prassides and A. N. Fitch, *J. Am. Chem. Soc.*, 2004, **126**, 15390–15391.

[154] A. E. Phillips, A. L. Goodwin, G. J. Halder, P. D. Southon and C. J. Kepert, *Angew. Chem.*, 2008, **120**, 1418–1421.

[155] S. Adak, L. L. Daemen, M. Hartl, D. Williams, J. Summerhill and H. Nakotte, *J. Solid State Chem.*, 2011, **184**, 2854–2861.

[156] S. J. Hibble, A. M. Chippindale, A. H. Pohl and A. C. Hannon, *Angew. Chem. Int. Ed.*, 2007, **46**, 7116–7118.

[157] A. L. Goodwin, M. T. Dove, A. M. Chippindale, S. J. Hibble, A. H. Pohl and A. C. Hannon, *Phys. Rev. B*, 2009, **80**, 054101.

[158] S. G. Duyker, V. K. Peterson, G. J. Kearley, A. J. Ramirez-Cuesta and C. J. Kepert, *Angew. Chem. Int. Ed.*, 2013, **52**, 5266–5270.

[159] A. M. Chippindale, S. J. Hibble, E. J. Bilbé, E. Marelli, A. C. Hannon, C. Allain, R. Pansu and F. Hartl, *J. Am. Chem. Soc.*, 2012, **134**, 16387–16400.

[160] A. L. Goodwin, M. Calleja, M. J. Conterio, M. T. Dove, J. S. O. Evans, D. A. Keen, L. Peters and M. G. Tucker, *Science*, 2008, **319**, 794–797.

[161] P. Ding, E. J. Liang, Y. Jia and Z. Y. Du, *J. Phys.: Cond. Matt.*, 2008, **20**, 275224.

[162] A. L. Goodwin and C. J. Kepert, *Phys. Rev. B*, 2005, **71**, 140301.

[163] K. W. Chapman, P. J. Chupas and C. J. Kepert, *J. Am. Chem. Soc.*, 2005, **127**, 15630–15636.

[164] H. Fang, A. E. Phillips, M. T. Dove, M. G. Tucker and A. L. Goodwin, *Phys. Rev. B*, 2013, **88**, 144103.

[165] S. J. Hibble, A. M. Chippindale, E. Marelli, S. Kroeker, V. K. Michaelis, B. J. Greer, P. M. Aguiar, E. J. Bilbé, E. R. Barney and A. C. Hannon, *J. Am. Chem. Soc.*, 2013, **135**, 16478–16489.

[166] S. G. Duyker, V. K. Peterson, G. J. Kearley, A. J. Ramirez-Cuesta and C. J. Kepert, *Angew. Chem. Int. Ed.*, 2013, **52**, 5266–5270.

[167] A. G. Sharpe, *The Chemistry of Cyano Complexes of the Transition Metals*, Academic Press, London, 1976.

[168] M. J. Conterio, A. L. Goodwin, M. G. Tucker, D. A. Keen, M. T. Dove, L. Peters and J. S. O. Evans, *J. Phys.: Cond. Matt.*, 2008, **20**, 255225.

[169] A. L. Goodwin, D. A. Keen, M. G. Tucker, M. T. Dove, L. Peters and J. S. O. Evans, *J. Am. Chem. Soc.*, 2008, **130**, 9660–9661.

[170] A. B. Cairns and A. L. Goodwin, *Chem. Soc. Rev.*, 2013, **42**, 4881–4893.

[171] I. M. Lifshits, *Zh. Eksp. Teor. Fiz.*, 1952, **22**, 475.

[172] R. Baughman, S. Stafstrom, C. Cui and S. Dantas, *Science*, 1998, **279**, 1522–1524.

[173] G. E. Bacon and E. J. Lisher, *Acta Cryst. B*, 1980, **36**, 1908–1916.

[174] S. Prawer, T. Smith and T. Finlayson, *Aus. J. Phys.*, 1985, **38**, 63–84.

[175] A. D. Fortes, E. Suard and K. S. Knight, *Science*, 2011, **331**, 742–746.

[176] W. Li, M. R. Probert, M. Kosa, T. D. Bennett, A. Thirumurugan, R. P. Burwood, M. Parinello, J. A. K. Howard and A. K. Cheetham, *J. Am. Chem. Soc.*, 2012, **134**, 11940–11943.

[177] A. L. Goodwin, D. A. Keen and M. G. Tucker, *Proc. Natl. Acad. Sci., U.S.A.*, 2008, **105**, 18708–18713.

[178] A. B. Cairns, A. L. Thompson, M. G. Tucker, J. Haines and A. L. Goodwin, *J. Am. Chem. Soc.*, 2011, **134**, 4454–4456.

[179] A. B. Cairns, J. Catafesta, C. Levelut, J. Rouquette, A. van der Lee, L. Peters, A. L. Thompson, V. Dmitriev, J. Haines and A. L. Goodwin, *Nature Mater.*, 2013, **12**, 212–216.

[180] R. J. Nelmes and A. Katrusiak, *J. Phys. C: Solid State Phys.*, 1986, **19**, L725–L730.

[181] A. Sani, M. Hanfland and D. Levy, *J. Phys.: Cond. Matt.*, 2002, **14**, 10601–10604.

[182] I. Loa, K. Syassen, R. K. Kremer, U. Schwarz and M. Hanfland, *Phys. Rev. B*, 1999, **60**, R6945–R6948.

[183] M. Seyidov and R. A. Suleymanov, *J. Appl. Phys.*, 2010, **108**, 063540.

[184] A. D. Fortes, E. Suard and K. S. Knight, *Science*, 2011, **331**, 742–745.

[185] W. Li, M. R. Probert, M. Kosa, T. D. Bennett, A. Thirumurugan, R. P. Burwood, M. Parinello, J. A. K. Howard and A. K. Cheetham, *J. Am. Chem. Soc.*, 2012, **134**, 11940–11943.

[186] H. J. Shepherd, T. Palamarciuc, P. Rosa, P. Guionneau, G. Molnár, J.-F. Létard and A. Bousseksou, *Angew. Chem. Int. Ed.*, 2012, **51**, 3910–3914.

[187] R. H. Baughman, S. Stafström, C. Cui and S. O. Dantas, *Science*, 1998, **279**, 1522–1524.

[188] F. Thébault, L. Öhrström and M. Haukka, *Acta Cryst. C*, 2011, **67**, O143–O145.

[189] J. E. Bai, J. Wang and X. C. Zeng, *Proc. Natl. Acad. Sci., U.S.A.*, 2006, **103**, 19664–19667.

[190] Y. Maniwa, H. Kataura, M. Abe, S. Suzuki, Y. Achiba, H. Kira and K. Matsuda, *J. Phys. Soc. Jpn.*, 2002, **71**, 2863–2866.

[191] S. Ghosh, K. V. Ramanathan and A. K. Sood, *Europhys. Lett.*, 2004, **65**, 678–684.

[192] Y. Maniwa, H. Kataura, M. Abe, A. Udaka, S. Suzuki, Y. Achiba, H. Kira, K. Matsuda, H. Kadowaki and Y. Okabe, *Chem. Phys. Lett.*, 2005, **401**, 534–538.

[193] O. Byl, J.-C. Liu, Y. Wang, W.-L. Yim, J. K. Johnson and J. Yates, J. T., *J. Am. Chem. Soc.*, 2006, **128**, 12090–12097.

[194] K. Koga, G. T. Gao, H. Tanaka and X. C. Zeng, *Nature*, 2001, **412**, 802–805.

[195] H.-X. Zhao, X.-J. Kong, H. Li, Y.-C. Jin, L.-S. Long, X. C. Zeng, R.-B. Huang and L.-S. Zheng, *Proc. Natl. Acad. Sci., U.S.A.*, 2011, **108**, 3481–3486.

[196] J. M. Ogborn, I. E. Collings, S. A. Moggach, A. L. Thompson and A. L. Goodwin, *Chem. Sci.*, 2012, **3**, 3011–3017.

[197] A. Goodwin, D. Keen and M. Tucker, *PNAS*, 2008, **105**, 18708–18713.

[198] M. J. Cliffe and A. L. Goodwin, *J. Appl. Crystallogr.*, 2012, **45**, 1321–1329.

[199] R. Jenkins and R. Snyder, *Introduction to X-ray powder diffractometry*, John Wiley & Sons, 2012, vol. 267.

[200] W. L. Bragg, *Proc. Camb. Phil. Soc.*, 1913, **17**, 43.

[201] C. Hammond, *The Basics of Crystallography and Diffraction*, OUP Oxford, 2009.

[202] P. P. Ewald, *Annalen der Physik*, 1917, **359**, 519–556.

[203] A. K. Cheetham and P. Day, *Solid State Chemistry Techniques*, Clarendon Press Oxford, 1978.

[204] A. L. Patterson, 1934, **46**, 372.

[205] M. Woolfson, *Rep. Progr. Phys.*, 1971, **34**, 369.

[206] 2014, http://www.diamond.ac.uk/Home/About.html.

[207] L. de Broglie, *Ann. Phys.*, 1925, **3**, 22.

[208] 2014, http://www.isis.stfc.ac.uk/aboutisis/aboutisis.html.

[209] G. Pawley, *J. Appl. Cryst.*, 1981, **14**, 357–361.

[210] H. Rietveld, *J. Appl. Cryst.*, 1969, **2**, 65–71.

[211] G. Gallavotti, *Statistical Mechanics: A Short Treatise*, Springer, 1999.

[212] L. Onsager, *Phys. Rev.*, 1944, **65**, 117–149.

[213] M. Lines, *Principles and applications of ferroelectrics and related materials*, Clarendon Press, Oxford England, 1977.

[214] Y. Chiang, *Physical Ceramics*, John Wiley & Sons, 1997.

[215] F. Birch, *Phys. Rev.*, 1947, **71**, 809–824.

[216] J. Cosier and A. Glazer, *J. Appl. Cryst.*, 1986, **19**, 105–107.

[217] O. Diffraction and P. CrysAlis, *Oxford Diffraction Ltd*, 2003.

[218] A. Altomare, G. Cascarano, C. Giacovazzo, A. Guagliardi, M. C. Burla, G. Polidori and M. Camalli, *J. Appl. Cryst.*, 1994, **27**, 435.

[219] P. Betteridge, J. Carruthers, R. Cooper, K. Prout and D. Watkin, *J. Appl. Cryst.*, 2003, **36**, year.

[220] G. J. Piermarini, S. Block, J. D. Barnett and R. A. Forman, *J. Appl. Phys.*, 1975, **46**, 2774–2780.

[221] A. Coelho, *Topas-Academic: General profile and structural analysis software for powder diffraction data. Version 4.1.*, 2007.

[222] 2014, http://www.diamond.ac.uk/Beamlines/Engineering-and-Environment/I15.html.

[223] H. K. Mao, J. Xu and P. M. Bell, *J. Geophys. Res., (Solid Earth Planets)*, 1986, **91**, year.

[224] 2014, http://www.isis.stfc.ac.uk/instruments/pearl/pearl2122.html.

[225] R. von Dreele and A. C. Larson, *Los Alamos National Laboratory Report LAUR*, 1986.

[226] 2014, http://www.physics.ox.ac.uk/Users/Kraus/research/Magnetometry.htm.

[227] 2014, https://www2.physics.ox.ac.uk/enterprise/services-and-specialist-equipment/material-properties-facility.

[228] 2014, http://caesr-web.chem.ox.ac.uk.

[229] C. J. Doonan, D. J. Tranchemontagne, T. G. Glover, J. R. Hunt and O. M. Yaghi, *Nat. Chem.*, 2010, **2**, 235–238.

[230] M. Hmadeh, Z. Lu, Z. Liu, F. Gándara, H. Furukawa, S. Wan, V. Augustyn, R. Chang, L. Liao, F. Zhou, E. Perre, V. Ozolins, K. Suenaga, X. Duan, B. Dunn, Y. Yamamto, O. Terasaki and O. M. Yaghi, *Chem. Mater.*, 2012, **24**, 3511–3513.

[231] J. D. Bernal and R. H. Fowler, *J. Chem. Phys.*, 1933, **1**, 515–548.

[232] S. T. Bramwell, *Nature*, 1999, **397**, 212–213.

[233] S. J. Singer and C. Knight, in *Advances in Chemical Physics*, ed. S. A. Rice and A. R. Dinner, Wiley-Blackwell, Malden, U.S.A., 2012, vol. 147, pp. 1–74.

[234] H. Fukazawa, A. Hoshikawa, Y. Ishii, B. C. Chakoumakos and J. A. Fernandez-Baca, *Astrophys. J. Lett.*, 2006, **652**, L57.

[235] M. J. Iedama, M. J. Dresser, D. L. Doering, J. B. Rowland, W. P. Hess, A. A. Tsekouras and J. P. Cowin, *J. Phys. Chem. B*, 1998, **102**, 9203–9214.

[236] X. Su, L. Lianos, R. Shen and G. A. Somorjai, *Phys. Rev. Lett.*, 1998, **80**, 1533–1536.

[237] C. F. Luo, W. Fa, J. Zhou, J. M. Dong and X. C. Zeng, *Nano Lett.*, 2008, **8**, 2607–2612.

[238] F. Mikami, K. Matsuda, H. Kataura and Y. Maniwa, *ACS Nano*, 2009, **3**, 1279–1287.

[239] S. J. Singer, J.-L. Kuo, T. K. Hirsch, C. Knight, L. Ojamäe and M. L. Klein, *Phys. Rev. Lett.*, 2005, **94**, 135701.

[240] L. E. Cheruzel, M. S. Pometum, M. R. Cecil, M. S. Mashuta, R. J. Witterbort and R. M. Buchanan, *Angew. Chem. Int. Ed.*, 2003, **42**, 5452–5455.

[241] B. Zhou, Y. Imai, A. Kobayashi, Z. Wang and H. Kobayashi, *Chem. Lett.*, 2011, **40**, 1098–1100.

[242] H. B. Cui, B. Zhou, L.-S. Long, Y. Okano, H. Kobayashi and A. Kobayashi, *Angew. Chem. Int. Ed.*, 2008, **47**, 3376–3380.

[243] R. J. Nelmes, R. O. Piltz, W. F. Kuhs, Z. Tun and R. Restori, *Ferroelectrics*, 1990, **108**, 165–170.

[244] T. L. Andresen, F. C. Krebs, N. Thorup and K. Bechgaard, *Chem. Mater.*, 2000, **12**, 2428–2433.

[245] F. Toda, K. Tanaka, M. Takeshi, T. Nakai, I. Miyahara and K. Hirotsu, *J. Phys. Org. Chem.*, 2000, **13**, 39–45.

[246] F. C. Krebs, N. C. Schiodt, W. Batsberg and K. Bechgaard, *Synthesis*, 1997, 1285–1290.

[247] J. Cosier and A. M. Glazer, *J. Appl. Cryst.*, 1986, **19**, 105–107.

[248] A. D. Fortes, I. G. Wood, D. Grigoriev, M. Alfredsson, S. Kipfstuhl, K. S. Knight and R. I. Smith, *J. Phys. Chem.*, 2004, **120**, 11376–11379.

[249] R. I. Cooper, A. L. Thompson and D. J. Watkin, *J. Appl. Cryst.*, 2010, **43**, 1100–1107.

[250] L. Plasseraud, H. Maid, F. Hampel and R. W. Saalfrank, *Chem. Eur. J.*, 2001, **7**, 4007–4011.

[251] L. Han and M. Hong, *Inorg. Chem. Comm.*, 2005, **8**, 406–419.

[252] Y.-Y. Yin, X.-Y. Chen, X.-C. Cao, W. Shi and P. Cheng, *Chem. Commun.*, 2012, **48**, 705–707.

[253] M. Szafrański, A. Katrusiak and G. J. McIntyre, *Phys. Rev. Lett.*, 2002, **89**, 215507.

[254] C. N. Yang, *Phys. Rev.*, 1952, **85**, 808–816.

[255] D. P. Landau, *Phys. Rev. B*, 1980, **21**, 1285–1297.

[256] A. Kalz, A. Honecker and M. Moliner, *Phys. Rev. B*, 2011, **84**, 174407.

[257] S. Jin, A. Sen, W. Guo and A. W. Sandvik, *Phys. Rev. B*, 2013, **84**, 144406.

[258] H. Yu and W. F. van Gunsteren, *J. Chem. Phys.*, 2004, **121**, 9549–9564.

[259] A. Barthram, R. Cleary, M. Ward *et al.*, *Chem. Commun.*, 1998, 2695–2696.

[260] M. Kinoshita, *Jpn. J. Appl. Phys.*, 1994, **33**, 5718–5733.

[261] A. K. Kazuo Mukai, Yasuo Deguchi, *Bull. Chem. Soc. Jap.*, 1969, **42**, 1525–1530.

[262] A. N. Holden, B. T. Matthias, P. W. Anderson and H. W. Lewis, *Phys. Rev.*, 1956, **102**, 1463–1474.

[263] J. S. Miller and J. L. Manson, *Acc. Chem. Res.*, 2001, **34**, 563–570.

[264] S. J. Blundell and F. L. Pratt, *J. Phys.: Condens. Mater.*, 2004, **16**, R771–R828.

[265] H. Akamatu, *Nature*, 1954, **173**, 168–169.

[266] P. W. Anderson, P. A. Lee and M. Saitoh, *Solid State Comm.*, 1973, **13**, 595–598.

[267] R. M. Jerome D, Mazaud A, *J. Phys. Lett.*, 1980, **41**, 95–98.

[268] K. Bechgaard, K. Carneiro, M. Olsen, F. B. Rasmussen and C. S. Jacobsen, *Phys. Rev. Lett.*, 1981, **46**, 13.

[269] S. Perruchas, J. Fraxedas, E. Canadell, P. Auban-Senzier and P. Batail, *Adv. Mater.*, 2005, **17**, 209–212.

[270] M. Mizuno, A. F. Garito and M. P. Cava, *Chem. Commun.*, 1978, 18–19.

[271] S. P. R. Parkin S. S. P., Engler E. M., *J. Phys.*, 1983, **44**, 791–797.

[272] M. R. Bryce, *Chem. Soc. Rev.*, 1991, **20**, 355–390.

[273] E. Coronado, J. R. Galan-Mascaros, C. J. Gomez-Garcia and V. Laukhin, *Nature*, 2000, **408**, 447–449.

[274] H. Kobayashi, A. Kobayashi and H. Tajima, *Chem. Asian J.*, 2011, **6**, 1688–1704.

[275] H. Tanaka, M. Tokumoto, S. Ishibashi, D. Graf, E. S. Choi, J. S. Brooks, S. Yasuzuka, Y. Okano, H. Kobayashi and A. Kobayashi, *J. Am. Chem. Soc.*, 2004, **126**, 10518–10519.

[276] A. Altomare, M. Camalli, C. Cuocci, C. Giacovazzo, A. Moliterni and R. Rizzi, *J. Appl. Cryst.*, 2009, **42**, 1197–1202.

[277] M. Dressel, *Naturwissenschaften*, 2007, **94**, 527–541.

[278] A. Lund and M. Shiotani, *EPR of Free Radicals in Solids I: Trends in Methods and Applications*, Springer, 2012.

[279] J. Konnert and D. Britton, *Inorg. Chem.*, 1966, **5**, 1193–1196.

[280] S. R. Batten, B. F. Hoskins and R. Robson, *New J. Chem.*, 1998, 173–175.

[281] J. Konnert and D. Britton, *Inorg. Chem.*, 1966, **5**, 1193.

[282] S. R. Batten, B. F. Hoskins and R. Robson, *New J. Chem.*, 1998, **22**, 173–175.

[283] Y. Mo and E. Kaxiras, *Small*, 2007, **3**, 1253–1258.

[284] Y. Mathey and C. Mazières, *J. Phys. Lett.*, 1975, 275.

[285] Y. Mathey, C. Mazières and R. Setton, *Inorg. Nucl. Chem. Lett.*, 1977, **13**, 1–3.

[286] M. J. Cliffe and A. L. Goodwin, *J. Appl. Cryst.*, 2012, **45**, 1321–1329.

[287] A. L. Goodwin, M. Calleja, M. J. Conterio, M. T. Dove, J. S. O. Evans, D. A. Keen, L. Peters and M. G. Tucker, *Science*, 2008, **319**, 794–797.

[288] J. M. Ogborn, I. E. Collings, S. A. Moggach, A. L. Thompson and A. L. Goodwin, *Chem. Sci.*, 2012, **3**, 3011–3017.

[289] R. E. Newnham, *Properties of Materials*, Oxford University Press, Oxford, 2005.

[290] A. C. Bailey and B. Yates, *J. Appl. Phys.*, 1970, **41**, 5088–5091.

[291] S. J. Hibble, A. M. Chippindale, A. H. Pohl and A. C. Hannon, *Angew. Chem. Int. Ed.*, 2007, **46**, 7116–7118.

[292] H. L. Zhang, S. Lu, M. P. J. Punkkinen, Q.-M. Hu, B. Johannson and L. Vitos, *Phys. Rev. B*, 2010, **82**, 132409.

[293] F. D. Murnaghan, *Proc. Natl. Acad. Sci. USA*, 1944, **30**, 244–247.

[294] C. Slebodnick, J. Zhao, R. Angel, B. E. Hanson, Y. Song, Z. Liu and R. J. Hemley, *Inorg. Chem.*, 2004, **43**, 5245–5252.

[295] I. M. Lifshits, *Zh. Eks. Teor. Fiz.*, 1952, **22**, 475–486.

[296] M. Hanfland, H. Beister and K. Syassen, *Phys. Rev. B*, 1989, **39**, 12598–12603.

[297] V. L. Solozhenko and T. Peun, *J. Phys. Chem. Solids*, 1997, **58**, 1321–1323.

[298] A. L. Goodwin, D. A. Keen and M. G. Tucker, *Proc. Natl. Acad. Sci., U.S.A.*, 2008, **105**, 18708–18713.

[299] I. Hamdi and N. Meskini, *Phys. B.: Condens. Matter*, 2010, **405**, 2785–2794.

[300] K. Kamali, C. Ravi, T. R. Ravindran, R. M. Sarguna, T. N. Sairam and G. Kaur, *J. Phys. Chem. C*, 2013, **117**, 25704–25713.

[301] R. Janes and E. Moore, *Metal-ligand Bonding*, Royal Society of Chemistry, 2004.

[302] Z. Mo, Y. Li, H. K. Lee and L. Deng, *Organomet.*, 2011, **30**, 4687–4694.

[303] A.-H. Yuan, R.-Q. Lu, H. Zhou, Y.-Y. Chen and Y.-Z. Li, *Cryst. Eng. Comm.*, 2012, **12**, 1382–1382.

[304] V. Gutmann and K. H. Wegleitner, *Chemical Monthly*, 1968, **99**, 368–379.

Appendix A

Experimental data for HHTP·4H_2O

A.1 SCXRD data

Table A.1: SCXRD data collection and refinement details for HHTP·4H_2O at T= 100 K on heating.

Radiation	Mo Kα, $\lambda = 0.71073$ Å
Formula	$C_{18}H_{20}O_{10}$
M, g mol^{-1}	396.35
Z	4
Crystal Size (mm)	0.03 × 0.10 × 0.19
Crystal System	Orthorhombic
Space Group	$P2_1cn$
a (Å)	14.20002(19)
c (Å)	16.7353(2)
c (Å)	7.17809(9)
V (Å^3)	1705.82(4)

Continued on next page

Table A1 — continued from previous page

No. of Reflections($I/\sigma > 2.0$)	3455
Goodness of Fit	1.0051
$R(I/\sigma > 2.0)$	0.0308

Atom	x	y	z	U_{eq}, Å^2
C1	0.45532(13)	0.26668(9)	0.7171(2)	0.0156
C2	0.41227(14)	0.33799(9)	0.67410(18)	0.0152
C3	0.45536(13)	0.41202(8)	0.7117(2)	0.0127
C4	0.40722(13)	0.48741(9)	0.66958(18)	0.0137
C5	0.31699(12)	0.48968(9)	0.58813(19)	0.0136
C6	0.27207(12)	0.56128(11)	0.5536(2)	0.0157
C7	0.31614(12)	0.63329(9)	0.6011(2)	0.0150
C8	0.40401(13)	0.63238(10)	0.68049(19)	0.0157
C9	0.45232(12)	0.55999(9)	0.7129(2)	0.0130
C10	0.54698(12)	0.56069(9)	0.7904(2)	0.0140
C11	0.59399(14)	0.63291(9)	0.82159(19)	0.0152
C12	0.68197(13)	0.63534(9)	0.8980(2)	0.0155
C13	0.72726(12)	0.56368(10)	0.9493(2)	0.0146
C14	0.68288(13)	0.49212(9)	0.9154(2)	0.0148
C15	0.59224(14)	0.48820(8)	0.83422(19)	0.0126
C16	0.54572(13)	0.41266(9)	0.7943(2)	0.0133
C17	0.58911(14)	0.33872(8)	0.83568(19)	0.0145
C18	0.54533(13)	0.26732(9)	0.7981(2)	0.0155
O1	0.41568(10)	0.19318(7)	0.68496(18)	0.0229
O6	0.18498(10)	0.56655(6)	0.47125(17)	0.0192
O7	0.26846(10)	0.70355(7)	0.56481(17)	0.0199
O12	0.72914(10)	0.70638(7)	0.93153(17)	0.0195
O13	0.81367(10)	0.57082(6)	1.03129(17)	0.0200

Continued on next page

Table A1 — continued from previous page

O18	0.58427(11)	0.19421(6)	0.83644(16)	0.0209
O100	−0.07227(11)	0.55742(9)	0.5735(2)	0.0304
O200	−0.11545(12)	0.67420(8)	1.30833(18)	0.0319
O300	0.10297(12)	0.66840(8)	1.21325(17)	0.0306
O400	0.08209(12)	0.56316(8)	0.9234(2)	0.0311
H11	0.3602	0.1971	0.6563	0.0352
H21	0.3526	0.3370	0.6185	0.0177
H51	0.2863	0.4426	0.5547	0.0156
H61	0.1600	0.5234	0.4498	0.0311
H71	0.3052	0.7414	0.5855	0.0314
H81	0.4311	0.6819	0.7111	0.0182
H111	0.5658	0.6826	0.7869	0.0171
H121	0.7011	0.7425	0.8696	0.0303
H131	0.8359	0.5278	1.0619	0.0306
H141	0.7134	0.4444	0.9501	0.0178
H171	0.6509	0.3383	0.8921	0.0170
H181	0.6372	0.1984	0.8850	0.0325
H1001	−0.0523	0.5894	0.6524	0.0484
H1002	−0.0205	0.5357	0.5320	0.0472
H2001	−0.1494	0.6542	1.2217	0.0504
H2002	−0.1002	0.6417	1.3946	0.0502
H3001	0.1314	0.6452	1.3042	0.0464
H3002	0.0475	0.6725	1.2555	0.0471
H4001	0.0922	0.5916	0.8282	0.0480
H4002	0.0803	0.5887	1.0241	0.0479

Estimated standard deviations are given in parentheses.

Table A.2: SCXRD data collection and refinement details for HHTP·4H_2O at T= 240 K on heating.

Space Group	*Pbcn*
a (Å)	14.2568(2)
b (Å)	16.7791(2)
c (Å)	7.2308(1)
V (Å^3)	1729.73(4)
No. of Reflections($I/\sigma > 2.0$)	1609
Goodness of Fit	0.9963
$R(I/\sigma > 2.0)$	0.0487

Atom	x	y	z	U_{eq}, Å^2
C1	0.45531(11)	0.26762(9)	0.7101(2)	0.0287
C2	0.41209(11)	0.33865(9)	0.6705(2)	0.0267
C3	0.45487(10)	0.41240(8)	0.7092(2)	0.0226
C4	0.40783(10)	0.48771(9)	0.66921(19)	0.0225
C5	0.31771(10)	0.49067(9)	0.5894(2)	0.0257
C6	0.27303(11)	0.56190(9)	0.5557(2)	0.0275
C7	0.31717(11)	0.63343(9)	0.6044(2)	0.0283
C8	0.40490(11)	0.63196(9)	0.6803(2)	0.0278
C9	0.45277(10)	0.56006(9)	0.7117(2)	0.0235
O1	0.41629(9)	0.19451(7)	0.6751(2)	0.0437
O6	0.18630(9)	0.56766(7)	0.4754(2)	0.0384
O7	0.26947(8)	0.70354(7)	0.5698(2)	0.0384
O100	−0.0671(3)	0.5590(3)	0.5476(6)	0.0558(12)
O200	−0.1287(3)	0.6728(2)	1.3105(5)	0.0534(10)
O300	−0.0997(3)	0.6703(2)	1.2830(5)	0.0458(8)

Continued on next page

Table A2 — continued from previous page

Atom	x	y	z	U_{eq}, Å^2
O400	−0.0838(3)	0.5616(2)	0.5923(6)	0.0466(10)
H21	0.3534	0.3384	0.6154	0.0287
H51	0.2892	0.4447	0.5538	0.0288
H81	0.4330	0.6795	0.7127	0.0312
H11	0.3654	0.1974	0.6341	0.0633
H61	0.1668	0.5263	0.4328	0.0532
H71	0.2989	0.7372	0.6232	0.0564
H1001	−0.0642	0.5858	0.6435	0.0763
H1002	−0.0162	0.5381	0.5158	0.0758
H2001	−0.1489	0.6481	1.2185	0.0721
H2002	−0.0994	0.6467	1.3865	0.0713
H3001	−0.1446	0.6692	1.2044	0.0649
H3002	−0.0478	0.6651	1.2312	0.0651
H4001	−0.1234	0.5859	0.6559	0.0644
H4002	−0.0709	0.5844	0.4924	0.0638

Estimated standard deviations are given in parentheses.

.

Table A.3: Temperature dependence of unit cell parameters (heating).

Temperature (K)	**a** (Å)	**b**(Å)	**c**(Å)	V(Å^3)
100	14.20002(19)	16.7353(2)	7.17809(9)	1705.82(4)
110	14.20532(15)	16.73488(19)	7.18143(7)	1707.20(3)
120	14.21093(16)	16.7346(2)	7.18522(8)	1708.75(3)
130	14.21481(15)	16.73492(19)	7.18961(8)	1710.29(3)
140	14.21987(16)	16.7376(2)	7.19397(8)	1712.21(3)
150	14.22557(16)	16.7401(2)	7.19826(8)	1714.18(3)
160	14.22928(16)	16.7414(2)	7.20240(8)	1715.74(3)
170	14.23442(16)	16.7428(2)	7.20560(8)	1717.27(3)
180	14.23847(15)	16.74459(19)	7.20989(8)	1718.96(3)
190	14.24309(16)	16.7493(2)	7.21389(8)	1720.96(3)
200	14.24638(16)	16.7531(2)	7.21670(8)	1722.42(3)
210	14.24903(15)	16.75843(19)	7.22030(8)	1724.14(3)
220	14.25171(15)	16.76451(19)	7.22359(8)	1725.88(3)
230	14.25477(16)	16.7711(2)	7.22697(9)	1727.74(4)
240	14.2568(2)	16.7793(2)	7.2308(1)	1729.73(4)

.

Table A.4: Temperature dependence of unit cell parameters (cooling).

Temperature (K)	**a** (Å)	**b**(Å)	**c**(Å)	V(Å^3)
240	14.2551(3)	16.7783(4)	7.23216(18)	1729.76(8)
230	14.2521(3)	16.7712(4)	7.22817(18)	1727.71(8)
220	14.2508(4)	16.7653(4)	7.22435(18)	1726.04(8)
210	14.2512(4)	16.7650(4)	7.22398(18)	90.005(2)
200	14.2517(4)	16.7647(4)	7.22358(18)	1725.90(8)

Continued on next page

Table A.4 — continued from previous page

Temperature (K)	**a** (Å)	**b**(Å)	**c**(Å)	V(Å^3)
190	14.2448(4)	16.7449(5)	7.2121(2)	1720.30(8)
180	14.2429(4)	16.7414(4)	7.20818(19)	1718.76(8)
170	14.2399(4)	16.7372(4)	7.2040(2)	1716.96(8)
160	14.2380(4)	16.7327(4)	7.2006(2)	1715.47(8)
150	14.2352(4)	16.7291(5)	7.1962(2)	1713.73(9)
140	14.2332(4)	16.7263(5)	7.1923(2)	1712.26(9)
130	14.2312(4)	16.7237(5)	7.1880(2)	1710.73(9)

A.2 The order parameter

Measured intensities for three representative systematic absence violations and the reference (042) reflection are given in Table A.5. The corresponding values of the order parameter ξ and their uncertainties are given in Table A.6; these results are plotted in Fig. A.1.

Table A.5: Selected reflection intensities, averaged over all symmetry equivalent reflections, for HHTP·4H_2O.

T(K)	$I(042)$	$\sigma_I(042)$	$I(071)$	$\sigma_I(071)$	$I(031)$	$\sigma_I(031)$	$I(011)$	$\sigma_I(011)$
100	28488	141	5345	81	763	21	1708	43
110	27580	139	5117	83	773	20	1687	41
120	28133	143	5195	83	789	20	1710	42
130	28433	148	5028	86	792	22	1652	43
140	28329	150	4922	78	780	22	1652	42
150	27562	147	4749	76	773	20	1562	41
160	28343	152	4759	78	796	21	1600	42
170	27993	149	4325	73	752	21	1514	40
180	28188	152	4063	73	693	21	1464	40
190	29205	160	3908	74	680	21	1419	41
200	29269	163	3464	71	597	22	1325	41
210	29772	166	2920	73	476	19	1080	39
220	31408	176	1994	64	365	19	790	36
230	31287	185	929	50	174	17	326	27
240	30318	175	152	29	39	14	74	19

Table A.6: Order parameters for selected reflections for HHTP·4H_2O.

Temperature (K)	$\xi(071)$	$\sigma_\xi(071)$	$\xi(031)$	$\sigma_\xi(031)$	$\xi(011)$	$\sigma_\xi(011)$
100	0.4332	0.0034	0.1637	0.0023	0.2448	0.0031
110	0.4307	0.0037	0.1674	0.0022	0.2473	0.0031
120	0.4297	0.0036	0.1675	0.0022	0.2465	0.0031
130	0.4205	0.0038	0.1669	0.0023	0.2410	0.0032
140	0.4168	0.0035	0.1659	0.0024	0.2415	0.0032

Continued on next page

Table A.6 — continued from previous page

150	0.4151	0.0035	0.1674	0.0023	0.2380	0.0032
160	0.4098	0.0035	0.1676	0.0023	0.2376	0.0032
170	0.3931	0.0035	0.1639	0.0023	0.2325	0.0031
180	0.3797	0.0035	0.1568	0.0024	0.2279	0.0032
190	0.3658	0.0036	0.1526	0.0024	0.2204	0.0032
200	0.3440	0.0037	0.1428	0.0026	0.2128	0.0034
210	0.3132	0.0040	0.1264	0.0026	0.1904	0.0035
220	0.2520	0.0041	0.1078	0.0029	0.1586	0.0037
230	0.1723	0.0047	0.0745	0.0036	0.1021	0.0042
240	0.0707	0.0067	0.0361	0.0063	0.0495	0.0063

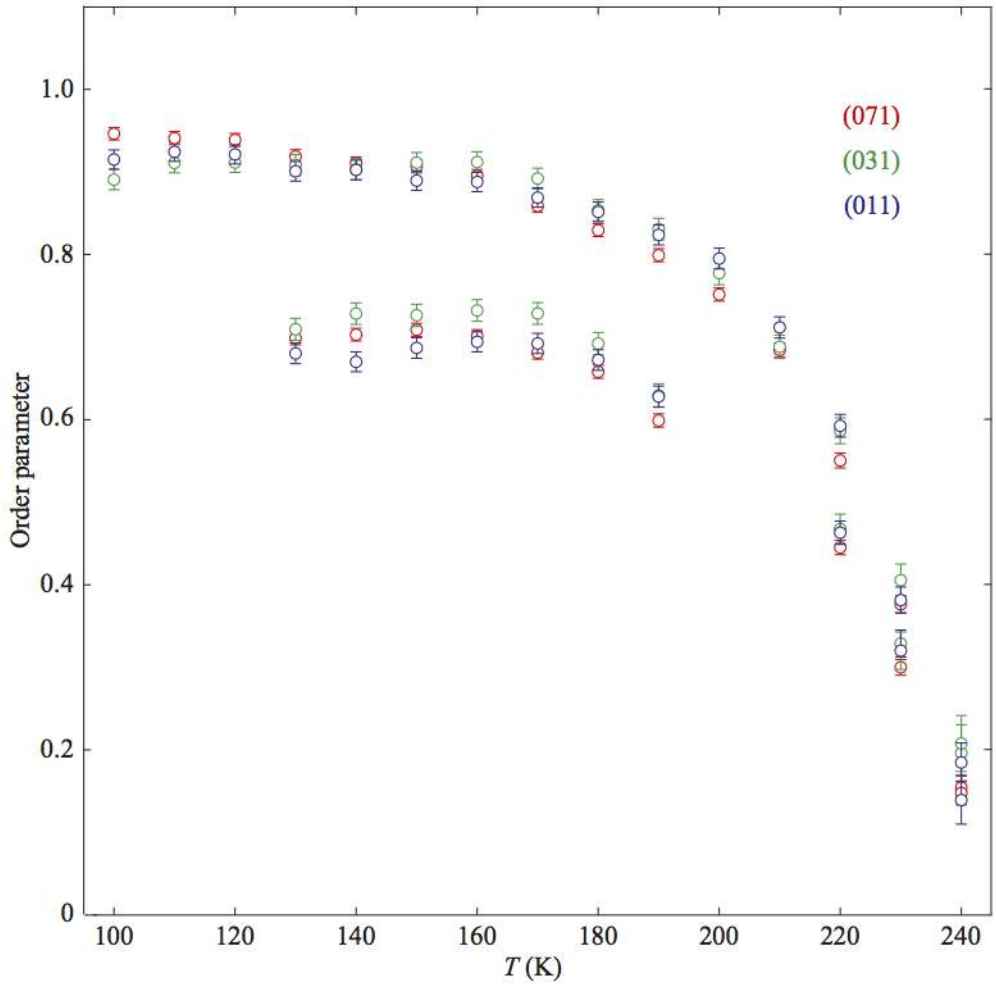

Figure A.1: Thermal dependence of the order parameter plot, indicating the lack of hysteresis on cooling. The discrepancy between the values of the order parameter at low temperature between heating and cooling runs is discussed in the main text.

Appendix B

Experimental data for Ag(tcm)

B.1 SCXRD data

Table B.1: Crystallographic data collection details common to all variable-temperature and variable-pressure SCXRD measurements.

Radiation	Mo $K\alpha$, $\lambda = 0.71073$ Å
Formula	AgC_4N_3
M, g mol^{-1}	197.93
Z	4
Crystal Size (mm)	0.044 mm × 0.052 mm × 0.094 mm
Crystal System	Orthorhombic
Space Group	$Ima2$

Table B.2: SCXRD data collection and refinement details for Ag(*tcm*) at $T = 100\,\mathrm{K}$ on heating.

a (Å)	8.0636(8)			
b (Å)	9.7766(9)			
c (Å)	6.2791(6)			
V (Å^3)	495.01(8)			
R ($I/\sigma > 2.0$)	0.0256			
Atom	x	y	z	U_{eq}, Å^2
Ag1	0.25	0.64736(5)	0.5546(2)	0.0176
N1	0.25	0.5139(8)	0.8313(11)	0.0257
C1	0.25	0.4525(9)	0.9888(12)	0.0162
N2	0.4718(6)	0.6835(5)	0.3470(7)	0.0191
C2	0.5973(7)	0.6570(6)	0.2735(8)	0.0145
C3	0.75	0.6219(9)	0.1798(12)	0.0156

Estimated standard errors are given in parentheses.

Table B.3: SCXRD data collection and refinement details for Ag(*tcm*) at $T = 150\,\mathrm{K}$ on heating.

a (Å)	8.0513(5)			
b (Å)	9.8484(7)			
c (Å)	6.2666(4)			
V (Å^3)	496.89(6)			
R ($I/\sigma > 2.0$)	0.0229			
Atom	x	y	z	U_{eq}, Å^2
Ag1	0.25	0.64833(5)	0.5555(2)	0.0259
N1	0.25	0.5135(7)	0.8310(10)	0.0356
C1	0.25	0.4534(8)	0.9878(11)	0.0234
N2	0.4711(5)	0.6833(4)	0.3439(7)	0.0279
C2	0.5967(6)	0.6559(5)	0.2720(7)	0.0205
C3	0.75	0.6216(8)	0.1795(10)	0.0195

Estimated standard errors are given in parentheses.

Table B.4: SCXRD data collection and refinement details for Ag(*tcm*) at $T = 200\,\mathrm{K}$ on heating.

a (Å)	8.0280(6)			
b (Å)	9.9637(10)			
c (Å)	6.2461(5)			
V (Å^3)	499.62(7)			
R ($I/\sigma > 2.0$)	0.0270			
Atom	x	y	z	U_{eq}, Å^2
Ag1	0.25	0.64942(6)	0.5569(3)	0.0355
N1	0.25	0.5137(9)	0.8300(12)	0.0451
C1	0.25	0.4531(10)	0.9854(13)	0.0297
N2	0.4709(7)	0.6832(5)	0.3420(9)	0.0375
C2	0.5970(8)	0.6562(6)	0.2696(9)	0.0277
C3	0.75	0.6199(9)	0.1765(12)	0.0267

Estimated standard errors are given in parentheses.

Table B.5: SCXRD data collection and refinement details for Ag(*tcm*) at $T = 250\,\mathrm{K}$ on heating.

a (Å)	8.0075(6)			
b (Å)	10.0716(11)			
c (Å)	6.2278(5)			
V (Å^3)	502.26(8)			
R ($I/\sigma > 2.0$)	0.0319			
Atom	x	y	z	U_{eq}, Å^2
Ag1	0.25	0.65070(6)	0.5580(3)	0.0444
N1	0.25	0.5129(9)	0.8300(13)	0.0525
C1	0.25	0.4533(12)	0.9843(16)	0.0451
N2	0.4702(7)	0.6826(5)	0.3389(10)	0.0462
C2	0.5970(8)	0.6557(6)	0.2683(9)	0.0332
C3	0.75	0.6189(10)	0.1742(13)	0.0351

Estimated standard errors are given in parentheses.

Table B.6: SCXRD data collection and refinement details for Ag(*tcm*) at $T = 200\,\mathrm{K}$ on cooling.

a (Å)	8.0260(6)			
b (Å)	9.9680(10)			
c (Å)	6.2459(4)			
V (Å^3)	499.69(7)			
R ($I/\sigma > 2.0$)	0.0300			
Atom	x	y	z	U_{eq}, Å^2
Ag1	0.25	0.64951(6)	0.5567(3)	0.0355
N1	0.25	0.5137(9)	0.8293(14)	0.0469
C1	0.25	0.4521(11)	0.9862(14)	0.0300
N2	0.4697(7)	0.6829(5)	0.3419(9)	0.0372
C2	0.5982(8)	0.6550(6)	0.2697(9)	0.0263
C3	0.75	0.6211(10)	0.1787(13)	0.0277

Estimated standard errors are given in parentheses.

Table B.7: SCXRD data collection and refinement details for Ag(*tcm*) at $T = 150\,\mathrm{K}$ on cooling.

a (Å)	8.047(5)			
b (Å)	9.871(5)			
c (Å)	6.261(5)			
V (Å^3)	497.3(6)			
R ($I/\sigma > 2.0$)	0.0279			
Atom	x	y	z	U_{eq}, Å^2
Ag1	0.25	0.64836(5)	0.5559(2)	0.0259
N1	0.25	0.5146(7)	0.8302(10)	0.0344
C1	0.25	0.4523(9)	0.9877(11)	0.0204
N2	0.4712(6)	0.6838(5)	0.3450(7)	0.0279
C2	0.5975(6)	0.6563(5)	0.2707(8)	0.0200
C3	0.75	0.6208(8)	0.1779(10)	0.0167

Estimated standard errors are given in parentheses.

Table B.8: SCXRD data collection and refinement details for Ag(*tcm*) at $T = 100\,\mathrm{K}$ on cooling.

a (Å)	8.0667(5)			
b (Å)	9.7791(6)			
c (Å)	6.2784(4)			
V (Å^3)	495.27(5)			
R ($I/\sigma > 2.0$)	0.0219			
Atom	x	y	z	U_{eq}, Å^2
Ag1	0.25	0.64735(4)	0.5547(2)	0.0172
N1	0.25	0.5144(7)	0.8319(10)	0.0249
C1	0.25	0.4534(8)	0.9888(10)	0.0155
N2	0.4715(5)	0.6830(4)	0.3459(6)	0.0190
C2	0.5977(6)	0.6562(5)	0.2736(7)	0.0153
C3	0.75	0.6208(7)	0.1795(10)	0.0138

Estimated standard errors are given in parentheses.

Table B.9: SCXRD data collection and refinement details for Ag(*tcm*) at $p = 0.08\,\mathrm{GPa}$.

a (Å)	7.9645(10)			
b (Å)	10.138(6)			
c (Å)	6.1945(10)			
V (Å^3)	500.2(3)			
R ($I/\sigma > 2.0$)	0.0451			
Atom	x	y	z	U_{eq}, Å^2
Ag1	0.25	0.6515(3)	0.5594(7)	0.0632
N1	0.25	0.514(4)	0.823(2)	0.050(3)
C1	0.25	0.459(4)	0.981(3)	0.048(3)
N2	0.4678(15)	0.6830(17)	0.3405(19)	0.050(2)
C2	0.5981(18)	0.652(3)	0.267(2)	0.048(2)
C3	0.75	0.615(3)	0.175(4)	0.048(2)

Estimated standard errors are given in parentheses.

Table B.10: SCXRD data collection and refinement details for Ag(*tcm*) at $p = 0.83\,\mathrm{GPa}$.

a (Å)	8.0121(13)			
b (Å)	9.646(6)			
c (Å)	6.2169(15)			
V (Å^3)	480.5(3)			
R ($I/\sigma > 2.0$)	0.0581			
Atom	x	y	z	U_{eq}, Å^2
Ag1	0.25	0.6517(4)	0.5559(10)	0.0557
N1	0.25	0.506(5)	0.828(4)	0.050(4)
C1	0.25	0.443(6)	0.987(4)	0.050(4)
N2	0.473(2)	0.684(2)	0.344(3)	0.050(4)
C2	0.600(2)	0.656(3)	0.272(3)	0.050(4)
C3	0.75	0.629(7)	0.180(5)	0.050(4)

Estimated standard errors are given in parentheses.

Lattice parameter values, y_{N2} values, and derived θ values obtained from structural refinements against variable-temperature SCXRD data are given in Tables B.11–B.20 (warming and cooling runs, respectively). The data at two temperatures (160 and 170 K) in the warming cycle were not of sufficient quality to obtain reliable positional parameters, so only lattice parameters are reported for these temperatures.

Table B.11: Variable-temperature structural parameter data as determined on warming using SCXRD.

T(K)	a (Å)	b (Å)	c (Å)	y_{N2}	θ (°)
100	8.0636(8)	9.7766(9)	6.2791(6)	0.6835(5)	59.49(13)
110	8.0597(6)	9.7942(7)	6.2760(4)	0.6845(4)	59.87(11)
120	8.0580(5)	9.8108(7)	6.2729(4)	0.6835(4)	59.71(11)
130	8.0556(5)	9.8297(7)	6.2697(4)	0.6838(5)	59.91(13)
140	8.0513(5)	9.8484(7)	6.2666(4)	0.6843(5)	60.17(13)
150	8.0584(6)	9.8752(8)	6.2692(5)	0.6833(4)	60.01(11)
160	8.0564(6)	9.8969(9)	6.2670(5)	0.6835(4)	60.19(11)
170	8.0523(6)	9.9156(9)	6.2625(5)	0.6830(4)	60.18(11)
190	8.0297(5)	9.9450(9)	6.2504(4)	0.6840(5)	60.70(14)
200	8.0280(6)	9.9637(10)	6.2461(5)	0.6832(5)	60.61(14)
210	8.0226(6)	9.9881(10)	6.2426(5)	0.6824(5)	60.54(14)
220	8.0197(6)	10.0080(11)	6.2384(5)	0.6825(5)	60.70(14)
230	8.0149(6)	10.0302(11)	6.2344(4)	0.6826(5)	60.87(14)
240	8.0109(6)	10.0514(11)	6.2310(4)	0.6825(5)	60.98(14)
250	8.0075(6)	10.0716(11)	6.2278(4)	0.6826(5)	61.13(14)

Estimated standard errors are given in parentheses.

Table B.12: Variable-temperature structural parameter data as determined on cooling using SCXRD.

T(K)	a (Å)	b (Å)	c (Å)	y_{N2}	θ (°)
240	8.0119(6)	10.0501(11)	6.2301(4)	0.6828(6)	61.06(16)
230	8.0148(6)	10.0301(10)	6.2349(4)	0.6828(6)	60.92(16)
220	8.0189(6)	10.0092(11)	6.2378(5)	0.6824(5)	60.69(14)
210	8.0224(6)	9.9884(10)	6.2417(4)	0.6828(5)	60.66(14)
200	8.0260(6)	9.9680(10)	6.2459(4)	0.6829(5)	60.55(14)
190	8.0318(6)	9.9472(9)	6.2491(4)	0.6833(5)	60.53(14)
180	8.0359(5)	9.9261(8)	6.2525(4)	0.6829(5)	60.29(14)
170	8.0389(6)	9.9083(8)	6.2553(4)	0.6839(5)	60.45(14)
160	8.0428(6)	9.8892(8)	6.2586(4)	0.6838(5)	60.30(14)
150	8.0469(6)	9.8711(8)	6.2615(4)	0.6838(5)	60.19(14)
140	8.0492(5)	9.8524(7)	6.2644(4)	0.6837(5)	60.04(14)
130	8.0526(5)	9.8334(7)	6.2677(4)	0.6835(4)	59.87(11)
120	8.0572(5)	9.8159(7)	6.2707(4)	0.6844(4)	60.00(11)
110	8.0621(5)	9.7970(7)	6.2755(4)	0.6832(4)	59.54(11)
100	8.0667(5)	9.7791(6)	6.2784(4)	0.6835(5)	59.51(140

Estimated standard errors are given in parentheses.

B.2 Powder neutron diffraction data

Table B.13: Lattice parameters and unit cell content obtained from powder neutron diffraction data refinement for Ag(*tcm*) at $p = 0.118(5)$ GPa.

a (Å)	7.9913(6)			
b (Å)	10.1589(5)			
c (Å)	6.2122(5)			
V (Å^3)	504.33(6)			
R_{wp}	0.04139			
Atom	x	y	z	U_{iso}, Å^2
Ag1	0.25	0.651(2)	0.542(3)	0.0521(7)
N1	0.25	0.5123(3)	0.8173(8)	0.0309(17)
C1	0.25	0.44925(13)	0.9803(3)	0.0309(17)
N2	0.4649(6)	0.6842(2)	0.3332(4)	0.0309(17)
C2	0.5939(3)	0.65754(13)	0.2605(2)	0.0309(17)
C3	0.75	0.62515(19)	0.1727(4)	0.0309(17)

Estimated standard errors are given in parentheses.

Lattice parameter values, y_{N2} values, and derived θ values obtained from structural refinements against variable-pressure powder neutron diffraction data are given in Table B.20.

Table B.14: Lattice parameters and unit cell content obtained from powder neutron diffraction data refinement for Ag(*tcm*) at $p = 0.190(5)$ GPa.

a (Å)	7.9910(6)			
b (Å)	10.1231(5)			
c (Å)	6.2142(5)			
V (Å^3)	502.69(6)			
R_{wp}	0.04078			
Atom	x	y	z	U_{iso}, Å^2
Ag1	0.25	0.648(2)	0.535(3)	0.046(6)
N1	0.25	0.5131(3)	0.8168(8)	0.039(2)
C1	0.25	0.44929(14)	0.9805(3)	0.039(2)
N2	0.4644(6)	0.6842(2)	0.3339(4)	0.039(2)
C2	0.5938(3)	0.65749(14)	0.2605(2)	0.039(2)
C3	0.75	0.6253(2)	0.1719(4)	4.3(4)

Estimated standard errors are given in parentheses.

Table B.15: Lattice parameters and unit cell content obtained from powder neutron diffraction data refinement for Ag(*tcm*) at $p = 0.265(6)$ GPa.

a (Å)	7.9924(7)			
b (Å)	10.0646(6)			
c (Å)	6.2175(6)			
V (Å^3)	500.13(7)			
R_{wp}	0.04126			
Atom	x	y	z	U_{iso}, Å^2
Ag1	0.25	0.646(2)	0.544(3)	0.047(7)
N1	0.25	0.5135(3)	0.8161(8)	0.037(2)
C1	0.25	0.44933(14)	0.9806(3)	0.037(2)
N2	0.4639(6)	0.6842(2)	0.3342(4)	0.037(2)
C2	0.5937(3)	0.65744(13)	0.2605(2)	0.037(2)
C3	0.75	0.6253(2)	0.1717(4)	4.0(4)

Estimated standard errors are given in parentheses.

Table B.16: Lattice parameters and unit cell content obtained from powder neutron diffraction data refinement for Ag(*tcm*) at $p = 0.336(6)$ GPa.

a (Å)	7.9931(7)			
b (Å)	10.0142(6)			
c (Å)	3.2207(7)			
V (Å^3)	497.93(8)			
R_{wp}	0.04109			
Atom	x	y	z	U_{iso}, Å^2
Ag1	0.25	0.652(2)	0.543(3)	0.060(8)
N1	0.25	0.5140(3)	0.8162(8)	0.032(2)
C1	0.25	0.44938(14)	0.9807(4)	0.032(2)
N2	0.4635(6)	0.6842(2)	0.3348(4)	0.032(2)
C2	0.5936(3)	0.65743(13)	0.2604(2)	0.032(2)
C3	0.75	0.6252(2)	0.1712(4)	4.1(4)

Estimated standard errors are given in parentheses.

Table B.17: Lattice parameters and unit cell content obtained from powder neutron diffraction data refinement for Ag(*tcm*) at $p = 0.409(6)$ GPa.

a (Å)	7.9930(10)			
b (Å)	9.9639(7)			
c (Å)	6.2228(10)			
V (Å^3)	495.59(10)			
R_{wp}	0.04092			
Atom	x	y	z	U_{iso}, Å^2
Ag1	0.25	0.651(2)	0.540(3)	0.055(7)
N1	0.25	0.5144(3)	0.8153(8)	0.035(2)
C1	0.25	0.44943(14)	0.9808(4)	0.035(2)
N2	0.4630(6)	0.6845(2)	0.3353(4)	0.035(2)
C2	0.5935(3)	0.65741(13)	0.2604(2)	0.035(2)
C3	0.75	0.6251(2)	0.1707(4)	0.035(2)

Estimated standard errors are given in parentheses.

Table B.18: Lattice parameters and unit cell content obtained from powder neutron diffraction data refinement for Ag(*tcm*) at $p = 0.500(6)$ GPa.

a (Å)	7.9990(11)			
b (Å)	9.9097(8)			
c (Å)	6.2218(12)			
V (Å^3)	493.19(12)			
R_{wp}	0.04243			
Atom	x	y	z	U_{iso}, Å^2
Ag1	0.25	0.646(2)	0.547(3)	0.046(7)
N1	0.25	0.5156(3)	0.8163(9)	0.029(2)
C1	0.25	0.44962(15)	0.9812(4)	0.029(2)
N2	0.4631(6)	0.6847(2)	0.3361(4)	0.029(2)
C2	0.5936(3)	0.65735(13)	0.2603(2)	0.029(2)
C3	0.75	0.6246(2)	0.1697(4)	0.029(2)

Estimated standard errors are given in parentheses.

Table B.19: Lattice parameters and unit cell content obtained from powder neutron diffraction data refinement for Ag(*tcm*) at $p = 0.615(6)$ GPa.

a (Å)	8.0013(10)			
b (Å)	9.8347(8)			
c (Å)	6.2239(11)			
V (Å^3)	489.77(11)			
R_{wp}	0.04119			
Atom	x	y	z	U_{iso}, Å^2
Ag1	0.25	0.648(2)	0.548(3)	0.034(6)
N1	0.25	0.5146(3)	0.8147(5)	0.036(2)
C1	0.25	0.44977(15)	0.9817(4)	0.036(2)
N2	0.4634(7)	0.6864(3)	0.3371(5)	0.036(2)
C2	0.5941(3)	0.65751(14)	0.2603(2)	0.036(2)
C3	0.75	0.6232(2)	0.1685(4)	0.036(2)

Estimated standard errors are given in parentheses.

Table B.20: Variable-pressure structural parameter data as determined using powder neutron diffraction.

p (GPa)	a (Å)	b (Å)	c (Å)	y_{N2}	θ (°)
0.118(5)	7.9913(6)	10.1589(5)	6.2122(5)	0.6842(2)	62.14(6)
0.190(5)	7.9910(6)	10.1231(5)	6.2142(5)	0.6842(2)	61.92(6)
0.265(6)	7.9924(7)	10.0646(6)	6.2175(5)	0.6842(2)	61.63(6)
0.336(6)	7.9931(7)	10.0142(6)	6.2207(7)	0.6842(2)	61.34(6)
0.409(6)	7.9930(10)	9.9639(7)	6.2228(10)	0.6845(2)	61.16(6)
0.500(6)	7.9990(11)	9.9097(8)	6.2218(11)	0.6847(2)	60.95(7)
0.615(6)	8.0013(10)	9.8347(5)	6.2239(11)	0.6864(3)	61.01(7)

Estimated standard errors are given in parentheses.

B.3 High pressure phase

Table B.21: Powder neutron diffraction data Pawley refinement and X-ray single-crystal unit cell determination for the high-pressure phase of Ag(*tcm*).

	Neutron powder	X-ray single-crystal	
p (GPa)	0.672(7)	1.47	2.39
a (Å)	7.9969(15)	8.028(4)	8.019(3)
b (Å)	9.7908(19)	9.290(18)	8.922(15)
c (Å)	6.2265(8)	6.193(3)	6.189(4)
β (°)	90.369(14)	90.30(6)	91.21(5)
V (Å^3)	487.50(14)	461.9(11)	442.7(8)

Estimated standard errors are given in parentheses.

Appendix C

Experimental data for $Ni(CN)_2$

Table C.1: Crystallographic data collection details common to all variable-pressure PXRD measurements for $Ni(CN)_2$.

Formula	NiC_2N_2
M, g mol^{-1}	110.73
Z	16
Crystal System	Tetragonal
Space Group	$I4_1/amd$

C.1 Powder neutron diffraction data

Table C.2: Lattice parameters for neutron diffraction data (GSAS Rietveld refinement) for tetragonal $Ni(CN)_2$.

Pressure (GPa)	**a** (Å)	**c**(Å)	V(Å^3)
0.00	4.8580(5)	12.803(4)	302.1(12)
0.18(5)	4.8565(5)	12.620(4)	297.6(11)
0.28(5)	4.8534(5)	12.516(4)	294.8(11)

Table C.2 — continued from previous page

0.38(5)	4.8535(5)	12.453(4)	293.3(11)
0.49(5)	4.8523(5)	12.385(4)	291.6(11)
0.54(7)	4.8521(6)	12.337(4)	290.4(13)
0.65(8)	4.8502(7)	12.279(5)	288.8(15)
0.78(5)	4.850(12)	12.195(9)	286.9(25)

C.2 Powder synchrotron X-ray diffraction data

Table C.3: Lattice parameters for synchrotron diffraction data (GSAS Rietveld refinement) for tetragonal $Ni(CN)_2$.

Pressure (GPa)	**a** (Å)	**c**(Å)	V(Å^3)
0.2(1)	4.8444(7)	12.718(5)	298.4(15)
0.58(8)	4.8355(6)	12.368(4)	289.2(14)
1.0(16)	4.8318(5)	12.184(3)	284.4(11)
1.53(8)	4.8280(8)	11.971(5)	279.0(17)
2.4(16)	4.8213(25)	11.61(15)	269.9(30)